Solution-Processable Oligomeric and Small Molecule Semiconductors for Organic Solar Cells

by
Mylène Le Borgne

A thesis

presented to the University of Waterloo

in fulfilment of the

thesis requirement for the degree of

Doctor of Philosophy

in

Chemical Engineering

Waterloo, Ontario, Canada, 2016

© Mylène Le Borgne 2016

Author’s Declaration

I hereby declare that I am the sole author of this thesis. This is a true copy of the thesis, including any required final revisions, as accepted by my examiners.

I understand that my thesis may be made electronically available to the public.

Abstract

Organic solar cells appear as a promising technology within photovoltaic field owing to their low-cost fabrication and their great flexibility enabling a widespread distribution. For now, they are still at the prototype stage due to their limited efficiency and lifetimes. Many efforts were realized in designing new materials as they are involved in every steps of the photovoltaic process and thus they dictate the cell efficiency. Along this thesis, two series of electron-donating semi-conductors were designed and synthesized. The first series consist in three oligomers containing three diketopyrrolopyrrole units, a well-studied chromophore. Those oligomers absorb up to the near infra-red region, a very interesting feature for light harvesting. Through the engineering of electron-rich spacers, various twists were generated in the oligomers backbone. The oligomer showing a coplanar conformation appears to be the most crystalline and thus exhibits the best charge transport properties with a hole mobility of 10^{-3} $cm^2.V^{-1}.s^{-1}$. However, bulk heterojunction organic solar cells, this high crystallinity results in an unfavorable morphology and a PCE inferior to 1%. As for the second series, the four small molecules combined 3,3'-(ethane-1,2-diylidene)bis(indolin-2-one) (EBI), an electron deficient unit, and various electron-rich units such as thiophene (EBI-T), benzofuran (EBI-BF) and bithiophene (EBI-2T). Among EBI derivatives, EBI-BF demonstrated the highest hole mobility of 0.021 $cm^2.V^{-1}.s^{-1}$ in field effect transistors due to its coplanar conformation. Meanwhile, in bulk heterojunction solar cells, the highest PCE of 1.92% was obtained with EBI-2T:$PC_{61}BM$ blend owing to a more appropriate morphology and the broadest absorption spectrum of EBI-2T.

Keywords: Oligomer, DPP, small molecules, EBI, organic solar cell

---

Research Units

IMS, CNRS UMR5218, 16 avenue Pey-Berland, 33607 PESSAC CEDEX

University of Waterloo (UW), QNC, 200 University Ave W, Waterloo, ON N2L 3G1, Canada

LOF, Solvay, 178, avenue du Dr Schweitzer F-33608 Pessac, France

MOBILITY SCHEME

	OCT-DEC 2012	JAN – AOUT 2013	SEPT-DEC 2013	2014	JAN 2015 – AVRIL 2016
IMS	**X**		**X**		**X**
UW		**X**		**X**	

Acknowledgements

I had the chance to realize this thesis at the University of Waterloo (Canada) and the University of Bordeaux (France) in the framework of IDS-FUNMAT program. In Waterloo, I was part of the chemical engineering department and in Bordeaux I studied at the laboratoire de l'Intégration du Matériau au Système (IMS). Moreover, I have the great opportunity to collaborate with Solvay on this research project.

I would like to acknowledge first the University of Bordeaux and the University of Waterloo to fund this thesis for three and a half years. I further acknowledge Solvay for their financial support to cover some of the research and travel expences

I acknowledge the committee members, Pr. Philippe Riche, Dr. Kathleen Moineau-Chane Ching, Dr. Nicolas Leclerc, Pr. Hany Aziz, Dr. Neil McManus for the interest they give to my work and the fruitful discussion along the defense.

I am truly grateful to Dr. Guillaume Wantz and Pr. Yuning Li for their guidance and help along this thesis. I would like to thank Dr. Wantz to trust me on this thesis and for his support all through these years and for his great advices in device fabrication and optimization. I would like to express my gratitude to Pr. Li for welcoming me in his group and for sharing with me his great expertise in organic chemistry and molecular design. I wish to address my sincere gratitude to Dr. Patrick Maestro to give me the opportunity to work at LOF and his availability and his concern for my PhD. I am highly grateful to Bertrand Pavageau and Dr. Marie Béatrice Madec for their constant and valuable advices and their great contribution to my research.

I further acknowledge Pr. Natalie Stingelin and Dr. Jaime Martin for welcoming me at Imperial College for two weeks and for teaching me how to elaborate a phase diagram, and for their sharp observations. I would like to thank Sabine Goma for the XRD measurements and Julien Jolly for his help in DSC measurements.

I had the great pleasure to work at IMS. I wish to thank all members of ELORGA and PRISM team, I have learnt so much along these three years thanks to you. I would like to thank Dr Sylvain Chambon and Dr. Mamatiminin Abbas for their help and insights on organic solar cell and field effect transistors. I have shared great times at coffee breaks, CAES and afterwork with Lionel, Léo, Fred (les BGs!!!!!), Clémence (et oui, je t'ai pas oublié), Yolande (bon courage pour le CAES!), Thérèse, Elo, Florence (la team des petites molécules), Geoffroy (Fillot !!!), Gildas

(compatriote breton), Frank (Terrible !), PH, William, Aurélien (Vive les squats !) , Damien, Marco, Marina.

I would like to thank Judy Caron for her constant guidance in all administrative papers and Jane Venne for her help in NMR measurements. I am grateful to my comrade from Waterloo, especially Jesse for DFT calculations but also his support and advices, An for welcoming me in the group, Wei for his great advices on DPP synthesis, Austin, Bin and Chang for their kindness.

This thesis would not have been possible without IDS FunMat program, I wish to express my sincere gratitude to Pr. Laurent Servant and Dr. Thierry Toupance for their availability each times I have administrative issues. I would like to express my sincere gratitude to my comrade from IDS-FunMat program, Uyxing (Mentor scientifique et sportif,! Merci pour ton aide!), Erin (Thanks for welcoming me in Waterloo, it would not have been the same without you !), Mehdi (à quand le prochain Gradhouse??), Edgar (I couldn't have done it without you, I would have been so lost!!!), Dan & Cameron, Edis, Jiang …

I would not have completed this thesis without the great support of my family and close friends. There is no word to thank you enough.

Table of Contents

List of Figures

List of Tables

List of Schemes

List of Acronyms

A: electron-deficient

Acceptor: electron-accepting

AFM: atomic force microscopy

AM: air mass

BDT: benzodithiophene

BDTP: benzodifurane

BHJ: bulk heterojunction

BT: benzothiadiazole

CIGS: copper indium gallium selenide

CN: 1-chloronaphtalene

CTE: charge transfer exciton

CV: cyclic voltammetry

D: electron-rich

DFT: density functional theory

DIO: 1,8-diiodooctane

Donor: electron-donating

DPP: diketopyrrolopyrrole

DSC: differential scanning microscopy

DSSC: dye sensitized solar cells

DTP: dihtienopyrane

DTS: dithienosilole

E_g: band gap

EBI: 3,3'-(ethane-1,2-diylidene)bis(indolin-2-one)

EQE: external quantum efficiency

Fc: ferrocene

FF: fill factor

HOMO: highest occupied molecular orbital

HR-MS: high resolution mass spectrometry

ICT: intramolecular charge transfer

I_{SC}: short circuit current

ITO: indium tin oxide

J_{SC}: short circuit current density

LUMO: lowest unoccupied molecular orbital

MW: molecular weight

NMR: nuclear magnetic resonance

OSC: organic solar cell

OTFT: organic thin film transistor

$PC_{61}BM$: [6,6]-phenyl-C_{61}-butyric acid methyl

$PC_{71}BM$: [6,6]-phenyl-C_{71}-butyric acid methyl ester

PCE: power conversion efficiency

PEDOT:PSS: poly(3,4-ethylenedioxythiophene) polystyrene sulfonate

P_{max}: maximal power

PDMS: polydimethylsiloxane

PS: polystyrene

PV: photovoltaic

R_S: series resistance

R_{SH}: shunt resistance

TPA: triphenyl amine

V_{OC}: open circuit voltage

XRD: X-ray diffraction

INTRODUCTION

World energy consumption has been increasing over the years while major conventional energy resources such as fossil oil, coal, and natural gas are rapidly depleting. Fossil fuel-based energy, which has, until now, satisfied the global world energy demand, is both limited and polluting. It is imperative that a green, sustainable and efficient alternative be found. Among the many renewable energy sources that have been proposed (such as wind, solar, nuclear, hydroelectricity or biofuels), solar energy is one of the most promising. The most common technique is to convert solar radiation into electricity via the photovoltaic process - first discovered by Becquerel in 1839 [1], and followed 44 years later by the fabrication of the first solar cell by Charles Fritts in 1883 [2].

To date, there are mainly three generations of photovoltaic devices. The first generation of solar cells is based on (multi)crystalline silicon semiconductors. This technology is currently dominating the solar cell market, thanks to the high efficiency, reliability and abundance of silicon. Power conversion efficiencies of first generation solar cells have reached as high as 25 % [3]. However, silicon solar panels are rigid and fragile, and their fabrication requires many energy-consuming steps. Solar cell grade silicon must have a high degree of purity and be processed at high temperatures. These requirements make the first generation solar cells expensive and limit their widespread application.

The second generation of solar cells is based on thin film inorganic semiconductors principally fabricated from amorphous silicon, cadmium telluride (CdTe), or copper indium gallium selenide (CIGS). These devices demonstrate decent power conversion efficiencies of 12-20% and appear less rigid than their predecessors. Nonetheless, the fabrication costs for these thin film solar cells remain high because high temperature processing is still required [4,5].

Organic solar cells (OSC) are considered to be part of the third generation of solar cells together with Dye Sensitized Solar Cells (DSSC) [6,7] and hybrid organic-inorganic perovskites [8,9]. OSC are made of π-conjugated organic semiconductor materials sandwiched between two electrodes. This new technology have the potential to allow fully flexible devices with lower fabrication costs than first and second generations [10,11]. Organic semiconductors can be deposited at low temperature by solution processing techniques such as roll-to-roll [12], ink jet printing [13] and screen printing techniques [14]. These deposition techniques are compatible with any substrate including plastic foils. The resulting mechanical flexibility and ability to be deposited on curved substrates allow OSCs to be fabricated on a wide range of objects and maximizes the use of surface areas [10,11]. However, OSCs have not reached the

commercialization stage yet. Figure 1 displays the NREL report of best research-cell efficiencies which enables to place OSCs into PV context. Even if production costs are effectively low, their rather low efficiencies and limited lifetimes present challenges that must be addressed to enable the large scale production.

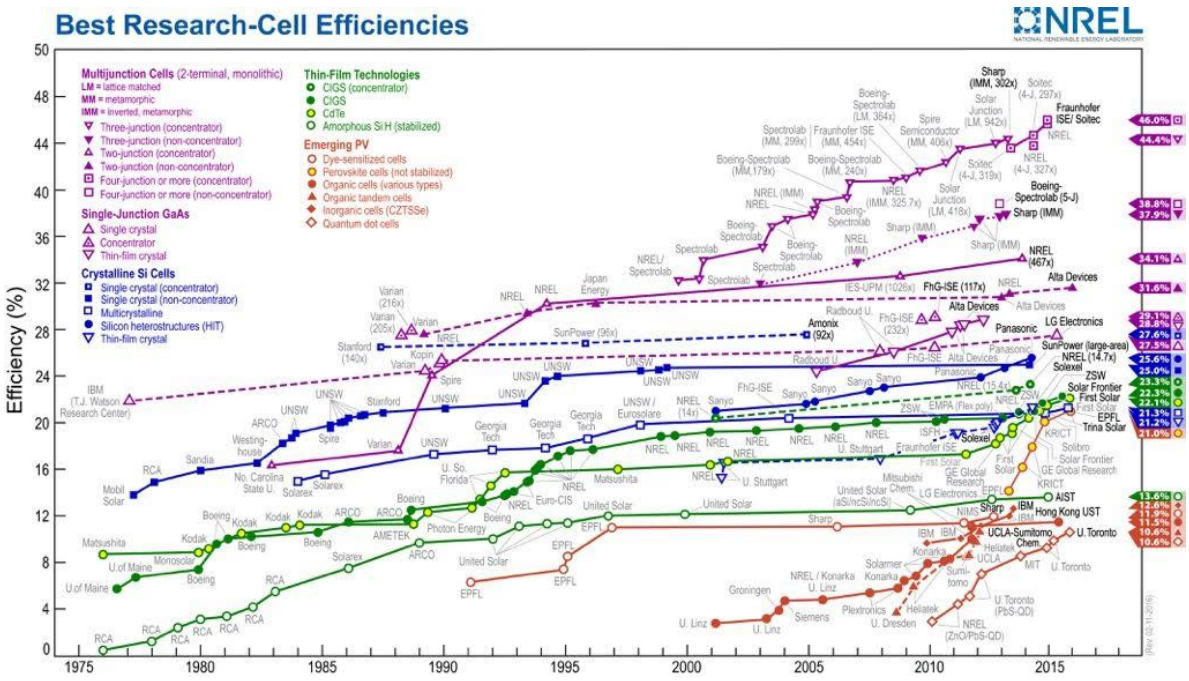

Figure 1: NREL's best research solar cell efficiencies as of February 11th, 2016

This thesis aims to develop and synthesize two sets of solution-processable electron donating semiconductors (donors): one based on the well-known diketopyrrolopyrrole (DPP) group and the other made of a new electron-deficient building block regarding OSC field, the 3,3'-(ethane-1,2-diylidene)bis(indolin-2-one) (EBI). The optoelectronic properties were investigated to confirm their potential for photovoltaic application and establish a correlation with their molecular backbone. In a second phase, all molecules were introduced in OSC devices to explore their photovoltaic properties. A particular attention was addressed to the morphology of the active layer which is critical to achieve high efficiency OSCs. The miscibility and the co-organization of electron donating and electron accepting semiconductors were studied to understand the build-up of the morphology and extract some insights into the optimization of the OSC fabrication process.

Chapter 1, first, describes the photovoltaic process and delineates the challenges in making efficient OSC and in designing novel donor semiconductors. In the second stage, it introduces the objectives of this research. Chapter 2 summarizes all the experimental methods used along this research. Chapter 3 is related to DPP derivatives and details their synthesis, their optoelectronic properties and behavior in OSC. Chapter 4 refers to EBI derivatives and, similarly

to chapter 3, presents the study on those materials. To finish, chapter 5 summarizes and concludes on this research embedding some perspectives for future works

CHAPTER 1: GENERAL BACKGROUND

1. ORGANIC SOLAR CELL

1.1. Principle

An organic solar cell (OSC) aims to convert the photon sent by the sun into free charge carriers and thereby into electrical power. An OSC is composed of an active layer containing an electron-accepting (acceptor) and an electron donating (donor) semiconductors sandwiched between two electrodes. The photovoltaic process can be divided into five steps:

1-Absorption of a photon and generation of an exciton by either donor or acceptor
2-Diffusion of the exciton to a donor/acceptor interface
3-Transfer of the charge from donor to acceptor or from acceptor to donor and formation of charge transfer exciton (CTE)
4-Separation of CTE into free charges
5-Charge transport and collection

These five steps are represented in Figure 2 through the energetic scheme of donor/acceptor and simulating a photon absorption by the donor.

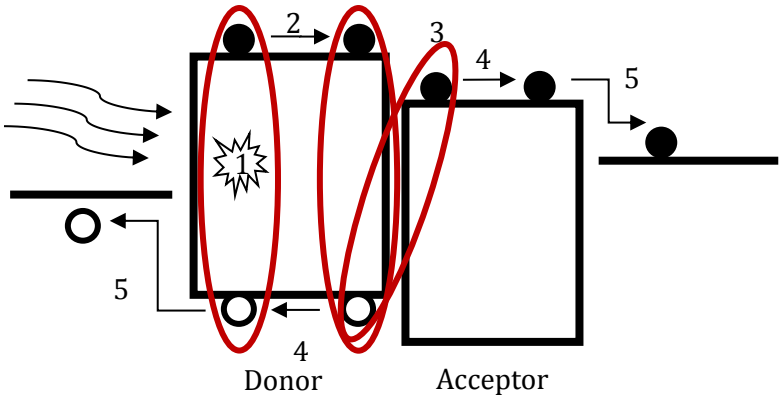

Figure 2: Photovoltaic process

The first step of the photovoltaic process consists in the absorption of photons received from the sunlight by the donor and acceptor organic semiconductors. Organic semiconductors are π-conjugated molecules that have alternating π and σ bonds. Their energy diagram is composed of discontinuous energy levels. In the ground state, electrons fill first the lower energy levels in accordance with the Pauli Exclusion Principle. The highest occupied molecular orbital and the

lowest unoccupied orbital by electrons are respectively called HOMO and LUMO level. The difference in energy between these two levels is referred to as the band gap. For a photon to be absorbed, its energy must be equal or greater than the band gap to excite an electron from the HOMO into higher energy levels. When excited, the empty site left in the HOMO by the excited electron (known as hole) remains electrostatically bound to the excited electron, forming a pair called exciton. There are two-types of excitons: the Frenkel exciton with a strong binding energy (E_b>0.1 eV) and the Wannier exciton with a weak binding energy (E_b < 0.01 eV). In inorganic semiconductors, Wannier excitons are formed with exciton binding energy lower than the thermal energy at room temperature (K_{bT} at 298 K) and as such, excitons are easily separated to generate free charges. However, in the case of organic semiconductors, the greater electric permittivity inherent to organic materials results in Frenkel excitons with a much higher exciton binding energy, so a higher driving force is required to separate the charges.

The first OSC fabricated by Kallmann [15], made of one semiconductor, showed efficiency lower than 0.1% because exciton did not have any driving force to separate in free charges and recombine instead. In 1986, Tang *et al.* discover that to successfully operate, an OSC needs two types of semiconductors: a donor and an acceptor [16]. The difference between their energy levels gives charges enough driving force to overcome the binding energy of the exciton. Therefore, an exciton generated within the donor, for instance, must migrate to a donor/acceptor interface where the electron will transfer to the acceptor's more stabilized LUMO. The remaining hole and the transferred electron are forming now a charge transfer exciton which is spontaneously further broken into free charges. Electrons then migrate through the acceptor semiconductor to the cathode and holes through the donor semiconductor to the anode. Both electrons and holes are finally collected by their respective electrodes.

1.2. Characterizations

The efficiency of a solar cell is determined by the efficiency of each step of the process: η_{abs} for photon absorption, η_{ED} for exciton diffusion, η_{CS} for charge separation and η_{cc} for charge collection. The external quantum efficiency η_{EQE} is the product of all of these efficiencies and represents the overall efficiency of OSCs [11,17–19]:

$$\boldsymbol{\eta_{EQE} = \eta_{abs}(\lambda) \times \eta_{ED} \times \eta_{CS}(V) \times \eta_{cc}}$$

1.2.1. Absorption efficiency

Prior to define absorption efficiency, a particular attention must be attributed to the solar spectrum. The sun presents similar emissive spectrum as a black body at 5 900 K, however, the atmosphere filters some solar radiations and thereby confines the solar spectrum between the far

infrared and the near ultraviolet. Some models called Air Mass (AM) were developed to characterize the sunlight emissive spectra at different path length through the atmosphere. For instance, AM0 corresponds to the spectrum outside the atmosphere and AM1 to a radiation arriving at normal incident at the Earth surface. Only equatorial and tropical regions are exposed to radiation of AM1, so the photovoltaic community agrees on using the model AM 1.5 to evaluate OSC efficiency [20]. AM 1.5 refers to an incident radiation arriving with an angle of 48.2° compared to Earth surface with an intensity fixed at 1 000 $W.m^{-2}$. Figure 3 shows the solar spectrum at AM 1.5.

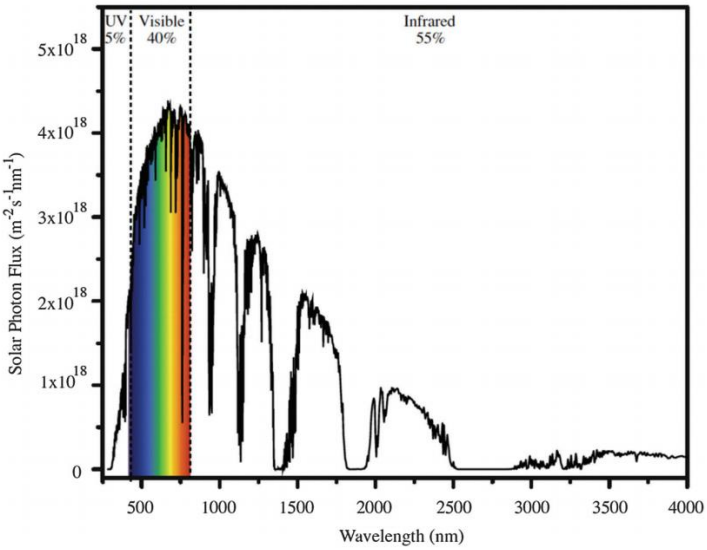

Figure 3: Solar emissive spectrum (AM 1.5) [21][1]

Absorption efficiency corresponds to the ratio of the number of generated excitons to the number of photons received by the active layer. The absorption step mainly relies on the broadness of the absorption spectrum of the donor/acceptor system and how it matches with the solar spectrum emitting from 300 nm to near infrared (Figure 3). Fullerene derivatives, generally employed as acceptor semiconductor, absorb in a limited range of 300-400 nm, overlapping poorly the solar spectrum. Consequently, the donor semiconductor becomes the main actor in light absorption and thereby must have a low band gap around 1.2 eV to optimally cover the solar spectrum up to 1 034 nm (infrared limit). Additionally, higher is the absorption coefficient of the donor and thicker is the active layer, more efficient is the absorption.

1.2.2. Exciton diffusion

Exciton diffusion is defined and limited by the semiconductor's exciton diffusion length, which is the average distance that excitons can diffuse before recombination [19]. In organic semiconductors, the exciton diffusion length is typically on the order of 1-10 nm [18,22], much

[1] Published by the Royal Society of Chemistry, reproduced here with permission

shorter than those of their inorganic counterparts. Only excitons that are formed within a distance from donor/acceptor interfaces not further than the exciton diffusion length can be separated into free charges, otherwise excitons recombine. Geminate recombination corresponds to excitons that recombine before being separated into free charges and is one of the main recombination mechanisms that limit the photovoltaic process. Exciton diffusion length can be stretched by increasing intermolecular interactions and improving the molecular packing.

1.2.3. Exciton separation

Charge separation efficiency is the ratio between generated free charges to the number of excitons. For instance, excitons, formed in donor, can efficiently get separated at the donor/acceptor interfaces if the gap between the LUMO's of both materials is large enough. According to the literature, 0.3 eV is the minimal value to give electrons enough driving force to transfer from donor to acceptor [23]. Then, the newly formed charge transfer exciton (CTE) requires some velocity to separate in free charges. Donor and acceptor should have high charge carrier mobility and procure pathways to enable CTE to drive away from each other as fast as possible. Limited charge transport ability would result in recombination.

1.2.4. Charge collection

Charge collection includes charge transport through the donor/acceptor system and charge injection at the electrodes. Charge transport is principally governed by the charge carrier mobility through the semiconductors. As for charge injection, the work functions of the electrode or of the charge transport layer are determinant and require a careful choice of the metal and the interlayers. Moreover, the quality of the interfaces is critical to get perfectly ohmic contacts; otherwise the OSC device will suffer from high series resistances.

To obtain high efficiency OSC, the device must satisfy the requisites of each steps of the process. To do so, delicate and challenging trade-offs must be accomplished by the molecular structure, the morphology and the device architecture which will be discussed along the manuscript.

1.2.5. Photovoltaic characteristics

In order to evaluate the quality of an OSC and the efficiency of each step in the photovoltaic process, the current through the device is measured as a function of an applied bias voltage – generating a so-called "I-V curve". This measurement is carried out in darkness and under illumination, each curve giving different information about the cell (Figure 4).

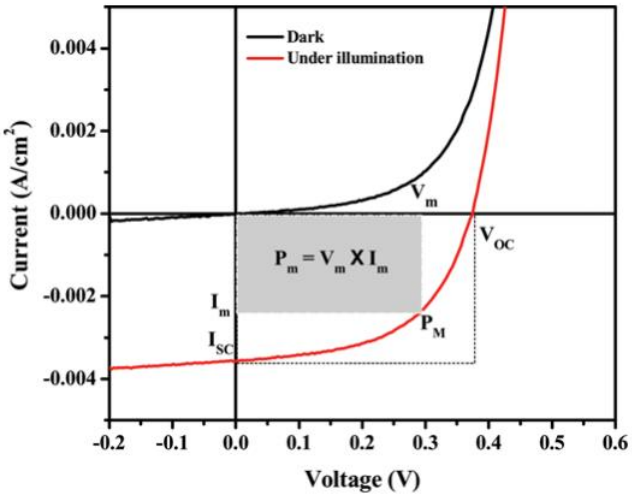

Figure 4: Typical IV curves measured in the dark and under solar illumination

From the illumination IV curve, five key parameters can be deduced:

-Short circuit current density (J_{SC}):

The short circuit current I_{SC} is the current flow at zero applied voltage. It is directly related to the efficiency of free charge carrier generation and collection. Furthermore, light harvesting and charge separation also influence the $I_{SC.}$ The photovoltaic community often employs the short circuit current density (J_{SC}), dividing I_{SC} by the cell surface.

-Open circuit voltage (V_{OC}):

Open circuit voltage (V_{OC}) is the voltage at zero current. The energy levels of the two semiconductors govern the V_{oc}, in conjunction with the choice of interlayers and electrodes on both sides. Brabec *et al*. demonstrate that the maximum theoretical V_{oc} value can be found from HOMO of the donor and LUMO of the acceptor with the following equation [23]:

$$\mathbf{V_{OC} = \frac{1}{e}\left(E_{HOMO}^{donor} - |E_{LUMO}^{acceptor}|\right) - 0.3 \quad (in\ eV)}$$ with e, the elementary charge

The driving force (corresponding to the energy needed to overcome the exciton binding energy – estimated to be 0.3 eV) is subtracted from the difference between donor HOMO and acceptor LUMO energy levels (the band gap). A lower V_{oc} is commonly observed in practice as it is hindered by imperfections in the film, by unfavorable morphology or any resistances within the device. The Voc is so strongly related to the two last steps of the photovoltaic process: charge separation and charge collection.

-Maximal power (P_{max}):

Maximal power corresponds to the grey area in Figure 4. It is the maximum power that can be supplied by the OSC.

-Fill factor (FF):

The fill factor is calculated using the following equation:

$$FF = \frac{P_{max}}{I_{SC}.V_{OC}}$$

Fill factor is related to the two last steps of the photovoltaic process: charge carrier transport and charge collection. It follows that an ideal OSC would exhibit a fill factor of one. To date, the best polymer-based solar cells have shown a fill factor of 0.80 [24].

-Power conversion efficiency (PCE):

The PCE can be regarded as a measure of the global efficiency of the solar cell, and is found from this equation:

$PCE = \frac{P_{max}}{P_{in}} = \frac{FF.I_{SC}.V_{OC}}{P_{in}}$, with P_{in} the incident power of solar radiation

According to the equation, a high PCE is reached for an OSC with high values of FF, I_{SC} and V_{OC}.

1.3. Device architectures

Since the first appearance of OSC, many advances have been made especially in the device's architecture [25,26]. The most important breakthroughs in OSC architecture was the discovery of bulk heterojunction (BHJ) [27] as it revolutionized exciton diffusion within the device. Interlayers and electrodes are critical for efficient charge collection and thereby have to be carefully chosen among a luxuriant literature [28]. This section introduces the different devices used along this research and their architecture. The advantages and the limitations for each device are detailed.

1.3.1. Bi-layer

The first OSC architecture was bi-layer devices, referring to their active layer in two successive layers: one of donor and one of acceptor. In this report, they are used for primary tests for new donor semiconductors and are composed of six layers: ITO/PEDOT:PSS/Donor/C_{60}/Ca/Aluminum (Figure 5). Indium tin oxide (ITO) is the transparent bottom electrode and is commercially available on glass substrates. The poly(3,4-ethylenedioxythiophene) polystyrene sulfonate (PEDOT:PSS) is the hole transport layer and is deposited by spin-coating. Then, the donor is deposited via spin-coating, followed by the thermal-deposition at 2×10^{-6} mbar of fullerene (C_{60}), the acceptor semiconductor. To finish, calcium and aluminum are successively deposited by thermal-deposition as electron's extraction layers and electrodes. For a bi-layer structure, the limiting step is the exciton diffusion. Excitons have to diffuse to a unique planar donor/acceptor junction. Only exciton generated not further than exciton diffusion length can be separated, meaning that only a thin layer of donor and acceptor contributes to the photovoltaic process. The rest of the excitons are lost due to geminate recombination and thereby increasing the thickness of the active layer is useless. Despite these disadvantages, this architecture shows an ideal charge transport and good charge collection. Free electrons and free holes never cross along their way to the electrodes after charge separation which hampers any recombination. The photovoltaic process is less sensitive to the OSC fabrication process than the following devices.

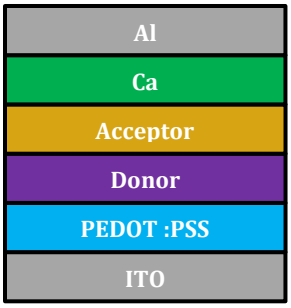

Figure 5: Bi-layer OSC architecture

1.3.2. Bulk heterojunction

In 1995, Heeger *et al.* introduced the concept of donor/acceptor blend network; later named bulk heterojunction (BHJ) [27]. A BHJ consists of an interpenetrated network between a donor and an acceptor semiconductor within one single composite layer. This interpenetrated network enables more donor/acceptor interfaces. The idea is that wherever excitons are generated, they will be close to an interface and will be able to separate. Short exciton diffusion length will no longer be an issue and OSC will not suffer of geminate recombination anymore.

To be successful, the donor/acceptor interpenetration needs to be tuned and controlled which is far to be evident. Many studies were conducted to understand how the photovoltaic process works within a BHJ and to define an ideal morphology [29–33]. Even if the BHJ photovoltaic process is still not fully understood, some statements have been clearly established. An ideal morphology should provide not only enough donor/acceptor interfaces to raise the chance of an exciton to be separated but also pure material domains to give CTE enough velocity to fully separate in free charges and finally percolating pathways to the electrodes for good charge collection.

In these regards, the ideal morphology should be composed of three phases: pure donor, pure acceptor and intermixing donor/acceptor domains (Figure 6). The intermixed domains are requisite to have fast exciton separation [31,32,34]. The pure donor and pure acceptor domains insure the separation of CTE into free charges [29]. As for charge transport, pure material domains should provide percolating pathways to the electrodes without overly overstepping the exciton diffusion length. Meanwhile, charge transport competes with bimolecular recombination, ascribing to the recombination of a hole and an electron that cross on their way to their respective electrodes. In this regards, crystalline domains of both donor and acceptor are desirable to improve the charge transport.

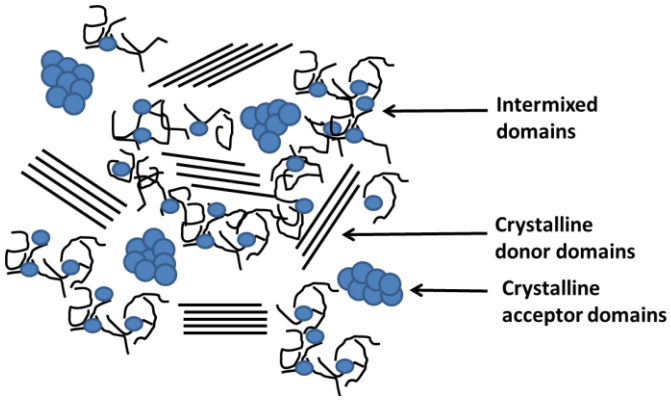

Figure 6: Scheme of an ideal BHJ

The control of the morphology is challenging and has been the subject of deep research. Various strategies have been investigated to control the morphology of a BHJ such as ink formulation and post processing steps. Regarding ink formulation, a large choice of solvents and additives can be tested to control and significantly improve the morphology [35]. For instance, using high boiling point solvents affords a slow solvent evaporation rate after deposition and sometimes a more homogeneous layer [36–38]. Semiconductors get more freedom to self-organize in a more favorable morphology. Additives like 1,8-diiodooctane (DIO) or 1-chloronaphtalene (CN) are widely used for their high potential in the optimization of

morphology for many donor/acceptor systems [39–43]. Ink formulation has to take into account either the ratio of solvents/additives and ratio of donor/acceptor concentrations of materials.

Likewise, the speed and the deposition time are key process parameters as they can tailor active layer's drying and thickness. On top of that, post treatments are also efficient to adjust the morphology [44–46]. Heating thin films after deposition allows materials to rearrange into a preferable network. Temperature and annealing time should be carefully chosen to get the right donor/acceptor domains. Another example of post treatment is solvent annealing for example for polythiophene [44]. Just after deposition, the device is introduced in a Petri box. Solvent saturates the atmosphere inside the box inducing a slow drying and ending in the most favorable morphology for polythiophene-based OSCs.

To conclude about bulk heterojunction devices, this architecture appears to be more adequate than bi-layers even if the tuning of the morphology required more time to optimize. To reach an optimal morphology, a panel of parameters has to be tuned such as the ink formulation, the process conditions, and post processing steps.

1.3.3. Conventional OSCs vs inverted OSCs

In this manuscript, conventional OSCs were mainly employed to test the newly developed donors for architecture: ITO/PEDOT:PSS/BHJ Donor:Acceptor/Ca/Al (Figure 7). The interlayers and electrodes are processed as in bi-layer solar cells. The donor and acceptor are dissolved together and spin-coated on top of PEDOT-PSS. Two acceptors were used along this research: [6,6]-phenyl-C_{61}-butyric acid methyl ester ($PC_{61}BM$) and [6,6]-phenyl-C_{71}-butyric acid methyl ester ($PC_{71}BM$). PCBM derivatives are the most commonly used in the literature. The principal advantage of this architecture comes from PEDOT:PSS and its ability to form a particularly smooth film. This property induces a better deposition and film formation of the BHJ and reduces the leakage currents and series resistance due to unfavorable interfaces and film defects.

Inverted OSCs are named in opposition to the conventional solar cells. The role of the top electrode and the bottom electrode are reversed. Electrons are then collected from the bottom interface and holes from the top interface. The structure of the inverted OSC used in this report is the following: ITO/ZnOx/BHJ donor:acceptor/MoO_3/Ag (Figure 7). Indium tin oxide (ITO) is the cathode and plays the role of the electron collecting electrode. Zinc oxide is deposited by spin-coating as electron transport layer. The BHJ is processed as in conventional OSC. Molybdenum oxide, the hole transport layer, is thermally evaporated followed by silver, the anode which plays the role of the hole collecting electrode. This type of architecture answers to the issue of aluminum degradation. Some studies showed that aluminum tends to degrade and to

diffuse into the active layer. By using ITO as the cathode, a more stable metal can be chosen such as silver for anode [47]. As a consequence, inverted solar cells are much more air stable than direct cells even without sophisticated encapsulation. Additionally, some vertical phase segregations of donor and acceptor can occur within the BHJ and, for instance, result in a rich bottom layer of acceptor and a rich top layer of donor. An inverted OSC will be more suitable for this typical morphology as electrons are collected at the bottom electrodes. Obviously, for opposite segregation, a conventional OSC will be the best choice.

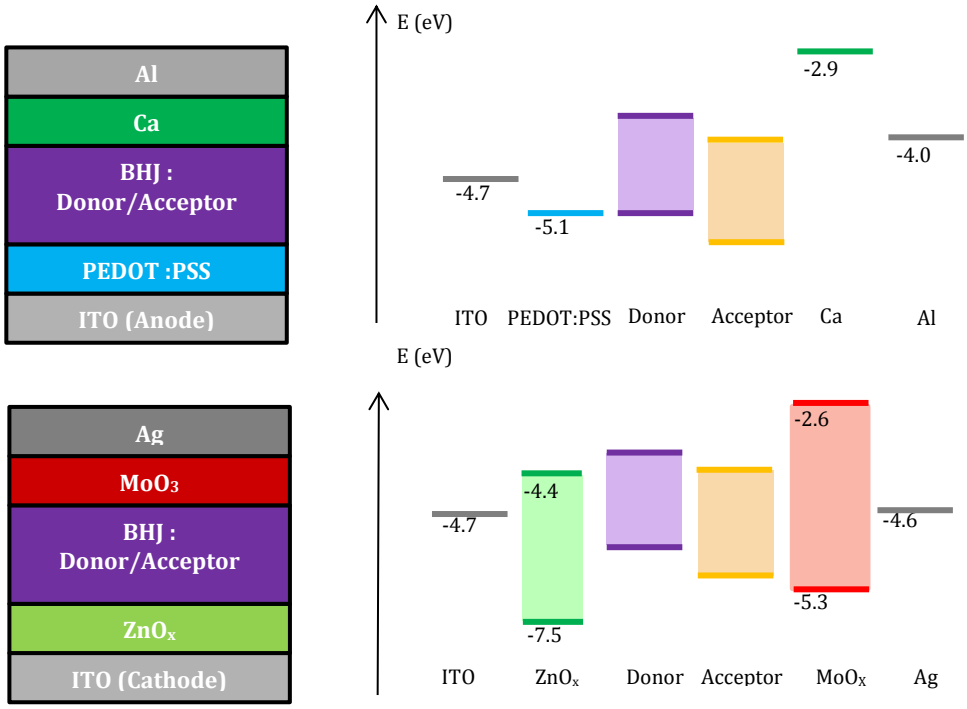

Figure 7: Conventional (top) and inverted (bottom) OSC architectures

To summarize, BHJ OSC is the most promising architecture to achieve high performances although its process optimization demands much more efforts than for bi-layers OSCs. Conventional and inverted OSCs are both tested for each material to determine the most appropriate architecture. Common and efficient interlayers and electrodes were chosen for each architecture.

2. DONORS REQUISITES AND DESIGN

OSCs are mainly limited by their low PCE and poor stability. To solve those issues, a widespread research, going from architecture optimization to morphology control and including design of new active materials, is essential. This report focuses on the lead consisting of designing new active material. For a long time, donors have monopolized attention as they play a

crucial role at each step of the photovoltaic process. This thesis follows this mainstream by developing and synthesizing two strategic series of donors. The goal is to investigate the effect of the molecular framework on the optoelectronic and charge transport properties. Furthermore, the behavior of these donors within BHJ OSC will be explored to address some correlations with their molecular structure. A better understanding of the morphology is helpful to control it and find out which additives or post treatment should be used.

2.1. Donor requisites

When designing new donor semiconductors, some requisites must be taken into account. Donor semiconductors are involved in each step of the process, all requesting essential properties. Consequently, donor backbones should respect energy levels, solubility, charge transport and morphology requirements.

2.1.1. Energy levels requisite

By looking at the photovoltaic process, donor energy levels obviously appear as crucial metrics. First, for efficient photon absorption, the band gap of the donor is preferably low about 1.7-1.2 eV to broaden the absorption spectrum. Then, for efficient electron transfer from donor to acceptor, the gap between the LUMOs of both semiconductors must be higher than the minimal value of 0.3 eV stated by Scharber *et al.* [23]. Finally, the V_{OC} is determined by the gap between the HOMO of the donor and the LUMO of the acceptor. Deeper is the HOMO of the donor, higher is the Voc. Combining this requirements and defining the ideal energy levels are far from straightforward and represents an important challenge for the OSC field.

For these reasons, Scharber *et al.* conducted an intensive study on donor polymers to establish ideal energy levels [23]. This work introduces a diagram correlating the LUMO and bang gap of the donor to the optimal PCE the donor can reach with $PC_{61}BM$ (Figure 8). The estimated PCE can be achieved only if it satisfies all morphology and device requirements. This diagram is a guideline to predict the potential of new donors according to their energy levels. The energy levels are mainly determined by the π-conjugated backbone which will be further detailed in the following sections.

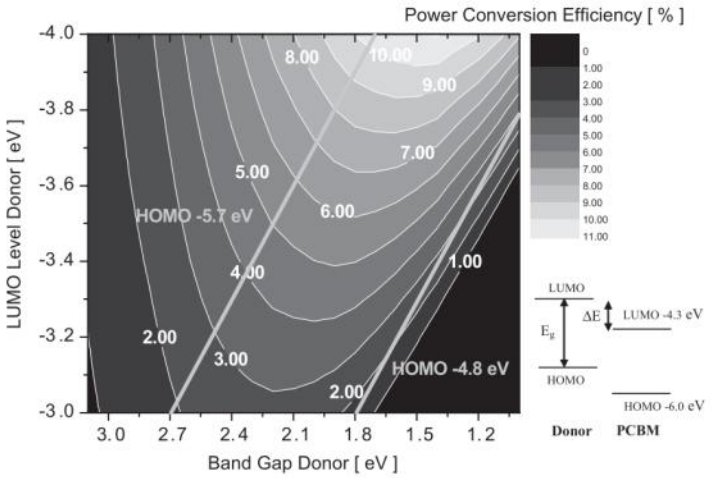

Figure 8: Scharber's diagram : Estimation of the PCE versus donor's LUMO and band gap [23] [2]

2.1.2. Solution process requisite

This report treats only about solution-processed semiconductors as this deposition process is more suitable for low-cost and large-area production. A solution deposition process also enables the use of flexible substrates. Obviously, this process requires a good solubility of the donor in commonly used solvents like chloroform or chlorobenzene. The solubility of semiconductors is generally tuned by the introduction of alkyl chains. The length and the branched or linear character of the alkyl chain have significant impacts on the solubility as well as the packing of the molecules [48–51]. Overly long alkyl chains can induce steric hindrance and hamper the packing of the molecule limiting the charge mobility. For this reason, the alkyl chains should be carefully chosen. The donor should also offer a good film formation as defects like pinholes can generate important leakage currents.

2.1.3. Hole mobility requisite

Donors are also in charge of the hole transport within the active layer of OSCs. Of course, high hole mobility is beneficial for efficient charge transport but not sufficient in the case of BHJ OSC. The hole and electron mobilities must also be balanced within the OSC. Otherwise, a space charge will be created and will exacerbate bimolecular recombination. The value of the FF is strongly affected by the presence of bimolecular recombination. Proctor *et al.* established a mobility guideline to achieve a FF superior to 0.65 [52]. In their study, the mobilities were measured in hole only diode with ITO/PEDOT:PSS or MoO_3/active layer/Au architecture following Mott-Gurney law for space charge limited current (SCLC). The charge carrier mobilities must be balanced within one order of magnitude to prevent the build-up of space

[2] Reproduce with permission: License number: 3831911369611

charge and superior to 2×10^{-4} $cm^2.V^{-1}.s^{-1}$ to get a low charge carrier sweep-out time. Longer the charge carrier sweep-out time is, more the charge collection will compete with bimolecular recombination. Another significant observation was that hole mobility of the donor neat film was generally superior to the one in the blend, meaning that the neat film mobility could correspond to the mobility's upper limit. If low mobility is observed in neat film transistors, the OSC based on the same material will suffer from low FF.

Charge carrier transport can be led by two mechanisms: band transport and hopping transport. In band transport, charge carriers are delocalized over the whole domains. Conversely, in hopping transport, charge carriers are localized on a single molecule and hop from one molecule to another. Hopping transport is less efficient than band transport because of the energy barriers that the charges must overcome to move from one molecule to another. To occur, band transport requires continuous energy band, however organic semiconductors present discontinuous energy levels. Nevertheless, to get more continuous behavior, intermolecular interactions should be favored to increase the splitting of the energy levels. Therefore, the donor should have high crystallinity and close molecular packing. A planar conformation or non-covalent bounding between the molecules can help to get closer packing [53–55].

2.1.4. Morphology requisite

As mentioned in the BHJ section, the donor and the acceptor must organize in three phases: intermixed donor/acceptor domain and pure crystalline domains. To respect these criteria, the donor material has to be partially miscible with the acceptor semiconductor to form intermixed domains.

Designing new donor semiconductors with respect to all these requirements is complex and challenging. The literature compiles a great deal of donors offering some insights for new donor frameworks. A state of art of the literature introducing some design strategies is directed in the following section.

2.2. Polymers versus small molecules

Organic semiconductors are commonly divided in two classes: small molecules and polymers. Small molecular semiconductors were the first tested in OSCs fabricated via vacuum deposition [2], but polymers have since attracted a tremendous amount of interest from the scientific community because of their compatibility with solution processing. A plethora of studies have been carried out on polymeric donor materials [56]. However, since polymers exhibit some limitations, small molecules have recently attracted renewed and increased attention as a credible challenger to polymers, emphasized by recent improvements in their film formation [57]. As

seen on Figure 9, for a long time polymers showed better PCE than small molecules but small molecule have been catching out. Nowadays, both polymer and small molecule reach a PCE of 10% [58,59].

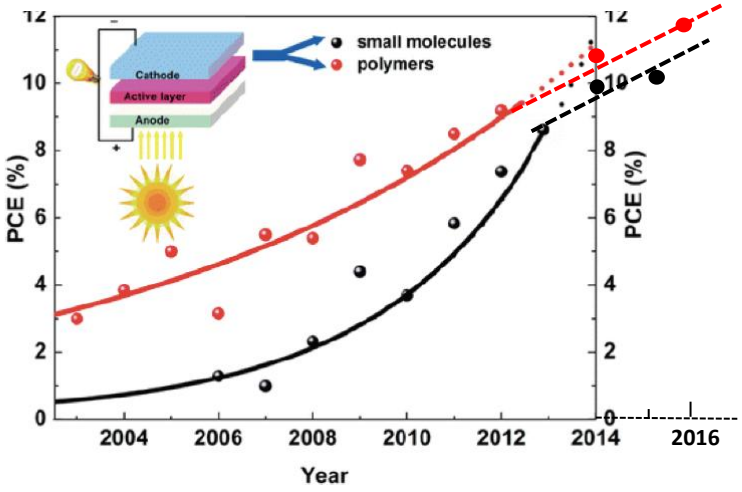

Figure 9: Evolution of the PCE over the years for polymers and small molecules according to Chen Y. *et al* review [60][3] with additional PCEs obtained between 2014 and 2016 for polymers [61,62] and small molecules [59,63] in single junction OSCs.

The majority of semiconducting polymers mentioned in the literature embed thiophene, benzothiadiazole, diketopyrrolopyrrole or benzodithiophene moities [64–67]. The best PCE reported with these materials is around 10% in single junction cells [58,61,62,68–70]. Generally, polymers offer good film formation, efficient hole transport and desirable mechanical properties. The tuning of polymer morphology has been the subject of extensive research, which has led to significant improvements in the OSC performances [71]. Despite the initial success of donor polymers, they show some limitations, such as the variation from batch to batch in the regioregularity, molecular weight and polydispersity. Consequently, device performances have poor reproducibility, and OSCs need to be optimized for each batch of polymer. For industrial applications, such limitations are undesirable. In the context of academic research, the poor reproducibility of syntheses makes correlation of molecular structure and device performance difficult.

In stark contrast, small molecules show well defined structure and are increasingly regarded as promising donor semiconductors [72–74]. Small molecule synthesis is simpler and the purity is more reproducible than their polymer counterparts. Very small batch-to-batch variations would be expected with small molecular semiconductors. From the point of view of commercialization, small molecules are more desirable. As the structure of small molecules is well defined, the effects of molecular structure on optical properties or energy levels can be readily studied. At

[3] Reproduce with permission

present, predicting new material's performance remains challenging but some links have been demonstrated.

Historically, small molecules were not known as efficient as polymers when used in OSC applications, but since the report of efficient solar cells based on solution-processed small molecules by Bazan and co-workers in 2012, the community has shown an increased interest in developing new solution processable small molecule semiconductors [75]. Recently, PCE as high as 9.95% and 10.1% have been demonstrated [59,63]. The higher solubility and better film formation of solution processed small molecules contribute significantly to the enhancement of the PCE. Nevertheless, small molecules were still meeting some difficulties to achieve high FF and remain less robust than polymer due to the lower flexibility of their structure. Researchers have therefore paid attention to the development of larger molecules close to the oligomer scale in the hope of combining small molecule and polymer's advantages [76]. According to Chen's group [60], the currently best photovoltaic (PV) parameters registered for small molecules are: Voc= 0.9-1.1 V [77–79], Jsc = 15 $mA.cm^{-2}$ [80] and FF >0.7 [77,81]. Compared to polymer OSCs, Jsc is now the limited factor for small molecule OSCs.

In the literature, small molecules comprise molecules with a very large range of molecular weights. In a recent review, Lin *et al.* redefine small molecules as molecules with molecular weight below 1000 $g.mol^{-1}$ and oligomers as molecules with molecular weight between 1000 and 10000 $g.mol^{-1}$. Even if the term oligomer should comprehend the notion of unit repetition, we still use this classification according to the molecular weight. In this report, the interest is shared between the promising large molecule-oligomeric derivatives using the well-known chromophore, DPP, and small molecule structure using a new chromophore, 3,3'-(ethane-1,2-diylidene)bis(indolin-2-one) (EBI).

2.3. Push-pull semiconductors

One of the most important progresses in donor molecular design was the discovery of push-pull semiconductors, molecules combining an electron rich (D) and an electron deficient (A) building block. The main advantage of push-pull semiconductors is their ability to get a low band gap and a broad absorption spectrum for efficient photon absorption. In 1996, Brocks *et al.* modeled the band gap of push-pull materials [82] and demonstrated how it results from the hybridization of the HOMO of the electron rich unit and the LUMO of the electron deficient unit (Figure 10). The hybridization reduces the band gap, which relies on intramolecular charge transfers between the electron rich and deficient group. The push-pull system is a tool to tailor energy levels by introducing weak or strong electron rich/deficient units and by changing the strength and the intensity of the intramolecular charge transfer between the push and pull units. Both push-pull polymers and small molecules have been extensively studied. Herein, an

overview focusing on the principal advances in push-pull small molecules is delineated to highlight the challenges in designing new donor small molecule semiconductors.

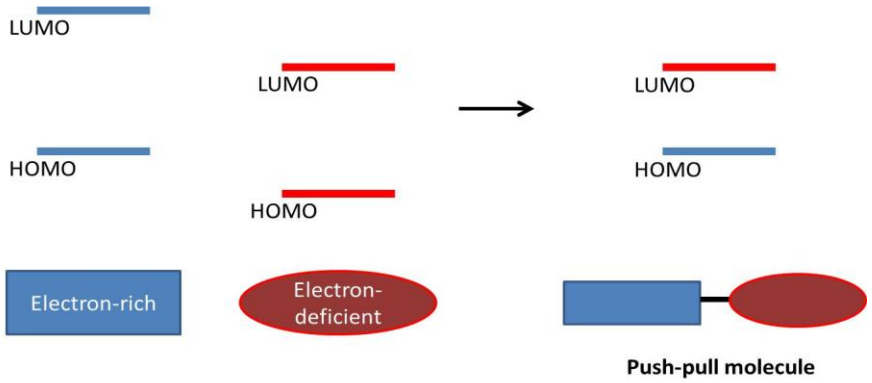

Figure 10: Push-Pull hybridization

For solution-processed push-pull small molecules, 2008 was a decisive year with the arrival of merocyanine [83], squaraine [84] and diketopyrrolopyrrole [85] derivatives in the OSC field which are all electron deficient groups. Combined with different electron rich units, they show promising PCEs of 1.77%, 1.24% and 2.3%, respectively. Since then, research on push-pull small molecules was boosted which was summarized in several excellent review papers [72,73,86–88]. Numerous electron rich and electron deficient units have been developed. Figure 11 summarizes some of the most promising building blocks.

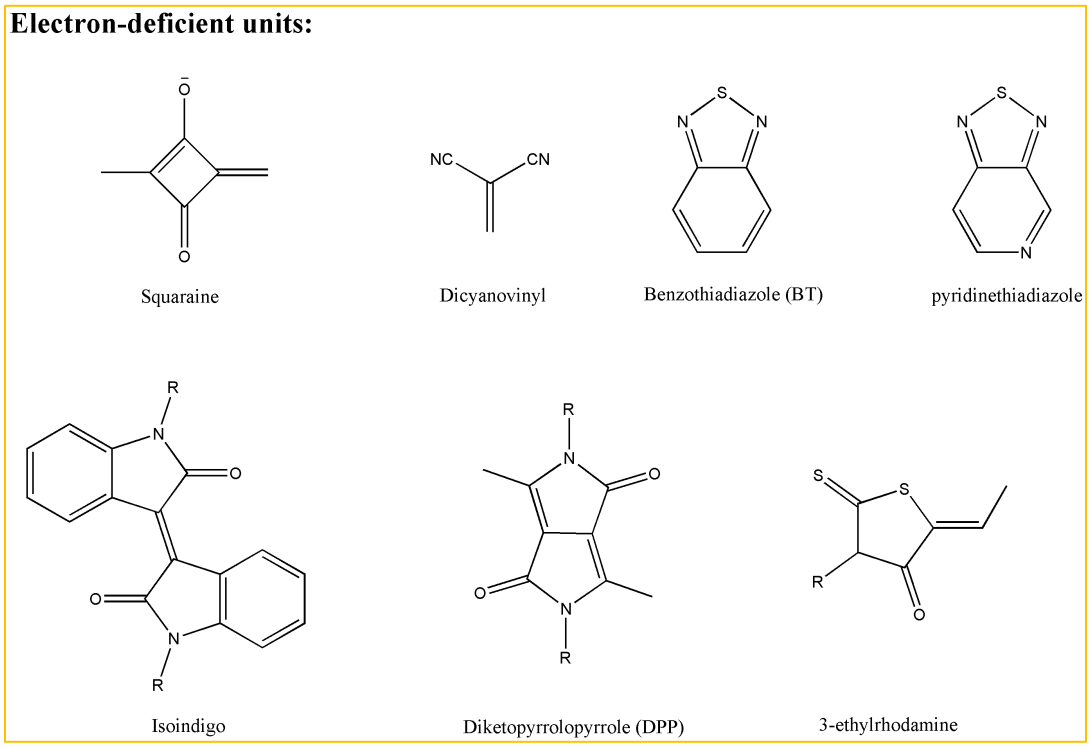

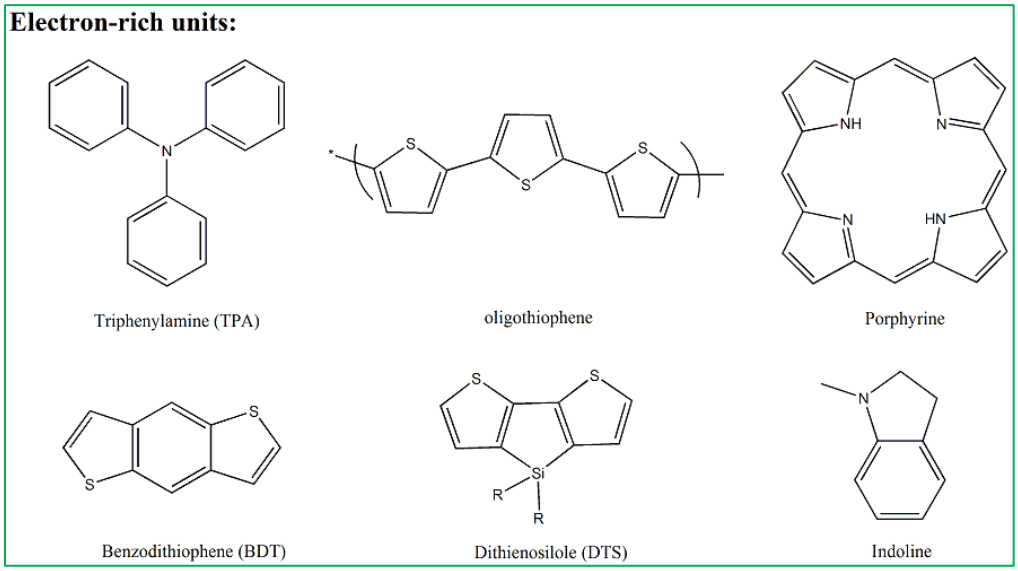

Figure 11: Electron-deficient units and electron-rich units reported in the literature

The build-up of new electron-deficient group entails great improvements in OSC performances. DPP and squaraine are among the most promising electron-deficient unit as they enabled to create materials with corresponding solar cells achieving PCE over 6-7% [89,90]. DPP compounds are highly conjugated, strongly absorbing, inexpensive and easy to synthesize. Nguyen's group introduced DPP as a building block for OSCs by aiming for improving the absorption property of oligothiophene derivatives (Figure 12a) [85]. This combination was a success and landed the records of solution processed small molecules with a PCE of 2.33% in 2008. In the following years, Nguyen's group kept surpassing small molecule OSC efficiency records by replacing *tert*-butoxycarbonyl with 2-ethylhexyl alkyl chain to achieve a better solubility and improved film formation [91], as well as replacing bithiophene with fused benzofuran to increase the π-conjugation and lower the HOMO (Figure 12b) [92]. All these improvements led to a high PCE of 4.4%. Larger molecules containing two or three DPP units and electron rich building blocks were developed (Figure 12c) [89,93,94]. The extension of the structure increases PCE up to 5-7%. The record PCE of 7% was achieved with a molecule containing two DPP units and a porphyrin core [89].

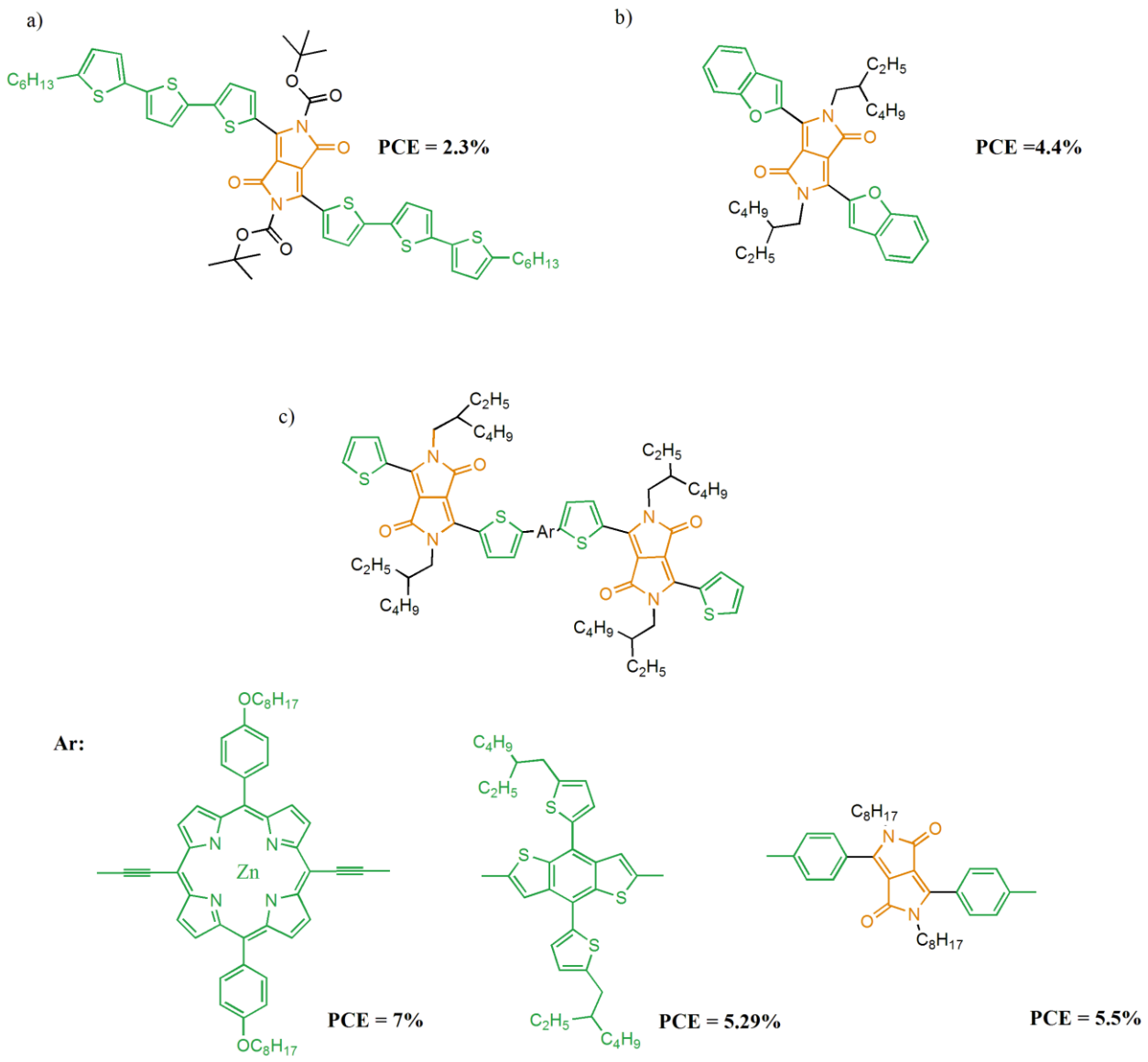

Figure 12: DPP derivatives reported in the literature [85,89,92–94]

As for the squaraine derivatives, they are composed of a very dense electron distribution on the central ring inducing a very high absorption coefficient [95]. Meanwhile, squaraines can be easily synthesized via condensation reaction avoiding the use of palladium catalyst and simplifying the large scale production and purification. Silvestri *et al.* notably introduced squaraines as solution-processed donors for OSCs in 2008 by achieving a PCE of up to 1% [84]. Since then, a set of squaraine small molecules have been designed. Squaraine small molecules are usually divided in two categories: symmetrical and unsymmetrical. The symmetrical category was the first one to achieve a PCE over 5%, which is represented by the diisobutylamino dihydroxyphenyl squaraine developed by Forrest's group (Figure 13a) [96,97]. The four hydroxyl and *N*-aryl group deepen the HOMO and provide interesting intermolecular

interactions. First, the molecule showed an encouraging PCE of 2.9 % in OSCs. Through the control of morphology using solvent annealing, the PCE was boosted to 5.5%. Other symmetrical squaraines have now been developed and reached PCE of 4-5 % [98,99]. As for unsymmetrical squaraines, for a long period, they have showed much lower performances than their symmetrical analogues, although they have drawn the interest of many researchers as their structures offer more flexibility for structure tailoring. After much effort made to tweak the energy levels, the optical band gap and molecular packing of unsymmetrical squaraines through careful design of the electron rich unit, PCE about 4-5% were achieved [100,101], catching up their symmetrical counterparts. Meanwhile, a breakthrough was made in 2014 by combining squaraine with an indoline unit (ASQ5) (Figure 13b) [102]. Indoline has a strong electron rich capability and small steric hindrance enabling the broadening of the absorption spectrum and thereby an improved short-circuit current J_{SC} of 11 mA.cm^{-2} was achieved. However, compared to its symmetrical counterpart, ASQ5 has a lower V_{oc} due to their relatively high HOMO levels. Embedding fluorine (ASQ5-DF) [90] and cyano (ASQ5-CN) [103,104] groups to the indoline motif decrease the HOMO level to -5.2 eV. Moreover, fluoro and cyano groups are known to improve the crystallinity. This property greatly improved the charge carrier transport and thereby raised the J_{SC} and FF. Without any post treatment, ASQ5-DF and ASQ5-CN yielded high PCEs of 4.6% and 5% with an enhanced V_{OC} of 0.93 V in comparison to 0.81 V for ASQ5. This raise in V_{OC} is the result of the synergistic effect applied by the cyano and fluoro group which lower the HOMO level [105]. By testing OSCs based on ASQ5-DF and ASQ5-CN at 80°C, the PCE increased to 6.04% and 6.11%, respectively.

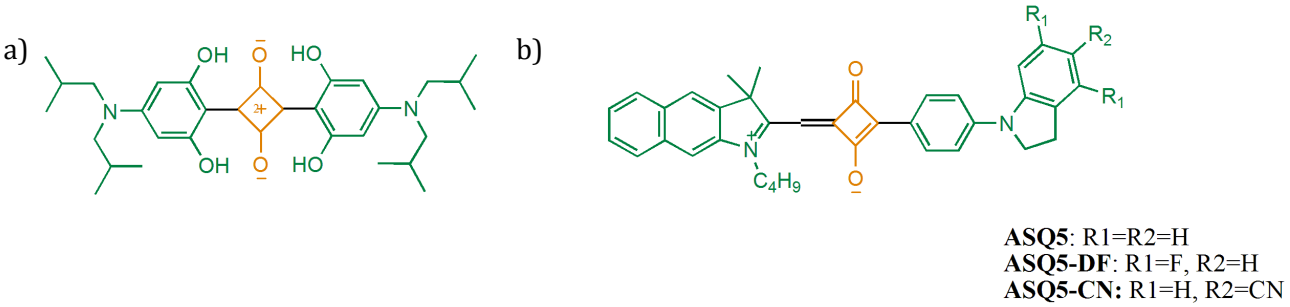

Figure 13: Squaraines derivatives, a) symmetrical [96,97] b) unsymmetrical [90,102–104]

Push-pull systems can also be improved by designing new electron rich units like triphenylamine (TPA), dithienosilole (DTS) and benzodithiophene (BDT). TPA is a non-planar unit generating amorphous derivatives. TPA can be placed at the center of molecules to form star-shaped derivatives or at extremities to give linear molecules. The first star-shaped molecules based on TPA achieving a PCE of 1% was vacuum-processable and tested in bi-layer by Cravino *et al.* [106]. Then, solution-processed star-shaped TPA were developed using dicyanovinyle [107], cyanoacetate [108] or benzothiadiazole [109] as electron deficient unit and offers respective PCE of 2%, 3.6% and 4.3%. After optimization of the alkyl chain length of TPA-

dicyanovinyl derivatives (Figure 14a), a PCE of 4.76% was achieved [48]. Shorter alkyl chains reduce steric hindrance and torsional interaction of the molecule and enhance the intermolecular interactions and charge transport. This study suggests that equal importance should be addressed to the alkyl chain design as the rest of the backbone. For linear molecules, TPA was bound to fluorinated benzothiadazole (Figure 14b) and exhibited a PCE of 4.24% which is in the range of star-shaped molecules [110]. Nowadays, even more complex structures are developed, combining TPA with other electron rich units such as DTS into star-shaped structure [111] and BDT into linear structure [112]. Four star-shaped derivatives based on the combination of TPA-benzothiadiazole-DTS have been developed to study the effect of fused-TPA and fluoro substituents. The fused TPA derivatives gave the highest PCE originating their planar conformation favorable for better charge transport. In presence of fluoride atom along its backbone, the PCE of the fused TPA derivatives raised up to 5.16%. As for the linear TPA-BDT derivatives, benzothiadiazole was placed between BDT, the electron rich center and TPA the electron rich end-capping (Figure 14c). By substituting BDT with an hexylthiophene, an impressive PCE of 6.13% was achieved [112].

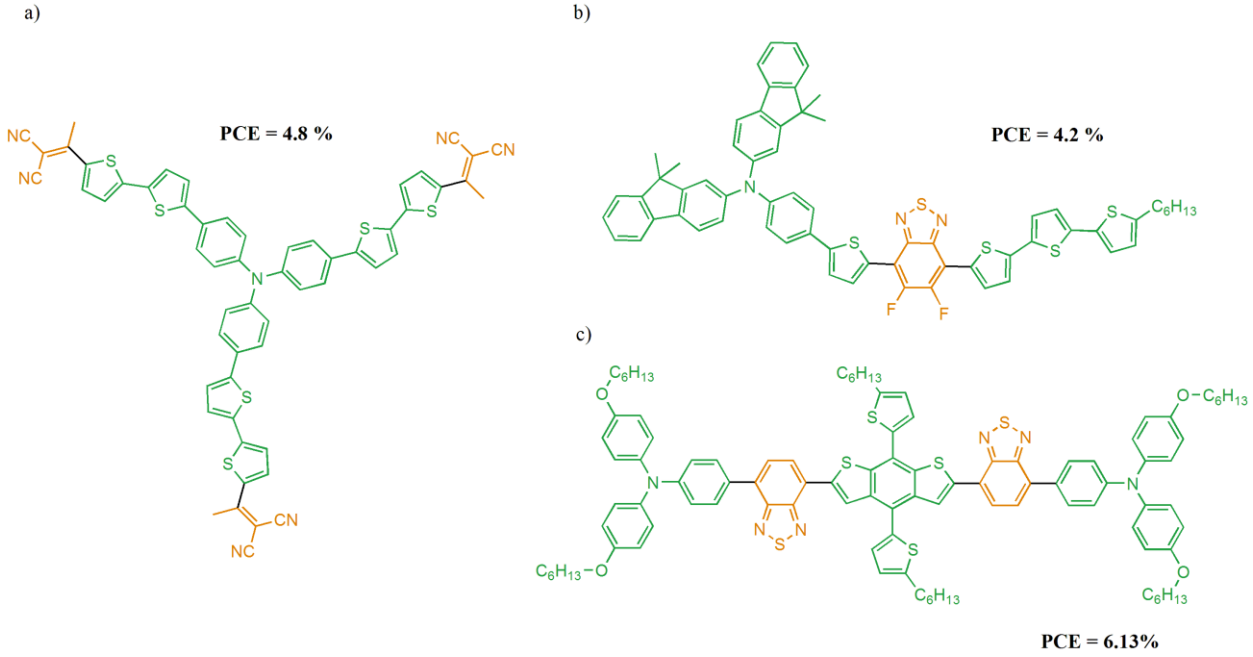

Figure 14: TPA derivatives [48,110,112]

DTS presents a rigid fused aromatic system promoting charge delocalization and co-facial π-π stacking and thereby beneficial for good charge transport. DTS has also a strong electronic density and therefore can be considered as a strong electron rich unit. In 2012, Bazan developed one of the first small molecules achieving PCE superior to 6%: a A-D-A structure (A: electron deficient unit; D: electron rich unit), called DTS($PTTh_2$)$_2$, with pyridinethiadiazole as electron-deficient group and DTS as electron rich group [75]. As DTS($PTTh_2$)$_2$ tends to react in acidic condition, a fluoro atom was introduced on the pyridinethiadazole to stabilize it and formed

DTS(FPTTh$_2$)$_2$ [113]. With 0.4% of DIO (as solvent additive, see section 1.3.2), this new fluorinated DTS derivative achieved an impressive PCE of 7% when blended with PC$_{71}$BM. Since then, DTS(FPTTh$_2$)$_2$ has appeared as a reference material for solution-processed small molecules for OPV application and a great deal of research have aimed at increasing its PCE. For now, the maximum PCE recorded for DTS(FPTTh$_2$)$_2$ is 9% [114], being among the highest PCE for solution processed small molecules. One needs to mention that this impressive value is also coming from improved device architecture, interlayers and high conductivity ITO electrodes. In our group, routine use of this compound in OPV give PCE in the range of 6 % when combined with PC$_{61}$BM which correspond the state-of-the-art in classical structures with well-known interlayers (ZnO$_x$, PEDOT-PSS, MoO$_3$/Ag, use of DIO as solvent additive).

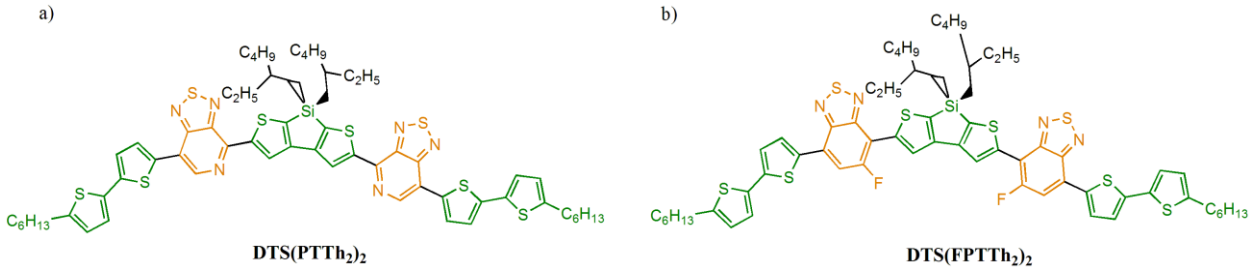

Figure 15: DTS derivatives [75,113]

BDT, like DTS, has a strong conjugated and planar backbone but a weak electron rich character which can maintain a low HOMO level. The most efficient push-pull combination based on BDT is with 3-ethylrhodamine as electron deficient unit. The two moieties are linked by a thiophene π-bridge as seen in Figure 16. This structure was first reported in 2012 with oxoalkylchain embedded on BDT unit (DR3TBDT) and achieved a noteworthy PCE of 6.92% [115]. By adding polydimethylsiloxane (PDMS) in the ink formulation, the PCE increased to 7.38%, due to an evener continuous interpenetrating network of the active layer. Numerous papers focused on improving this molecular backbone by changing the substitution of the phenyl ring of the BDT moiety. Yongsheng's group aimed at increasing the J_{SC} by extending the conjugation of the molecule [77]. To do so, they incorporated a thiophene (DR3BDTT) or a bithiophene (DR3BDT2T) on the BDT unit. Without any special treatments, DR3BDTT, BDT derivative with an additional thiophene, showed higher performances (PCE = 7.51%) and more precisely a higher J_{SC} of 13.15 mA.cm^{-2}. Further increasing the number of thiophene did not further improve the J_{SC} but interestingly enhanced the FF. With PDMS additives, the PCE of both DR3BDTT and DR3BDT2T raised up to 8.12% and 8.02%. Other common additives like DIO and CN had been tested however no effect was observed on the morphology or the performance. The design of BDT substitution was pursued with the introduction of branched alkyl chain (DR3TDOBDT) [116] and thienoalkyl chain (DR3TSBDT) [59]. First, both molecules shows similar PCE around 6.6%, but an optimization of the morphology by a successive thermal annealing and solvent annealing boosted their PCEs to 8.26% and 9.95%.

Through a careful scaffold of BDT substitution, a record PCE near 10% was achieved highlighting the great importance of molecular design to tweak the optoelectronic properties and molecular packing.

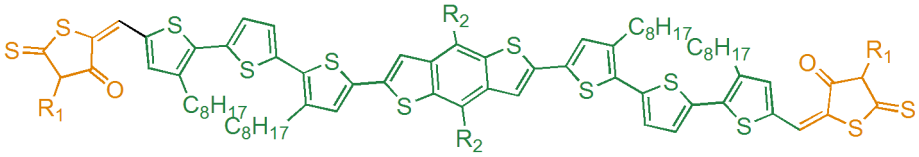

DR3TBDT: $R_1 = C_2H_5$, R_2 = 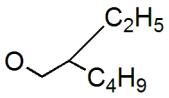 **PCE =7.4 %**

DR3TBDTT: $R_1 = C_2H_5$, R_2 = 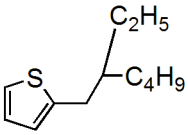 **PCE =8.1 %**

DR3TBDT2T: $R_1 = C_2H_5$, R_2 = 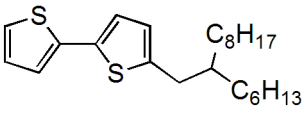 **PCE =8.0 %**

DR3TSBDT : $R_1 = C_2H_5$, R_2 = 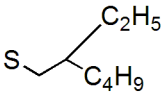 **PCE =8.3%**

DR3TDOBDT: R_1 = 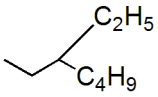 **$R_2 = C_8H_{17}$** **PCE = 9.95 %**

Figure 16: BDT-rhodamine derivatives [59,77,115,116]

This overview highlights the complexity of designing new donor semiconductors. The donor framework should be composed of efficient and more importantly well-combined electron rich and electron deficient group. To improve the push-pull system, chemists can focus on designing new electron rich/deficient building blocks or new combinations. An ideal electron rich or deficient unit should be a readily tunable and high absorbing chromophore, which can be easily synthesized from inexpensive reagents. Moreover, when elaborating a new backbone, alkyl chains should be carefully chosen as they govern the solubility and the packing of the molecule. Furthermore, the substituents along the backbone like fluoro, cyano or hydroxyl can be incorporated to refine the energy levels and the molecular packing. The conformation of the molecule also plays a rule in the molecular packing.

Additionally, this state of art points out the importance of morphology optimization in bulk heterojunction OSC and how performances can be boosted if an ideal morphology is achieved. On the other way round, an unfavorable morphology can inhibit the photovoltaic effect, making the evaluation of the potential of a novel donor semiconductor difficult. Nowadays, predicting the effect of additives or post treatments on the morphology is still challenging, therefore, a complementary study of the morphology is necessary to understand the behavior of the donor within the OSC.

3. OBJECTIVES

This thesis focuses on the synthesis of novel donor materials and their integration in BHJ - OPV devices. For the prospect of large scale production, this work focuses on solution-processable materials. Another key interest for the industrialization of OSC is the reproducibility of material synthesis which implies small batch-to-batch variations. To this end, we chose to study two families of materials: one series based on oligomers and one series based on small molecules.

The main objective of this thesis is to design novel push-pull donor semiconductors for OSC application and to establish correlations between their molecular structures and their optoelectronic and photovoltaic properties. Two different strategies were employed for the design of the two series. To build the series based on oligomers, the well-studied electron deficient building block DPP was employed and various electron rich spacers were investigated. As for the series based on the small molecules, a new chromophore in the field of OSC was employed: the 3,3'-(ethane-1,2-diylidene)bis(indolin-2-one) (EBI) (Figure 17).

The study of both series aims at the following objectives:

1) To elucidate if DPP oligomers could represent a trade-off between small molecules and polymers regarding synthesis, batch-to-batch variations, and film-forming properties.
2) To elucidate if EBI is a suitable chromophore to build novel donor semiconductors for OSC application
3) To elucidate the effect of the molecular backbone curvature on the opto-electronic properties as well as their PV properties

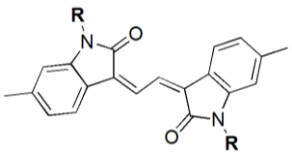

Figure 17: EBI structure

CHAPTER 2: EXPERIMENTAL METHODS

1. MATERIAL SYNTHESIS AND IDENTIFICATION

1.1. Materials used in the synthesis

All materials and chemicals used for the synthesis of DPP oligomers and EBI small molecules were purchased from commercial sources such as *Sigma Aldrich* or *Alfa Aesar*. If not specified, the chemicals and solvents were used without further purification.

1.2. ^{1}H and ^{13}C nuclear magnetic reasonance (NMR)

^{1}H and ^{13}C nuclear magnetic resonance (NMR) spectroscopy was performed using 400 MHz or 300 MHz Bruker NMR at the University of Waterloo. The samples were prepared in deuterated solvents like chloroform, dimethylsulfoxyde and tetrachloroethylene. The chemical shifts are calibrated with tetramethylsilane (TMS, 0 ppm) or the residual non- deuterated solvent.

1.3. Mass spectrommetry

Mass spectrometry was conducted by CESAMO institute in Bordeaux. For DPP final oligomers and by-product, MALDI-TOF technique was used. High-resolution mass spectrometry of final EBI compounds were realized by field desorption.

2. CHARACTERIZATION OF OPTO-ELECTRONIC PROPERTIES

2.1. UV-Visible spectroscopy

The UV-Visible absorption spectra of all materials were recorded between 300 nm and 1000 nm, using a SAFAS spectrometer. Samples were prepared in dilute chloroform solution and in thin-film resulting from the spin-coating of a chloroform solution of the material. The optical band gap was assessed with the off-set of absorption spectra (Figure 18) following this equation:

$$E = \frac{h\,c}{\lambda} \text{ in eV}$$

where h is the Planck constant of 4.14×10^{-15} eV.s, c is the speed of light of 3×10^{-8} m.s^{-1} and λ is the photon wavelength.

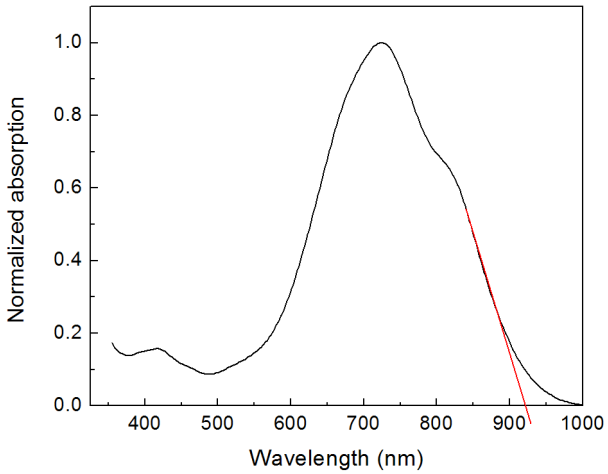

Figure 18: Method to extract the off-set of UV-visible absorption spectrum

2.2. Density functional theory (DFT) calculations

DFT calculations were realized by Jesse Quinn from University of Waterloo. The Beckès three parameter exchange functional and LYP correlation functional (B3LYP) were employed on the standard 6-31G basis set. To speed up the calculation, methyl side chains were chosen as alkyl chain.

2.3. Cyclic Voltammetry (CV)

To perform CV measurement, two platinum electrodes were used as working and counter electrode along with a Ag/AgCl (0.1 M) reference electrode. The three electrodes were dipped in a 0.1 M tetrabutylammonium hexafluorophosphate acetonitrile electrolyte solution at room temperature. All materials were drop-casted on the working electrode from chloroform solution. DY2000EN electrochemical workstation was employed to collect the electrochemical data. The red/ox couple, Ferrrocene/Ferrocenium (Fc/Fc^{+}), was used as reference. HOMO level was estimated from the onset of the oxidation peak using this following equation [117,118]:

$$E_{HOMO} = -(E_{OX} - E_{1/2}^{Fe} + 4.8) \text{ in eV}$$

In this work, the reduction peak was not or poorly visible therefore the LUMO levels were estimated by adding the optical band gap to the HOMO level.

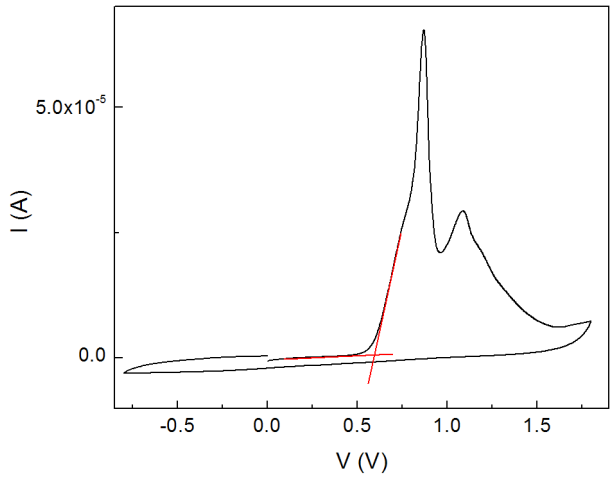

Figure 19: Method to extract the onset of the oxidation peak

2.4. Organic thin-film transistor (OTFT)

Bottom-gate/bottom contact OTFTs were fabricated using silicon wafer with gold electrodes patterned at the surface (Figure 20). *Fraunhofer IPMS* provides two types of substrates with two different channel widths (W): substrates with a W = 10 mm were used for Tri-BTDPP and all EBI derivatives and substrates with W = 2 mm were used for Tri-DPP-PT and Tri-DPP-PT-C6. Each substrate is composed of 16 devices with 4 different channel lengths (L) of 2.5 µm, 5 µm, 10 µm and 20 µm. For DPP derivatives, a channel length of 5 µm was chosen and for EBI derivatives, channel lengths of 5µm and 10 µm were chosen. All substrates were cleaned in successive baths of acetone, ethanol and isopropanol for 5 min, followed by a UV-ozone treatment of 15 min. Then, a chloroform solution of 5 mg.ml^{-1} of the material was spin-coated on top of these bottom-gate bottom-contacts backplanes.

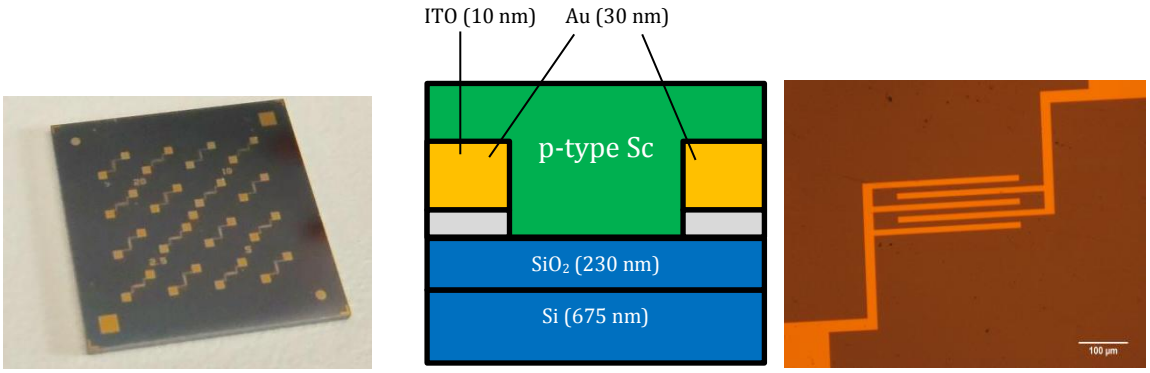

Figure 20: OTFT transistors: substrates (left), vertical view (center) and top view (right)

The devices were characterized using a semiconductor analyzer (Keithley 4200) coupled with a probe station. For transfer curve, V_{DS} was fixed at -30 V for DPP derivatives and at -40 V for

EBI derivatives. A saturation regime is recorded where the drain-source current (I_{DS}) can be expressed following this equation [119]:

$$I_{DS} = \frac{1}{2} \mu C_{ox} \frac{W}{L} (V_{GS} - V_{th})^2$$

where μ is the mobility, C_{ox} is the capacitance of 1.5×10^{-8} F.cm^{-2}, W is the width of the channel, L is the length of the channel, V_{GS} is the gate voltage and V_{th} is the threshold voltage.

By plotting the square root of I_{DS} as a function of V_{GS}, a linear curve was obtained following this equation:

$$\overline{I_{DS}} = \overline{\frac{1}{2} \mu C_{ox} \frac{W}{L}} V_{GS} - \overline{\frac{1}{2} \mu C_{ox} \frac{W}{L}} V_{th}$$

The mobility was extracted from the slope of this curve. For output characteristics, V_{GS} was varied from 0 V to 30 V for all materials.

3. CHARACTERIZATION OF PHOTOVOLTAIC PROPERTIES

3.1. Organic solar cell fabrication and characterization

3.1.1. Bi-layer organic solar cells

ITO substrates (Figure 4a) are cleaned in three successive baths of soap, water and isopropanol, followed by a UV-ozone treatment for 15 min. A solution of PEDOT:PSS (Heraeus, Clevios Ph, 2014POZ90) filtrated on 0.2 µm RC filter, is spin-coated at 3000 rpm for 60 sec onto ITO to elaborate a film of 40 nm. This film is annealed at 120°C for 10 min to remove any trace of water. The donor material are then spin-coated under nitrogen atmosphere to create a film with a thickness of 30-40 nm followed by the thermal evaporation at 400°C under secondary vacuum of 10^{-6} mbar of a 30 nm-thick fullerene layer (C_{60}). Finally, 20 nm of calcium and 100 nm of aluminum are successively evaporated under $2\text{-}6 \times 10^{-6}$ mbar onto the active stack through a shadow mask (Figure 4 b,c).The effective active area of the solar cells is 10 mm².

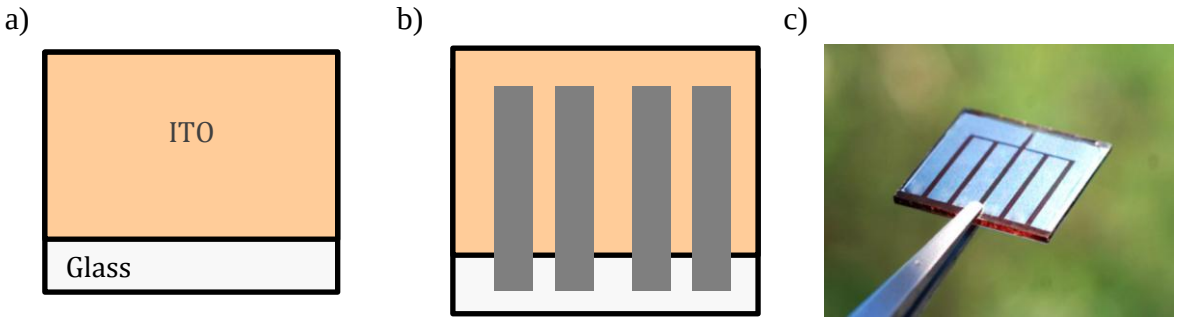

Figure 21: a) ITO substrates (1.5 cm × 1.5 cm); b) electrode patterns; c) The picture shows a typical OSC sample (the electrodes on the side are here to take the contact on the underneath ITO)

3.1.2. Conventional OSC

ITO substrates are cleaned in three successive baths of soap, water and isopropanol, followed by a UV-ozone treatment of 15 min. PEDOT:PSS (Heraeus, Clevios Ph, 2014POZ90) filtrated on 0.2 µm RC filter, is spin-coated at 3000 rpm for 60 sec onto ITO to elaborate a film of 40 nm. This film is annealed at 120°C for 10 min to remove any trace of water. A solution mixing donor: acceptor in various solvents at various concentrations is then spin-coated as an active layer under nitrogen atmosphere. The resulting thickness varies from 40 to 250 nm depending on solution concentration, solvent and spinning conditions. Finally, 20 nm of calcium and 100 nm of aluminum are successively evaporated under 2-6 × 10^{-6} mbar onto the active layer through shadow masks. The effective active area is 10 mm².

3.1.3. Inverted OSC

ITO substrates are cleaned in three successive baths of soap, water and isopropanol, followed by a UV-ozone treatment of 15 min. A solution of zinc oxide precursor prepared by dissolving zinc acetate (Sigma Aldrich, 96459, 99%) with ethanol amine (Sigma Aldrich, 15014-25mL, 99%) in ethanol, is spin-coated onto ITO to elaborate a ZnO_x film of 60 nm. The film was annealed at 180°C for 1h. A donor: acceptor solution is then spin-coated under nitrogen atmosphere. Finally, 10 nm of molybdenum oxide (MoO_3) followed by 60 nm of silver are successively evaporated under 2-6 × 10^{-6} mbar onto the active layer through a shadow mask.

3.1.4. Device characterization

The devices were characterized using a *K.H.S SolarCelltest-575* solar simulator with AM 1.5G filters set at 100 mW.cm^{-2} with a calibrated radiometer (IL 1400BL). The current density-

voltage (J-V) measurements are processed with *Labview* controlled *Keithley 2400 SMU*. Devices are characterized under nitrogen in a set of glove boxes (O_2 and H_2O < 1ppm).

3.1.5. External quantum efficiency (EQE)

The sample was first encapsulated between two glass substrates using NOA61 glue (EPOTECNY) activated with 2 min of UV treatment (365 nm from a UV-oven from *Fisher Scientific*) in a glovebox. For the quantum efficiency measurements, a setup provided by *Horiba Scientific* (500 W Xenon lamp and Triax 180 monochromator) were used. The incident photon flow was controlled by the calibrated, integrated sphere (Labsphere), and a Keithley 6487 Picoammeter was used to acquire data. Neither white-light bias nor lock-in acquisition was used. The EQE measurement shows the quantum efficiency at a particular wavelength, i.e the current that the OSC produces when irradiated by photons of a particular wavelength. The integration of the quantum efficiency over the entire spectra provides information on the maximum J_{SC} with AM1.5 spectrum. The thicknesses of the active layer were measured using an alpha-step JQ profilometer.

3.2. Thin film morphology characterizations

3.2.1. Atomic force microscopy (AFM)

AFM imaging was carried out at room temperature using a *Nanoman* from *Bruker Instrument* with *Nanoscope 5* controller. Images were obtained in tapping mode using silicon tips (*pointProbe Plus AFM-probe, Nanosensors,* Switzerland). The scanned area was usually 2µm × 2µm. The roughness was measured from the height images. Phase images were also recorded.

3.2.2. Differential scanning calorimetry (DSC)

Samples are prepared by drop-casting donor:acceptor blend solutions with various ratios onto glass substrates. After leaving the film to dry for 2 hours at room temperature, the layer is scratched and collected in a capsule. Differential scanning calorimetry (DSC) is performed on a *Mettler–Toledo DSC 1 Stare* system at a heating/cooling rate of 10 °C.min^{-1}, under a nitrogen flow protection. Every sample was submitted to three heating-cooling cycles between 25°C and 350°C. The phase diagram was built by compiling the endothermic peaks of the first heating curve of each blend film as a function of their blend ratio.

3.2.3. X-ray diffraction (XRD)

DPP samples were prepared by drop-casting similarly to DSC samples. The X-ray diffraction measurements were performed at Imperial College London with the help of Dr. Jaime Martín. The molecular packing was characterized by wide-angle X-ray diffraction (XRD, PANalytical X'Pert Pro MPD) using the Cu Kα radiation. θ/2θ scans were performed to the films at room temperature.

EBI samples were spin-coated from chloroform solution. The X-ray diffraction measurements were conducted at ISM (Bordeaux) by Sabine Goma on a D8 advance diffractometer using the Cu Kα radiation. The molecular packing was characterized in grazing incidence with θ constant (<1.5°). The scans were performed to the films at room temperature as a function of 2θ.

The d-spacing was calculated according to Bragg's law:

$$d = \frac{n\,\lambda}{2\sin(\theta)}$$

where n is an integer; λ is the X-ray wavelength of 1.54 nm and θ is the angle between the incident rays and the surface of the crystal.

The crystallite size was calculated according to Scherrer equation:

$$\tau = \frac{k\,\lambda}{\beta\cos(\theta)}$$

where k is the dimensionless shape factor of 0.9; λ is the X-ray wavelength of 1.54 nm, β is the full width at half maximum in radians, and θ is the angle between the incident rays and the surface of the crystal.

CHAPTER 3:

DIKETOPYRROLOPYRROLE OLIGOMERS

In this chapter, three oligomers based on diketopyrrolopyrrole (DPP) building blocks were designed and synthesized: Tri-BTDPP, Tri-DPP-PT and Tri-DPP-PT-C6 (see chemical structure on Figure 22). These three oligomers possess the same A-D-A-D-A (A = electron-deficient, D = electron-rich) structure with three DPP cores as electron-deficient groups and differ from the nature of their electron-rich spacers. Their optoelectronic properties, their morphologies as well as their photovoltaic (PV) performances will be compared. A first section will present the state-of-the-art on DPP derivatives in order to understand why they have attracted lots of attention as donor semiconductors in OSCs. This will be followed by three sections each dedicated to one of the designed molecule.

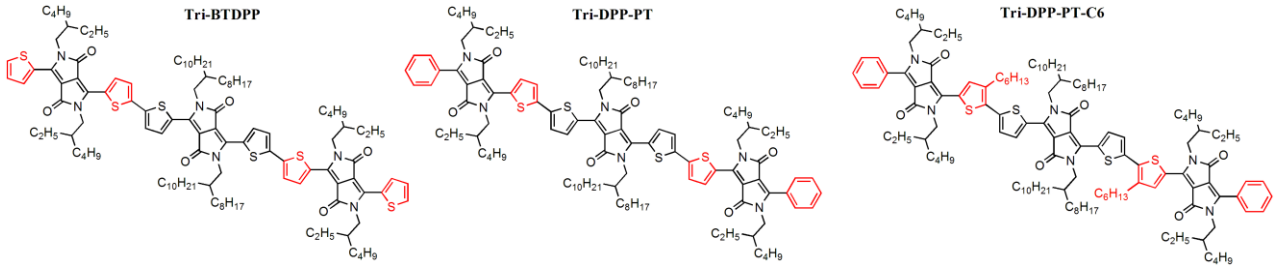

Figure 22: Chemical structure of Tri-BTDPP, Tri-DPP-PT and Tri-DPP-PT-C6

1. INTRODUCTION

The interest in oligomers relies on their intermediate molecular weight (MW), between 1 000 g.mol^{-1} and 10 000 g.mol^{-1} suggesting that oligomers could be a compromise between small molecules and polymeric semiconductors [76]. Ideally, oligomers would display a well-defined structure and poor batch-to-batch variations like small molecules and simultaneously backbone flexibility and good film forming properties like polymers. For these reasons, more and more oligomers were recently developed for solution processed solar among which some demonstrated PCEs of 7-9% [59,89,114,115]. As reviewed in Chapter 1, DPP is one of the most efficient electron-deficient building block, offering small molecules and oligomers with remarkable PCEs of 5-7% [80,89,120,121]. It is also noteworthy that DPP offers easy chemical modification and great potential to attach various moieties at its 2,5-position, which is a very

important feature to elaborate relatively large molecules. Hence, DPP was chosen in this study to build oligomeric semiconductors.

1.1. DPP-based oligomers

A large panel of DPP derivatives with a broad range of MW from 600 g.mol^{-1} to 2700 g.mol^{-1} has been developed. In order to investigate the potential effect of the MW on the PV performance, a literature survey was conducted. The PV characteristics of 76 published DPP derivatives were plotted as a function of the MW (see Figure 23). If MW does not clearly nor monotonously affect the J_{SC} nor the PCE, the figure suggests that increasing MW causes a decrease in V_{OC}. This can be ascribed to exacerbate splitting of energy levels due to extended π-conjugation which, in turn, causes an increase in the HOMO level. Conversely, the FF appears to increase with increasing molecular weight. This is possibly due to better film forming and / or improved charge transport. Such a large discrepancy on these charts highlights the challenge in predicting new potential materials.

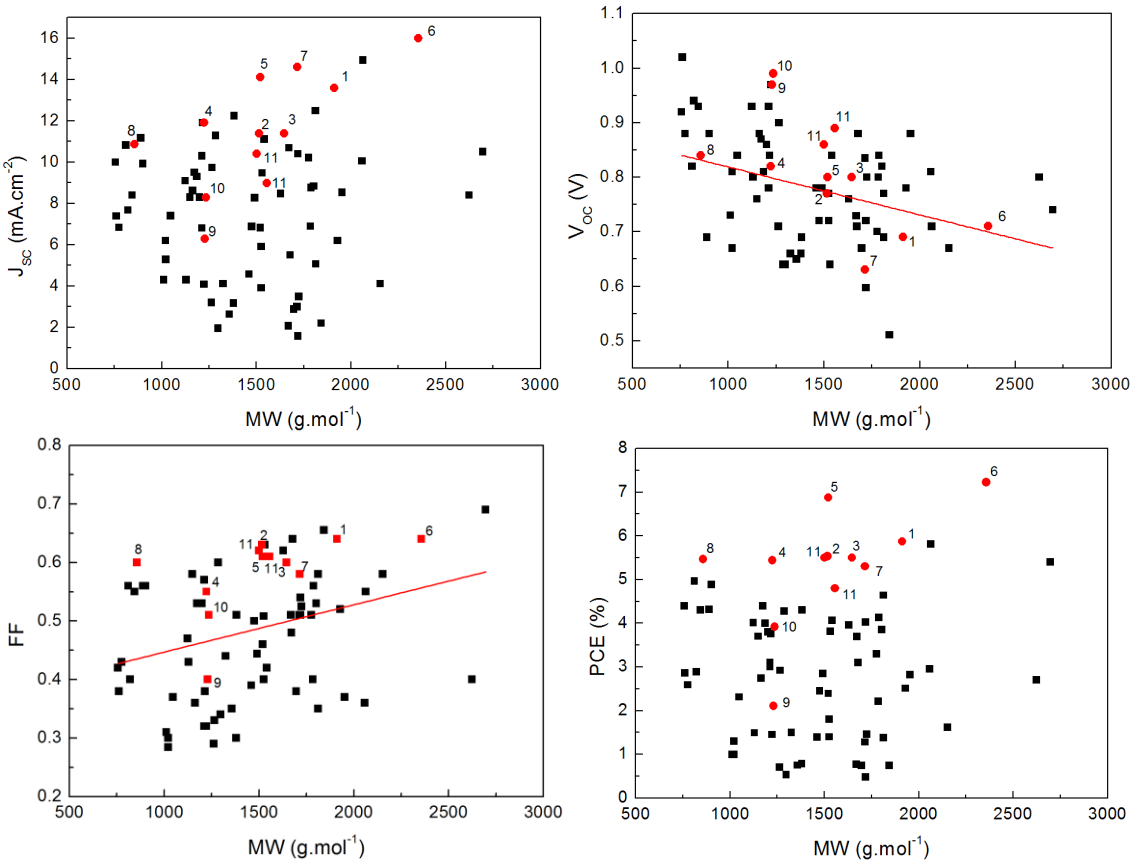

Figure 23: PV characteristics of OSCs$_s$ based on DPP derivatives versus molecular weight; each data corresponds to an individual molecule reported in peer-reviewed publications. As a matter of fact, this chart has been drawn from a survey of 33 independent papers (List of papers available in Appendix 1). The guideline on V_{oc} and FF are fitted linear regression from the raw data

1.2. Structure of DPP derivatives

Prior to design new DPP-based oligomers, the structure and the various combinations of DPP derivatives were explored. DPP derivatives were classified into three categories as a function of their D-A (D: electron-rich; A: electron-deficient) structures:

1. **D-A-D structure:** molecules composed of a DPP central core and two electron rich extremities.
2. **A-D-A structure:** molecules composed of two end-capping DPP core and a central electron rich unit.
3. **A-D-A-D-A structure:** molecules alternating more than three electron rich and deficient units

The PV characteristics of DPP derivatives in OSCs were compiled and plotted as a function of their structures, as illustrated in Figure 24. This study reveals that the three structures can provide PCEs up to 5%. To date, A-D-A and D-A-D are the two most studied structures but the champion cells for DPP derivatives were obtained with A-D-A molecules due to a high J_{SC} and FF [89].

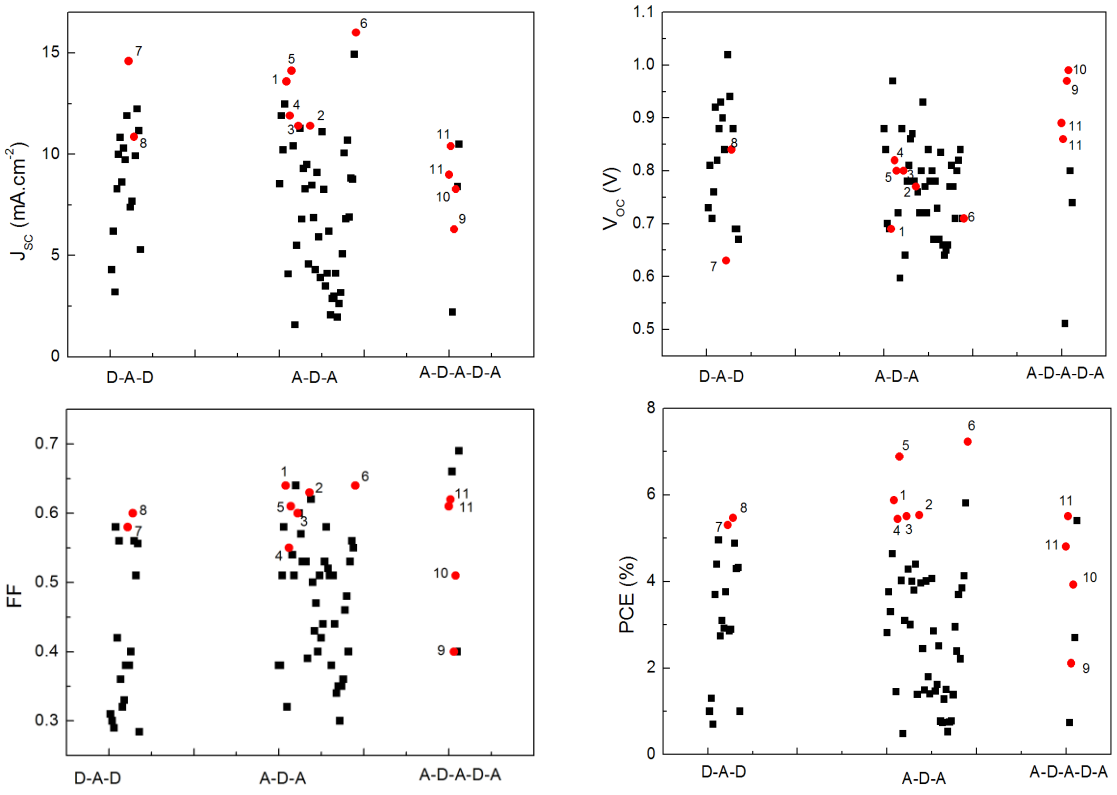

Figure 24: PV Characteristics of OSCs based on DPP derivatives versus their D-A structure; each data corresponds to an individual molecule reported in peer-reviewed publications. As a matter of fact, this chart has been drawn from a survey of 36 independent papers (List of papers available in Appendix 1)

In the next section, the best materials of each structure are listed - together with their advantages.

1.2.1. A-D-A archetype

For A-D-A archetype, the main challenge is to find the suitable electron rich central core. The most efficient combinations are with benzodithiophene (BDT) [122–124], benzodifuran [124], anthracene [125], dithienopyrane (DTP) [121], and porphiryn [89,126]. The combination of DPP and BDT was well-studied as BDT is among the most promising electron rich units. Besides a weak electron rich feature, BDT has an extended π-conjugated planar structure beneficial for π-π packing and charge transport. The best A-D-A framework associating BDT and DPP units used a substituted BDT with an hexylthiophene and trifluoromethyl phenyl end-capping units (Figure 25a) [122]. The large conjugation due to the thiophene substitution and the strong intermolecular interactions provided by the trifluoromethyl units, resulted in a high J_{SC} of 13.6 mA.cm^{-2}, a high FF of 0.64, and an impressive PCE of 5.9%. Other derivatives incorporating BDT and DPPs were realized by embedding different alkyl chains on BDT which controlled the molecular packing (Figure 25b) [123]. As a matter of fact, incorporating 3,7-dimethyloctyl instead of 2-ethylhexyl prevented an excessive aggregation and enabled a better intermixed network for improved exciton separation. This optimization led to an improved PCE of 5.5% over 3.3%. Another strategy to diminish the strong aggregation behavior of BDT was to replace BDT by benzodifuran (Figure 25c) [124]. Benzodifuran derivatives had a better miscibility with $PC_{61}BM$ allowing a better morphology. An increased PCE of 5.5% was therefore achieved over 3.1% for its BDT counterpart.

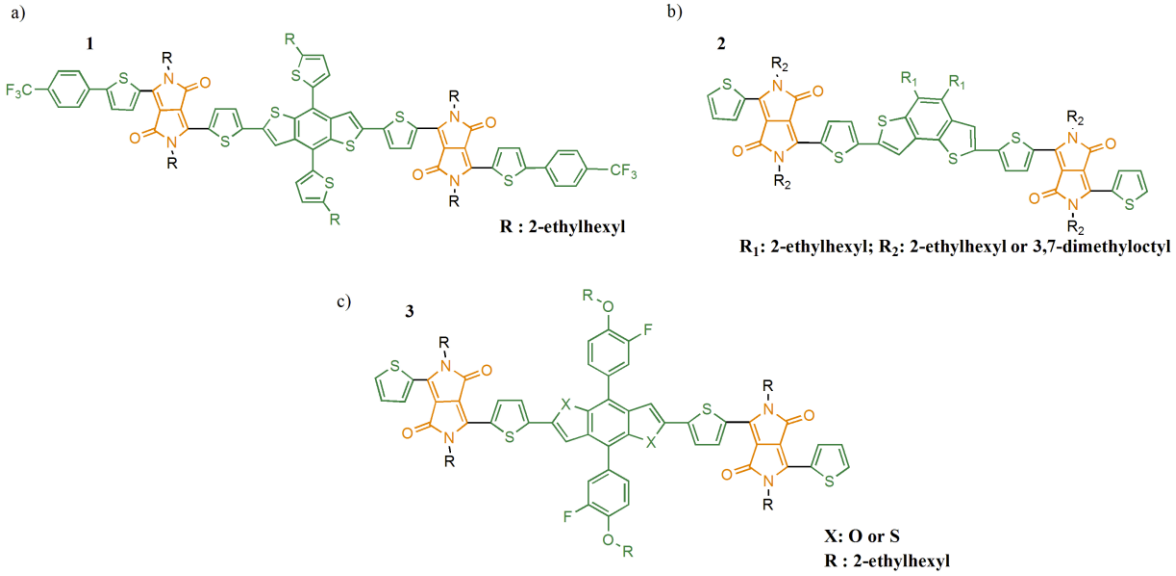

Figure 25: A-D-A derivatives composed of DPP as electron-deficient units and BDT or BDF as electron-rich units [122–124]

Similarly to BDT, anthracene was flanked by two DPPs as weak electron-rich, enlarged π-conjugation and coplanar unit (Figure 26a) [125]. In the right orientation, anthracene endowed the molecule of an impressive molecular packing, conveniently red-shifting the maximum of absorption. With the use of DIO, DPP-anthracene derivative exhibited a PCE of 5.4%. A strong electron-rich unit was also tested in A-D-A archetype, the dithienopyran group (Figure 26b) [121], in order to raise the HOMO level and to reduce the band gap. A low band gap was expected to rise the J_{SC} of the molecule however an increase in the HOMO level may also cause a decrease in V_{OC}. As predicted, the J_{SC} remarkably increased up to 14.1 mA.cm^{-2} whereas the V_{OC} favorably remained around 0.8 V. The resulting PCE reached a distinct value of 6.9%. To date, the best DPP derivatives displayed a PCE of 7% originating from the combination of two DPP units with a porphyrin electron rich unit (Figure 26c) [89]. Porphyrin was inspired from natural photosynthesis. This record PCE came along with the highest J_{SC} of 16 mA.cm^{-2} reported for solution-processed small molecules and oligomers. As a conclusion, the literature showed that using a strong electron rich unit in a A-D-A archetype is a promising route to pursue because it can cause both decrease the band gap and broaden the absorption spectrum. These advantages enable to reach high J_{SC}.

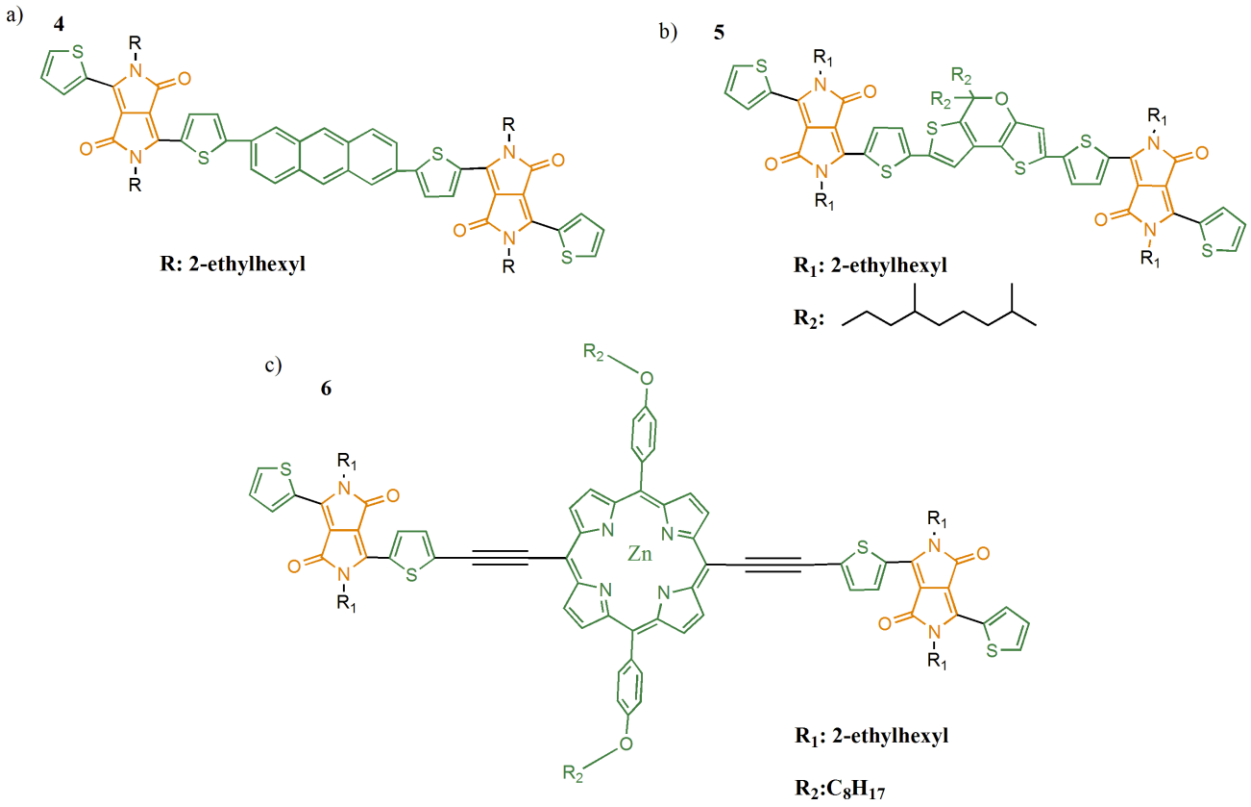

Figure 26: A-D-A derivatives composed of DPP as electron-deficient unit and a) anthracene [125], b) dithienopyrane [121] c) porphyrine [89] as electron-rich units

1.2.2. D-A-D archetype

As for a D-A-D archetype, the potential of the molecule is ascribed to the right selection of the electron rich end-capping such as triazatruxene and phenyl. A triazatruxene consists of three fused carbazoles (Figure 26a) and is a planar moiety promoting molecular self-assembly for efficient charge carrier transport [120]. With this unit, an impressive J_{SC} of 14.6 $mA.cm^{-2}$ could be achieved, leading to a PCE as high as 5.3%. Phenyl group [127] appeared to be a good end-capping unit as well when a fine engineering of the phenyl substitution with trimethyloxyl is performed (Figure 26b). A PCE of 5.5% was reached owing to a precise control of the morphology with two successive steps: a thermal annealing treatment and a solvent annealing treatment.

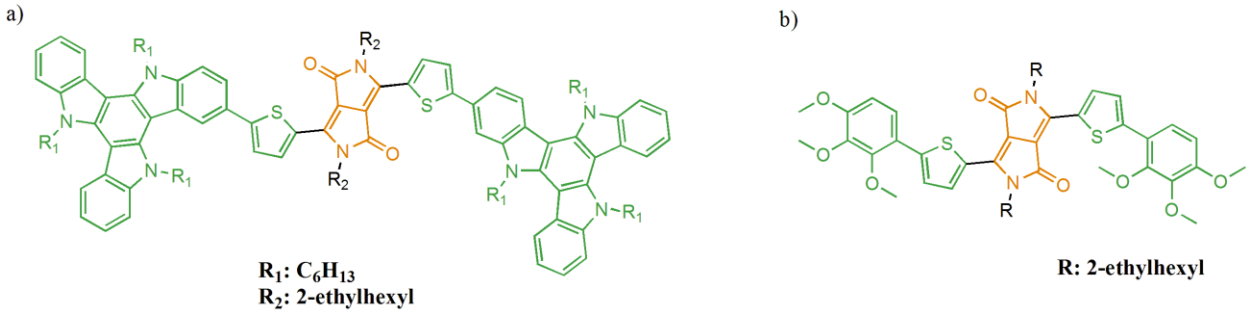

Figure 27: D-A-D derivatives composed of DPP as electron-deficient unit and a) triazatruxene [120], b) substituted phenyl [127] as electron-rich units

1.2.3. A-D-A-D-A archetype

Only a few A-D-A-D-A molecules have been reported in the literature so far however as shown in Figure 24, this archetype appears to enable decent fill factors around 0.6 and high open-circuit voltages around 0.9 V. Increasing the number of electron deficient units in the framework lowers the LUMO and in the same time reduces the band gap without impacting the HOMO level. This appears as a good strategy to broaden the absorption spectrum without sacrificing the V_{OC}. Two DPP units were first associated with a central benzothiadazole (BT) unit, a fused-ring with an electron deficient feature (Figure 28a) [128]. The energy levels of the resulting molecule (DPPBT) were promising with a low band gap of 1.59 eV for a broad absorption up to 750 nm and a deep HOMO level of -5.10 eV for a high V_{OC} of 0.97 V. The device still suffered from low FF and J_{SC}, limiting the PCE to 2.1%. Thiazolothiazole, another electron deficient group, was introduced instead of benzothiadazole (Figure 28b) [128]. The thiazolothiazole based molecule (DPPTT) exhibited a larger phase separation with $PC_{71}BM$ and could therefore provide better percolated pathways for charge carriers. The donor/acceptor morphology in the active layer is improved relative to the one obtained when DPPBT is used (Figure 29). Hence, the PCE could be increased up to 3.9%.

To date, the best A-D-A-D-A structure combined three DPP cores: bithiophene-DPP as end-capping moieties and phenyl DPP as central core (Figure 28c) [129]. Both linear and branched alkyl chains were introduced on the central DPP core. Both derivatives presented deep HOMO levels to achieve high V_{OC} of 0.85-0.9 V. Linear alkyl chain offered a better molecular packing and therefore a higher hole mobility of 4.3 x 10^{-3} $cm^2.V^{-1}.s^{-1}$ compared to 6.1 x 10^{-4} $cm^2.V^{-1}.s^{-1}$ for branched alkyl chain. In OSCs, the use of linear and branched tri-DPP provided PCEs of 5.5% and 4.8% respectively. This could be achieved by delicate tuning of the morphology via the introduction of solvent additives in the formulation. Interestingly, the optimal morphology of the two tri-DPPs did not employ the same additives.

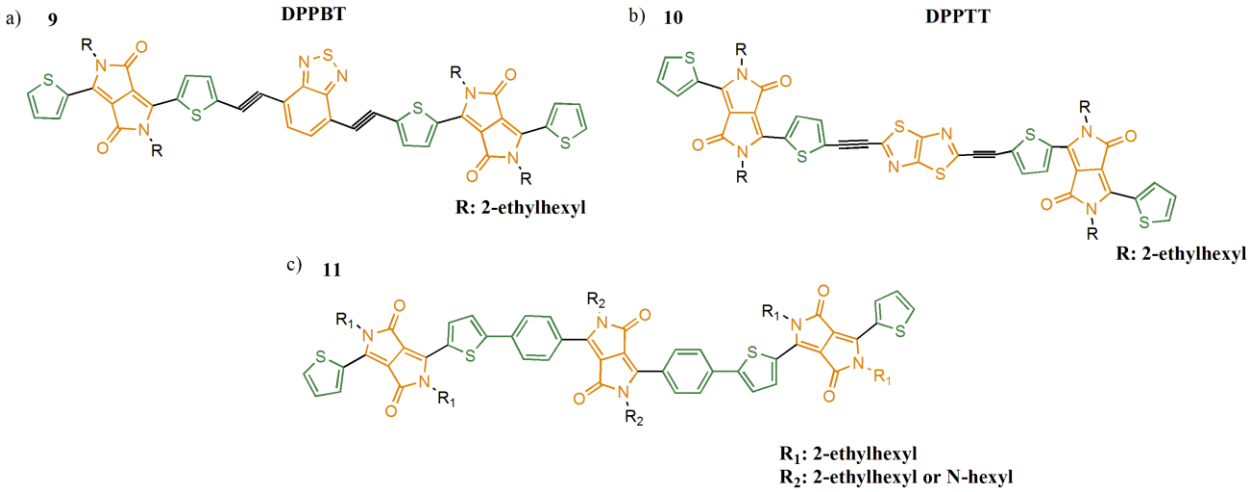

Figure 28: A-D-A-D-A derivatives composed of DPP and a) BT [128], b) Thiazolothiazole [128], C) DPP [129] as electron-deficient unit

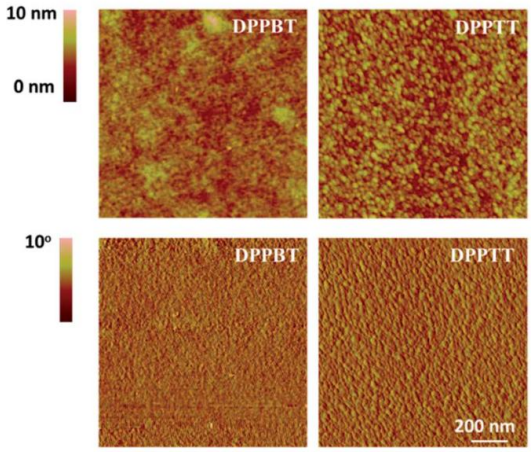

Figure 29: AFM height and phase images (2.0 µm x 2.0 µm) of as- prepared thin films of DPPBT and DPPTT with $PC_{71}BM$ (1 : 1, w/w) [128][4]

[4] Reproduce with permission, license number: 3831920734523

Even if A-D-A-D-A structures have been less studied than their A-D-A and D-A-D counterparts, they show great potential to achieve devices with high V_{OC} above 0.9 V. Therefore, this report focuses on the most efficient A-D-A-D-A structure, combining three DPP cores.

1.3. Target DPP-based oligomers

As explained in Section 1.2., changing the side chains of an oligomer containing three DPP cores can tune the molecular packing of the material and can allow better charge transport and higher PCEs [80]. To pursue this momentum, we aimed at tailoring the curvature of DPP-oligomer by replacing the phenyl electron-rich spacers - known for having a large dihedral angle of 26° with DPP [130] (Figure 30a) - by a thiophene electron-rich spacers. The resulting oligomer, 6,6'-((2,5- octyldodecyl)-3,6- dioxo-2,3,5,6- tetrahedropyrrolo [3,4-c]pyrrole-1,4-diyl) bis([2,2'- bisthiophene]-5',5-diyl))bis(2,5-bis(2- ethylhexyl)-3-(thiophen-2-yl)-2,5-dihydropyrrolo[3,4-c] pyrrole-1,4-dione) (Tri-BTDPP) is shown in Figure 30b. Tri-BTDPP is expected to be more planar enforcing a closer molecular packing and thus a better charge transport. Additionally, the intramolecular charge transfer between thiophenes and DPP is expected to be stronger due to a better overlapping of the orbitals entailing lower band gap. A narrow band gap would broaden the absorption spectrum and increase the J_{SC}. Moreover, Tri-BTDPP can be compared to its corresponding dimer (presented in Figure 30c) to investigate the effect of unit repetition [79].

a)

Tri-DPP, developped by Nguyen *et al.*

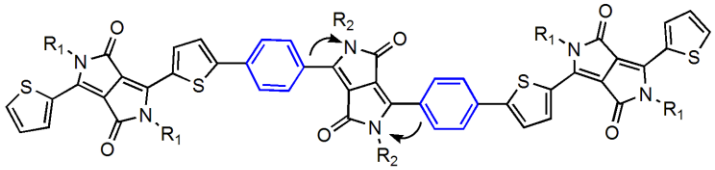

b)

Tri-BTDPP

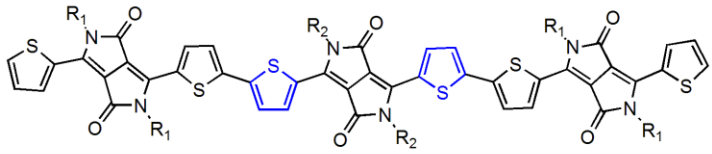

c)

Di-DPP, developped by Lee *et al.*

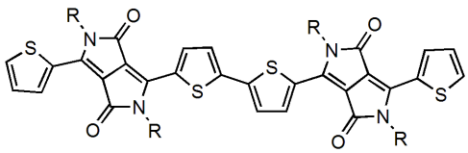

Figure 30: a) Tri-DPP developed by Nguyen *et al.* [80], b) Tri-BTDPP, c) Di-DPP developed by Lee *et al.*[79]

2. TRI-BTDPP: A COPLANAR OLIGOMER INTO OSC[5]

The first targeted oligomer based on DPP, contains three bithiophene-DPPs in order to obtain a perfectly planar backbone. First, 2-ethylhexyl side chains were introduced on the nitrogen of the three DPP units. However the resulting oligomer was not solution-processable due to its poor solubility in common solvents. In order to ensure a good solubility, 2-octyldodecyl side chains were embedded on the central DPP core as shown in Figure 31, forming 6,6'-((2,5-octyldodecyl)-3,6- dioxo-2,3,5,6- tetrahedropyrrolo [3,4-c]pyrrole-1,4-diyl) bis([2,2'-bisthiophene]-5',5-diyl))bis(2,5-bis(2- ethylhexyl)-3-(thiophen-2-yl)-2,5- dihydropyrrolo[3,4-c] pyrrole-1,4-dione) (Tri-BTDPP).

Tri-BTDPP

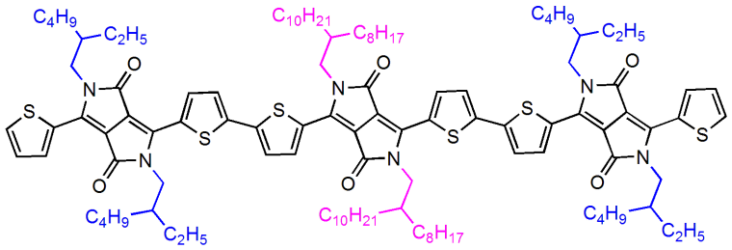

Figure 31: Tri-BTDPP, the first targeted molecule

2.1. Synthesis of Tri-BTDPP

The synthesis route to Tri-BTDPP is shown in Scheme 1. The mono-brominated DPP compound **1** and the bis(trimethylstannyl) DPP compound **2** were synthesized according to the methods reported in the literature (Appendix 2) [131,132]. The synthesis of Tri-BTDPP was conducted via Stille cross coupling reaction between **1** and **2** in a 2.1:1 molar ratio in toluene under reflux for 60 h in the presence of $Pd_2(dba)_3$ / $P(o\text{-}tolyl)_3$ as a catalyst/ligand system. Over this reaction, three co-products were formed: the target molecule Tri-BTDPP, compound **3** corresponding to the DPP-dimer resulting from the mono-coupling of **1** and **2** and compound **4** corresponding to DPP-dimer resulting from the homo-coupling of **1**.

[5] The majority of the material in this section was published by Dyes & Pigments, License number: 875910762153. The text was adapted.

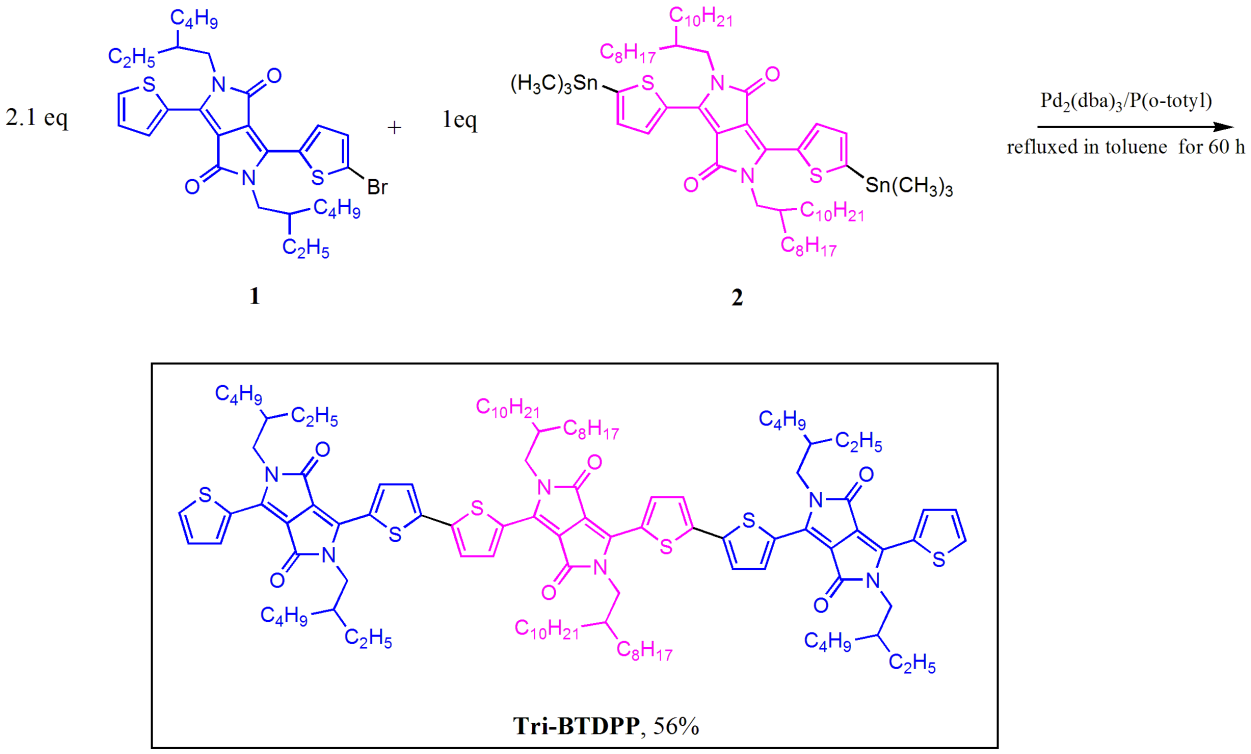

Scheme 1:Tri-BTDPP synthetic route

Separation of the target product Tri-BTDPP was accomplished by column chromatography, which was not straightforward due to the close polarity of the Tri-BTDPP and the by-product **4**. First, column chromatography on silica gel using DCM:hexane and then chloroform was conducted to remove compound **3** (26%) and other impurities to yield a crude product (72%), which still contained compound **4** as proved by MALDI-TOF mass spectrometry (Figure 32). Further purification was conducted by using a heated (50 °C) silica gel column using a mixture of chloroform and toluene (with a volume ratio of 1:1) as eluent, which enabled separation of Tri-BTDPP and **4** as confirmed by the MALDI-TOF mass spectra (Figure 32) with the disappearance of compound **4** peak. Pure Tri-BTDPP was obtained in 56% yield, with the molecular structure further confirmed by ^{1}H (Figure 33) and ^{13}C (Figure 34) NMR and HRMS. The yield of homo-coupling dimer by-product **4** yield was 16%. Compound **4** was only

characterized by MALDI-TOF mass spectrometry as NMR spectra could not be obtained due to the strong aggregation tendency of this compound. Formation of a notable quantity (~16%) of homo-coupling by-product in a Stille coupling reaction of a similar brominated DPP compound under similar conditions was recently reported. [133]

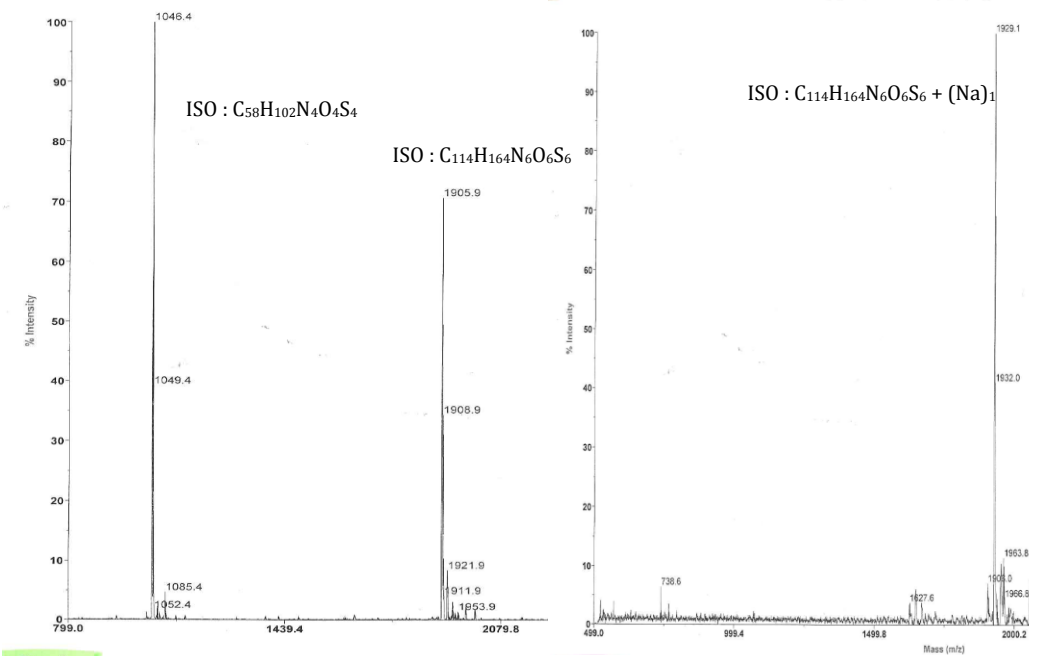

Figure 32: Mass spectrum before (left) and after (right) hot column

Data for Tri-BTDPP:

^{1}H NMR (400 MHz; $CDCl_3$) δ 8.93 (2H, d, J = 4.2 Hz), 8.91 (2H, d, J = 4.2 Hz), 8.85 (2H, dd, J = 3.9, 1.1 Hz), 7.49 (2H, dd, J = 5.0, 1.0 Hz), 7.25 (4H, dd, J = 3.9, 3.5 Hz), 7.14 (2H, dd, J = 4.9, 4.0 Hz), 3.96 (12H, d, J=5.2 Hz), 2.00 - 1.71 (6H, m), 1.39 - 1.23 (35H, m), 1.22 - 1.05 (70H, m), 0.92 – 0.72 (41H, m)

^{13}C NMR (400 MHz, $CDCl_3$) δ 161.81, 161.69, 141.49, 141.19, 140.67, 139.33, 139.28, 137.43, 137.15, 135.95, 131.03, 130.14, 130.02, 129.95, 128.77, 126.12, 109.37, 109.08, 108.44, 77.56, 46.76, 46.30, 39.73, 39.46, 38.41, 32.26, 32.24, 31.60, 30.68, 30.56, 30.51, 30.45, 30.05, 29.99, 29.97, 29.92, 29.72, 29.70, 28.84, 28.69, 26.65, 24.02, 23.87, 23.47, 23.44, 23.03, 14.45, 14.38, 10.91, 10.83

HR-MS (ESI): Found m/z $[M_{+}H]^{+}$ 1906.11094; calculated for $C_{114}H_{164}N_6O_6S_6$ 1906.08759

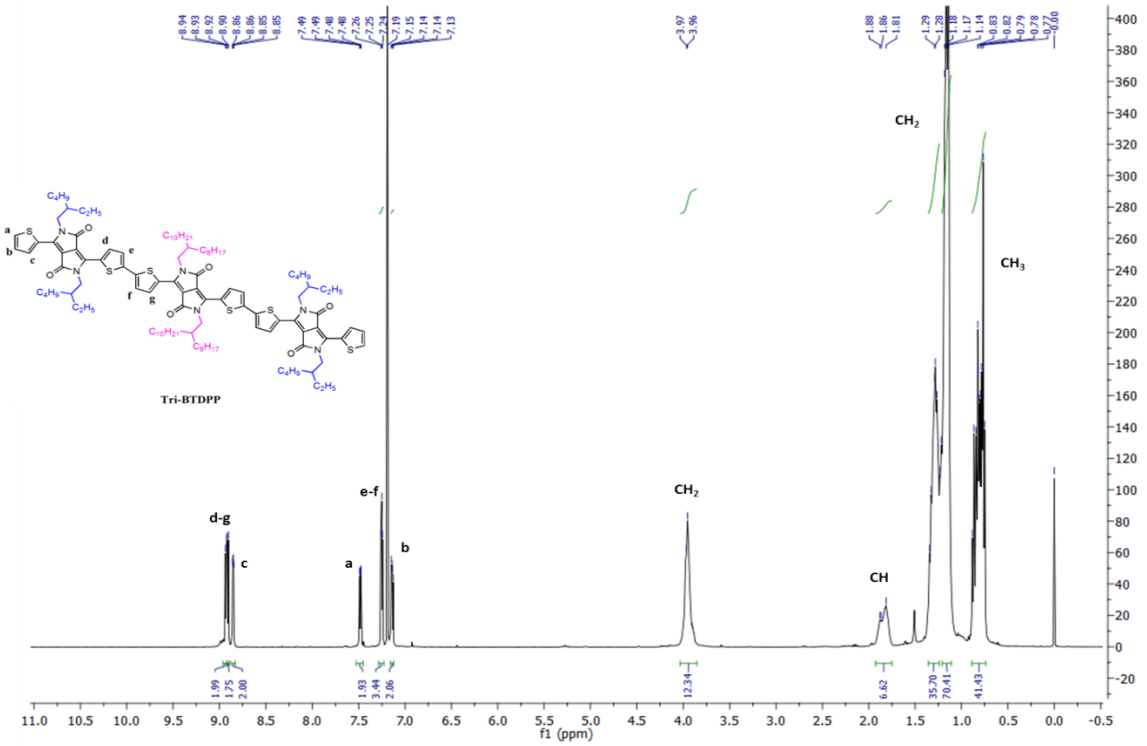

Figure 33: ^{1}H NMR of Tri-BTDPP

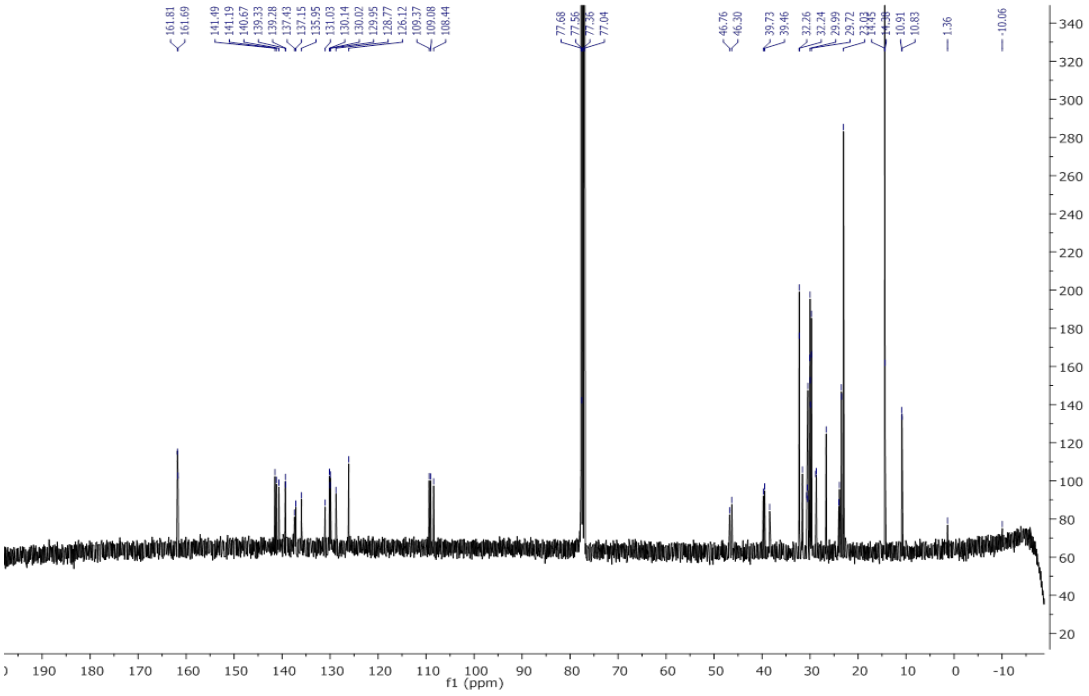

Figure 34: ^{13}C NMR of Tri-BTDPP

Data for 3:

^{1} H NMR ($CDCl_3$, 300 MHz) δ 9.05-8.84 (4H, m), 7.65 (2H, d, J=4.9 Hz), 7.43 (2H, d, J=4.2 Hz), 7.33 – 7.28 (1H, m), 7.23 – 7.18 (1H, m), 4.04 (8H, d, J= 7.1 Hz), 1.92 (4H,s), 1.44 – 1.07 (8H, m), 1.04-0.67 (26H, m). (Spectra in Appendix 2)

^{13}C NMR ($CDCl_3$, 300 MHz) δ161.62, 140.88, 140.55, 139.15, 136.68, 135.58, 130.80, 129.79, 128.50, 125.99, 108.85, 108.14, 46.30, 45.94, 39.31, 39.07, 37.97, 37.75, 31.91, 31.21, 30.05, 29.65, 29.36, 28.50, 28.34, 26.26, 23.63, 23.08, 22.68, 14.12, 10.56. (Spectra in Appendix 2)

HR-MS (ESI): Found m/z $[M+H]^+$ 1383.87347; calculated for $C_{84}H_{127}N_40_4S_4$ 1383.87110

Data for 4:

MALDI-TOF: Found m/z $[M+H]^+$ 1046.4; calculated for $C_{60}H_{79}N_40_4S_4$ 1046. 7

We performed solubility tests with five solvents: hexane, chloroform, toluene, chlorobenzene and o-dichlorobenzene. Among all these solvents, only chloroform provides solubility above 10 $mg.mL^{-1}$ for Tri-BTDPP confirming the need of long alkyl chains on the central DPP unit. The thermal properties of Tri-BTDPP were studied by differential scanning calorimetry (DSC) (Figure 35). Tri-BTDPP presents an endothermic peak corresponding to its melting point at 253 °C in the heating scan and an exothermic peak at 232 °C corresponding to its crystallization temperature in the cooling scan.

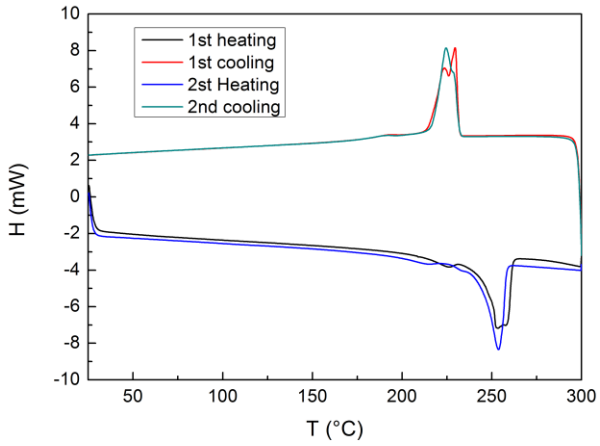

Figure 35: DSC measurement of Tri-BTDPP powder

2.2. Characterization of Tri-BTDPP

To assess the potential of Tri-BTDPP as a donor semiconductor for OSC applications, we investigated its optoelectronic properties with UV-visible absorption spectra and the measurements of its energy levels. We also conducted mobility studies in order to investigate the ability of Tri-BTDPP to transport charge carriers.

2.2.1. Optical properties

The UV-Visible absorption spectra of Tri-BTDPP in chloroform solution (concentration of 0.25 mg.mL^{-1}) and neat film are shown in Figure 36. Tri-BTDPP absorbs in the range of 600 to 850 nm in solution with the maximum absorption peak (λ_{max}) at 707 nm and a maximum absorption coefficient around 6×10^4 L.mol^{-1}.cm^{-1}. Compared with the Tri-DPP containing a central bisphenyl DPP unit from Nguyen and co., showing an absorption onset at ~670 nm [129], Tri-BTDPP presents a much longer absorption onset at ~810 nm, owing to the increased conjugation length as a result of higher coplanarity and a more efficient intramolecular charge transfer from the electron-rich thiophene units to the central electron-deficient DPP unit.. In films, the λ_{max} red-shifts to 725 nm and an additional shoulder at ~830 nm appears. The spectrum extends up to almost 1000 nm. The large red-shift of the absorption spectrum from solution to film originates from the planarization of the molecule and the strong intermolecular interactions in the solid state. The optical band gap (E_g) was calculated from the onset absorption wavelength to be 1.33 eV, which is much lower than its tri-DPP analogues (E_g = 1.65 eV) [129] and di-bithiophene DPP (E_g = 1.51 eV) [79]. The band gap remains in the range of 1.2 eV to 1.7 eV needed for optimal harvesting of sunlight to achieve a high PCE [23].

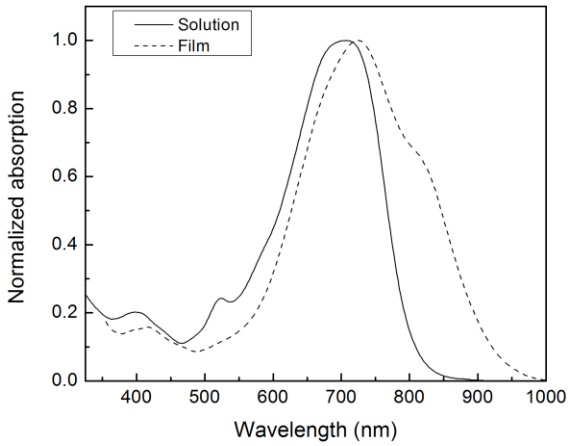

Figure 36: UV-Visible spectra of Tri-BTDPP in solution and thin film

2.2.2. Energy levels

Energy levels are also key parameters for OSCs and were investigated through density functional theory (DFT) calculations and cyclic voltammetry. Besides energy levels, DFT calculations were also carried out on Tri-BTDPP to study its optimized molecular geometry. Methyl side chains were chosen to facilitate the calculation. As shown in Figure 37a-b, Tri-BTDPP adopts a coplanar structure as the lowest energy conformation, which would be beneficial for intermolecular interactions and potentially close π-π stacking. According to the electron density distribution analysis (Figure 37c-d), the HOMO and the LUMO of Tri-BTDPP

extend over the entire molecule, revealing an efficient conjugation and intramolecular charge transfer (ICT) between thiophene and DPP moieties. This strong conjugation lower the band gap as observed earlier in UV-Visible spectra. The theoretical values of the HOMO and LUMO levels were evaluated to be -4.76 eV and -3.15 eV, respectively.

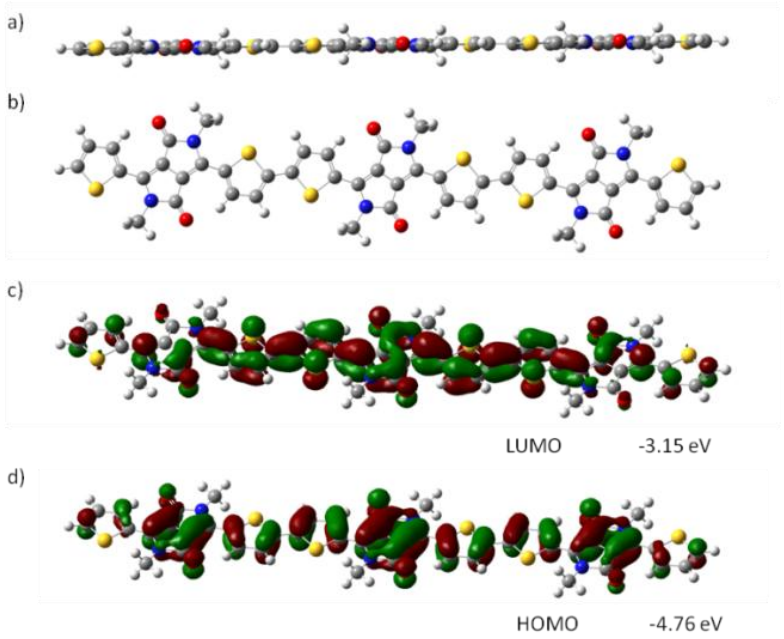

Figure 37: DFT calculations on Tri-BTDPP: a-b) lowest energy conformation c-d) electron density of the LUMO and HOMO levels

The electrochemical properties of Tri-BTDPP were investigated by cyclic voltammetry (CV) and shown in Figure 38. The HOMO level was calculated from the onset of the first oxidation peak using the equation: $E_{HOMO} = - (E^{ox}_{onset} - (E_{Fc} - 4.8))$ eV, where -4.8 eV is the HOMO energy level of ferrocene (Fc) [117,118]. Since no reduction peak was observed, the LUMO was estimated by adding the optical band gap to the HOMO. The HOMO and the LUMO of Tri-BTDPP were evaluated to be -5.34 eV and -3.99 eV, respectively. By comparing tri-BTDPP energy levels with those of bithiophene DPP [91] and di-bithiophene DPP [134], increasing the number of bithiophene DPP units results in a lower band gap and lower LUMO level but maintain the same HOMO level. Consequently, the three electron-deficient DPP units ensure a deep HOMO level, providing V_{OC} with a promising theoretical value of 0.74 eV for a blend of Tri-BTDPP and PCBM, based on Scharber's methods [23]. The gap between the LUMOs of Tri-BTDPP (-4.01 eV) and $PC_{61}BM$ (-4.3 eV) [135] was estimated to be 0.3 eV, which is equivalent to the value needed for electron transfer from donor to acceptor with minimal energy loss [23].

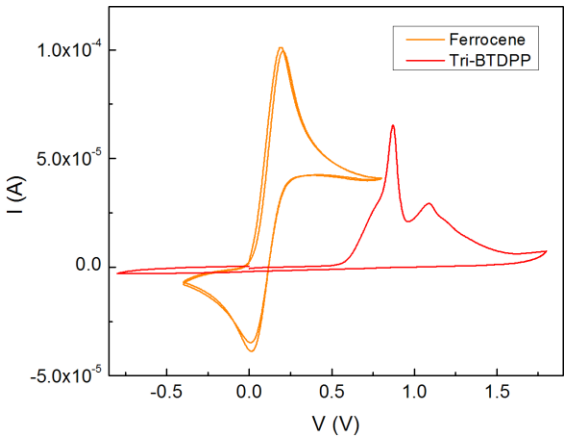

Figure 38: Cyclic voltammetry of Tri-BTDPP

The data from DFT calculations and CV are summarized in Table 1. The coplanar conformation and the deep HOMO level of Tri-BTDPP are interesting feature for high performances in OSCs. Brabec *et al.* proposed a diagram predicting the best PCE that can be achieved by a specific donor/$PC_{61}BM$ system according to their energy levels (cf Chapter 1) [23]. Using Tri-BTDPP as donor material, a PCE of 10% can be predicted (Figure 39). Although achieving such a PCE requires an ideal morphology and efficient and balanced charge transport, this analysis confirmed that Tri-BTDPP is a promising donor for OSCs.

Table 1: Energy levels according to DFT calculations and CV

	HOMO (eV)	**LUMO (eV)**	**E_g (eV)**
DFT	-4.76	-3.15	1.61
Experimental	-5.34	-3.99	1.33

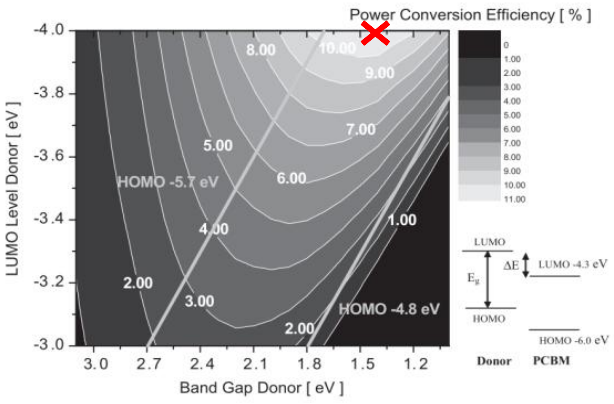

Figure 39: Tri-BTDPP on Scharber's diagram [23]

2.2.3. Charge transport properties

As donor semiconductors are responsible for hole transport in the active layer, the charge transport properties of Tri-BTDPP were investigated. According to Proctor *et al.* [52], to reach a FF superior to 0.65, electron and hole mobilities within the active layer, should be balanced and superior to 10^{-4} $cm^2.V^{-1}.s^{-1}$. Additionally, they highlighted that hole mobility of donor measured in neat film can be considered as the mobility upper limit, meaning that material with limited mobility in neat film will probably suffer from low FF. Therefore, the charge transport property of Tri-BTDPP was studied in neat film using bottom-gate bottom-contact field effect transistors (OTFTs). The devices were fabricated by spin-coating a solution of Tri-BTDPP (10 $mg.mL^{-1}$ in chloroform) on top of a heavily n-doped Si/SiO_2 wafer substrates patterned with gold source-drain electrodes. The devices based on Tri-BTDPP showed p-type hole transport behaviour. The average saturation hole mobility of the as-cast thin films was evaluated to be 1.2×10^{-4} cm^2 V^{-1} s^{-1}. The devices with Tri-BTDPP films annealed at 100 °C and 150 °C for 10 min exhibited higher hole mobilities with average values of 7.4×10^{-4} cm^2 V^{-1} s^{-1} and 9.4×10^{-4} cm^2 V^{-1} s^{-1} respectively (Table 2). The increase mobility indicates improved molecular ordering in the films upon annealing. Figure 40 shows the transfer curves of the best device, annealed at 150 °C, which shows the highest mobility of 1.2×10^{-3} $cm^2.V^{-1}.s^{-1}$ with a $I_{on/off}$ ratio of 3×10^4. Those values are likely underestimated as the output characteristics present a strong non-linear behavior due to contact resistance effects. In comparison with Nguyen's branched tri-DPP [129], tri-BTDPP presents a higher hole mobility even with longer branched alkyl chains on the central DPP core, indicating that the improved backbone coplanarity enhances the charges transport. However, Tri-BTDPP's hole mobility remains lower than tri-DPP with linear alkyl chains. Linear alkyl chains would not provide enough solubility to tri-BTDPP. According to OTFT results in neat film, Tri-BTDPP provides relatively high hole mobility for solution-processed small molecules owing to its coplanar conformation. This is encouraging to reach high FF and further confirms its great potential for OSC application.

Table 2: Hole mobilities measured in saturation regim before and after thermal annealing of 100°C and 150°C

Annealing	**As cast**	**100°C**	**150°C**
Average μ_h 4 devices ($cm^2.V^{-1}.s^{-1}$)	1.21×10^{-4} $\pm 5.9 \times 10^{-5}$	7.44×10^{-4} $\pm 1.32 \times 10^{-4}$	9.41×10^{-4} $\pm 1.91 \times 10^{-4}$
Maximal μ_h ($cm^2.V^{-1}.s^{-1}$)	1.63×10^{-4}	8.13×10^{-4}	$1.22.10^{-3}$

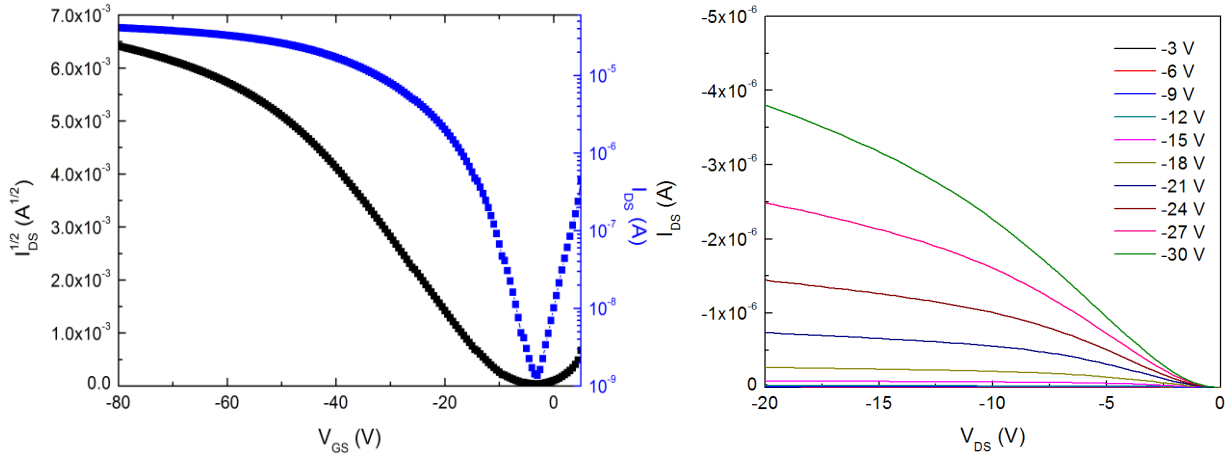

Figure 40: OTFT characteristics of Tri-BTDPP after annealing at 150°C and at V_{DS} = -30 V and the corresponding output curves.

2.2.4. Discussion

Using only thiophene spacers in between three DPP-cores provided a coplanar conformation. As predicted, the planarity of the molecule entailed lower band gap and absorption spectrum up to the near infrared region along with strong intermolecular interplays ensuring high hole mobility approaching 10^{-3} cm² V^{-1} s^{-1}. A deep HOMO level of -5.34 eV was obtained for a promising V_{OC}. All these features make Tri-BTDPP a good candidate for OSC application. Compared to molecules with one or two DPP units, the purification of Tri-BTDPP was more challenging due to the formation of dimers but remained feasible. As for the optoelectronic properties, the addition of a DPP unit decreases the LUMO and thus the band gap.

2.3. Photovoltaic properties of Tri-BTDPP

2.3.1. OSCs based on Tri-BTDPP

The photovoltaic properties of a blend of Tri-BTDPP as a donor and [6,6]-phenyl-C_{61}-butyric acid methyl ester ($PC_{61}BM$) as an acceptor were investigated in bulk heterojunction (BHJ) OSCs. Here, the optimizations made on the device architecture and the blend formulation are detailed. First, a conventional architecture: ITO/PEDOT:PSS/Tri-BTDPP:$PC_{61}BM$/Al (see Chapter 1) was used. The active layer was deposited by spin-coating a 20 $mg.mL^{-1}$ solution of Tri-BTDPP:$PC_{61}BM$ 1:1 in chloroform. Very low PCE values of < 0.1% (V_{OC}= 0.36 V; FF = 0.28; J_{SC} = 0.56 mA cm^{-2}) were obtained. Even by varying the active layer thickness from 40 nm to 150 nm and the donor:acceptor ratio (3:1, 2:1, 1:1, 1:2, 1:3), the PCE remains low < 0.1%. The poor performance was most likely due to a poor morphology, specifically, a poor nanophase separation of the donor and the acceptor in the film. Using solvent additives is a common and often efficient way to tailor the morphology and to improve the OSC performances [42,136]. 1,8-

diiodooctane (DIO) is one of the most commonly used additives, therefore it was used to improve the film morphology of the Tri-BTDPP:$PC_{61}BM$ blend. Different concentrations (vol% relative to the solvent) of DIO (0.1%, 0.2%, 0.4%, 0.5%, 0.8%, 1%, 2%, 3%, 4% and 5%) were added in the Tri-BTDPP:$PC_{61}BM$ 1:1 blend solution. Figure 41 shows that the PCE increases with the introduction of 1% of DIO however further increase in DIO concentration does not bring further enhancement. Other solvent/additive systems have been tested such as chlorobenzene with DIO or 1-chloronaphtalene (CN) and o-dichlorobenzene with DIO and CN but the limited solubility of Tri-BTDPP in those systems prevents a good quality of film and thus high PCE.

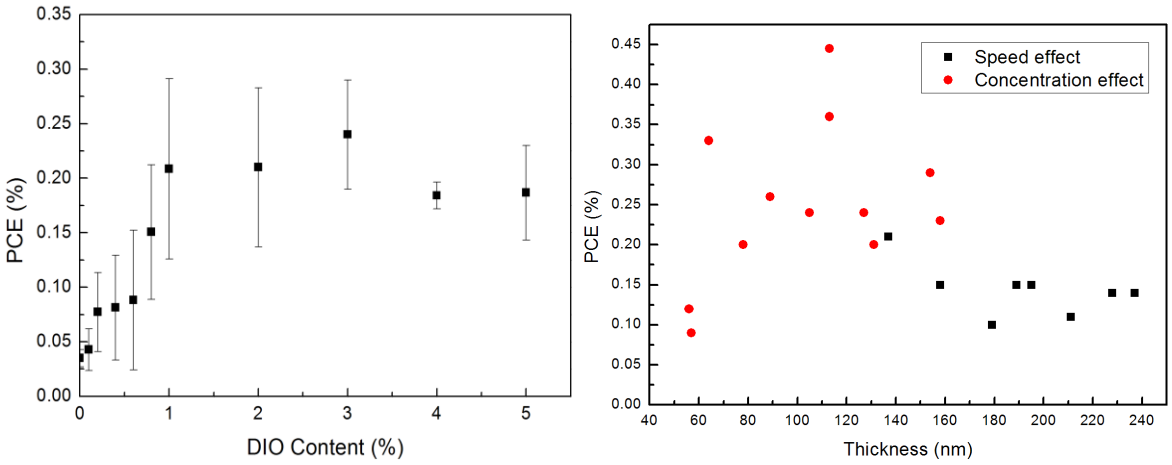

Figure 41: PCE of OSC as a function of DIO concentrations (left) and of active layer's thickness (right)

The optimization was pursued by defining the optimal thickness of the active layer and the right donor: acceptor ratio. To do so, a panel of thicknesses between 60 to 240 nm, resulting from various solution concentrations (10, 15 and 20 $mg.ml^{-1}$) and deposition speeds (1000, 2500 and 5000 rpm) were tested. Figure 41 depicts a maximal PCE for devices with a thickness of 100 nm, corresponding to the best trade-off between photon absorption and charge transport. As for Tri-BTDPP and $PC_{61}BM$ ratio, Tri-BTDPP content was varied between 20% and 80%, keeping a total concentration of 15 $mg.ml^{-1}$. The devices showed a decrease in J_{SC} with high concentration of Tri-BTDPP whereas V_{OC} and FF increased. As seen in Figure 42, the best PCE was achieved for a 50% content of Tri-BTDPP. To conclude on this primary optimization, with 1% DIO and at optimized active layer thickness and Tri-BTDPP/$PC_{61}BM$ ratio, an improved PCE of 0.27% was obtained, which is, however, still very low.

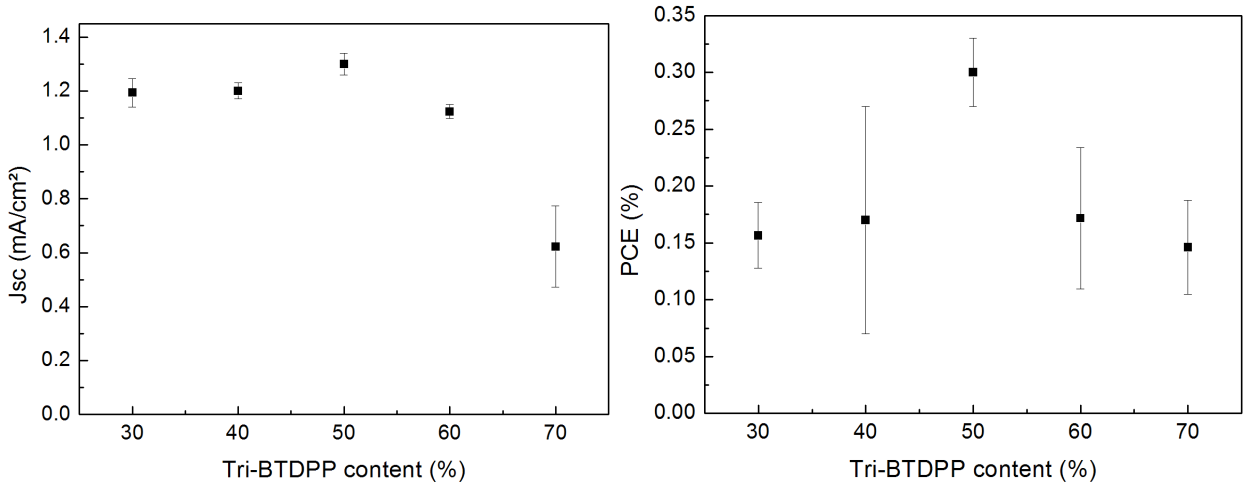

Figure 42: Evolution of J_{SC} and PCE with Tri-BTDPP content

Those first devices were realized with Tri-BTDPP batches containing a small amount of dimer **3**. In the literature, it has been reported that even a small amount of by-products or impurities can have a strong and unfavorable effect on the OSC performances by acting as recombination center or by breaking the crystallinity [137]. As the presence of dimer **3** may hamper the photovoltaic process, an important effort was furnished to separate Tri-BTDPP and dimer **3** with heated silica gel column as described in section 2.1. In comparison with Tri-BTDPP crude, devices using pure Tri-BTDPP exhibited a similar even slightly decreased PCE around 0.20%, refuting the harmful effect of dimer **3**.

The low PCE was mainly due to the low J_{SC} and FF, which might originate from the inefficiency of exciton diffusion, charge dissociation, charge transport, and charge collection. In order to improve the electron collection, a thin layer (~10 nm) of calcium (Ca) was introduced between the active layer and the aluminum electrode. Calcium acted as an electrode with a much lower work function (2.9 eV) than that of aluminum (4.3 eV) which increased the built-in voltage within the device. Additionally, $PC_{71}BM$ was used instead of $PC_{61}BM$ for a better matching of the energy levels [138]. The PCE increased to 0.43% due to improved charge collection and thus FF (Table 3, Figure 43). Next, an inverted OSC structure, ITO/ZnO_x/Tri-BTDPP:$PC_{71}BM$ /MoO_3/Ag, was adopted to examine if they offer better charge collection and charge transport. Higher J_{SC} of 2.15 mA cm^{-2}, V_{OC} of 0.67 V, and FF of 0.50 were achieved, which led to an increased PCE up to 0.72%.

Table 3: Average performances on 8 devices of OSC with various device architectures

	Architecture	J_{sc} (mA cm^{-2})	V_{oc} (V)	FF	PCE (%)
1	**Conventional: ITO/ PEDOT:PSS/Tri-BTDPP:$PC_{61}BM$ (1:1)/Al**	1.30	0.56	0.38	0.27
2	**Conventional: ITO/ PEDOT:PSS/Tri-BTDPP:$PC_{71}BM$ (1:1)/Ca/Al**	1.61	0.57	0.47	0.43
3	**Inverted: ITO/ZnO_x/Tri-BTDPP:$PC_{71}BM$ (1:1) /MoO_3/Ag**	2.15	0.67	0.50	0.72

The J-V curves in dark and under illumination of the best devices of each architecture are represented in Figure 43. For conventional OSCs, important leakage currents were observed suggesting that the devices suffered from inefficient charge transport, strong recombination or non-ohmic contact between the interfaces. In comparison, inverted OSC showed much reduced leakage currents along with lower series resistance of 636 Ω over 914 Ω in conventional OSC and enhanced the shunt resistance to 526 k Ω over 53 k Ω in conventional OSC, confirming a better charge transport and charge collection in the inverted device. However, the cell performance is still very low compared to other small molecules reported in the literature, mainly due to the low J_{SC} [139]. It is noteworthy that Tri-BTDPP in inverted OSCs shows very low dark current and thus high shunt resistance compared to p-DTS, a reference in solution-process small molecules [140], which confirm its great film forming ability.

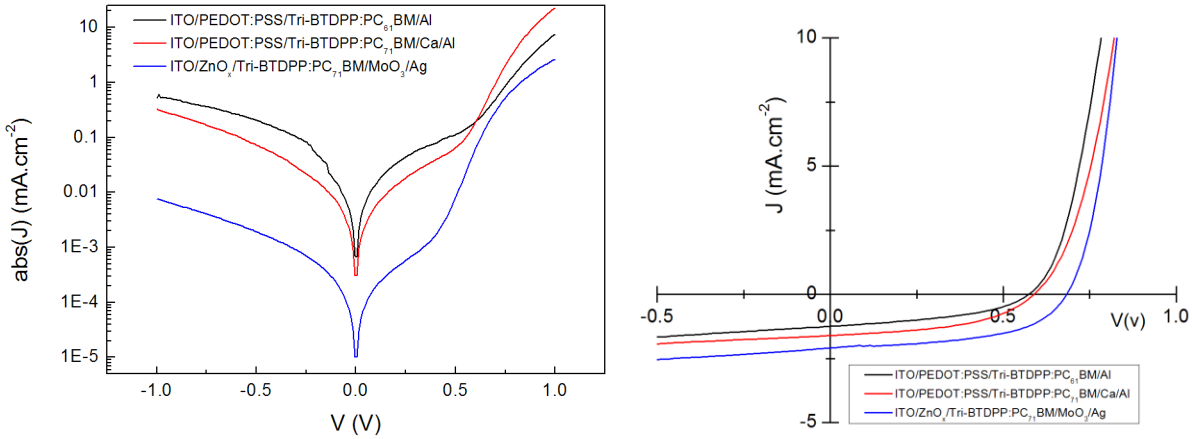

Figure 43: J-V curves in dark (left) and under illumination (right) of the best OSC of each device architectures

To elucidate the origin of the low J_{SC}, external quantum efficiency (EQE) was measured for the OSC with an optimal PCE of 0.72%. Figure 44 shows that the current is mainly generated in the wavelength range from 300 nm to 600 nm. This spectrum region corresponds to the $PC_{71}BM$ absorption band indicating that the current is mainly resulting from the excitons generated within $PC_{71}BM$. The lack of Tri-BTDPP's exciton contribution revealed that excitons formed in Tri-

BTDPP do not separate in free charges and recombine instead. This phenomenon can occur in the case of an unfavorable morphology with too large domains of Tri-BTDPP causing large phase separation with the $PC_{71}BM$. In order to contribute to the generation of charge carriers, an exciton has to be formed at a distance in the range of the exciton diffusion length from a donor / acceptor interface. If the phase separation is too large, excitons can not separate and contribute to the generation of current. As a second possibility, the donor/acceptor system may not provide enough driving force for the electron to transfer from donor to acceptor, owing to the narrow offset of 0.3 eV between the LUMO of the donor and the LUMO of the acceptor.

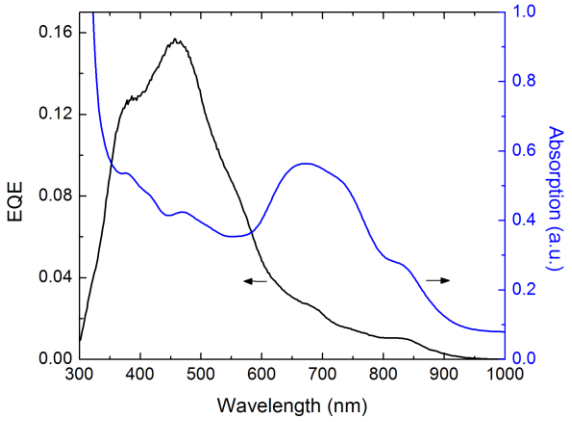

Figure 44: EQE and absorption of Tri-BTDPP based OSCs

To conclude, the best device was obtained using an inverted architecture offering better charge transport and charge collection. 1% of DIO also helped the photovoltaic properties of Tri-BTDPP. In spite of these optimization, the performance remains under 1% due to limited J_{SC} caused by the non-participation of Tri-BTDPP's photo-generated excitons in the photovoltaic process.

2.3.2. Morphology analysis

In order to determine the reasons of the low performance obtained, the morphology of the active layer was examined as it strongly dictates the PV performances in BHJ OSC. As presented in Chapter 1, the morphology should be composed of three phases: intermixed donor/ acceptor domains and pure crystalline domains of the acceptor and the donor. Due to the short exciton diffusion length of organic semiconductors around ~1-10 nm [22,141], the donor/acceptor segregation should be controlled to achieve domain sizes of pure donor and pure acceptor in the range of their exciton diffusion lengths for an optimum charge separation. Additionally, donor and acceptor domains should ensure efficient charge transport to prevent from charge recombination. Therefore, the analysis of the morphology is fundamental and was proceeded using AFM, DSC and XRD measurements.

AFM was used on a Tri-BTDPP:$PC_{71}BM$ (1:1) blend film prepared using the same conditions as for the one that achieved the best OSC performance to elucidate the morphology at the active layer top surface. As shown in Figure 45, large grains of ~100-200 nm were observed in both height and phase images. Since the phase image is very similar to the height image, each grain seems uniform in composition. Because the Tri-BTDPP phase is highly crystalline as revealed by the XRD measurements (to be discussed below), the grains appearing in the AFM images are likely the Tri-BTDPP phase. The $PC_{71}BM$ phase might be present at the boundaries of the Tri-BTDPP (the grain boundaries in the phase image are larger than in the height image). It is also possible that a vertical phase separation occurred with $PC_{71}BM$ enriched at the bottom of the film [142–144] but can not be revealed by AFM as a technique examining the top surface only of thin films. The increase in J_{SC} observed in the inverted devices compared to the standard devices supports this hypothesis because the charge collection would be more favorable for the inverted structure if $PC_{71}BM$ is enriched at the bottom and Tri-BTDPP is enriched on the top. The large domain size of the Tri-BTDPP phase (~100-200 nm) greatly exceeded its exciton diffusion length, which is possibly in the range of ~1-10 nm [22,141] and would make the exciton diffusion to a donor/acceptor interface very difficult. This, in turn, would cause poor charge carrier generation due to geminate recombination of excitons and thus a low J_{SC}. Consequently, the lack of Tri-BTDPP's exciton contribution, observed in EQE spectrum, originates from a harmful morphology. Further reduction in the domain size down to the exciton diffusion length is required to improve the charge generation.

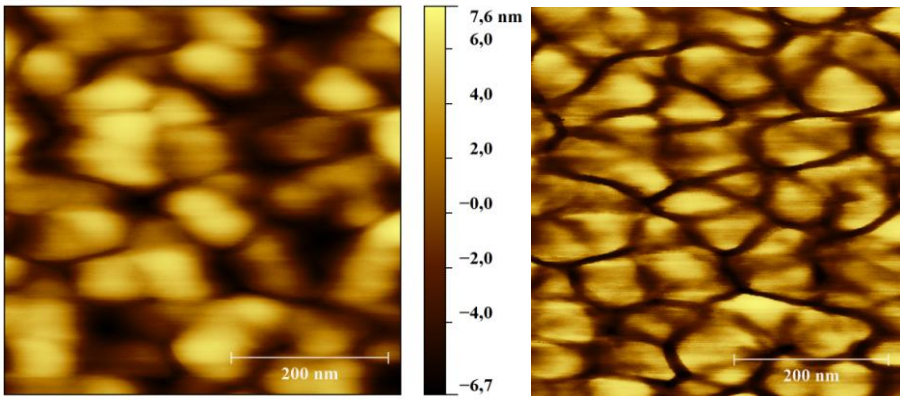

Figure 45: AFM images of Tri-BTDPP: $PC_{71}BM$ 1:1 as prepared in the best device; Height images (left) Phased images (right)

To further understand the formation and composition of the phases of the blend film morphology, the interaction of Tri-BTDPP and $PC_{71}BM$ was investigated using differential scanning calorimetry (DSC). The measurements were completed on films prepared by drop-casting solutions of Tri-BTDPP and $PC_{71}BM$ with different ratios in chloroform. The DSC trace of the first heating scan of each sample is shown in Figure 46. The melting points of both Tri-BTDPP and $PC_{71}BM$ do not exhibit a notable melting point depression with varying blend ratio,

indicating their very low miscibility. This suggests that Tri-BTDPP and $PC_{71}BM$ do not intermix and rather form respective pure domains, which explains the resembling height and phase AFM images. According to previous studies, an ideal donor/acceptor blend layer morphology for OPVs should provide not only pure domains of donor and acceptor to extract the charges but also donor-acceptor intermixed domains for ultrafast charge separation [31,32,34]. The immiscibility of Tri-BTDPP and $PC_{71}BM$ induces the formation of over-sized pure domains and prevents the formation of such intermixed domains, leading to hampered exciton dissociation as well as charge separation.

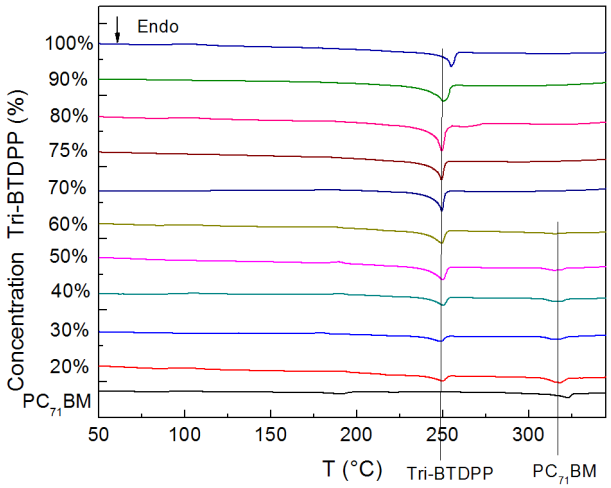

Figure 46: First heating scans of Tri-BTDPP:$PC_{71}BM$ blend films with different Tri-BTDPP concentrations, using DSC.

XRD measurements were carried out to study the nature of the molecular packing of the neat Tri-BTDPP and Tri-BTDPP:$PC_{71}BM$ films. As shown in Figure 47, for the Tri-BTDPP neat film, sharp and intense diffraction peaks at 2θ = 4.50°, 8.96°, 13.28°, 17.72° and 22.64° are clearly seen. The crystallinity of Tri-BTDPP is much higher than tri-DPP where the diffraction peaks were barely or not visible [129]. According to the Bragg's law, the first four peaks represent the 1st to 4th order peaks of planes with a *d*-spacing distance of 1.96 nm, while the last peak represents another set of planes with a *d*-spacing distance of 0.39 nm. This XRD pattern is reminiscent of a lamellar packing motif, which has been frequently observed for many crystalline polymers such as regioregular head-to-tail poly(3-hexylthiophene) (P3HT) [145]. Therefore, it is reasonable to consider that the Tri-BTDPP molecules adopted a lamellar packing motif, with an interlayer distance of 1.96 nm, separated by the alkyl chains, and a π- π stacking distance of 0.39 nm between the conjugated backbones. The high crystallinity of Tri-BTDPP neat film is consistent with the relatively good hole transport observed in OTFTs as an ordered and close molecular packing helps hopping transport.

For the 1:1 Tri-BTDPP:$PC_{71}BM$ blend film, the primary and secondary diffraction peaks were still observed at the same positions meaning Tri-BTDPP remained well-ordered. The size of the

crystallites in neat and blend film was determined from the primary diffraction peak by the Scherrer equation to be both equal to 27.4 nm, which confirmed that $PC_{71}BM$ did not intermix with Tri-BTDPP to influence the crystal structure of the Tri-BTDPP phase. The size of the crystallites represents the dimension of the crystallites in the vertical direction while the grain size observed in AFM images is the lateral dimension. Nonetheless, the crystallite size of the Tri-BTDPP phase is relatively large compared to the exciton diffusion length and suggest the formation of large domains.

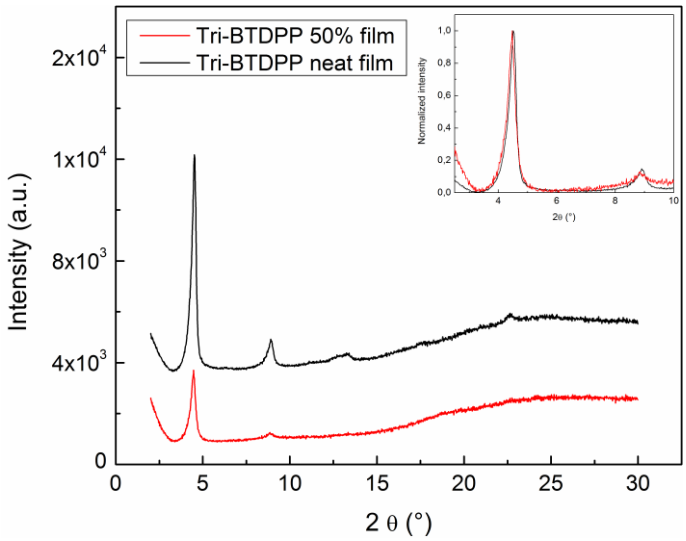

Figure 47: XRD measurements on Tri-BTDPP neat film and blended with $PC_{71}BM$ (1:1 in weight) films

According to this study, devices based on Tri-BTDPP and $PC_{71}BM$ suffer from unfavorable morphology with too large crystalline domains of donor and acceptor and without any intermixed donor/acceptor domain, hampering good charge separation. The non-miscibility of Tri-BTDPP and $PC_{71}BM$ is responsible of this strong phase separation where Tri-BTDPP and $PC_{71}BM$ crystallize separately. To achieve a better morphology and reach higher performances in OPVs, the size of Tri-BTDPP's crystallites have to be reduced. In some accounts, nucleating agents were used to increase the number of nuclei and to limit the formation of large crystals [146,147], although in this case, introducing 1% of nucleating agent (isotactic polypropylene (i-PP):1,3:2,4-bis(3,4- dimethylbenzylidene)sorbitol (DMDBS; Millad 3988)) reduced the PCE to 0.3%.

2.4. Conclusion

Tri-BTDPP showed interesting optoelectronic properties with an absorption spectrum up to the near infrared region and a deep HOMO level of -5.34 eV. Besides, the coplanar conformation of Tri-BTDPP enabled a close π-π stacking and thus a high crystallinity degree, beneficial for

efficient charge transport as demonstrated in OTFT transistors with a hole mobility approaching 1 x 10^{-3} $cm^2.V^{-1}.s^{-1}$. This limitation came from the immiscibility of Tri-BTDPP with $PC_{71}BM$ which generates large crystalline domains preventing good charge separation. This incompatibility may originate from the strong intermolecular interactions between Tri-BTDPP molecules which must surpass that of Tri-BTDPP with the solvent [148]. As a result, Tri-BTDPP molecules strongly self-assemble and aggregate, preventing $PC_{71}BM$ to insert among them and even being repulsed. Testing various host solvent, additives or nucleating agent did not bring further improvements. This self-assemble was not observed with Nguyen's tri-DPP which has strong dihedral angles along their molecular backbone and low crystallinity [129]. This suggests that the curvature of the molecular backbone dictates the miscibility between Tri-BTDPP and $PC_{71}BM$.

3. DESIGN AND SYNTHESIS OF TWISTED DPP OLIGOMERS

Novel oligomers based on DPP were designed, in order to identify the role played by the curvature of the molecular backbone on the miscibility between the donor and the acceptor materials. As Tri-BTDPP showed interesting optoelectronic properties, the three DPP moieties were maintained in the design of the new oligomers. Many works have studied the effect of backbone curvature on the solid-state arrangement by anchoring different side chains on thiophene spacers of polymer [149–151] and also small molecules [113]. The position of side chains has a great importance as it changes the strength and the location of the disorder [152]: anchoring side chains on as α position of a thiophene spacer would induce large dihedral angles between DPP and thiophene and thus significant disorder [113,150,151] whereas side chains embedded on a β position of thiophene spacers seems to cause a much moderate disorder [152,153]. As demonstrated by Huang *et al.*, a moderate aggregation is more desirable than strong or poor aggregation for efficient OSCs as its offer moderate domain size [113]. Therefore, we aim at increasing the tilt angle between the two thiophene spacers to achieve a moderate backbone curvature and thus a moderate aggregation. To do so, hexyl chain can be embedded at β position as illustrated in Figure 48.

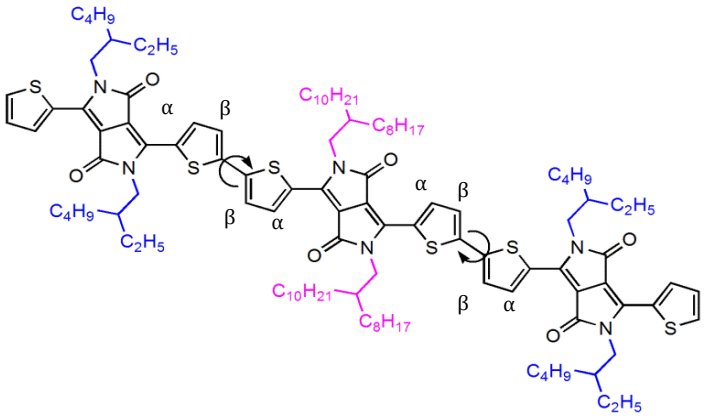

Figure 48: Positions to introduce hexyl chains

3.1. Introduction of hexyl chains on stannyl DPP intermediate

To induce the right twisting, hexyl chains can first be embedded at a β position of the thiophene spacer linked to the central DPP core as shown in Scheme 2. To this end, 3,6-bis(4-hexylthiophen-2-yl)pentalene-1,4(*2H,5H*)-dione, intermediate **5,** was successfully synthesized with a yield of 40%, by mixing 4-hexylthiophene-2-carbornitrile with di-*N*-ethylsuccinate. Then, both nitrogen of DPP were substituted with 2-octyldodecyl alkyl using K_2CO_3 base and 2-octyldodecyl iodide. After heating the solution at 140°C overnight, intermediate **6** was obtained yielding 25%. To proceed at the trimethylstannyl substitution, lithium diisopropylamide base was added to a solution of **6** in THF at -78°C under nitrogen atmosphere. After stirring 1 hour at this temperature, the solution was slowly warmed up to -20 °C over 2 hours. After cooling down again the temperature to -78°C again, trimethyltin chloride was added. Finally, the solution was allowed to warm to room temperature and stirred overnight. The NMR spectra of the crude revealed that the target compound was not formed and the starting material **6** was no longer present, meaning that **6** degraded. Hexyl side chains could not be introduced on β position of the spacer flanked to the central DPP.

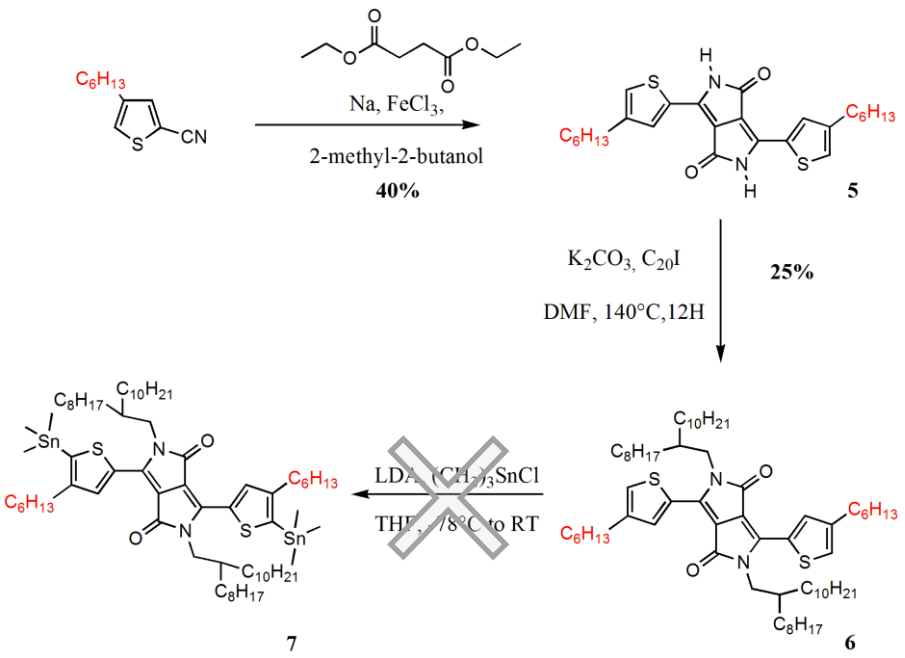

Scheme 2: Synthesis route of central DPP monomer with hexyl chain

3.2. Introduction of hexyl chains on mono-brominated DPP intermediate

Incorporation of hexyl side chains at β position of thiophene spacer attached to end-capping DPP was attempted by synthesizing 3-(5-bromo-4-hexylthiophene-2-yl)-2,5-bis(2-ethylhexyl)-6-(4-hexylthiophen-2-yl)pyrrolo[3,4-*c*]pyrrole-1,4(*2H,5H)*-dione, intermediate **9** as shown in Scheme 3. Like for compound **7**, **5** was synthesized followed by the substitution of DPP nitrogen with this time 2-ethylhexyl, offering compound **8** in 16% yield. Then, the mono-bromination was conducted by mixing **8** and NBS in a 1:1 molar ratio at 0°C in chloroform. The solution was allowed to warm up to room temperature and was stirred overnight. In general, the crude obtained after mono-bromination of DPP is a mixture of the target molecule, the starting material and a by-product resulting from the di-bromination of DPP. Those three compounds has relatively close polarity which make challenging their separation on silica gel chromatography column. If the separation was still feasible for DPP without hexyl chains, this was no longer the case for DPP with hexyl chains. Compound **9** remained mixed to **8** and dibromohexylDPP.

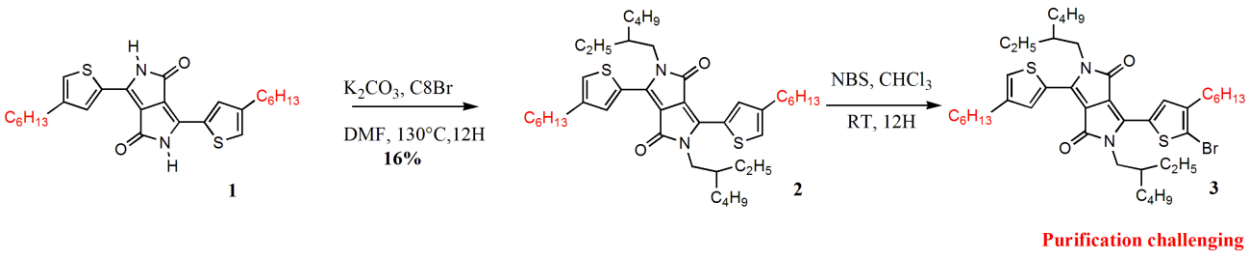

Scheme 3: Synthesis of brominated monomer with hexyl chains

3.3. Toward unsymmetrical DPP

Prior to introduce hexyl chains, the synthesis of DPP-oligomer must be simplified in order to facilitate on the subsequent functionalization. To address this issue, the bithiophene DPP units at both extremities of the molecules were replaced by unsymmetrical DPP cores with a phenyl ring on one side and a thiophene ring on the other. Two oligomers were synthesized using those unsymmetrical DPPs by adding or not hexyl chains on thiophenes spacers, like this, the effect of unsymmetrical DPP and hexyl side chains can be distinguished. The synthesis of their brominated intermediates is described in Scheme 4. Unsymmetrical DPPs were produced according to literature methods using ethylbenzoylacetate to form the intermediate **10** in 45% [154] which were further reacted with 2-thiophenecarbonitrile and 4-hexylthiophene-2-carbonitrile to furnish respectively compound **11a** and **11b** in similar yield (67%-69%) [155]. 2-ethylhexyl alkyl were then embedded on both derivatives, offering compound **12a** with a low yield of 28% similarly to bithiophene DPP derivatives whereas **12b** was obtained with an increased yield of 52%. The mono-bromination was preceded by mixing **11a** and **11b** with NBS reactant in a 1:1 molar ratio in chloroform at 0°C. The mixture was allowed to warm up to room temperature and was stirred overnight. As bromination using NBS occurred only on thiophene ring, only the mono-brominated DPP is this time formed, simplifying the separation at two compounds: **13** the monobrominated DPP and **12** the starting material. After purification, both unsymmetrical mono-brominated derivatives were obtained with satisfactory yield of 57% without hexyl and 50% with hexyl (Appendix 2).

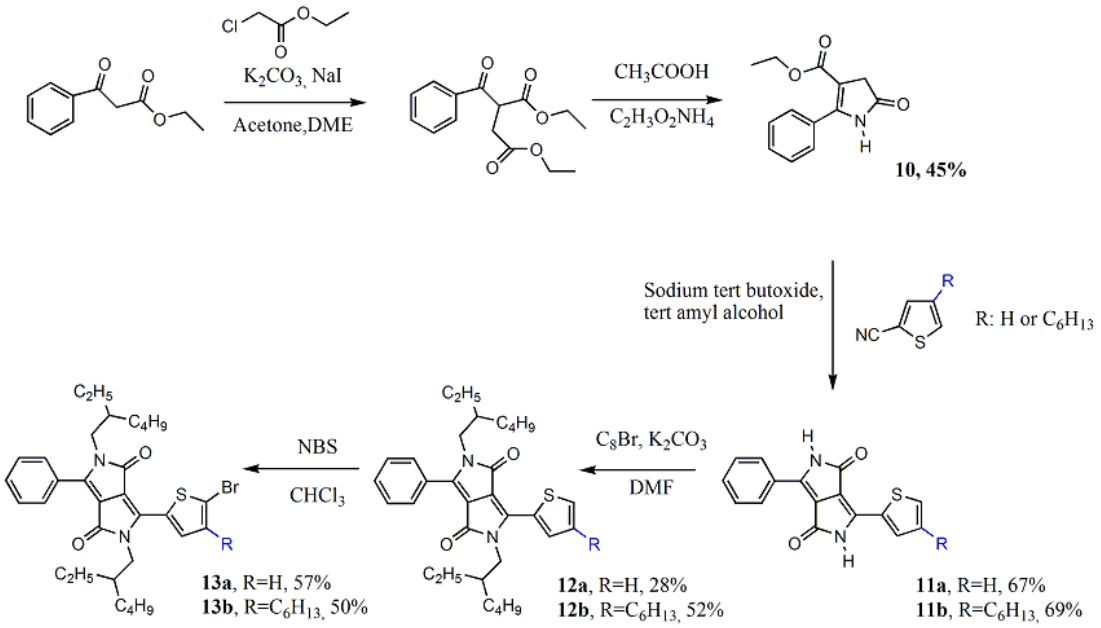

Scheme 4: Synthesis route for brominated unsymmetrical DPP intermediate

As illustrated in Scheme 5, two DPP oligomers, Tri-DPP-PT and Tri-DPP-PT-C6, can now be synthesized via Stille coupling reaction by mixing **13a** and **13b** with stannyl DPP monomer **2** in a 1:1 molar ratio in toluene. In presence of $Pd_2(dba)_3$ and P(*o*-totyl)$_3$ and after 60 hours at 120°C, both compounds were obtained and were purified as Tri-BTDPP with a successive silica gel chromatography columns, one using Hex:DCM 80:20 eluent and a second using toluene:chloroform 70:30 eluent at 50°C. Tri-DPP-PT-C_6 was obtained in a lower yield of 31% compared to 42% for Tri-DPP-PT, probably due to the steric hindrance generated by the hexyl chains. Both compounds were characterized by ^{1}H (Figure 49, Figure 51) and ^{13}C NMR (Figure 50, Figure 52) and MALDI-TOF mass spectrometry.

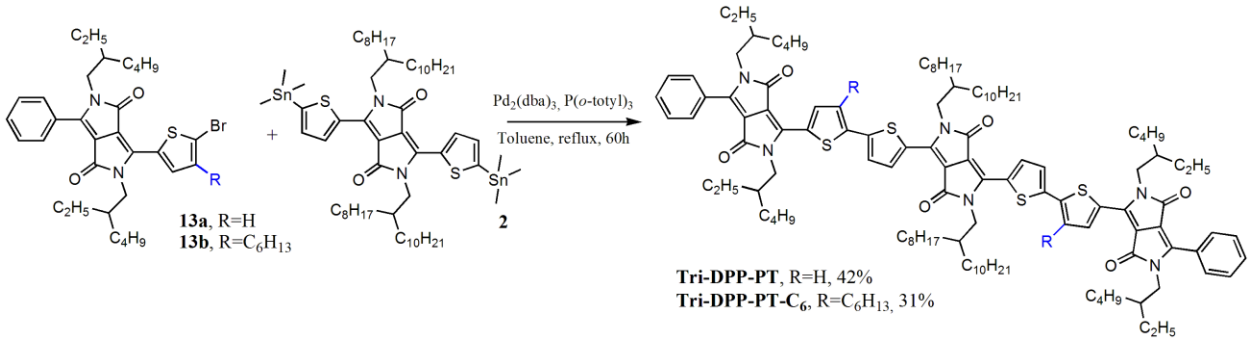

Scheme 5: Stille coupling reaction for Tri-DPP-PT and Tri-DPP-PT-C6

Data for Tri-DPP-PT:

^{1}H NMR(300 MHz,$CHCl_3$) δ 8.91 (d, J = 3.2 Hz, 4H), 7.74-7.73 (m, 4H), 7.47 (m, 6H), 7.41 (d, J = 2.9 Hz, 4H), 4.05 (d, J = 6.8 Hz, 4H), 3.97 (d, J = 7.7 Hz, 4H), 3.83 (d, J = 6.8 Hz, 4H), 1.95 (S, 2H), 1.86 (s, 2H), 1.49 (s, 2H), 1.34 (m, 22H), 1.21 (m, 62H), 1.09 (m, 12H), 0.87 (m, 24H), 0.78 (t, J = 6.7 Hz, 6H), 0.70 (t, J = 7.3 Hz, 6H)

^{13}C NMR(300 MHz,$CHCl_3$) δ 162.24, 162.07, 161.56, 147.43, 141.49, 141.37, 140.77, 139.30, 136.80, 129.94, 128.88, 128.84, 128.59, 126.25, 126.14, 109.69, 109.20, 108.89, 46.48, 45.83, 45.16, 39.31, 38.49, 38.04, 32.06, 31.43, 30.43, 30.23, 29.78, 29.52, 28.71, 28.37, 26.47, 23.90, 23.83, 23.25, 22.98, 22.85

MS (MALDI-TOF): Found m/z [M+Na] 1917.2; calculated for $C_{118}H_{168}N_6O_6S_4$ 1917.2

Data for Tri-DPP-PT-C6:

^{1}H NMR(300 MHz,$CHCl_3$) δ 9.07 (d, J = 4.02 Hz, 2H), 8.91 (s,2H), 7.80-7.74 (m, 4H), 7.56-7.48 (m, 6H), 7.42 (d, J = 4.02 Hz, 2H), 4.08 (d, J = 7.2Hz, 4H), 3.96 (d, J = 7.6 Hz, 4H), 3.85 (d, J= 7.1 Hz, 4H), 3.01-2.85 (m, 4H), 2.00 (s,2H), 1.90 (s, 2H), 1.87-1.70 (m, 4H), 1.57 (s,2H), 1.42-1.30 (m, 23 H), 1.27-1.17 (m, 62H), 1.16-1.05 (m, 12H), 0.98-0.74 (m, 37H), 0.7 (t, J = 7.3 HZ, 6H)

^{13}C NMR(300 MHz,$CHCl_3$) δ 162.26, 162.14, 161.63, 146.96, 142.34, 140.99, 140.44, 139.52, 139.26, 136.60, 135.91, 130.78, 130.23, 128.84, 128.66, 128.19, 127.68, 109.85, 108.93, 108.60, 46.57, 45.77, 45.17, 39.32, 38.49, 38.07, 31.93, 31.90, 31.72, 31.18, 30.30, 30.22, 30.13, 29.93, 29.66, 29.57, 29.44, 29.38, 29.35, 28.52, 26.25, 23.72, 23.64, 23.12, 22.86, 22.69

MS (MALDI-TOF): Found m/z [M+Na] 2085.2; calculated for $C_{130}H_{192}N_60_6S_4$ 2085.4

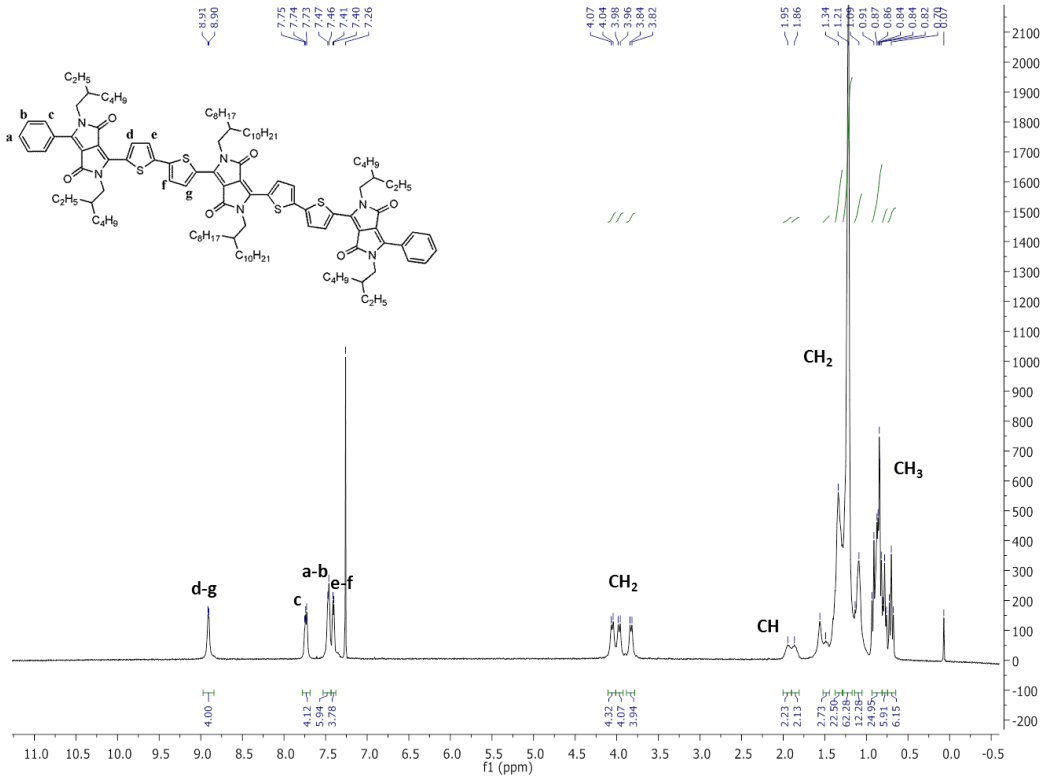

Figure 49: ^1H NMR of Tri-DPP-PT

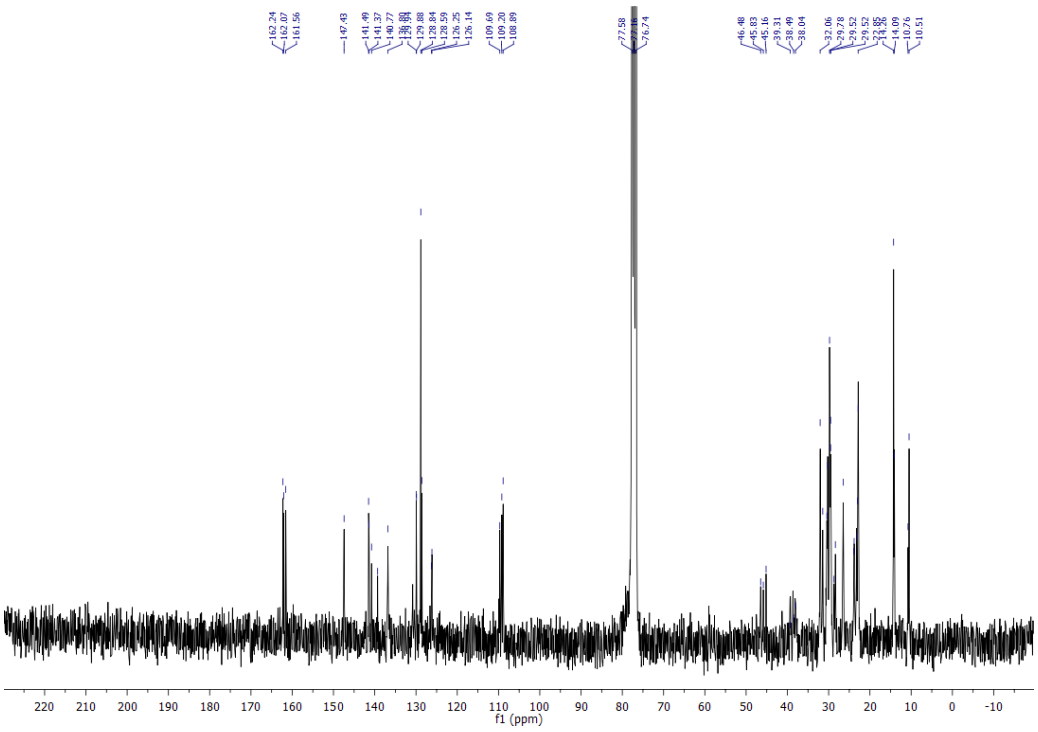

Figure 50: ^{13}C NMR of Tri-DPP-PT

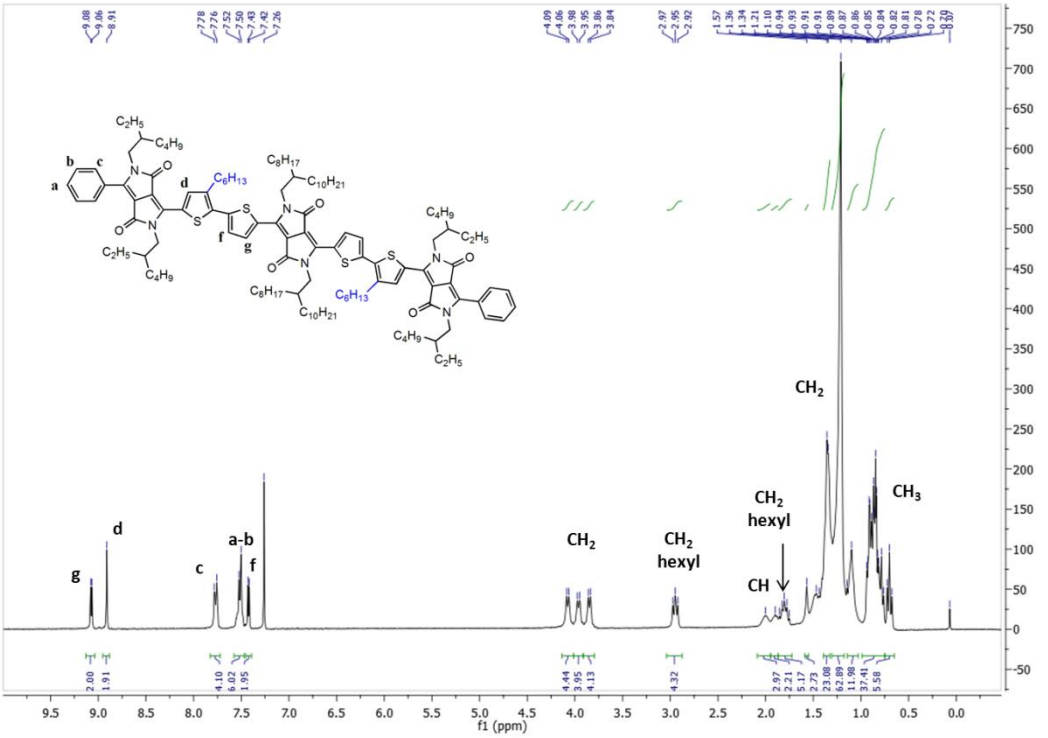

Figure 51: ^{1}H NMR of Tri-DPP-PT-C6

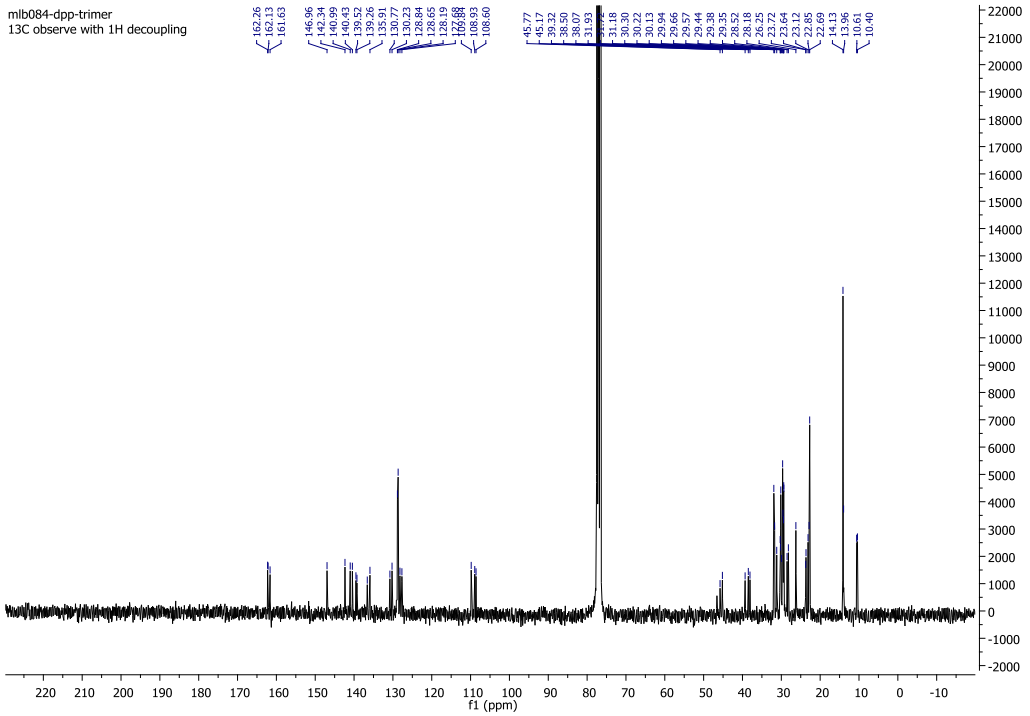

Figure 52: ^{13}C NMR of TRI-DPP-PT-C6

4. FROM TRI-BTDPP TO TRI-DPP-PT: EFFECT OF PHENYL UNIT

This section examines the effect of replacing the thiophene groups at the extremities by phenyl rings. Even if the phenyl ring was originally embedded to simplify the synthesis, it was not excluded that it may have an effect on both optoelectronic and photovoltaic properties and may already introduce a slight twisting in the molecular backbone as desired. Therefore, a full characterization of Tri-DPP-PT was conducted in comparison to Tri-BTDPP as they only differ from phenyl rings (Figure 53).

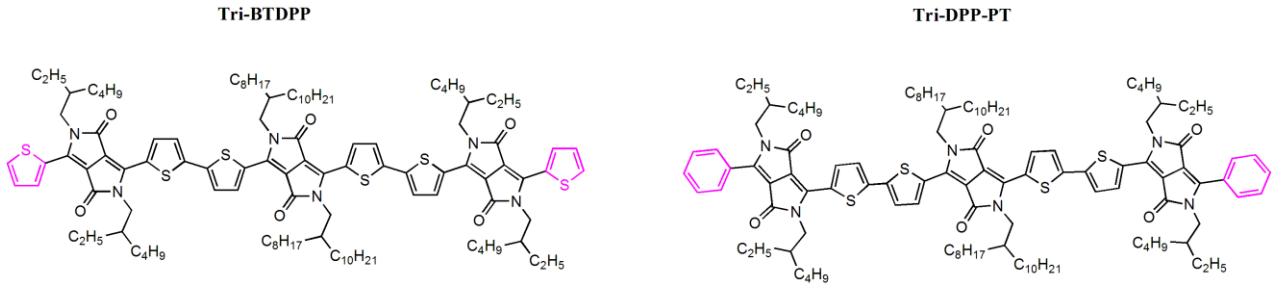

Figure 53: Molecular backbone of Tri-BTDPP and Tri-DPP-PT

4.1. Characterization of Tri-DPP-PT compared to Tri-BTDPP

4.1.1. Optical properties

The optical properties of Tri-DPP-PT were analyzed by comparing its UV-Visible absorption spectra in chloroform solution (with a concentration of 0.25 $mg.ml^{-1}$) and thin film to those of Tri-BTDPP, as shown in Figure 54. In solution, similar vibronic features were observed in Tri-DPP-PT spectra relative to Tri-BTDPP but with a blue-shift of 21 nm, giving a maximum of absorption at 686 nm. This blue-shift originates from the large dihedral angle between DPP and phenyl ring [130] which shorten the π-conjugation. In solid-state, the maximum of absorption of Tri-DPP-PT is red-shifted to 700 nm along with the appearance of a shoulder at 780 nm. A spectral broadening is observed in the UV-Visible spectra of thin films suggesting intermolecular ordering in the solid state. Similar shift was observed for Tri-BTDPP and Tri-DPP-PT. The optical band gap of Tri-DPP-PT is assessed to be 1.40 eV, which is higher than Tri-BTDPP (1.33 eV).

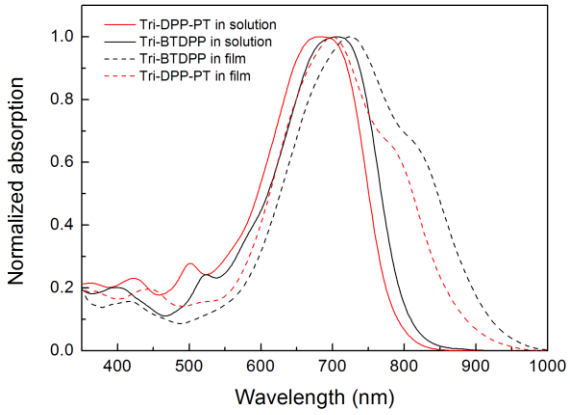

Figure 54: UV-Visible absorption spectra in solution and in the solid state of Tri-DPP-PT and Tri-BTDPP

4.1.2. Energy levels

To further investigate the effect of the phenyl end-capping group on the optoelectronic properties, DFT calculations were conducted using the same technics as for Tri-BTDPP. As illustrated in Figure 55, the lowest energetic conformation revealed an almost planar structure at the exception of phenyl ring which shows large dihedral and angle of 28° with DPP. In comparison with Tri-BTDPP, the phenyl ring disturbs the perfect planarity of the molecules which could weaken π-π stacking. As for the electron density distribution, the HOMO and LUMO extended over the whole molecular backbone except the phenyl due to the large dihedral angle. The weaker-participation of terminal phenyl ring represented a decrease in π-conjugation and therefore enlarged the band gap as observed in the UV-Visible spectrum. The HOMO and

LUMO energy levels were calculated to be -4.8 eV and -3.02 eV, respectively. The major change in comparison with Tri BTDPP is the increased LUMO level.

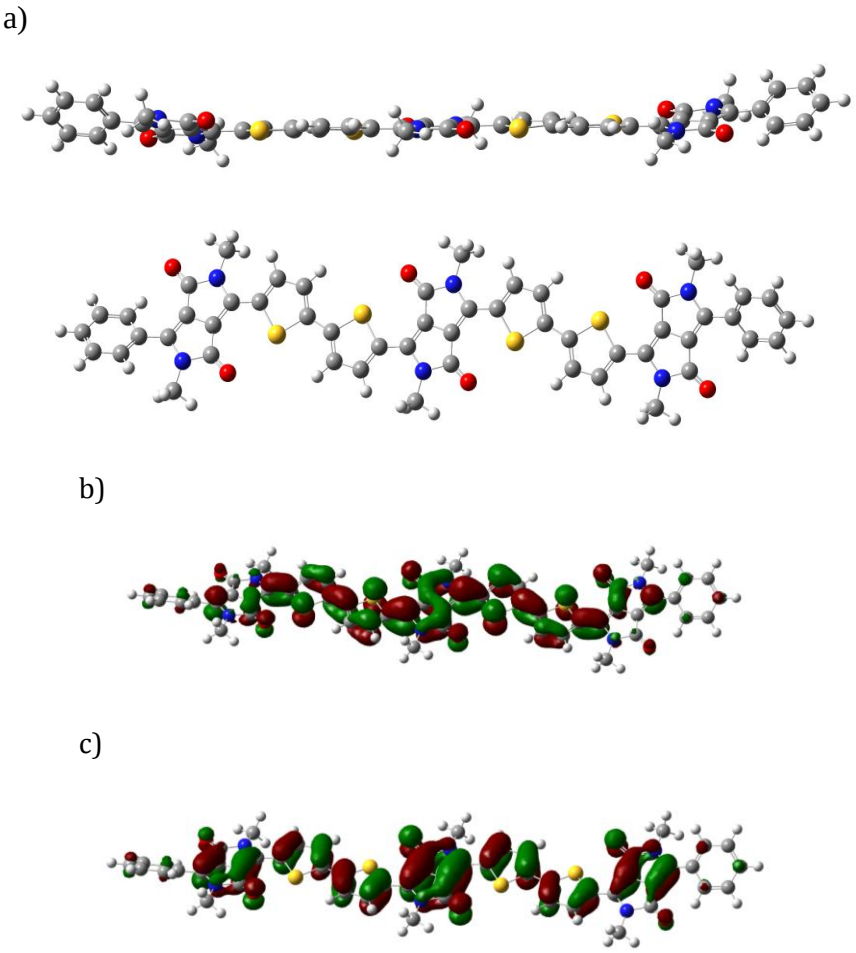

Figure 55: DFT calculations of Tri-DPP-PT: a) Lowest conformation, b) Electron density distribution in LUMO (bottom) and HOMO (top)

Cyclic voltammetry measurement was carried out on Tri-DPP-PT to evaluate its electrochemical properties. As depicted in Figure 56, the oxidation peak of both Tri-DPP-PT and Tri-BTDPP showed identical onset, meaning they have a similar HOMO level, consistent with DFT calculation. By adding the optical band gap to the HOMO value, the LUMO of Tri-DPP-PT was estimated to be -3.93 eV. Tri-DPP-PT displayed a higher LUMO level that should enhance electron transfer from donor to acceptor compared to Tri-BTDPP, where the gap between donor and acceptor's LUMO was equaled to the minimal required value of 0.3 eV for electron transfer.

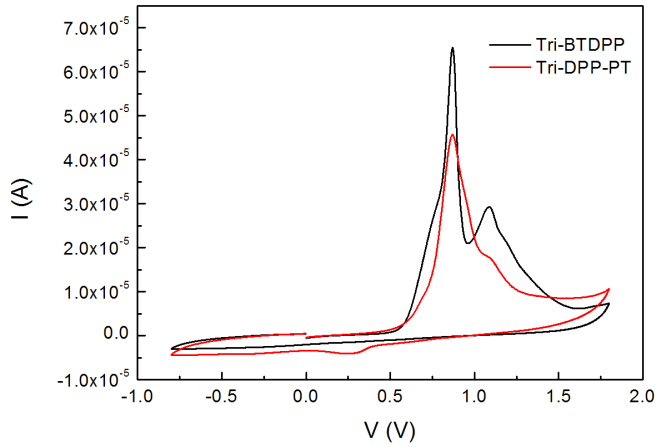

Figure 56: Cyclic voltammetry of Tri-DPP-PT film

In comparison with Tri-BTDPP, Tri-DPP-PT displays a larger band gap of 1.4 eV due to its more disordered backbone and thus shortened π-conjugation. Meanwhile, Tri-DPP-PT maintains a deep HOMO level for a promising V_{OC}. According to Tri-DPP-PT energy levels, a PCE of 10 % can be expected in condition of ideal devices using Tri-DPP-PT:PCBM (Figure 57) [23].

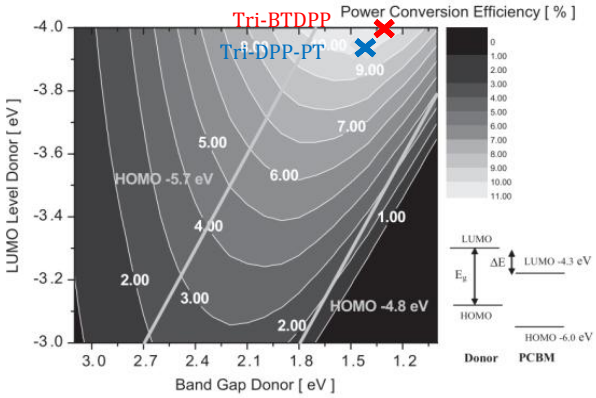

Figure 57: Tri-BTDPP and Tri-DPP-PT on Scharber diagram

4.1.3. Molecular packing and charge transport

According to DFT calculations, the phenyl ring induces small dihedral angles along Tri-DPP-PT's molecular backbone and larger ones at extremities, thus breaking the perfect planarity observed with Tri-BTDPP. According to the hypothesis we formulated in Section 3, the backbone curvature may reduce the material self-assembly property. Therefore, the study of the molecular packing of Tri-DPP-PT is of high interest. XRD measurement is performed on neat film and further compared with Tri-BTDPP. The XRD patterns of the two molecules are presented in Figure 58. As shown in this figure, Tri-DPP-PT organizes in a similar manner than Tri-BTDPP in a lamellar crystalline structure with the identical d-spacing of 1.96 nm. This was expected, as this structure is ascribed to the arrangement of alkyl chains, identic in both

oligomers. However, only two order of (h 0 0) can be seen revealing a weaker molecular ordering owing to the more twisted molecular backbone. The crystallite size was calculated from the first order peak and was estimated to be 20.4 nm, which is much smaller than Tri-BTDPP crystallite (27.4 nm). Besides, Tri-DPP-PT thin film exhibits a broader and less distinct (0 h 0) diffraction peak with a d-spacing of 3.6 nm, assignable to π-π stacking. This findings support the hypothesis that Tri-DPP-PT display a weaker arrangement due to more twisted backbone.

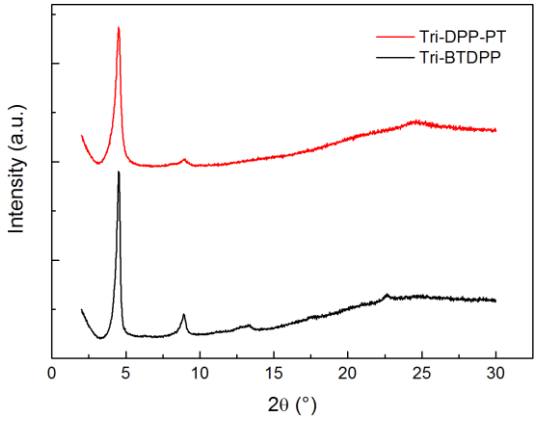

Figure 58: XRD of neat film Tri-DPP-PT and Tri-BTDPP

The charge transport properties of Tri-DPP-PT were investigated in p-type OTFTs. The hole mobilities were calculated in the saturation regime for as cast and annealed OTFTs at 100°C, 150°C and 200°C. Table 4 summarizes those mobility data and reveals that an annealing at 100°C provides the highest hole mobilities with an average and maximal value of 3.89×10^{-5} $cm^2.V^{-1}.s^{-1}$ and 4.52×10^{-5} $cm^2.V^{-1}.s^{-1}$ respectively along with a $I_{on/off}$ ratio of 3×10^5. The transfer curves of the optimal transistors are illustrated in Figure 59. The hole mobility achieved with Tri-DPP-PT is much lower than with Tri-BTDPP (1×10^{-3} $cm^2.V^{-1}.s^{-1}$). This is likely due to the loss in planarity and in crystallization ability. The mobility of Tri-DPP-PT may not be sufficient to get high FF. As a matter of fact, the hole mobility in neat film, supposed to be the upper limit of the material mobility, is below 10^{-4} $cm^2.V^{-1}.s^{-1}$, inferring an important competition between charge transport and bimolecular recombination within OSC.

Table 4: Hole mobilities in saturation regim before and after thermal annealing at 100°C, 150°C and 200°C

	As-cast	**100°C**	**150°C**	**200°C**
Average μ_h 8 devices ($cm^2.V^{-1}.s^{-1}$)	2.04×10^{-5} $+/- 5.67 \times 10^{-6}$	3.89×10^{-5} $+/- 3.77 \times 10^{-6}$	2.33×10^{-5} $+/- 3.01 \times 10^{-6}$	2.59×10^{-5} $+/- 1.44 \times 10^{-6}$
Maximal μ_h ($cm^2.V^{-1}.s^{-1}$)	2.67×10^{-5}	4.52×10^{-5}	2.94×10^{-5}	2.73×10^{-5}

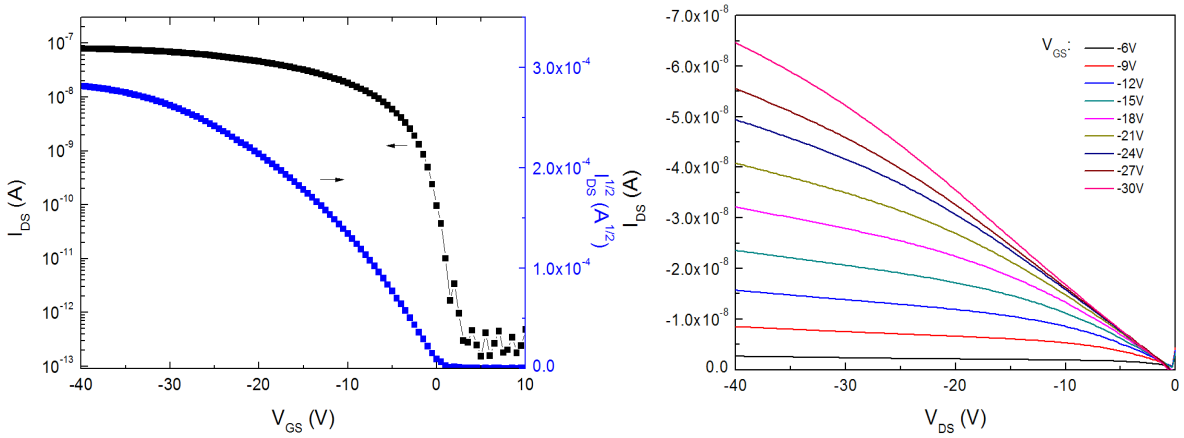

Figure 59: Transfer curves of the best Tri-DPP-PT based OTFTs annealed at 100°C

4.1.4. Discussion

Tri-DPP-PT displays an almost planar conformation but the phenyl ring as end-capping unit induces small dihedral angles along the molecular backbone compared to Tri-BTDPP. In comparison with Tri-BTDPP, the UV–visible absorption spectra demonstrate a blue shift (in solution and in the solid state). This demonstrates that a small change in the dihedral angles can cause changes in the optical properties of the material. As for the energy levels, the LUMO is raised. This can enhance the energetic driving force for electron transfer from donor to acceptor. The slight molecular curvature strongly impacts the molecular packing which is weakened by the loss in planarity. This packing consideration results in a decrease in hole mobility.

4.2. Tri-DPP-PT photovoltaic properties

In this section, Tri-DPP-PT photovoltaic properties were studied to elucidate the effect of a less planar structure owing to the phenyl addition. To this end, similar device optimizations - as carried out with Tri-BTDPP - were performed. A particular attention was paid to the morphology of the active layer in order to estimate if a better miscibility between Tri-DPP-PT and $PC_{71}BM$ could be achieved with the slightly more twisted conformation.

4.2.1. Tri-DPP-PT in OSCs

The PV properties of Tri-DPP-PT were investigated in conventional OSCs with $PC_{71}BM$ as acceptor with the following architecture: ITO/PEDOT:PSS/ Tri-DPP-PT: $PC_{71}BM$/Ca/ Al. The donor/acceptor blend formulation was prepared using chloroform as the host solvent and various concentrations of DIO were introduced. The ratio of Tri-DPP-PT : $PC_{71}BM$ was set at 1:1 and the thickness of the active layer at 100 nm. The device performances are summarized in Table 5. The maximum PCE of 0.42 % was obtained from a formulation containing 1% of DIO along

with a J_{SC} of 1.76 mA.cm^{-2}, a V_{OC} of 0.62 V and a FF of 0.38. Further increase in DIO concentration induced an annihilation of the photovoltaic effect.

Table 5: PV parameters of OSCs prepared with various concentrations of DIO

DIO content	J_{SC}(mA.cm^{-2})	V_{OC}(V)	FF	PCE (%)
0	0.41	0.18	0.42	0.03
0.5%	1.42	0.61	0.39	0.36
1%	1.76	0.62	0.38	0.42
2.5%	0	0	0	0

The optimization was pursued by tuning the donor/acceptor ratio with a fixed solid content of 20 mg.ml^{-1} in chloroform and using 1% of DIO in the formulation. The thickness was kept at 100 nm. Figure 60 shows the evolution of the PV parameters as a function of the Tri-DPP-PT content. The main parameters affected by the change in donor:acceptor ratio is the J_{SC}. The J_{SC} reaches a maximal value of 1.8 mA.cm^{-2} for a Tri-DPP-PT content of 50%. The PCE followed the same trend to reach an average value of 0.55% and a maximum value of 0.76%.

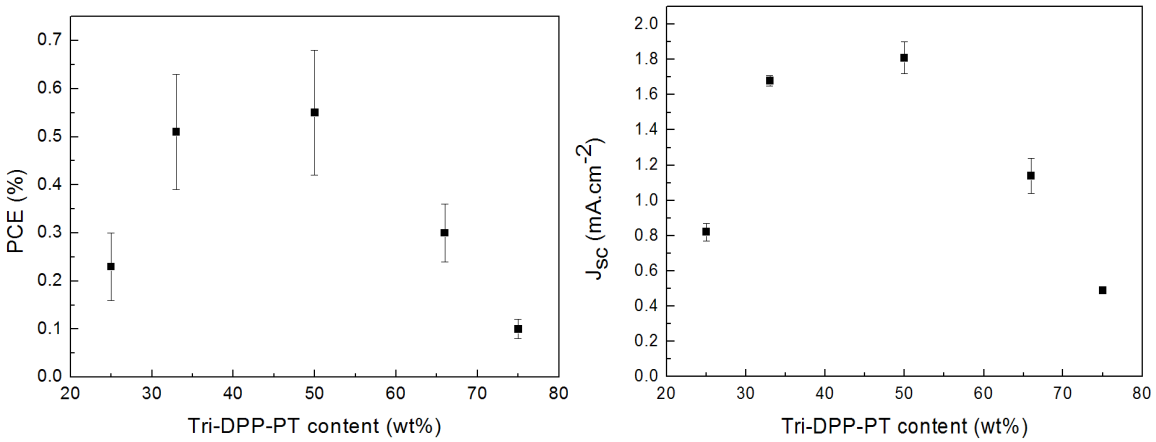

Figure 60: PCE and J_{SC} of OSCs based on Tri-DPP-PT and $PC_{71}BM$ with varying ratios

The PV performances of optimal conventional OSCs based on Tri-BTDPP and Tri-DPP-PT are summarized in Table 6 to study the effect of phenyl ring end-capping versus thiophene. Tri-DPP-PT displayed an improved V_{OC} of 0.7 V over 0.57 V for Tri-BTDPP. This, in turn, could improve the PCE to 0.55%.

Table 6: Average on 8 devices of PV characteristics of optimal conventional OSC based on Tri-BTDPP and Tri-DPP-PT

	J_{SC} (mA.cm^{-2})	V_{OC} (V)	FF	PCE (%)
Tri-BTDPP	1.61	0.57	0.47	0.43
Tri-DPP-PT	1.81	0.7	0.43	0.55

The EQE was conducted on the best cells based on Tri-DPP-PT to investigate at which wavelength the power was generated. As depicted in Figure 61, the EQE shows a maximum in the range of 300 – 500 nm., revealing a low participation of Tri-DPP-PT's excitons. Excitons formed within Tri-DPP-PT must recombine before separating in free charges, probably due to the lack of donor-acceptor interfaces. This finding suggests that the morphology of the active layer remains unfavorable with the formation of large domains of Tri-DPP-PT, inferring that the backbone curvature of Tri-DPP-PT did not provide better miscibility with $PC_{71}BM$.

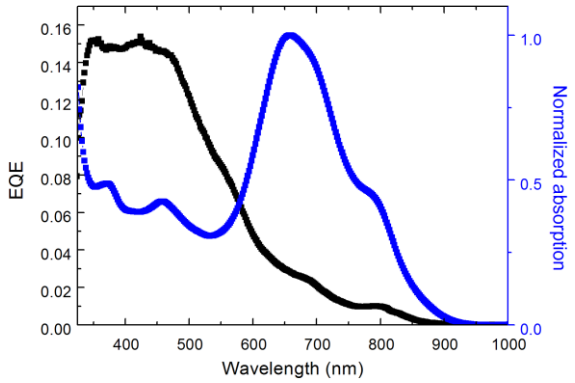

Figure 61: EQE of Tri-DPP-PT: $PC_{71}BM$ based OSC and normalized absorption of a Tri-DPP-PT : $PC_{71}BM$ blend film

4.2.2. Discussion

Tri-DPP-PT in conventional OSC exhibits a PCE of 0.55% along with an enhanced V_{OC} of 0.7 V relative to Tri-BTDPP. However, the J_{SC} remains lower than 2 $mA.cm^{-2}$ due to the poor contributions of Tri-PTDPP's excitons in the PV process, similarly to Tri-BTDDP. The slight curvature of the backbone, originating from the introduction of a phenyl end-capping, did not improve the miscibility with $PC_{71}BM$ and results in strong self-assembly like with Tri-BTDPP.

4.3. Conclusion

Tri-DPP-PT molecular backbone differs from Tri-BTDPP with the introduction of phenyl rings instead of thiophene rings as end-capping unit. This difference induced small tilt angles over the all molecules and larger ones between the phenyl and the DPP unit. This curvature slightly shortened the conjugation raising the band gap to 1.4 eV and the LUMO to -3.93 eV compared to Tri-BTDPP. As for the molecular packing, Tri-DPP-PT exhibited a lamellar packing like Tri-BTDPP but with a weaker order degree which appeared to diminish the charge transport properties. In conventional OSC, Tri-DPP-PT :$PC_{71}BM$ displayed an interesting V_{OC} of 0.7 V meanwhile the J_{SC} was still relatively low due to the poor participation of Tri-DPP-PT excitons in the PV process. The curvature of Tri-DPP-PT may not be sufficient to improve the Tri-DPP-PT :$PC_{71}BM$ miscibility.

5. FROM TRI-DPP-TP TO TRI-DPP-TP-C6: EFFECT OF HEXYL CHAINS

This section explores the effect of the addition of hexyl side chains on thiophene spacers by comparing the properties of Tri-DPP-PT and Tri-DPP-PT-C6 (Figure 62). The molecule Tri DPP-PT-C6 is expected to exhibit a more twisted backbone than that of Tri-DPP-PT. The objective is to elucidate if such a curvature could induce a reduced self-assembly - and in turn smaller domains sizes - together with a good miscibility with $PC_{71}BM$ compared to Tri-DPP-PT. In this regards, the optoelectronic properties of Tri-DPP-PT-C6 were investigated and compared to those of Tri-DPP-PT. Next to the optoelectronic properties, Tri-DPP-PT-C6 was tested as a donor material in conventional OSC.

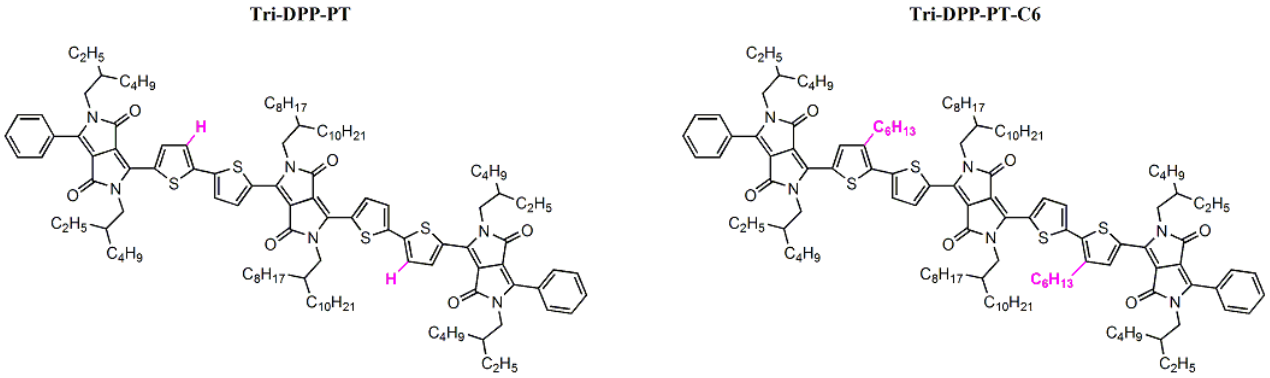

Figure 62: Tri-DPP-PT and Tri-DPP-PT-C6 molecular backbone

5.1. Characterization Tri-DPP-TP-C6

5.1.1. Optical properties

The UV-Visible absorption spectra of Tri-DPP-PT-C_6 were recorded in chloroform solution (with a concentration of 0.25 $mg.ml^{-1}$) and thin film and were then compared to those of Tri-DPP-PT (Figure 63). In solution, the maximum absorption of Tri-DPP-PT-C6 was blue-shifted by 20 nm compared to Tri-DPP-PT. This is likely to be due to the molecular distortion induced by the alkyl chains which reduces the π-conjugation. In solid state, the maximum of absorption of Tri-DPP-PT-C6 is strongly red-shifted by 44 nm relative to its dilute solution against 14 nm for Tri-DPP-PT. However the additional shoulder is less intense in the case of Tri-DPP-PT-C6. As the red-shift in solid state is ascribed to intermolecular interactions, the hexyl side chains on thiophene spacers seem to have a strong influence on intermolecular interactions and thus molecular packing of the molecules. In the end, the absorption spectrum in thin film of Tri-DPP-PT-C6 had almost the same offset that of Tri-DPP-PT, indicating that Tri-DPP-PT-C6 molecules

get more planer in solid-state. The optical band gap of Tri-DPP-PT-C6 was estimated to be 1.38 eV.

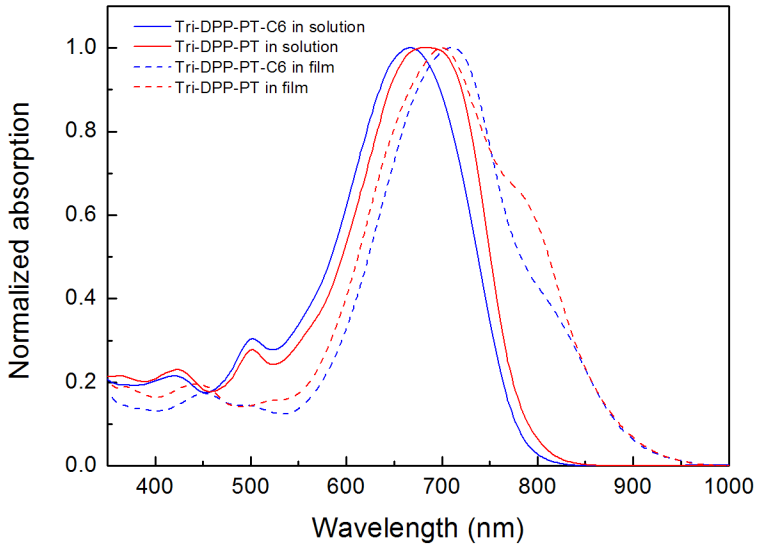

Figure 63: UV-visible absorption spectra of Tri-DPP-TP-C6 in solution and thin film

5.1.2. Energy levels

CV measurements were performed on Tri-DPP-PT-C6 film to investigate its electrochemical properties as illustrated in Figure 64. In comparison with Tri-DPP-PT, the oxidation peak of Tri-DPP-PT-C6 exhibited the same onset and thus had a similar HOMO level to that of Tri-DPP-PT. As Tri-DPP-PT-C6 has a similar band gap as Tri-DPP-PT, the LUMO obtained by adding the band gap to the HOMO was also close, -3.95 eV. The introduction of hexyl chains at β position on thiophene spacer as shown in Figure 48 did not significantly affect the electronic properties of the molecules.

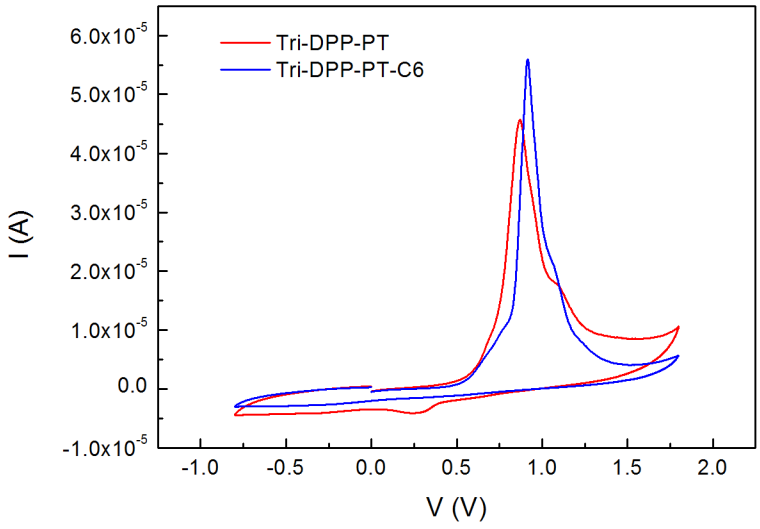

Figure 64: Cyclic voltammetry measurements on Tri-DPP-PT-C6

5.1.3. Molecular packing and charge transport

The molecular packing of Tri-DPP-PT-C6 was assessed through XRD measurements on neat film, as prepared with Tri-BTDPP and Tri-DPP-PT. As shown in Figure 65, Tri-DPP-PT-C6 displays different XRD pattern compared to its DPP analogues. Those multiple peaks suggested the presence of crystallites with different orientation. It was demonstrated in the literature that introducing side chains onto thiophene spacers can modified the crystallite orientation and give a mixture of face-on and edge-on crystallite [151]. An intense peak corresponding to the first order of (h 0 0) diffraction peak appears at $2\theta = 4.26°$ referring to a d-spacing of 2.07 nm which is larger than its analogue. Surprisingly, the crystallite size was calculated to be 29.9 nm which appears to be larger than Tri-DPP-PT indicating a high crystallinity degree.

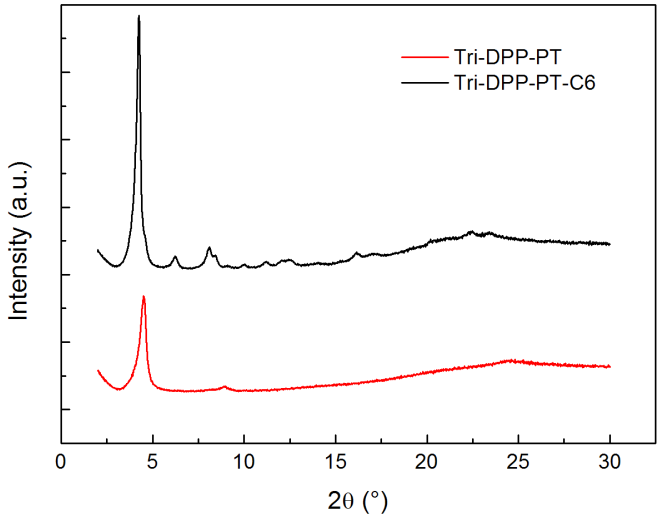

Figure 65: XRD measurements of neat film of Tri-DPP-PT-C6 compared to Tri-DPP-PT

The charge transport properties of Tri-DPP-PT-C6 were assessed in p type OTFT. The hole mobilities were calculated in saturation regime for as-cast and annealed transistors at 100 °C and 150 °C. Table 7 summarizes the mobility data. The as-cast transistors exhibit the highest mobility with an average and maximal hole mobility of 2.01×10^{-5} $cm^2.V^{-1}.s^{-1}$ and 2.54×10^{-5} $cm^2.V^{-1}.s^{-1}$ together with a $I_{on/off}$ ratio of 6×10^4. The transfer curves of the best transistors are illustrated in Figure 66. When compared to Tri-DPP-PT, we observe that Tri-DPP-PT-C6 shows similar hole mobility. This suggests that hexyl side chains do not strongly disturb horizontal charge transport.

Table 7: Hole mobilities for OTFT based on Tri-DPP-PT-C6 before and after thermal annealing at 100°C and 150°C

	As-cast	100°C	150°C
Average μ_h (8 devices) ($cm^2.V^{-1}.s^{-1}$)	2.01×10^{-5} $+/- 6.2 \times 10^{-6}$	1.91×10^{-5} $+/- 2.5 \times 10^{-6}$	1.41×10^{-5} $+/- 4.7 \times 10^{-6}$
Maximal μ_h ($cm^2.V^{-1}.s^{-1}$)	2.54×10^{-5}	2.36×10^{-5}	2.02×10^{-5}

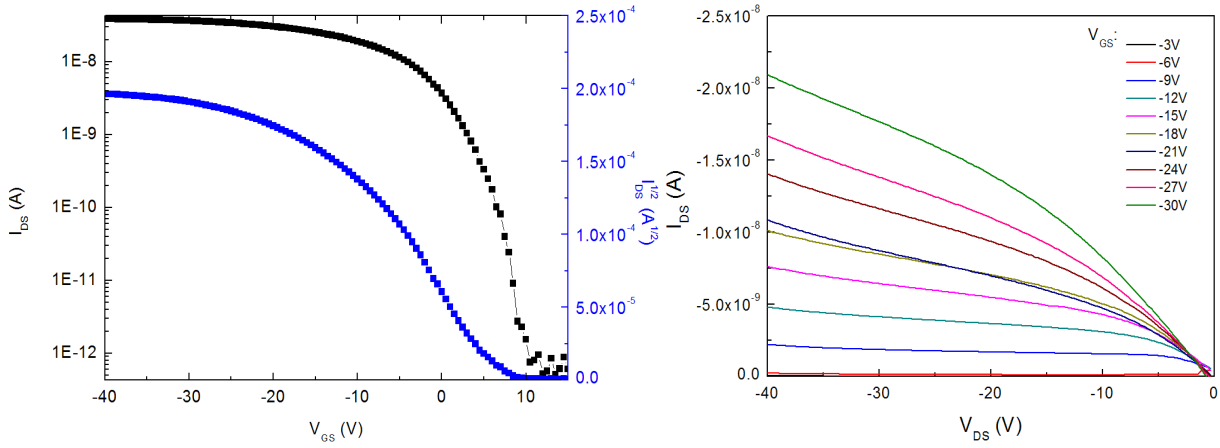

Figure 66: Transfer curves for Tri-DPP-PT-C6 transistors

5.1.4. Discussion

The comparison between Tri-DPP-PT and Tri-DPP-PT-C6 shows that embedding hexyl side chains at the β position of thiophene spacers do not affect the energy levels. According to UV-Visible absorption spectra in solid-state and XRD measurements on neat film, we can see that the crystal orientation changes due to the presence of the hexyl chains - however this does not impact significantly the hole mobility as could be observed in transistor measurements.

5.2. Tri-DPP-PT-C6 photovoltaic properties

5.2.1. Tri-DPP-PT-C6 in OSCs

Tri-DPP-PT-C6 was tested as a donor material in conventional OSCs using the following device architecture ITO/PEDOT-PSS/ Tri-DPP-PT-C6: $PC_{71}BM$/ Ca/Al. Chloroform was chosen as the host solvent for all the studies. The thickness was first optimized by varying the ink concentration (10, 15 and 20 $mg.ml^{-1}$) and the deposition spin speed (1000, 2500 and 5000 rpm). In the blend formulation, the Tri-DPP-PT-C6: $PC_{71}BM$ ratio was fixed at 1:1 and 1% DIO was

introduced. Figure 67 shows the PCE of the OSCs as a function of the thickness. As shown in this Figure 67, the optimal thickness was in the range of 40 - 70 nm. Hereafter, a total concentration of 20 mg/ml and a deposition spin speed of 5000 rpm were used.

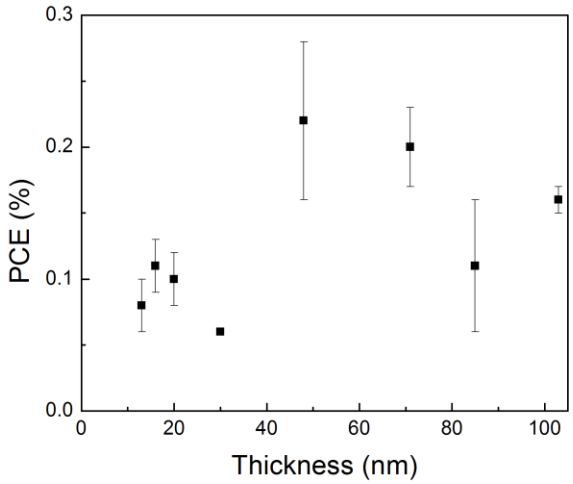

Figure 67: Thickness optimization on TRI-DPP-PT-C6 based devices

Then, various DIO concentrations of 0, 0.5%, 1%, 2% and 3% were tested, in blend formulations containing Tri-DPP-PT-C6: $PC_{71}BM$ in a ratio of 1:1. The results are depicted in Figure 68. The Jsc was maximum for a concentration of 1% of DIO whereas Voc and FF were optimal with 2% of DIO. The highest PCE of 0.46% was achieved with the use of 2% of DIO.

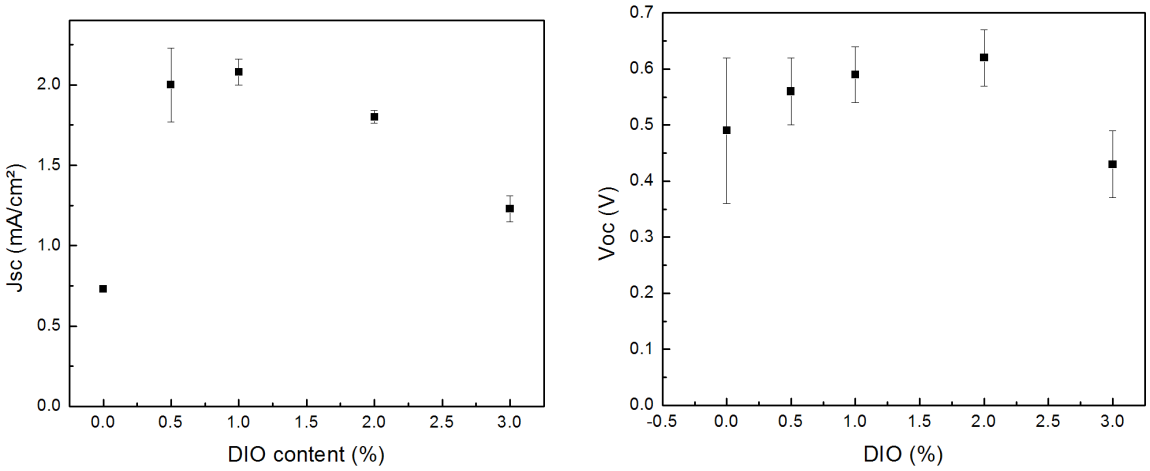

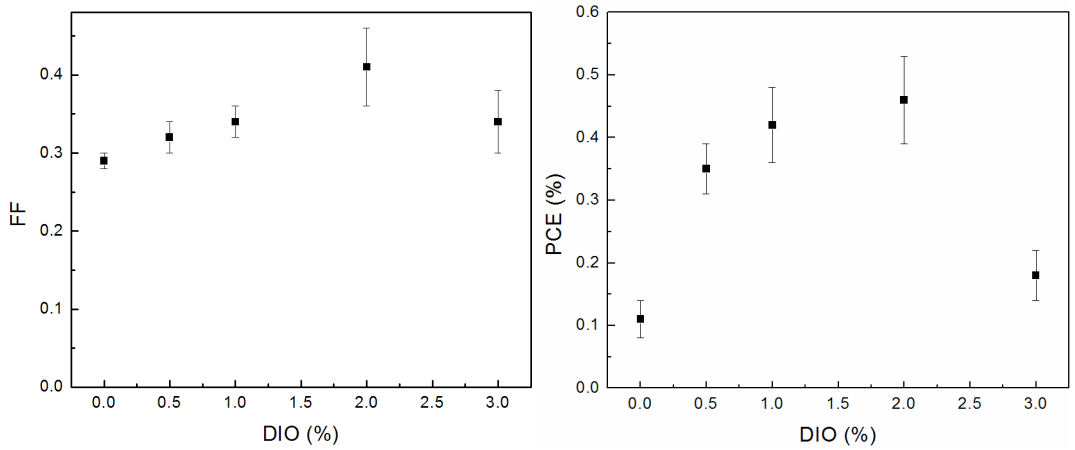

Figure 68: PV parameters of OSC based on Tri-DPP-TP-C6:$PC_{71}BM$ as a function of DIO concentrations on based OSC devices

The donor: acceptor ratio was finally tailored using a thickness of 60 nm and a DIO concentration of 2%. While the V_{OC} and the FF remained constant, the J_{SC} reached a maximum value for a Tri-DPP-PT-C6 content between 30% and 60% as shown in Figure 69. The PCE follows this same trend and is optimal for a concentration in Tri-DPP-PT-C6 between 30% and 60%.

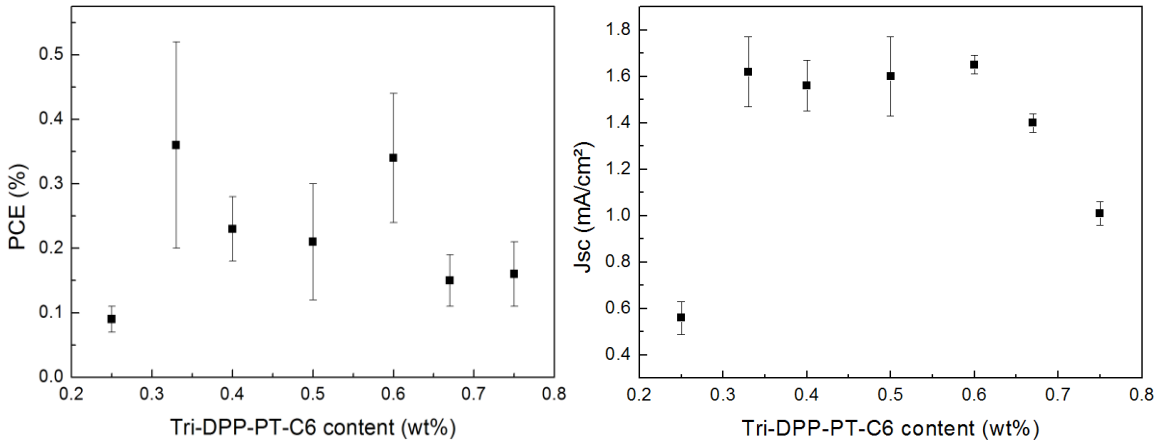

Figure 69: PCE and J_{SC} of OSCs with various ratios of Tri-DPP-PT-C6:$PC_{71}BM$

Figure 70 shows the EQE spectra obtained together with the UV-visible absorption spectra of TRI-DPP-PT-C6. As shown in the EQE spectrum, the photocurrent is mainly generated in the range of 300-600 nm which corresponds to the absorption wavelength range of $PC_{71}BM$. This observation suggests that most of the photocurrent arise from the absorption of $PC_{71}BM$ and not from the Tri-DPP-PT-C6.

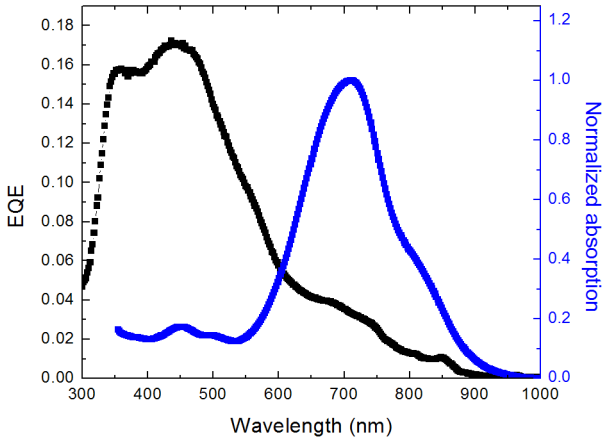

Figure 70: EQE of the best conventional OSC based on Tri-DPP-PT-C6 and absorption of Tri-DPP-PT-C6 neat film

Table 8 summarizes the best photovoltaic characteristic of TRI-DPP-PT and TRI-DPP-PT-C6. Both semiconductors display similar PV parameters and poor contribution of donor excitons, suggesting that the introduction of hexyl chains did not affect PV properties of the material.

Table 8: PV characteristics of conventional OSC based on Tri-DPP-PT and Tri-DPP-PT-C6

	Jsc (mA.cm²)	**Voc (V)**	**FF**	**PCE**
Tri-DPP-PT	1.81	0.7	0.43	0.55
Tri-DPP-PT-C.	1.8	0.62	0.41	0.46

5.2.2. Morphology

The morphology of the active layer is crucial for good charge separation and good charge transport. The objective was to reduce the self-assembly of DPP oligomers by embedding hexyl side chains on thiophene spacers, forming Tri-DPP-PT-C6. This oligomer was expected to have an improved miscibility with $PC_{71}BM$ and therefore enables an appropriate phase separation with the acceptor. However, EQE measurement on OSCs based on Tri-DPP-PT-C6 revealed a bad charge separation, suggesting the presence of large domains of Tri-DPP-PT-C6, therefore, the morphology was further investigated.

To address this question, AFM was performed on a Tri-DPP-PT-C6: $PC_{71}BM$ blend film. The film was prepared using the same condition as the one used to obtain the best conventional OSC film. The AFM image is presented in Figure 71. As shown on the images, large domains of 100-200 nm were observed indicating that Tri-DPP-PT-C6 still suffered from strong phase segregation.

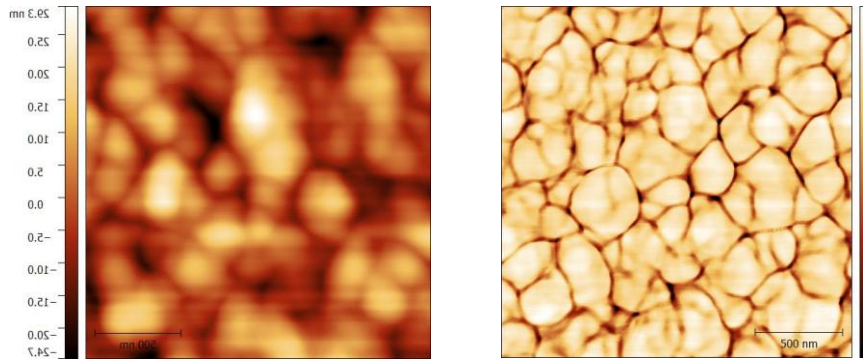

Figure 71: AFM images 2µm × 2µm of Tri-DPP-PT-C6:$PC_{71}BM$ 1:1 as prepared in the best device: Height (left) and Phase (right)

AFM was then conducted for Tri-DPP-PT-C6: $PC_{71}BM$ blend film with various ratios: 1:3, 1:1, and 3:1. The height and phase images of each ratio are illustrated in Figure 72 and demonstrate that strong phase segregation is present at any ratio even with a large amount of $PC_{71}BM$. Tri-DPP-PT-C6 aggregates without intermixing with $PC_{71}BM$, proving that Tri-DPP-PT-C6 and $PC_{71}BM$ are not miscible.

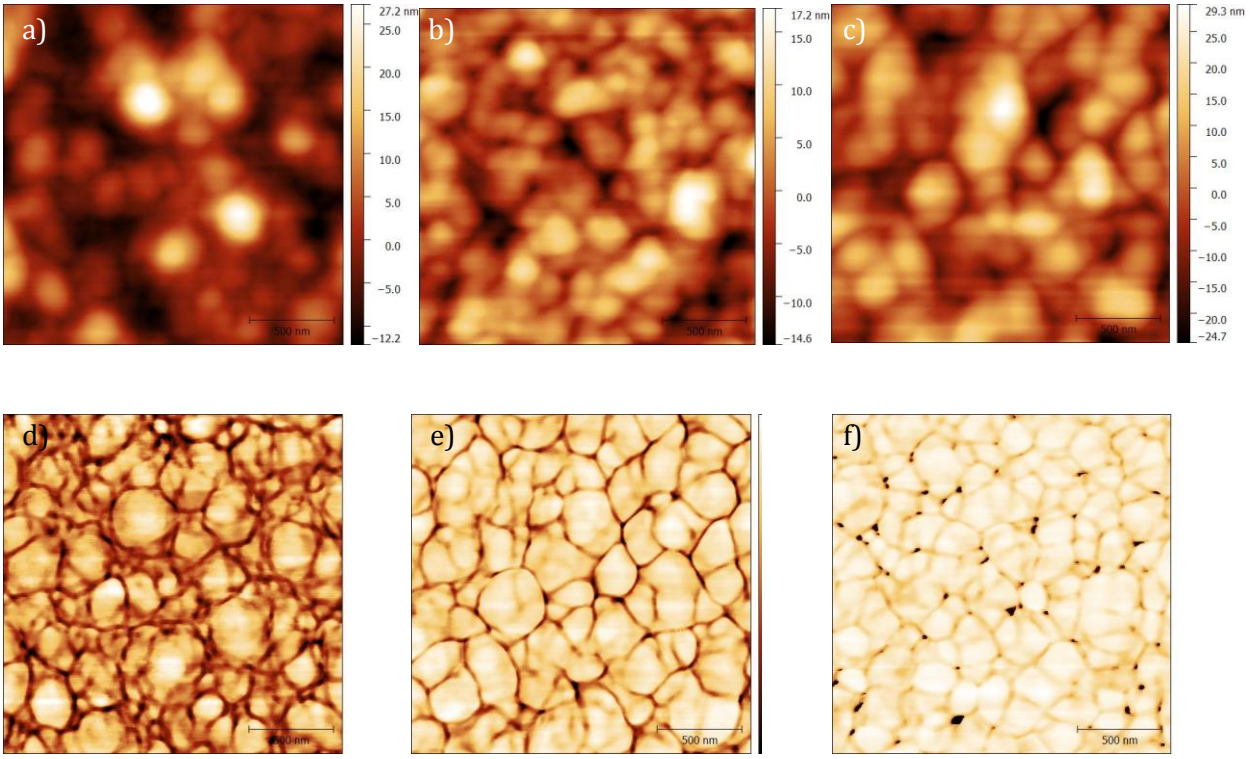

Figure 72: AFM images 2µm × 2µm - Height (a,b,c) and phase (d,e,f) Images of various ratios of Tri-DPP-PT-C6: $PC_{71}BM$ ratio 1:3 (a,d), 1:1 (b,e) and 3:1 (c,f)

5.2.3. Discussion

Tri-DPP-PT-C6 exhibited similar OSC performances as Tri-DPP-PT with a PCE of 0.46%. Like its predecessor, Tri-DPP-PT-C6 did not intermix with $PC_{71}BM$ which generated a morphology with large domains of 100-200 nm of Tri-DPP-PT-C6. This morphology did not provide enough donor:acceptor interfaces and therefore Tri-DPP-PT-C6's exciton mostly recombined instead of separating in free charge carriers, justifying their poor participation to the photovoltaic process. The hexyl chains placed on thiophene spacers did not reduced the strong self-assembly of the molecule.

5.3. Conclusion

Introducing hexyl side chains on thiophene spacers did not affect the energy levels of the molecules but changed the orientation of the crystal resulting in a mixture of face-on and edge-on crystal. The mix in crystal orientation did not affect horizontal charge transport properties as suggested by mobility result. As for OSC devices, similar performances were observed with Tri-DPP-PT-C6 and Tri-DPP-PT. According to UV-Visible absorption analysis, the hexyl chains induce a twisted backbone in solution but seem to get planer in solid-state, explaining the strong self-assembly of Tri-DPP-PT-C6. As Tri-DPP-PT-C6 maintained similar aggregations as its counterpart, similar morphology was observed with large domains hampering Tri-DPP-PT-C6's exciton dissociation into free charges. To avoid this molecular planarization in solid state, hexyl side chains could be embedded at α position of thiophene spacers.

6. CONCLUSION

Three oligomeric DPP-based semiconductors were designed, all containing three DPP cores but with different electron-rich spacers tuning the backbone curvature. The measurements of their energy levels and band gaps suggested, at first, that they have promising optoelectronic properties to be used as donor materials in OSCs. The HOMO levels are equal to -5.24 eV and the band gaps are around 1.3-1.4 eV for the three DPP oligomers. Tri-BTDPP has the most planar structure and was expected to exhibit a high hole mobility. This was confirmed by mobility measurements in OTFT configurations. Hole mobility as high as 10^{-3} cm^2. $V^{-1}.s^{-1}$ was obtained for a device annealed at 150 °C. Despite these promising properties, the fabrication of OSCs using Tri-BTDPP showed low performances. AFM images revealed a large phase separation between Tri-BTDPP and the $PC_{71}BM$ preventing an efficient charge separation. Through DSC measurements, the origin of this unfavorable morphology appears to be the non-miscibility of Tri-BTDPP with $PC_{71}BM$, emphasizing the importance of intermixing properties of donor/acceptor.

We suspected the strong self-assemble feature of Tri-BTDPP to be responsible of the non-intermixing with $PC_{71}BM$. Therefore to address this limitation, DPP oligomers with slightly twisted structure were designed and synthesized. The use of a phenyl as end-capped moieties weakened the molecular packing and decreased the charge transport properties. As for the introduction of hexyl side chains, the crystal orientation could be changed into a mixture of face-on and edge-on orientations. The OSCs based on Tri-DPP-PT and Tri-DPP-PT-C6 exhibited similar PV performances to Tri-BTDPP. Table 9 shows the average values obtained with each material. As a matter of fact, the devices still suffered from unfavorable morphology composed of large domains of donor. The miscibility with $PC_{71}BM$ was not improved by the more twisted backbone of Tri-DPP-PT and Tri-DPP-PT-C6.

Table 9: Summary of PV performances of Tri-BTDPP, Tri-DPP-PT and Tri-DPP-PT-C6 in conventional OSCs

	Jsc (mA.cm²)	**Voc (V)**	**FF**	**PCE**
Tri-BTDPP	1.61	0.57	0.47	0.43
Tri-DPP-PT	1.81	0.7	0.43	0.55
Tri-DPP-PT-C.	1.8	0.62	0.41	0.46

CHAPTER 4: EBI SMALL-MOLECULES

This chapter delineates the synthesis and the design of four 3,3-(Ethane-1,2-diylidene)bis(indolin-2-one) (EBI) based small molecules using different electron-rich end-capping moieties. The optoelectronic properties were investigated to clarify the impact of the end-capping group. All molecules were studied in OTFTs as p-type materials and in OSCs as donor semiconductors.

1. INTRODUCTION

Herein, we aim at introducing 3,3-(Ethane-1,2-diylidene)bis(indolin-2-one) (EBI) - an electron-deficient building-block - into push-pull semiconductors for OSC application. The EBI unit has attracted our interest for its similitude with the well-known isoindigo unit. EBI and isoindigo are both composed of two indolin-2-one moieties but differ from their π-bridge. As shown in Figure 73, isoindigo has a simple double bond whereas EBI has a butadiene π-bridge.

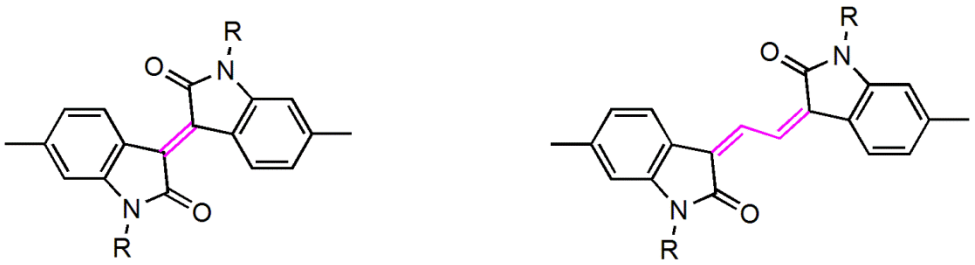

Isoindigo **EBI**

Figure 73: Isoindigo and EBI backbones

1.1. From isoindigo toward EBI derivatives

1.1.1. Isoindigo

Isoindigo is a strong electron deficient dye, naturally abundant with a high optical stability. Reynolds was the pioneer of isoindigo-based semiconductors for OSC application [156]. He developed a polymer achieving an encouraging PCE of 1.76%. Polymers based on isoindigo have received much more attention than their molecular analogs owing to their highest performance in OSC and OTFT applications. As a matter of fact, polymers based on isoindigo recently achieved high PCEs of 7 to 9%, [157–162] which place them among the best performing polymeric OSCs. Starting with isoindigo-bithiophene polymer [157], an high PCE of 5.55% was

achieved although important dihedral angles between the thiophene spacers broke the planarity of the molecule (Figure 74a). To suppress this torsion in the polymer, a vinylene bridge was introduced between the thiophene moieties which enabled a closer molecular packing and a higher crystallinity. The PCE rose up to 7% due to better charge transport. Meanwhile, isoindigo was also combined with highly planar and rigid electron rich unit such as dithienocarbazole (Figure 74b) [161]. In spite of its amorphous feature, the dithienocarbazole-isoindigo polymer exhibited an impressive PCE of 8%. Recently, the isoindigo passed the 9% PCE by incorporating fused-thiophene to isoindigo unit (Figure 74c) [162]. The resulting large fused isoindigo structure reduced the polymer disorder and increased the crystallinity which is beneficial for high charge transport. According to this study, the use of rigid and planar building blocks benefits a good charge carrier transport and a high PCE.

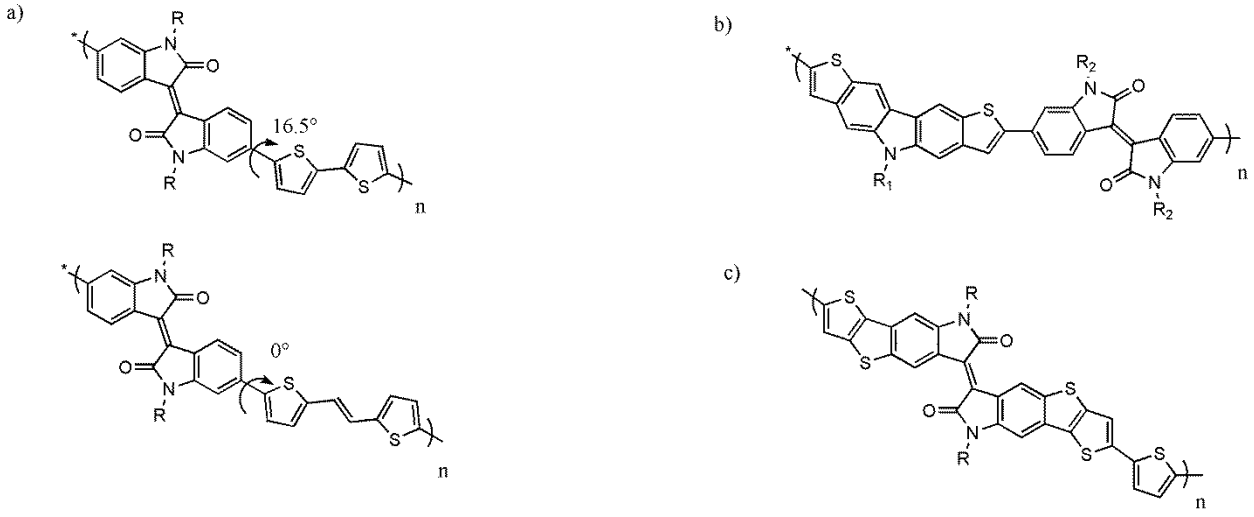

Figure 74: Isoindigo polymers [157,161,162]

In stark contrast, small molecules based on isoindigo are leg behind with PCEs about 3-4 % [163–166]. Those PCEs are also relatively low compared to small molecules achieving nowadays PCEs of 7-9% [59,114,167]. Isoindigo small molecules suffer from low J_{SC} of 8-11 $mA.cm^{-2}$ and low FF of 0.40, originating from a limited charge transport within the device. To tackle this limitation, the molecular packing needs to be improved. One of the drawbacks of isoindigo originates from the slight dihedral angle at the level of the double bond due to steric hindrance between the phenyl proton and the carbonitryl oxygen. This dihedral angle induces a non-planar conformation hampering close molecular packing and good charge transport. Many publications have focused on minimizing the curvature in isoindigo derivatives. One strategy was to replace the phenyl by a thiophene ring forming a thienoisoindigo. The perfectly planar conformation of thienoisoindigo affords great improvements in charge carrier transport for polymers [168–170] as well as for small molecules [171–173], reaching respective hole mobilities of 14.4 $cm^2.V^{-1}.s^{-1}$ and 0.13 $cm^2.V^{-1}.s^{-1}$ in OTFT devices. Odajima *et al.* compared

isoindigo and thienoisoindigo units by combining them with benzothiophene end-capping moieties (Figure 75) [53]. DFT analysis reveals that a planer structure was indeed obtained with thienoisoindigo allowing a delocalization of the frontier orbitals along the whole molecule. This delocalization increased the π-conjugation which conveniently decreased the band gap. The thienoisoindigo molecule was also more crystalline and induces better charge carrier transport and photovoltaic properties than its isoindigo analog. Several small molecules based on thienoisoindigo were designed and then tested in OSCs [173–175]. They revealed good charge transport properties due to a nearly planar backbone. However, they suffered from low Voc as thienoisoindigo exhibits a high-lying HOMO level.

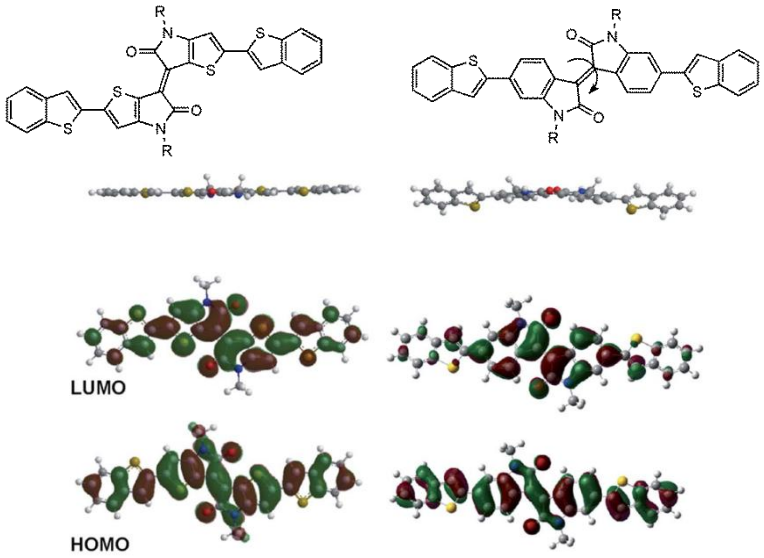

Figure 75: Thienoisoindigo versus isoindigo [53][6]

In their review, Lei *et al.* suggested to insert various π-conjugated skeleton instead of the double bond of isoindigo as a new strategy to modulate the optoelectronic properties and the curvature of the building block [176]. New electron deficient groups were developed by introducing oligophenylvinylene (BDOPV) (Figure 76a) [177,178] or divynilbithiophene (IBTI) (Figure 76b) [179] between the two indolin-2-one rings. The BDOPV polymer showed strong intramolecular hydrogen bond between the carbonitryl oxygen and the neighboring phenyl proton maintaining a good planarity and strong crystallinity. High electron mobilities of 1-1.74 $cm^2.V^{-1}.s^{-1}$ were achieved confirming the potential of this strategy. As for the introduction of divynilbithiophene in isoindigo, the steric hindrance disappeared as predicted and interesting sulfur-oxygen coulombic interactions promoted the planar conformation of the polymer. Such molecules could exhibit a high PCE of 6.41%.

[6] Reproduce with permission, License number 3831940701558

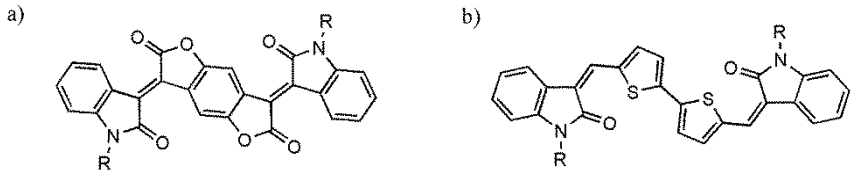

Figure 76: Introduction of π-conjugated skeleton in isoindigo: a) BDOPV [177,178] b) IBTI [179]

1.1.2. EBI

EBI unit follows Lei *et al.* strategy by incorporating a butadiene π-bridge between the two indolin-2-one moieties. This extended π-bridge sufficiently pushes away the phenyl proton and the carbonitryl oxygen to prevent from sterical hindrance and to provide a coplanar geometry. EBI building block was first synthesized in 1965 by Katner *et al.* [180] and was only used as building block for polymer semiconductors in 2014 by Li *et al* [181].The polymers - alternating EBI and bithiophene units - were originally meant for field effect transistors applications and showed impressive hole mobility of 0. 044 $cm^2.s^{-1}.V^{-1}$. EBI-based polymers absorb up to 800 nm and have a deep HOMO level of -5.38 eV. Based on the interesting optoelectronic properties of EBI, we performed an in depth study on the use EBI as an electron deficient building block in D-A-D solution-processable type of small molecules.

1.2. Electron-rich end-capping moieties

Four solution-processable small molecules based on EBI were designed by using different electron-rich end-capping moieties such as thiophene, bithiophene, and benzofuran (Figure 77).

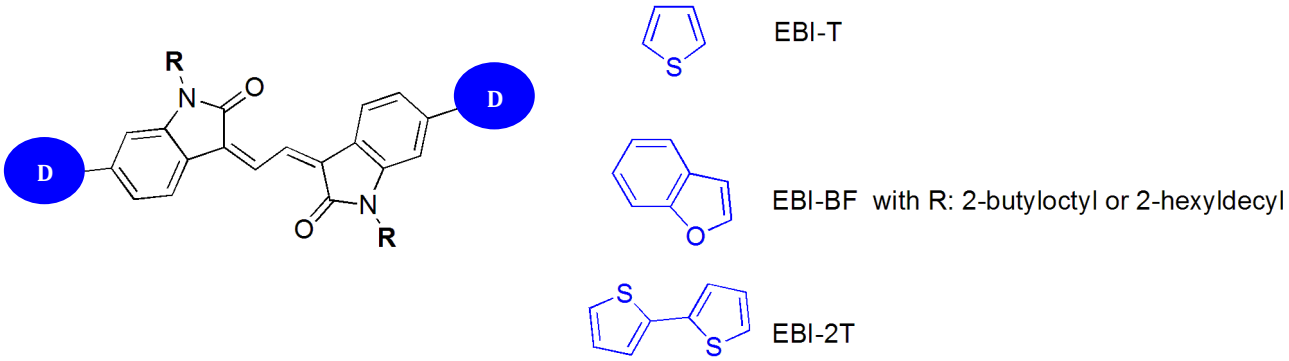

Figure 77: EBI-derivatives studied in this work

1.2.1. Oligothiophene as end-capping moiety

Thiophenes were widely used to form donor semiconductors for both polymers and small molecules [182,183]. The best example is P3HT, a polythiophene which is one of the most studied semiconductors in the field of OSC [184]. As for isoindigo based small molecules, the highest PCEs of 3-3.7% were achieved by combining isoindigo with oligothiophene as electron-rich unit [163,166]. Isoindigo-bithiophene molecule (ID2T) displays a broad absorption up to 700 nm and good charge transport enabling a PCE of 2.6%. Several studies in the literature attended to control the morphology of ID2T via the introduction of solvent additives in the formulation [166,185]. By using a mixture of poly(dimethylsiloxane) (PDMS) and triethylene glycol (TEG), the PCE of ID2T was boosted up to 3.67% which hold the PCE record for isoindigo small molecule OSCs [166]. Meanwhile, Chen *et al.* demonstrated that isoindigo with three thiophenes (ID3T) provided higher PCE of 3.2% over 2.6% for ID2T [163] due to a broader absorption. As bithiophene affords, for now, the highest PCE for isoindigo based small molecules, EBI was combined with bithiophene end-capping moieties.

1.2.2. Benzofuran as end-capping moiety

Benzofuran end-capping appeared as a good electron rich moieties when combine with DPP derivatives [92,186–188]. In 2009, Nguyen *et al.* developed a DPP-benzofuran solution-processable small molecule giving a record PCE of 4.4% [92]. Fused-benzofuran had a highly planar conjugated structure that broadened the absorption spectrum and an oxygen atom that stabilized the HOMO level for high Voc. Moreover, the molecule appeared to be very crystalline offering good charge transport. Ascribing to DPP derivatives, benzofuran permits a better morphology with $PC_{61}BM$ than benzothiophene and benzoindole [187].

Benzofuran was also combined with isoindigo [189,190] and thienoisoindigo [53,172,174] giving optimal PCEs of 0.65% [190] and 2.4% [53] respectively. Compared to benzothiophene, benzofuran leads to a more planar structure with isoindigo owing to the small radius of the oxygen atom [189]. A more regular molecular packing and a higher crystallinity was thus obtained. The ability of benzofuran to make planar framework was emphasized with thienoisoindigo. Stronger vibronic structures were observed on the UV-Visible absorption spectrum due to stronger intramolecular charge transfer. In neat film, benzothiophene-thienoisoidigo exhibited a higher hole mobility compared to benzofuran (0.022 $cm^2.V^{-1}.s^{-1}$ against 5.4 x 10^{-4} $cm^2.V^{-1}.s^{-1}$). However, once blended with $PC_{61}BM$, benzofuran showed a higher degree of crystallinity together with a higher mobility [53]. The good morphology of benzofuran derivatives with $PC_{61}BM$ resulted in an enhanced PCE of 2.4% against 1.5% for benzothiophene derivatives. Similarly, in spite of its weaker lamellar packing of and its lowered charge carrier mobility, benzofuran-thienoisoindigo derivatives still exhibited similar PCEs than

its naphthalene analog [174]. Therefore, benzofuran was employed as an end-capping group for EBI small molecules.

2. SYNTHESIS

The synthesis routes of the new EBI small molecules are described in Scheme 6 . (3Z)-6-bromo-3-((*Z*)-2-(6-bromo-2-oxoindolin-3-ylidene)ethylidene)indolin-2-one (1), starting reagent to form all EBI derivatives, was prepared using the published procedure.[180,181].

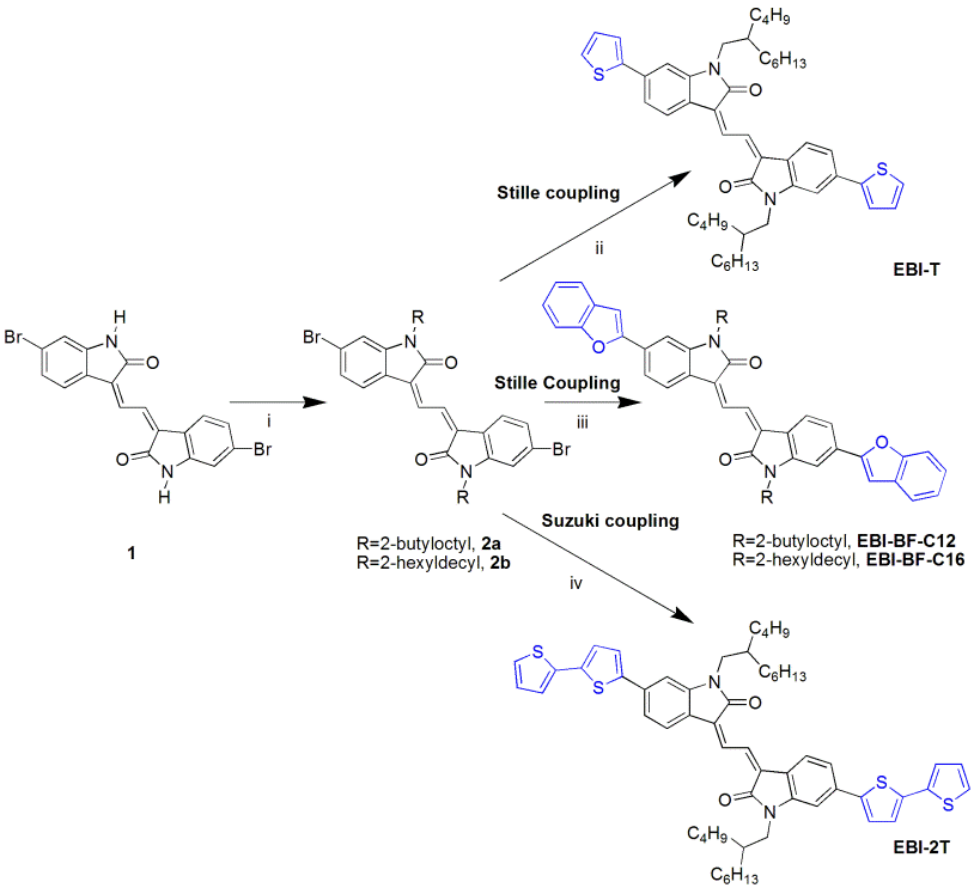

Scheme 6: Synthesis routes of EBI derivatives: i) K_2CO_3, 2-butyloctyl bromide or 2-hexyldecyl iodide, DMF, 70°C, 20 hrs; ii) tributyl(thiophen-2-yl)stannane, $Pd_2(dba)_3$, P(o-totyl)$_3$, toluene, 90°C for 60 hrs; iii) trimethyl(benzofuran-2-yl)stannane, $Pd_2(dba)_3$, P(*o*-totyl)$_3$, toluene, 110°C for 24 hrs; iv) 4,4,5,5-tetramethyl-2(5-(thiophen-2-yl)thiophen-2-yl)-1,3,2-dioxaborolane, $Pd(PPh_3)_4$, K_2CO_3, toluene, 85°C for 24 hrs

2.1. Synthesis of EBI-T

First, 2-butyloctyl chains were introduced onto the nitrogen of the indoline unit of compound **1** to obtain the intermediate (**2a**). EBI functionalized with thiophene (EBI-T) was then prepared

through Stille coupling reaction of a commercial tributyl(thiophen-2-yl)stannane with **2a** for 60 hours at 90°C. The catalytic system for the Stille coupling was a mixture of $Pd_2(dba)_3$ and P(o-totyl)$_3$. The final compounds EBI-T was obtained with moderate yields of 74% after purification by column chromatography using a mixture of hexane : DCM in 60:40 ratio as eluent. EBI-T was fully characterized using ^{1}H NMR (Figure 78), ^{13}C NMR (Figure 79) and field desorption mass spectrometry.

^{1}H NMR ($CDCl_3$, 300MHz) δ 8.96 (s,2H), 7.61 (d, J=7.9 Hz, 2H), 7.35 (dd, J1= 3.6 Hz, J2= 1.0 Hz, 2H), 7.32 (dd, J1= 5.1 Hz, J2= 1.0 Hz), 7.27 (dd, J1=7.9 Hz, J2= 1.5 Hz, 2H), 7.09 (dd, J1= 5.1 Hz, J2=3.6 Hz, 2H), 6.97 (d, J=1.1 Hz, 2H), 3.65 (d, J =7.4 Hz, 4H), 1.91 (s, 2H), 1.37-1.12 (m, 32H), 1.02-0.69 (m, 12H)

^{13}C NMR ($CDCl_3$, 300MHz) δ 167.66, 144.27, 143.98, 136.31, 130.27, 128.59, 128.21, 125.55, 123.69, 122.61, 121.70, 119.57, 105.80, 44.17, 36.42, 31.82, 31.76, 31.46, 29.65, 28.83, 26.60, 23.03, 22.63, 14.08

HR-MS (FD): calculated for C_{50} H_{64} O_2 N_2 S_2: 788.44092; found (M^+): m/z 788.44010

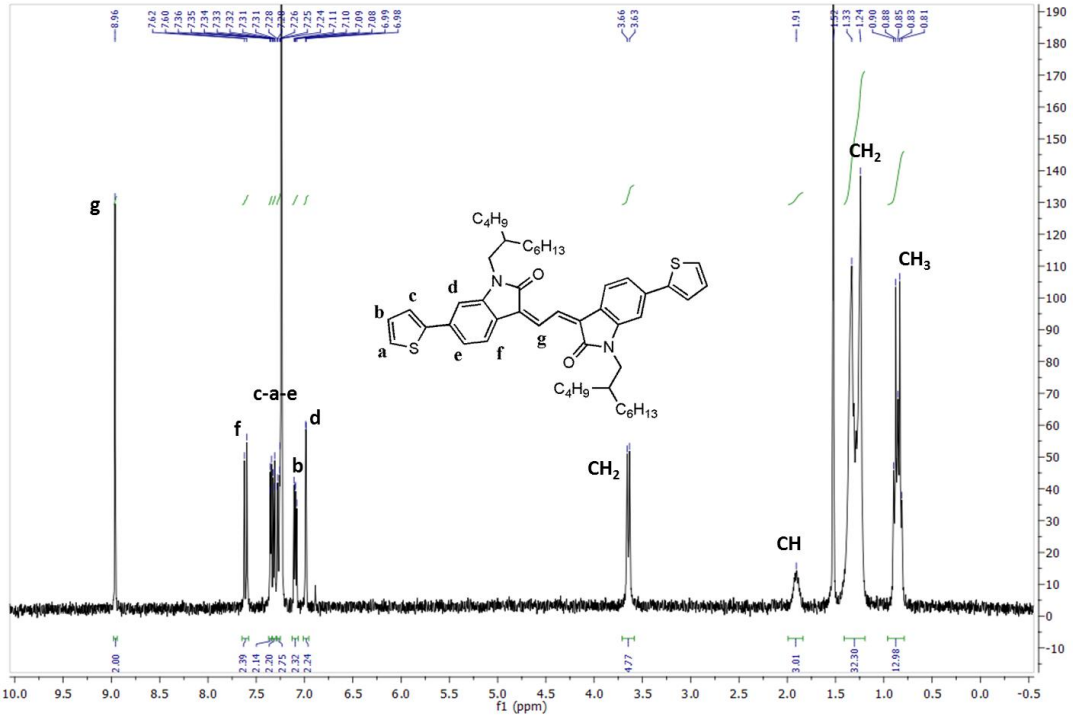

Figure 78: ^{1}H NMR of EBI-T

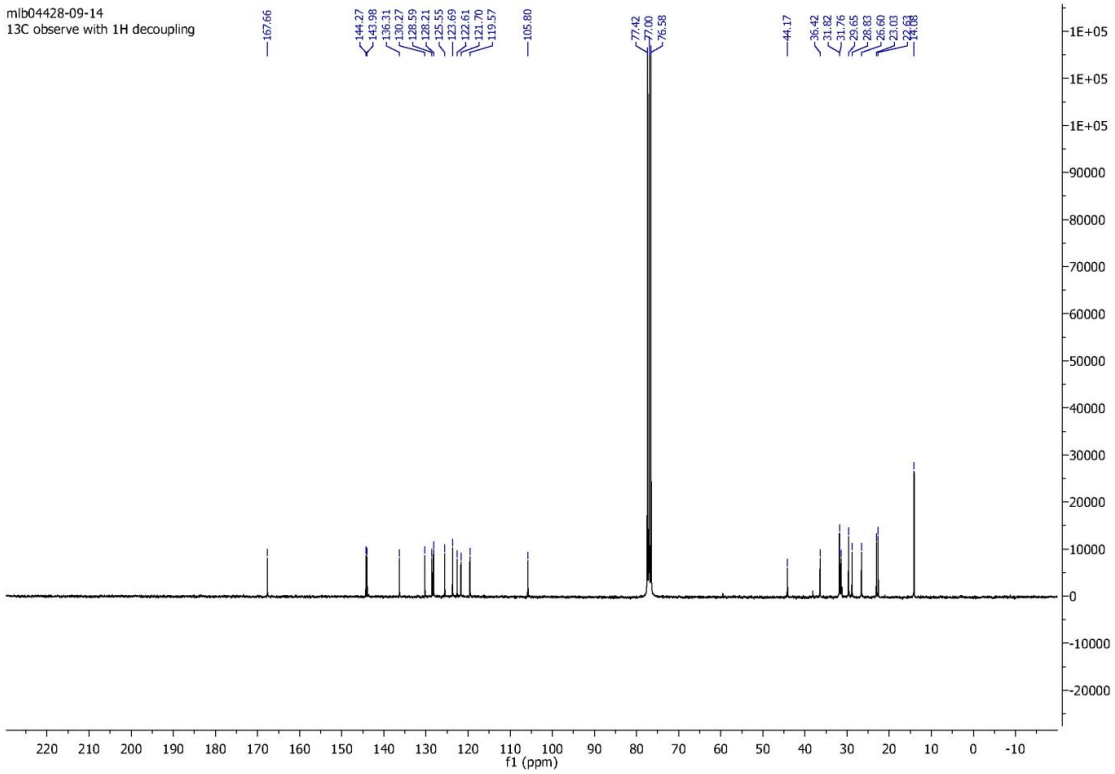

Figure 79: ^{13}C NMR of EBI-T

2.2. Synthesis of EBI-BF derivatives

2.2.1. EBI-BF-C_{12}

EBI functionalized with benzofuran (EBI-BF) was similarly prepared through Stille coupling reaction of a trimethyl(benzofuran-2-yl)stannane with **2a** for 60 hours at 110°C. The benzofuran stannyl was produced using benzofuran along with n-butyllithium and tri-methyl tin chloride reagents. The catalytic system for the Stille coupling was a mixture of $Pd_2(dba)_3$ and $P(o\text{-}totyl)_3$. The final compounds EBI-BF-C_{12} was obtained with yields of 55% after purification by column chromatography using a mixture of hexane : DCM in 50:50 ratio as eluent. EBI-BF-C_{12} was fully characterized using ^{1}H NMR (Figure 80), ^{13}C NMR (Figure 81) and field desorption mass spectrometry.

^{1}H NMR ($CDCl_3$, 300MHz) δ 8.98 (s, 2H), 7.68 (d, *J* = 7.9 Hz, 2H), 7.59 (d, *J* = 7.4 Hz, 2H), 7.52 (d, *J* = 7.6 Hz, 4H), 7.38 – 7.18 (m, 6H), 7.07 (s, 2H), 3.70 (d, *J* = 5.2 Hz, 4H), 1.97 (s, 2H), 1.46 – 1.17 (m, 32H), 1.01 – 0.74 (m, 12H).

^{13}C NMR ($CDCl_3$, 300MHz) δ 167.55, 155.50, 154.94, 143.91, 132.05, 130.32, 129.06, 128.86, 124.80, 123.52, 123.14, 121.56, 121.06, 118.71, 111.19, 104.61, 102.55, 44.22, 36.42, 31.87, 31.74, 31.44, 29.68, 28.82, 26.58, 23.06, 22.64, 14.15, 14.10

HR-MS (FD): calculated for $C_{58}\ H_{68}\ O_4\ N_2$: 856.51857; found (M^+): m/z 856.51791

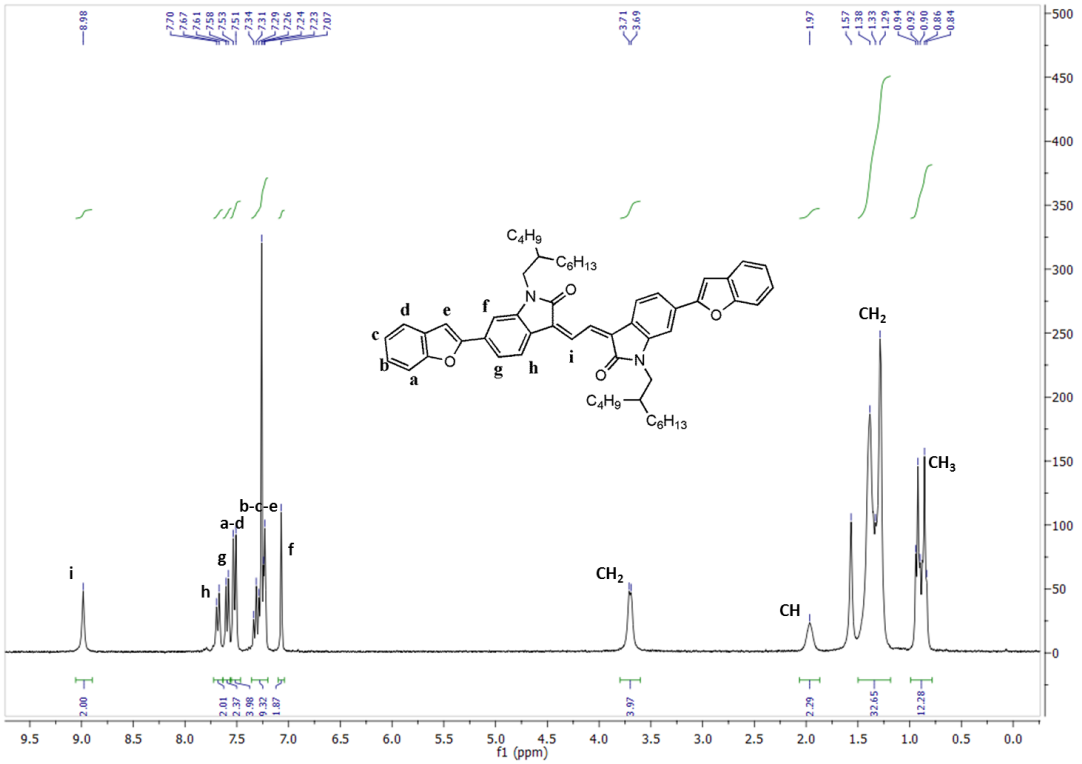

Figure 80: ^1H NMR of EBI-BF-C_{12}

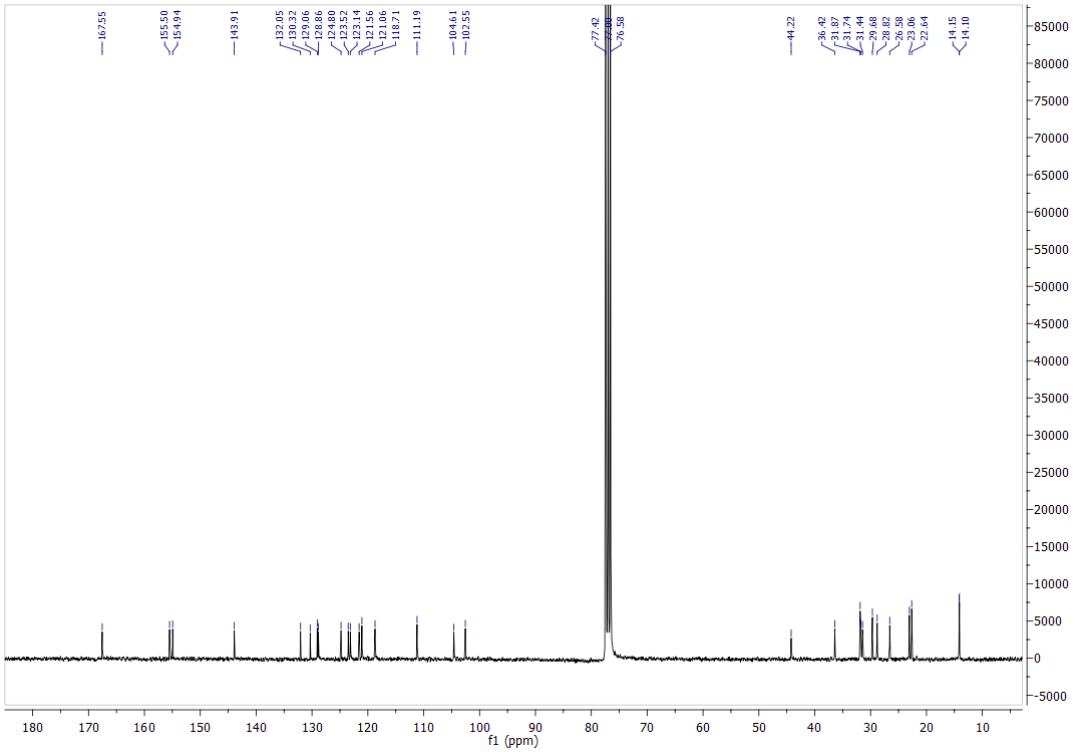

Figure 81: ^{13}C NMR of EBI-BF-C_{12}

The solubility of EBI-BF-C12 was found to be much inferior to that of EBI-T in chloroform, indicating stronger intermolecular interactions. To improve the solubility of EBI-BF, longer alkyl chains, 2-hexyldecyl, were incorporated.

2.2.2. EBI-BF-C_{16}

2-hexyldecyl chains were introduced onto the nitrogen of the indoline unit of compound **1** to obtain the intermediate (**2b**). EBI functionalized with benzofuran (EBI-BF) was then prepared through Stille coupling reaction of a trimethyl(benzofuran-2-yl)stannane with **2b** for 60 hours at 110°C. The benzofuran stannyl was produced using benzofuran along with n-butyllithium and tri-methyl tin chloride reagents. The catalytic system for the Stille coupling was a mixture of $Pd_2(dba)_3$ and P(o-totyl)$_3$. The final compounds EBI-BF-C_{16} was obtained with moderate yields of 68% after purification by column chromatography using a mixture of hexane : DCM in 50:50 ratio as eluent. EBI-BF-C_{16} was fully characterized using ^1H NMR (Figure 82), ^{13}C NMR (Figure 83) and field desorption mass spectrometry

^1H NMR (TCE-d_2, 300MHz): δ 8.94 (s, 2H), 7.67 (d, *J* = 7.9 Hz, 2H), 7.57 (d, *J* = 7.5 Hz, 2H), 7.51 (d, *J* = 5.8 Hz, 4H), 7.36 – 7.18 (m, 6H), 7.08 (s, 2H), 3.65 (d, *J* = 7.3 Hz, 4H), 1.92 (s, 2H), 1.46 – 1.08 (m, 49H), 0.90 – 0.73 (m, 13H).

^{13}C NMR ($CDCl_3$, 300MHz) δ 167.51, 155.51, 154.93, 143.88, 132.02, 130.27, 129.06, 128.82, 124.78, 123.52, 123.13, 121.53, 121.04, 118.69, 111.19, 104.59, 102.52, 44.21, 36.41, 31.88, 31.75, 30.00, 29.68, 29.61, 29.32, 26.59, 22.65, 14.09

HR-MS (FD): calculated for $C_{66}\ H_{84}\ O_4\ N_2$: 968.64311; found (M^+): m/z 968.64439

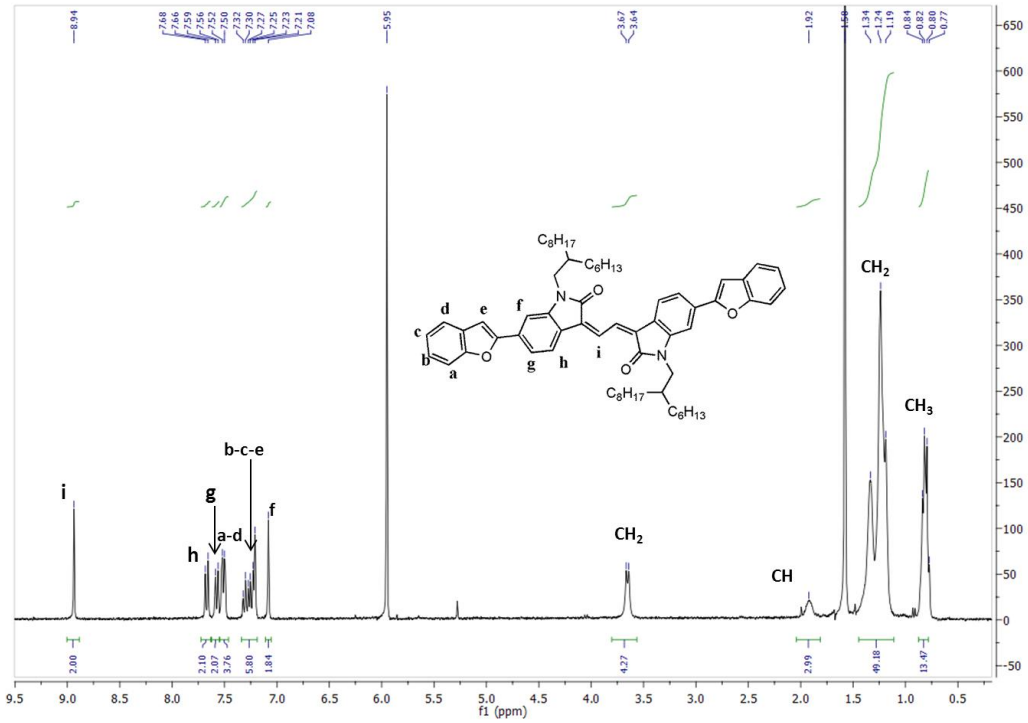

Figure 82: ^1H NMR of EBI-BF-C_{16}

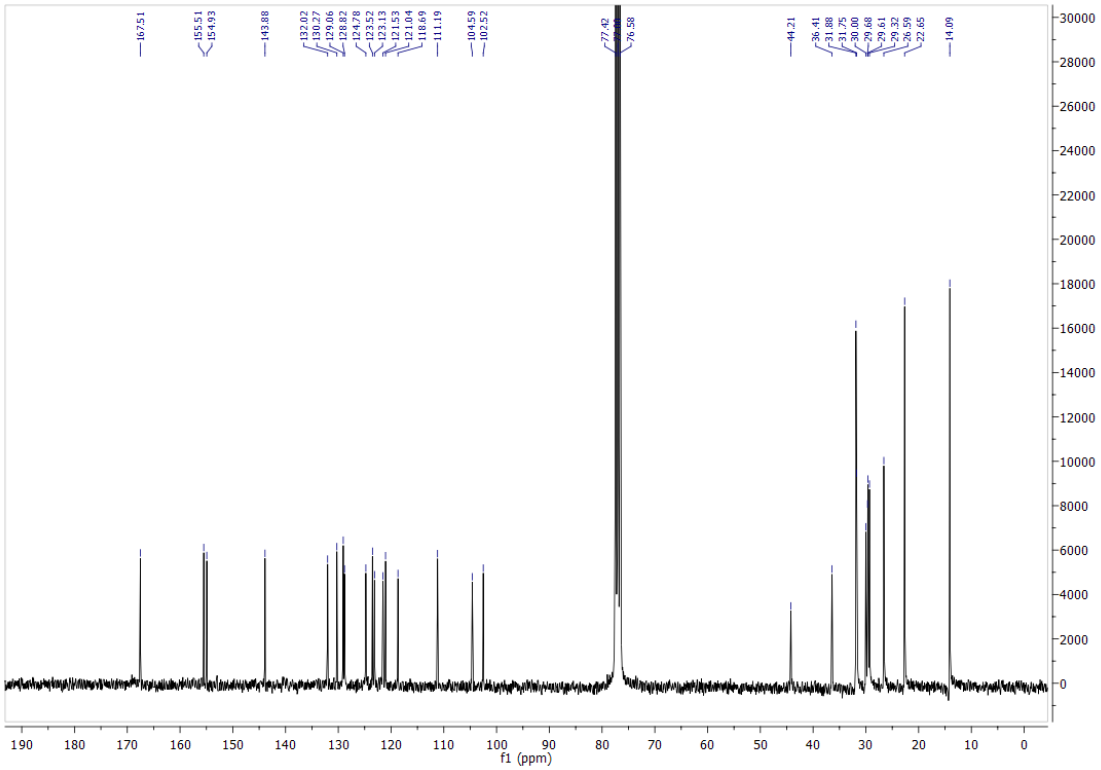

Figure 83: ^{13}C NMR of EBI-BF-C_{16}

2.3. Synthesis of EBI-2T

For EBI functionalized with bithiophene, a Suzuki coupling reaction was carried out between **2a** and a commercial 4,4,5,5-tetramethyl-2(5-(thiophen-2-yl)thiophen-2-yl)-1,3,2-dioxaborolane in presence of the catalyst $Pd(PPh_3)_4$ and a base K_2CO_3 (2M) for 24 hours at 85°C. EBI-2T was obtained with a yield of 67% after purification by column chromatography using a mixture of chloroform : hexane 1:1 as eluent. All four EBI molecules were fully characterized by ^1H NMR (Figure 84), ^{13}C NMR (Figure 85) and HRMS mass spectrometry.

^1H NMR ($CDCl_3$, 300MHz): δ 8.82 (s, 2H), 7.51 (d, J= 7.9 Hz, 2H), 7.24-7.15 (m, 6H), 7.13 (d, J=3.3 Hz, 2H), 7.07 (d, J=2.6 Hz, 2H), 6.96 (t, J= 4.0 Hz, 2H), 6.84 (s, 2H), 3.56 (d, J= 6.6 Hz, 4H), 1.82 (s, 2H), 1.43-1.10 (m, 33 H), 0.91-0.68 (m, 12H)

^{13}C NMR ($CDCl_3$, 300MHz) δ 167.7, 144.03, 142.87, 137.55, 137.19, 135.94, 130.19, 128.60, 127.95, 124.73, 124.70, 124.42, 123.88, 122.75, 121.74, 119.19, 105.36, 44.22, 36.50, 31.88, 31.84, 31.54, 29.69, 28.90, 26.67, 23.07, 22.66, 14.13, 14.09

HR-MS (FD): calculated for $C_{58}\ H_{68}\ O_2\ N_2\ S_4$: 956.41636; found ($M^+$): m/z 952.41883

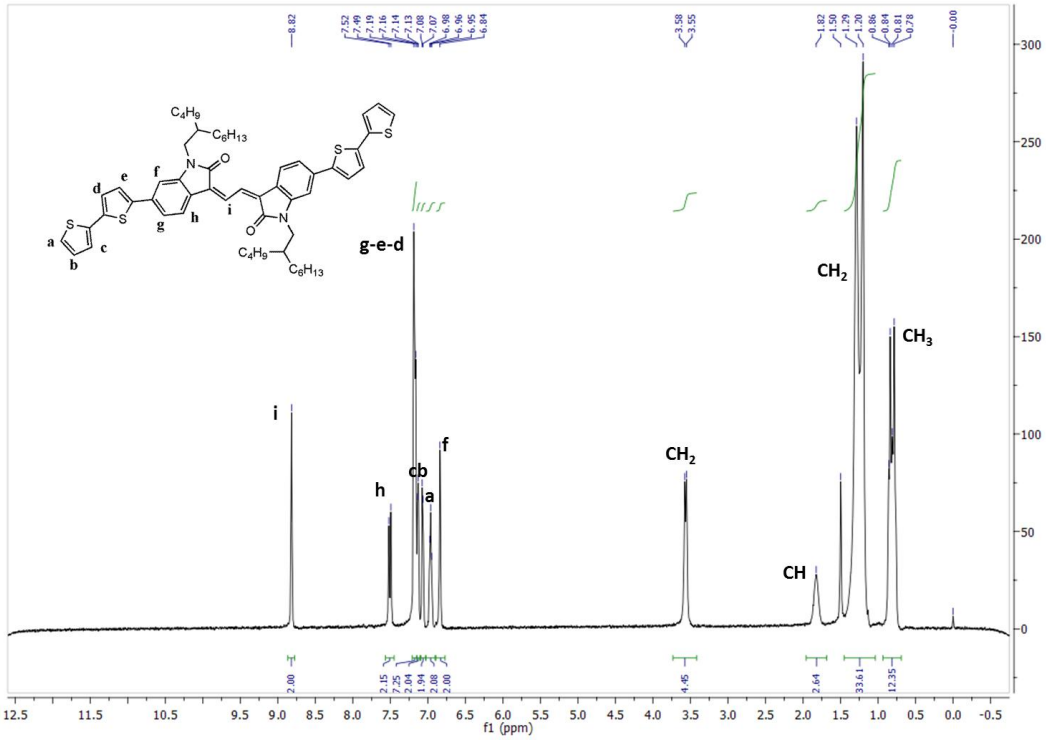

Figure 84: ^{1}H NMR of EBI-2T

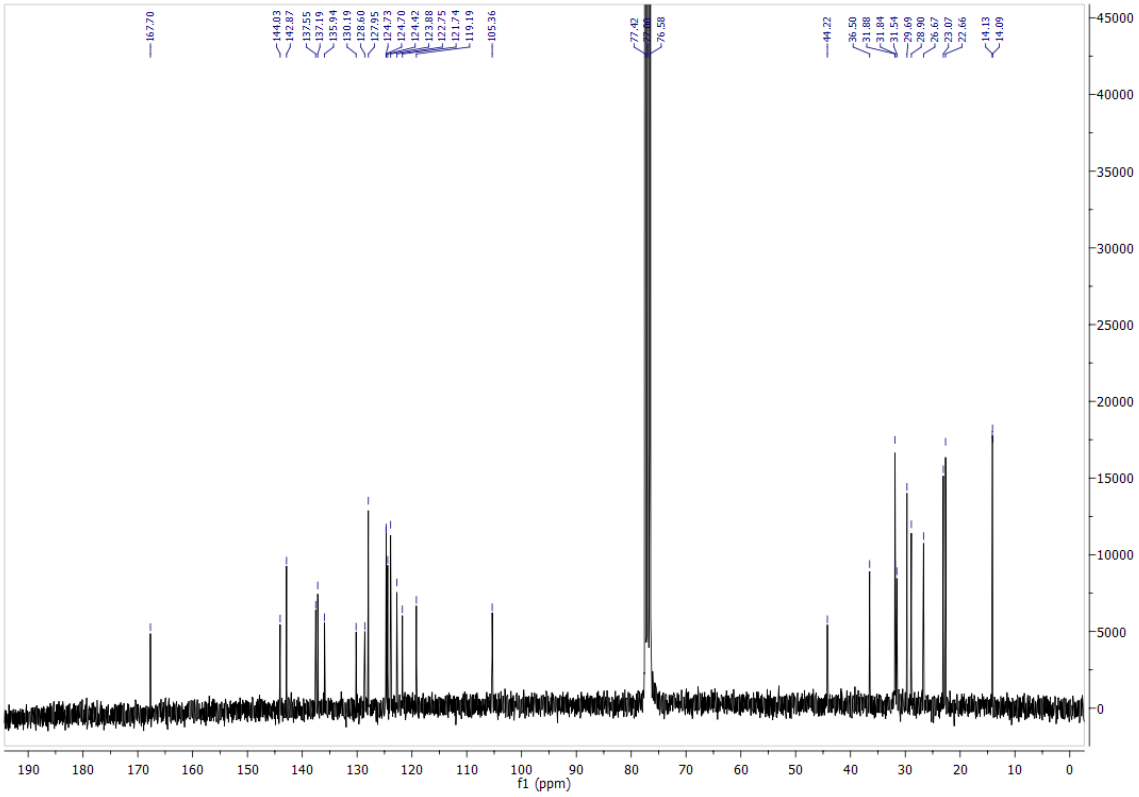

Figure 85: ^{13}C NMR of EBI-2T

3. CHARACTERIZATION

In this section, the optoelectronic properties of EBI derivatives were studied: the energy levels and the mobility were measured and the molecular packing properties were evaluated. The properties of the different molecules were compared in order to establish the effect of the different end-capping.

3.1. Optical properties

The UV-Visible absorption spectra of the EBI derivatives were recorded in chloroform solution and in thin film and are illustrated in Figure 86. In solution, all EBI derivatives exhibited two-band profiles. The 300-500 nm band corresponds to the π- π* transition within the electron rich end-capping whereas the 500-700 nm band can be assigned to intramolecular charge transfer (ICT) from the electron-rich unit to the electron deficient EBI. EBI-T showed a weaker absorption in the second band than in the first band revealing weak interactions between thiophene and EBI. In comparison, EBI-2T and EBI-BF compounds presented stronger ICT. The maximum absorption (λ_{max}) of 549 nm and 565 nm also red-shifted compared to EBI-T (λ_{max}-II band = 531 nm). The maximum absorption coefficients were estimated from the spectra in solution to be around 1.9×10^{-3} L.mol^{-1}.s^{-1} for EBI-T, 2.6×10^{-3} L.mol^{-1}.s^{-1} for both EBI-BF derivatives and 4.3×10^{-3} L.mol^{-1}.s^{-1} for EBI-2T. In solid-state, only the λ_{max} of EBI-2T red-shifted whereas an additional shoulder appeared for all EBI derivatives originating from intermolecular interactions. It is noteworthy that both EBI-BF compounds have similar UV-visible spectra in both solution and solid-state suggesting that the length of the alkyl chains do not impact the optical properties. The optical band gaps of EBI-T, EBI-BF and EBI-2T, estimated from the absorption edge of the film, is 1.88 eV, 1.85 eV and 1.76 eV, respectively. EBI-2T is most propitious for harvesting sunlight.

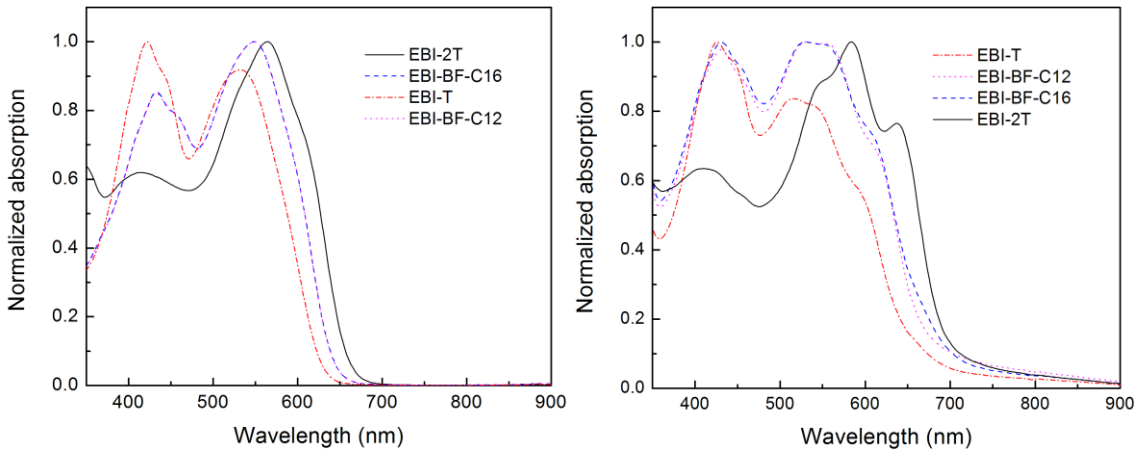

Figure 86: UV-Visible spectra of EBI derivatives in solution (left) and in thin-film (right)

3.2. Energy levels

To depict the electronic structures of these EBI molecules, computer simulations based on the DFT were conducted on three model compounds with methyl substituents for the convenience of computation. The optimized backbone conformations of each EBI derivatives are depicted in Figure 87a and confirmed the planarity feature of EBI core units. As for the whole molecule's conformations, EBI-T and EBI-2T exhibited dihedral angles of 26° and 22° between the EBI and thiophene units, respectively, whereas EBI-BF had a perfectly planar conformation. The high planarity of EBI-BF should be favorable for the intramolecular charge transport and allow closer π-π stacking that is good for efficient intermolecular charge transport. To gain further information concerning the impact of electron-rich moieties on the energy levels, the HOMO and LUMO electron density distributions of these model compounds were calculated and shown in Figure 87c,b. The HOMO electron densities of EBI-T, EBI-BF and EBI-2T are distributed along the entire backbones whereas the LUMO electron densities are localized on the EBI units and thus the donor moieties should mainly impact the HOMO levels of these molecules. The calculated HOMO and LUMO levels are listed in Table 10. EBI-T has the largest band gap due to its shortest π-conjugation consistent with the UV-Vis data. EBI-BF has the deepest HOMO indicating the weakest electron-donating effect of benzofuran among the three donor moieties.

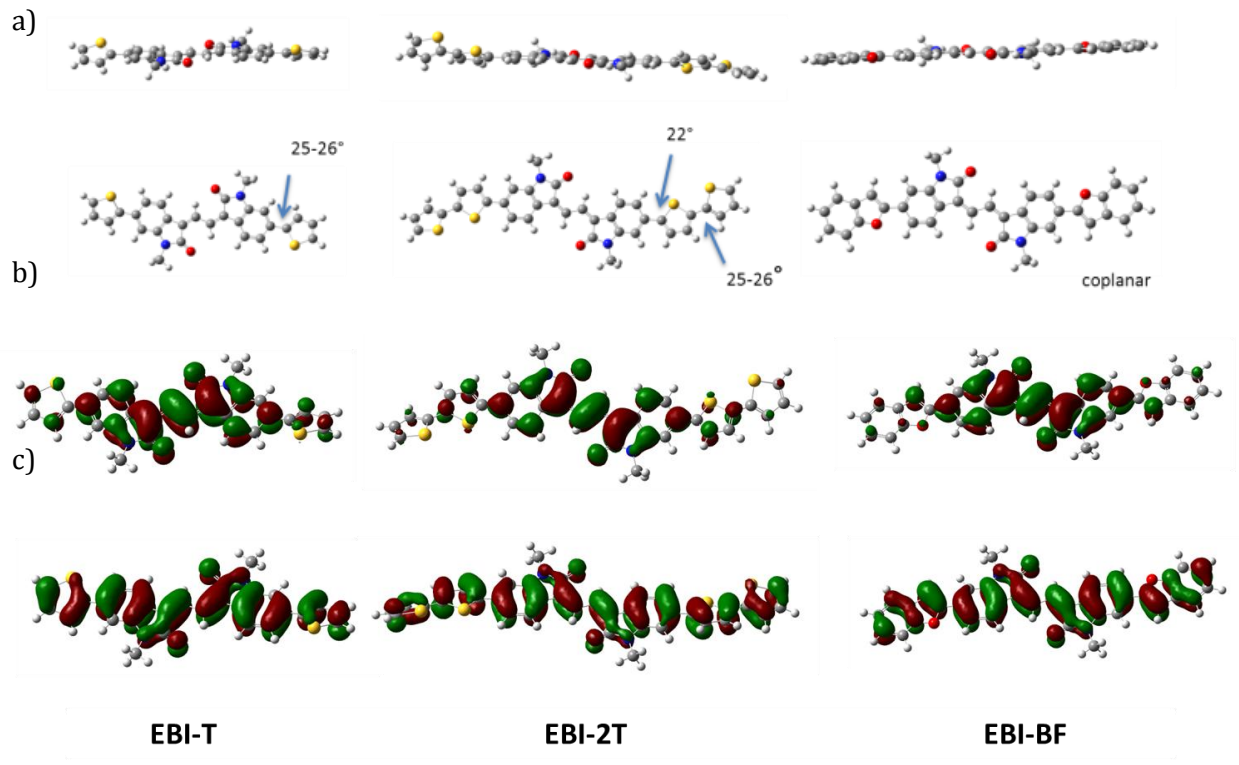

Figure 87: DFT calculations of EBI-derivatives – Lowest energy conformation (a) electron density of the LUMO (b) and the HOMO (c)

The electrochemical properties were investigated by cyclic voltammetry. EBI derivatives were deposited by drop-casting on the working electrode the oxidation peaks of each compound is represented in Figure 88. HOMO levels were estimated to be -5.71 eV for EBI-T, -5.73 eV for EBI-BF and -5.66 eV for EBI-2T, all promising to achieve Voc superior to 1 V according to Scharber equation [23]. Since the reduction peaks were very weak, the LUMO levels were obtained by adding the optical band gap to the HOMO levels to be -3.83 eV for EBI-T, -3.89 eV for EBI-BF and -3.90 eV for EBI-2T. The offsets between the LUMO level of EBI derivatives and that of $PC_{61}BM$ (- 4.3 eV) are larger than the minimum value of 0.3 eV required for efficient electron transfer from the donor molecules to $PC_{61}BM$.

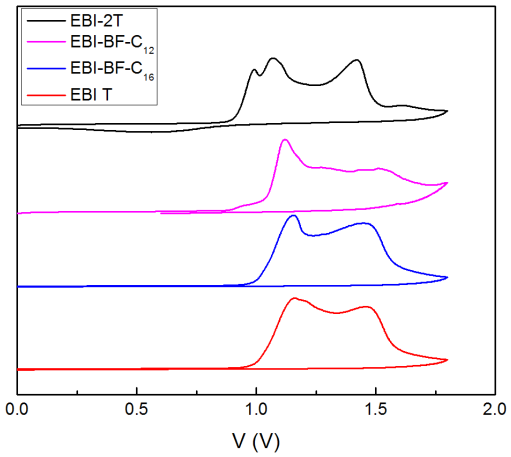

Figure 88: Cyclic voltammetry measurements on EBI-derivatives

Table 10 summarizes the energy levels calculated by DFT calculations and evaluated by cyclic voltammetry. The same trends are observed with both technics: EBI-2T exhibits the lowest band gap and the higher HOMO level while EBI-T displays the largest band gap and EBI-BF the deepest HOMO. By reporting the energy levels of EBI derivatives on Scharber diagram (Figure 89)., PCEs of 9%, 8% and 7% can be expected for EBI-2T, EBI-BF and EBI-T respectively This confirms the strong potential of these compounds as donor materials for OSCs.

Table 10: Energy levels of EBI derivatives according to DFT calculations and CV measurements

In eV	$HOMO_{DFT}$[a]	$LUMO_{DFT}$[a]	E_g DFTa	$HOMO_{CV}$	LUMO	E_g opt
EBI-T	-5.21	-2.79	2.42	-5.71	-3.83	1.88
EBI-BF-C_{12}	-5.18	-2.87	2.31	-5.74	-3.89	1.85
EBI-BF-C_{16}				-5.73	-3.91	1.82
EBI-2T	-5.06	-2.82	2.24	-5.66	-3.90	1.76

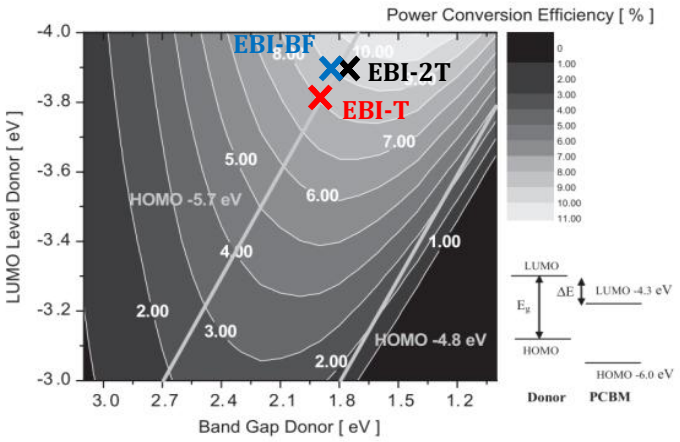

Figure 89: EBI derivatives on Scharber diagram [23]

3.3. Charge transport properties

The charge transport properties of EBI derivatives were evaluated in OTFTs and showed typical hole transport characteristics. Different speed depositions and thermal annealing were tested in order to control the crystallization and molecular packing of each EBI derivatives.

3.3.1. EBI-T in OTFTs

When varying the speed deposition, a signal was detected only for a film formed at 2 500 rpm while only noise was recorded for films prepared with faster deposition speed. The as-cast device of EBI-T gave an average saturated hole mobility (μ_h) of 6.38×10^{-5} $cm^2.V^{-1}.s^{-1}$ as described in Table 11. A thermal annealing step at 150 °C did not further improve the charge transport properties exhibiting a similar hole mobility of 1.67×10^{-5} $cm^2.V^{-1}.s^{-1}$.

Table 11: EBI-T based OTFTs of the as-cast and annealed film at 150°C for 10 minutes.

Speed deposition	**Thermal annealing**	**$\mu_{h\ average}$ (L=10 µm) ($cm^2.V^{-1}.s^{-1}$)**	**$\mu_{h\ max}$ (L=10 µm) ($cm^2.V^{-1}.s^{-1}$)**
2500 rpm	RT	6.38×10^{-5} $^{+/-}$ 1.09×10^{-4}	2.28×10^{-4}
2500 rpm	150°C	1.67×10^{-5} $^{+/-}$ 5.62×10^{-6}	2.33×10^{-5}

3.3.2. EBI-2T in OTFTs

Concerning EBI-2T, various speed depositions (2500 rpm, 5000 rpm and 10000 rpm) were tested in order to form the EBI-2T active films of OTFT devices. The results are summarized in Table 12. The highest hole mobility of 1.67 x 10^{-3} $cm^2.V^{-1}.s^{-1}$ is achieved using a slow deposition speed of 2500 rpm which leads to a slow drying and enables the formation of larger crystals as can be seen in the microscopic images in Figure 90. The transfer curves of the best devices are shown in Figure 91. This device displays a maximum hole mobility of 3.17 × 10^{-3} $cm^2.V^{-1}.s^{-1}$ along with a high $I_{on/off}$ ratio of 4 × 10^4 and a small threshold voltage of 4 V.

Table 12: EBI-2T in OTFTs with channel length of 5 and 10 µm with the active film prepared at various speed depositions

Speed deposition	**$\mu_{h\ average}$* (L=5µm) ($cm^2.V^{-1}.s^{-1}$)**	**$\mu_{h\ max}$ (L=5µm) ($cm^2.V^{-1}.s^{-1}$)**	**$\mu_{h\ average}$* (L=10µm) ($cm^2.V^{-1}.s^{-1}$)**	**$\mu_{h\ max}$ (L=10µm) ($cm^2.V^{-1}.s^{-1}$)**
2 500 rpm	1.52×10^{-3} $^{+/-}$ 1.15×10^{-3}	3.17×10^{-3}	1.67×10^{-3} $^{+/-}$ 1.09×10^{-3}	2.56×10^{-3}
5 000 rpm	4.43×10^{-5} $^{+/-}$ 5.5×10^{-6}	5×10^{-5}	5.3×10^{-5} $^{+/-}$ 5.13×10^{-5}	1.26×10^{-4}
10 000 rpm	2.52×10^{-5} $^{+/-}$ 5.5×10^{-6}	3.1×10^{-5}	1.92×10^{-5} $^{+/-}$ 1.9×10^{-6}	2.18×10^{-5}

*average on 4 devices

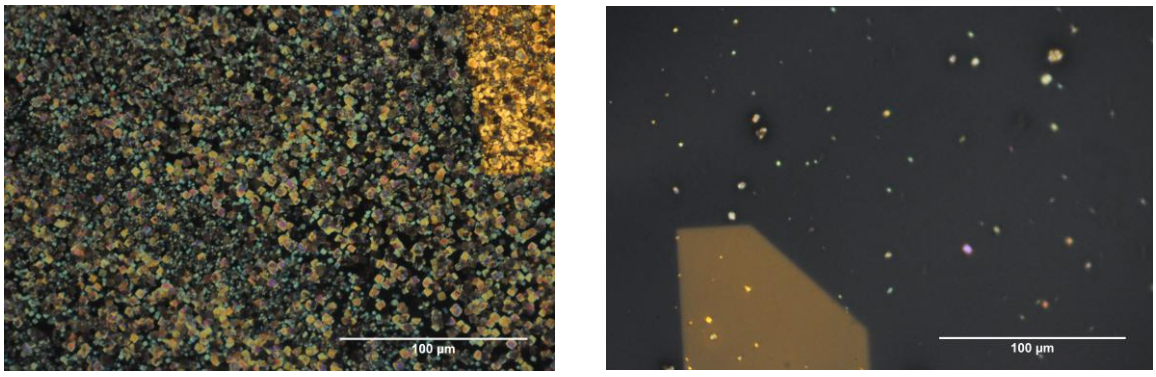

Figure 90: Microscope images at x50 under cross-polarization of EBI-2T deposited with a speed deposition of 2500 rpm (left) and 5000 rpm (right)

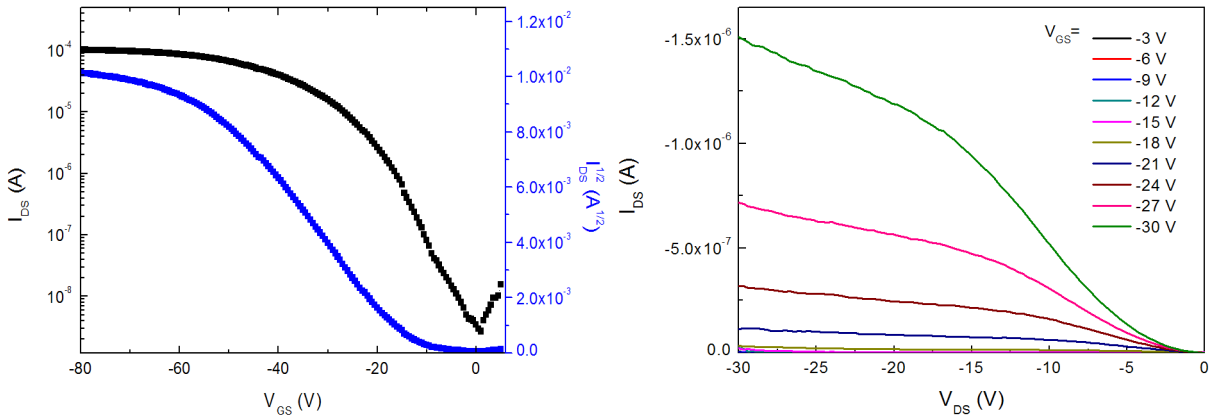

Figure 91: Transfer curves of the best EBI-2T based OTFTs with a channel length of 5µm and an active film prepared with a speed deposition of 2500 rpm and V_{DS} = 40 V and the corresponding output curves

3.3.3. EBI-BF in OTFTs

All transistors were prepared by spin-coating a chloroform solution of EBI-BF at 2500 rpm. Without any post treatment, EBI-BF derivatives exhibited low hole mobilities of 4.51×10^{-4} $cm^2.V^{-1}.s^{-1}$ for EBI-BF-C_{12} and 2.95×10^{-5} $cm^2.V^{-1}.s^{-1}$ for EBI-BF-C_{16}. EBI-BF-C_{16} displayed the lowest mobility. Successive thermal annealing at 100°C, 150°C and 200°C for 10 min were performed on each device. Figure 92 details the hole mobilities as a function of the thermal annealing temperature for both EBI-BF. The hole mobilities of EBI-BF-C_{12} and EBI-BF-C_{16} increased up to 4.35×10^{-3} $cm^2.V^{-1}.s^{-1}$ and 0.021 $cm^2.V^{-1}.s^{-1}$ upon respective thermal annealing of 100°C and 150°C. In the optimal condition, EBI-BF-C_{16} thin film transistors displayed better charge transport than EBI-BF-C_{12} due to a better uniformity of the film and showed lower leakage currents, and improved $I_{on/off}$ ratio of 10^6 over 10^4 for EBI-BF-C_{12}. The transfer curves of the best devices based on EBI-BF-C_{12} and EBI-BF-C_{16} are shown in Figure 93.

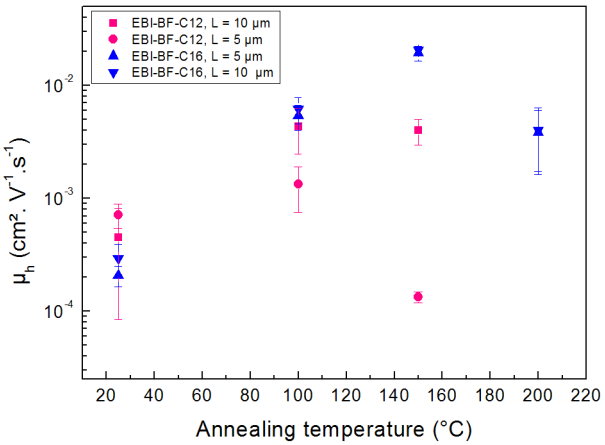

Figure 92: Hole mobilities of EBI-BF derivatives after successive thermal annealing

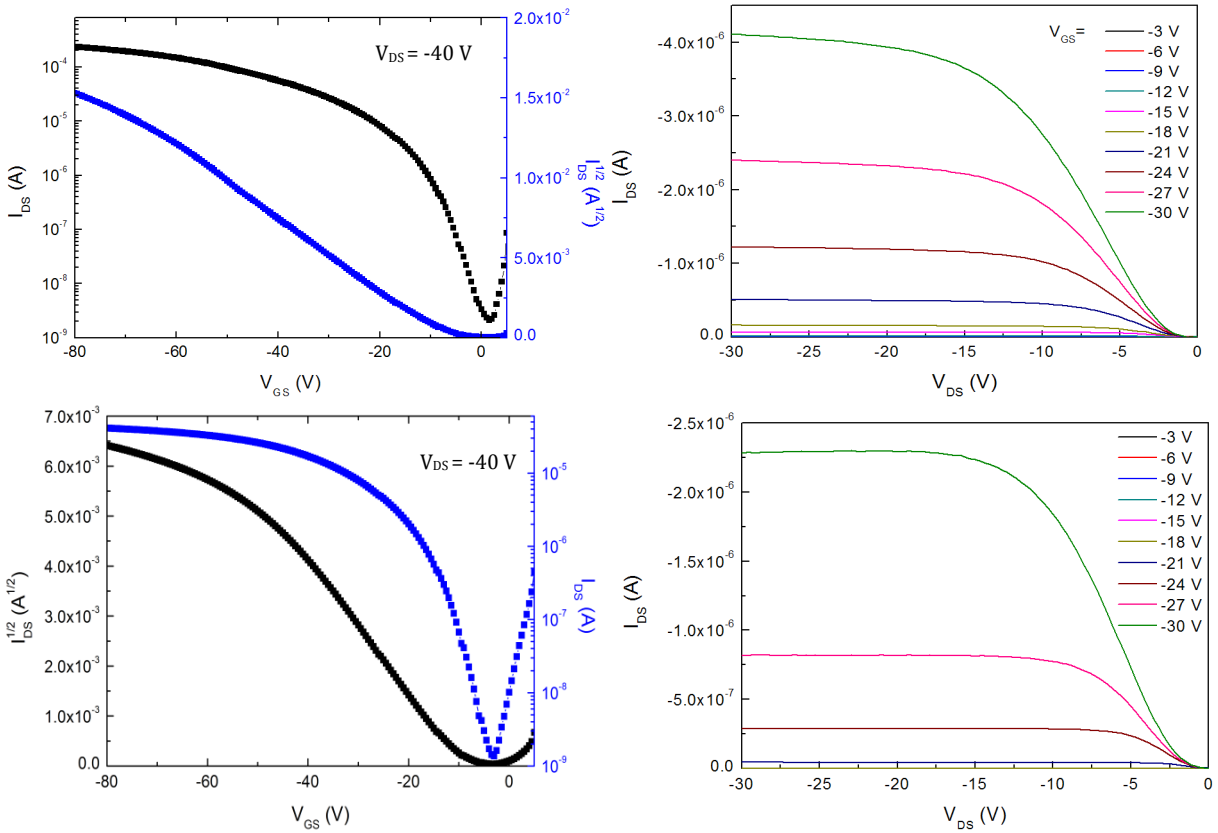

Figure 93: Transfer and output curves of OTFT based on EBI-BF-C_{12} (top) and EBI-BF-C_{16} (bottom)

The effect of thermal annealing on EBI-BF films was investigated by comparing the UV-Visible absorption spectra of as cast and annealed films of both EBI-BF derivatives, as presented in Figure 94. For EBI-BF-C_{12}, an additional shoulder clearly appeared at 653 nm upon a thermal annealing at 140°C indicating the appearance of a new type of intermolecular interaction. The enhanced charge transport properties observed after annealing at 100°C can be ascribed to a better molecular packing offering new intermolecular interplay. As for EBI-BF-C_{16}, a finer vibronic structure and an increase in the peak intensity at 650 nm is observed upon thermal annealing at 100°C. Both changes suggest a better packing of the molecules with thermal annealing which is beneficial for a better charge transport as observed in the OTFT studies.

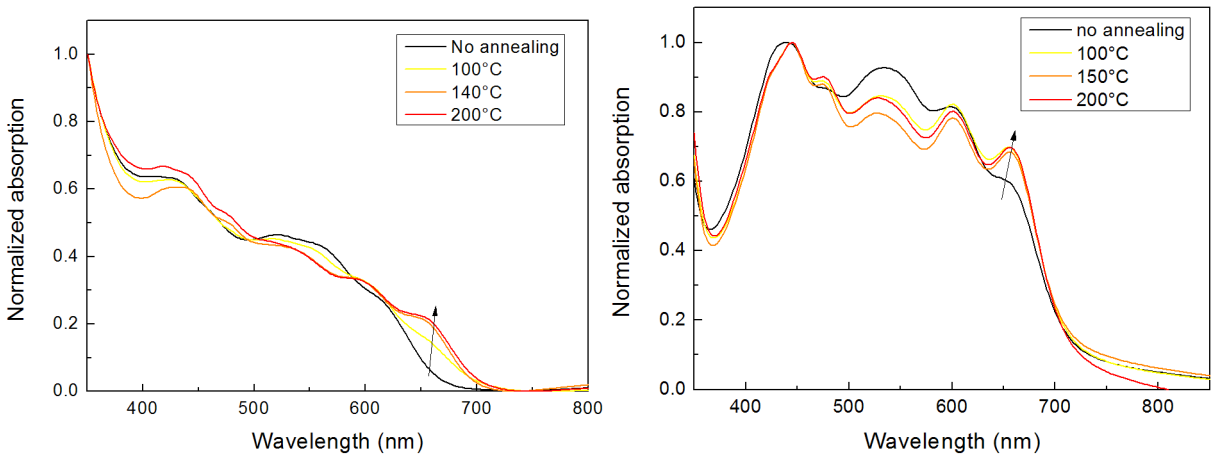

Figure 94: UV-visible absorption spectra of EBI-BF-C_{12} (left) and EBI-BF-C_{16} (right) thin films upon various thermal annealing

3.3.4. Discussion

Among EBI-derivatives, EBI-BF derivatives exhibited the highest hole mobility owing to their coplanar conformations giving closer π-π packing. EBI-BF and EBI-2T demonstrated promising hole mobilities to reach FF superior to 0.65 [52]. The mobility of EBI-T appeared lower than 10^{-4} $cm^2.V^{-1}.s^{-1}$ which would lead to large carrier sweep-out time and therefore important bimolecular recombinations could be expected in solar cells [52].

3.4. Molecular packing

To further study the molecular ordering of EBI-T, EBI-BF-C_{12}, EBI-BF-C_{16} and EBI-2T, X-ray diffraction measurements were performed on their as-cast thin films, spin-coated from chloroform solution. As shown in Figure 95, EBI-BF-C_{12}, EBI-BF-C_{16} and EBI-2T display strong and narrow diffraction peaks. This is consistent with their good charge transport properties. Based on the peak position, the d-spacing are calculated using the Bragg's equation to be 2.0 nm for EBI-BF-C_{12}, 2.3 nm for EBI-BF-C_{16} and 1.6 nm for EBI-2T. Those diffraction peaks correspond to the periodical π-π stacking or alkyl chains packing of the molecules. On the other hand, EBI-T showed only a weak broad peak. This suggests that this molecule exhibits a poor crystallinity which is likely to be the reason for the low mobility observed in OTFT devices.

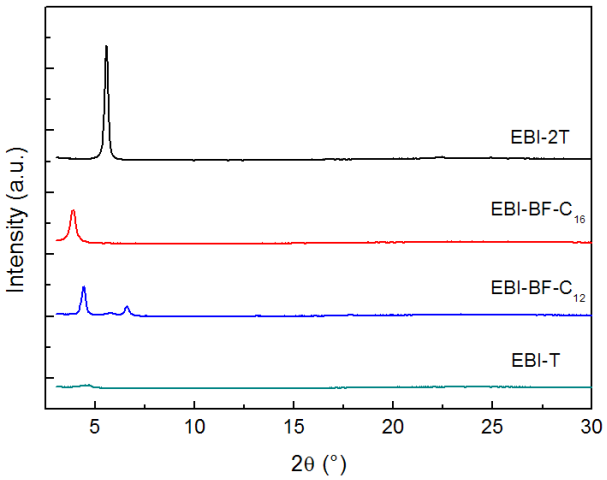

Figure 95: X-ray diffraction spectra of the neat films of EBI derivatives

3.5. Conclusion

The optoelectronic properties of EBI derivatives were studied. This study could underline their advantages and drawbacks:

- EBI - 2T exhibits the broadest absorption spectrum together with a high mobility of 1.67×10^{-3} $cm^2.V^{-1}.s^{-1}$
- EBI-BF-C_{16} exhibits the highest mobility of 0.021 $cm^2.V^{-1}.s^{-1}$ after thermal annealing. This could be attributed to its planar confirmation. Additionally, it exhibits a deep homo level that could lead to a theoretical Voc of 1.14 V when blended with $PC_{61}BM$ in OSCs. [23]
- EBI-T demonstrates has a narrow absorption spectra and poor charge transport properties which may limit the PV process.

4. PHOTOVOLTAIC PROPERTIES

The photovoltaic properties of EBI derivatives were investigated in planar and BHJ OSCs. The morphology of the active layer of each EBI derivatives was analysed by AFM and XRD for a better understanding of their PV process.

4.1. Bi-layers OSC devices

The PV properties of EBI-T, EBI-BF-C_{12} and EBI-2T were first investigated in bi-layer OSCs with the following architecture: ITO/PEDOT:PSS/EBI/C_{60}/Ca/Al. EBI derivatives were deposited from chloroform solutions to form films with a thickness around 30 nm. The PV performances are listed in Table 13. Among all EBI derivatives, EBI-2T exhibited the highest J_{SC} due to its broadest absorption spectrum. EBI-T shows almost no photovoltaic effect.

Table 13: PV performances of bi-layer OSCs based on EBI-T, EBI-BF-C_{12} and EBI-2T

	J_{SC} (mA.cm^{-2})	V_{OC} (V)	FF	PCE (%)
EBI-T	0.15	0.33	0.26	0.01
EBI-BF-C_{12}	0.60	0.51	0.44	0.14
EBI-2T	1.24	0.62	0.41	0.31

4.2. BHJ OSC devices

4.2.1. Phase diagram

To move towards bulk heterojunction (BHJ) OSCs, particular attention was paid first to the compatibility of EBI derivatives with the acceptor $PC_{61}BM$ with the concern of reaching an ideal phase separation. To do so, DSC measurements with three heating and cooling cycles for each sample were conducted on the blend films with various ratios of EBI and $PC_{61}BM$. Those films were prepared by drop-casting chloroform solutions. Figure 96 juxtaposes the first heating curve of every blend ratios for each EBI derivatives. In the case of EBI-T and EBI-2T, the endothermic peaks of EBI and $PC_{61}BM$ converged to a unique temperature: 209°C for EBI-T blend and 246°C for EBI-2T blend. Then, phase diagrams were obtained for both EBI-T and EBI-2T by reporting endothermic peaks over the EBI /$PC_{61}BM$ weight ratios of the blend samples (Figure 97). Both blend systems are typical eutectic phase diagrams. The eutectic compositions and the eutectic temperatures are 55% and 209°C for EBT-T and 50% and 246°C for EBI-2T. These results demonstrate that both EBI-T and EBI-2T are compatible with $PC_{61}BM$. As for the EBI-BF-C_{12}, the endothermic peaks do not clearly converge to a unique temperature but a significant depletion in temperature was still visible. Therefore, it is hard to conclude for EBI-BF-C_{12}: $PC_{61}BM$ system. Concerning EBI-BF-C_{16}:$PC_{61}BM$ system, EBI-BF-C_{16} and $PC_{61}BM$'s endothermic peaks did not converge to a unique temperature and were weakly impacted by the donor:acceptor ratio suggesting that both materials are poorly miscible.

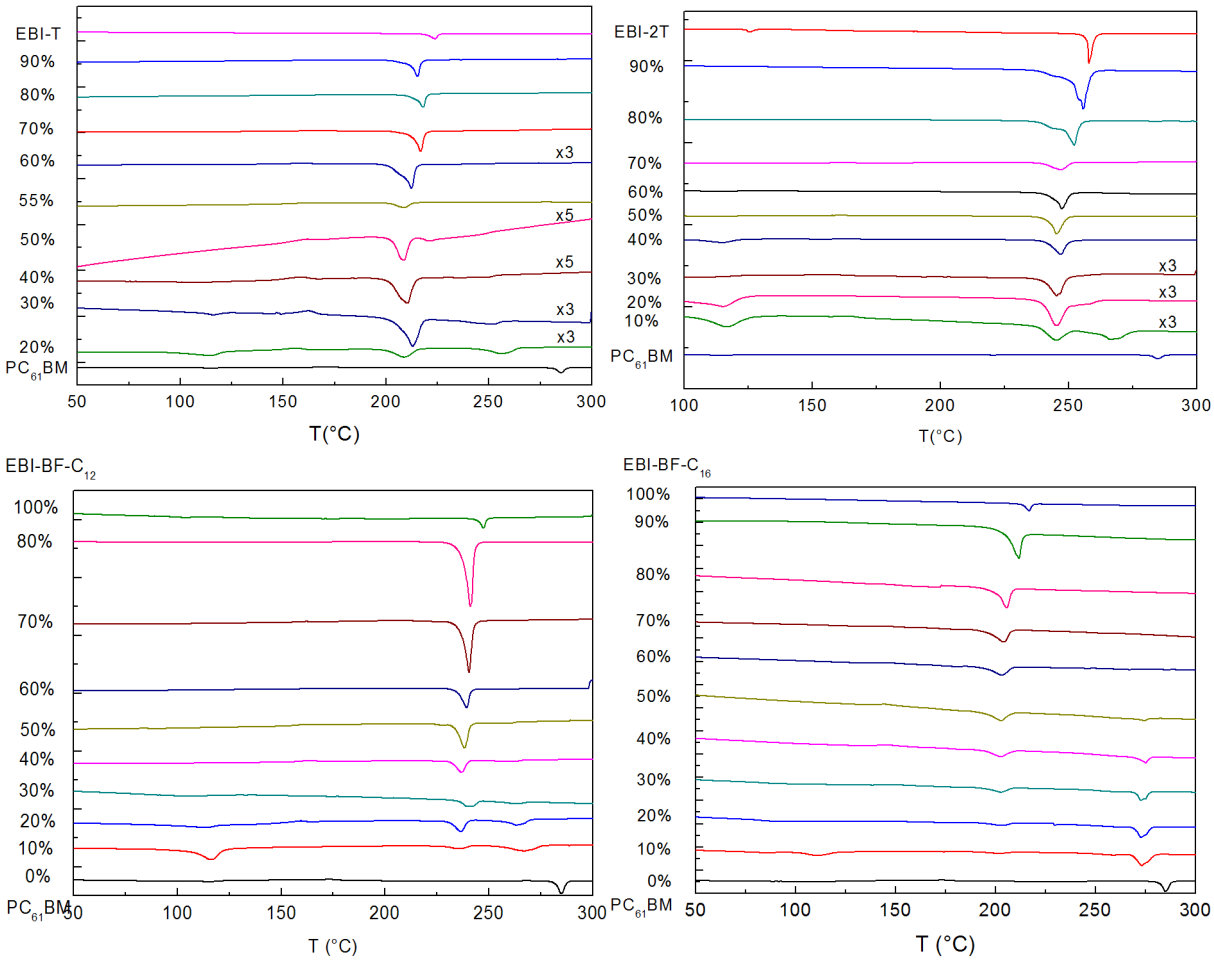

Figure 96: DSC analysis of the EBI derivatives of this work blended with PC_{61BM}

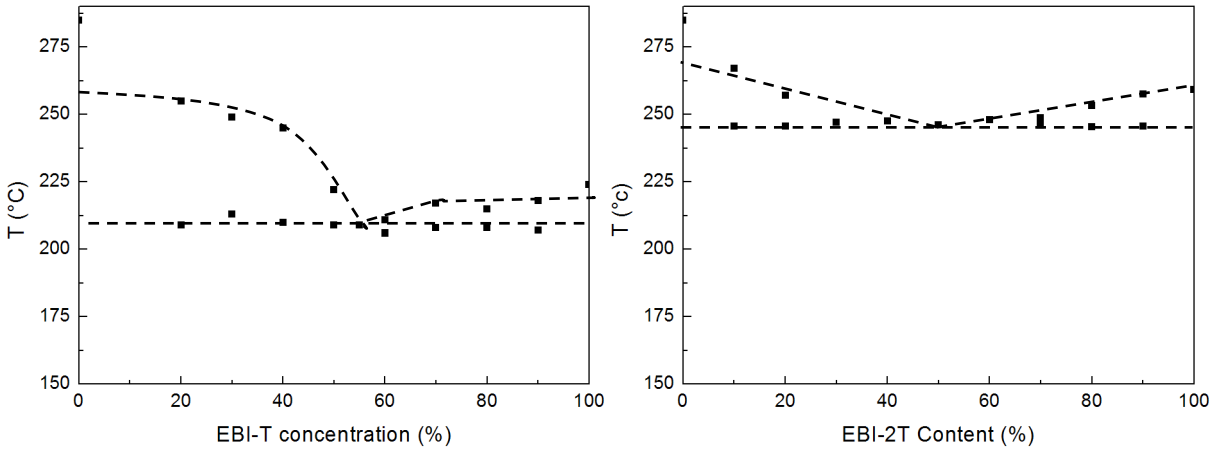

Figure 97: Phase diagrams of EBI-T and EBI-2T

4.2.2. EBI-T in BHJ OSCs

Optimization of active layer's thickness

EBI-T was tested in conventional BHJ using ITO/PEDOT:PSS/EBI:$PC_{61}BM$/Ca/Al architecture. The active layer's thickness was first optimized by varying the ink concentration and the speed deposition. Chloroform was chosen as the host solvent and the donor:acceptor ratio was set at 1:1. Figure 98 displays the PCE of the BHJ OSCs as a function of thickness of the active layer's. A thickness of 120-160 nm provides the highest PCE of 0.12%.

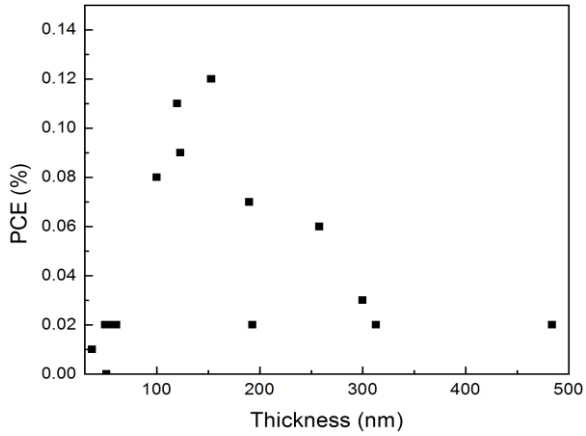

Figure 98: PCE of BHJ OSC_s based on EBI-T : $PC_{61}BM$ system versus the thickness of the active layer

Optimization of donor: acceptor ratio

According to the literature, donor/acceptor systems, showing eutectic feature like EBI-T and EBI-2T, present the most finely intermixing at their eutectic concentration [191,192]. Although this concentration generates the biggest amount of donor / acceptor interfaces desirable for good charge separation, it is rarely the optimal ratio in OSCs. Numerous papers reported that a slight hypoeutectic concentration was necessary as crystals of pure acceptor improve electron transport [192–194]. More balanced hole and electron mobilities were therefore achieved, minimizing charge recombination. Therefore, the donor: acceptor blend ratio was investigated around its eutectic concentration, from 30% to 70% of EBI-T. The EBI/$PC_{61}BM$ ratio mainly affected the J_{SC}. By superposing the J_{SC} trend to the phase diagram (Figure 99a), it reveals that the optimal J_{SC} of EBI-T was achieved in a slight hypoeutectic region (40%) for an efficient trade-off between charge separation and charge transport. The PCE followed the same trend as illustrated in Figure 99b, with a maximum PCE of 0.18%.

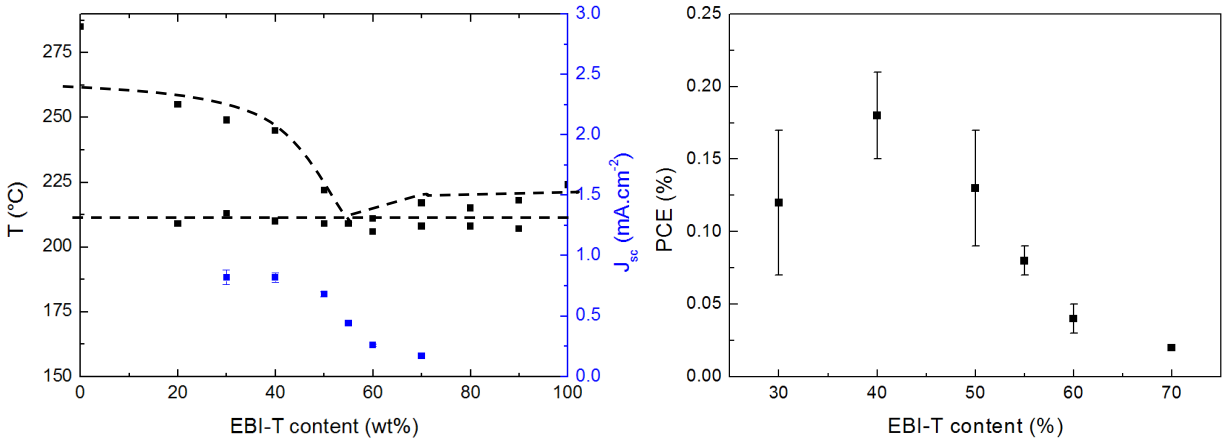

Figure 99: a) J_{SC} of BHJ OSC versus EBI-T content and superposed to EBI-T phase diagram b) PCE versus EBI-T content

In summary, EBI-T presents low PV properties with a maximum PCE of 0.18%. EBI-T's poor charge transport capability may not give enough driving force to CTE to efficiently separate into free charge carrier and thus recombines. The device may also suffer from unfavorable morphology which will be explored in section 4.3.

4.2.3. EBI-2T in BHJ OSCs

Optimization of the donor:acceptor ratio

EBI-2T was tested in conventional BHJ using ITO/PEDOT:PSS/EBI:$PC_{61}BM$/Ca/Al architecture. Following the same argument as EBI-T, the donor: acceptor blend ratio was investigated around EBI-2T eutectic concentration, from 20% to 70% of EBI-2T content. Like in the literature and with EBI-T, the EBI-2T/$PC_{61}BM$ ratio mainly affected the J_{SC}. Figure 100a superposes the J_{SC} onto EBI-2T phase diagram revealing that the optimal J_{SC} was achieved in a slight hypoeutectic region (40%) for an efficient trade-off between charge separation and charge transport. The PCE followed the same trend as illustrated in Figure 100b, with a maximum PCE of 0.8%.

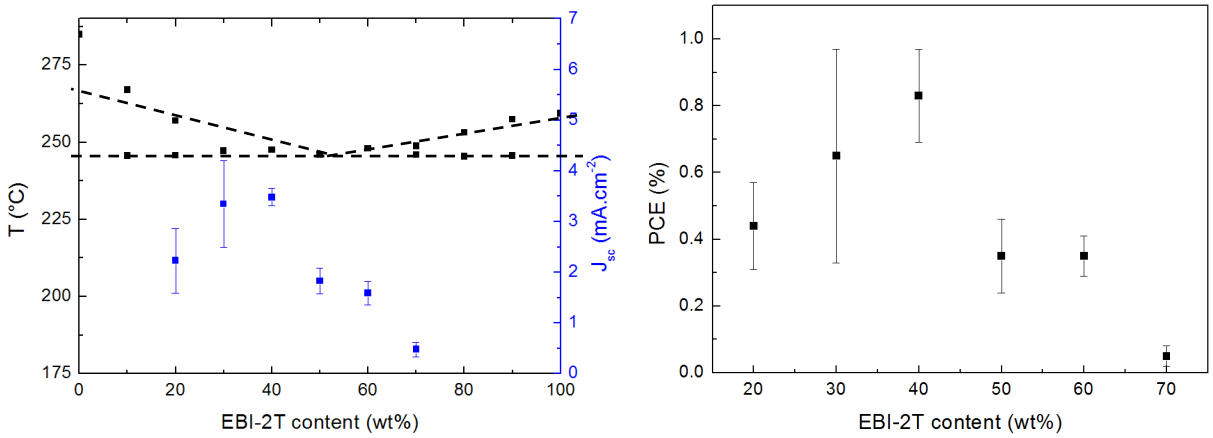

Figure 100: EBI-2T BHJ OSCs, a) J_{SC} versus EBI-2T content superposed to phase diagram b) PCE versus EBI-2T content

Optimization of the thickness of the active layer

The thickness was optimized by varying the speed deposition and the ink concentration but maintaining an EBI-2T: $PC_{61}BM$ ratio of 2:3. Figure 101 depicts the PCE as a function of the thickness and exhibits maximum PCEs around 1.5-1.6 % for a thickness of 80 nm.

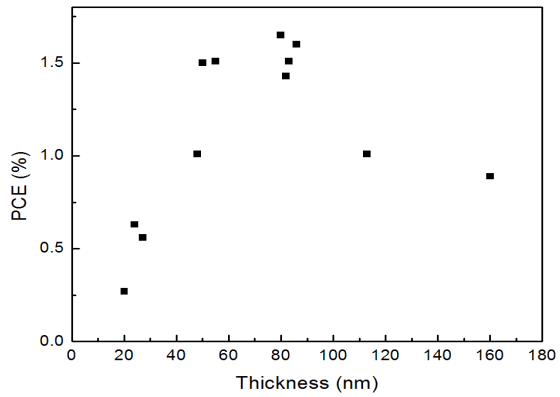

Figure 101: PCE of OSCs based of EBI-2T:$PC_{61}BM$ 2:3 blend versus the thickness of the active layer

As EBI-2T shows promising PV performances, many efforts was attempted to improve EBI-2T based BHJ OSCs. In order to improve the BHJ morphology, several strategies were applied:

- The introduction of solvent additives : DIO and CN
- Thermal treatment
- The introduction of insulating polymer: Polystyrene (PS) and polydimethylsiloxane (PDMS) - used also to improve the film quality and diminish the leakage currents.

However, none of them brought higher PCE.

The highest PCE was achieved with a 2:3 EBI-2T : $PC_{61}BM$ ratio and a thickness of 80 nm. To assess the reproducibility of the devices, the performances of 25 reference cells were compiled. An average PCE of 1.61% +/- 0.16% was obtained along with a J_{SC} of 5.44 +/- 0.36 $mA.cm^{-2}$, a Voc of 0.84 V +/- 0.08 and a FF of 0.36 +/- 0.02. The maximum PCE, achieved with EBI-2T, was 1.92% along with a J_{SC} of 5.25 $mA.cm^{-2}$, a Voc of 0.91 V and a FF of 0.40, its J-V curves is illustrated in Figure 102. A relatively low shunt resistance (R_{SH}) of 13.10 kΩ and a high series resistant (R_S) of 930 Ω were extracted inferring significant leakage currents and limited charge extraction within the devices which decrease the PV performances.

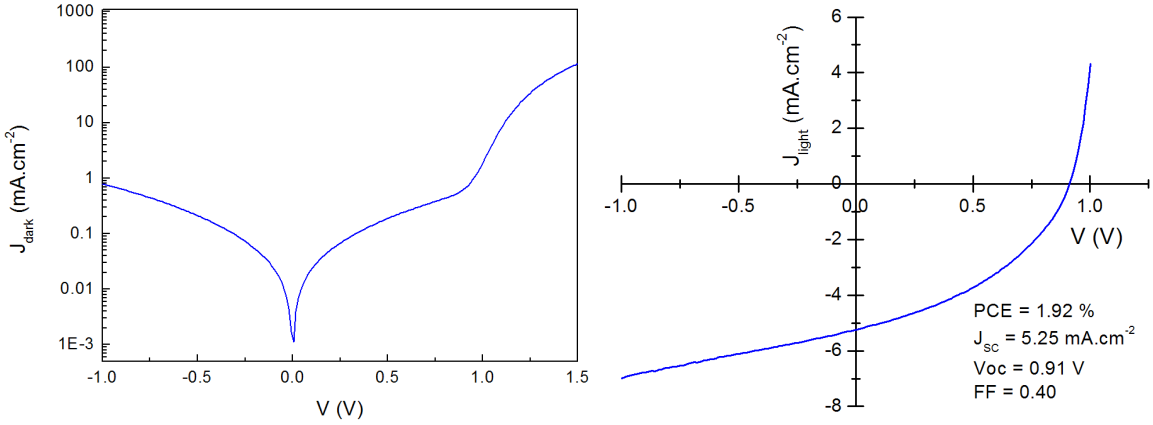

Figure 102: J-V curves in dark (left) and under illumination (right) of the best OSCs based on EBI-2T : $PC_{61}BM$ system

Figure 103 depicts the EQE measured on this best device and the UV-Vis spectra of the corresponding active layer. An EQE of 30%-35% was reached from 350 nm to 680 nm revealing a distinct participation of EBI-2T excitons in the process.

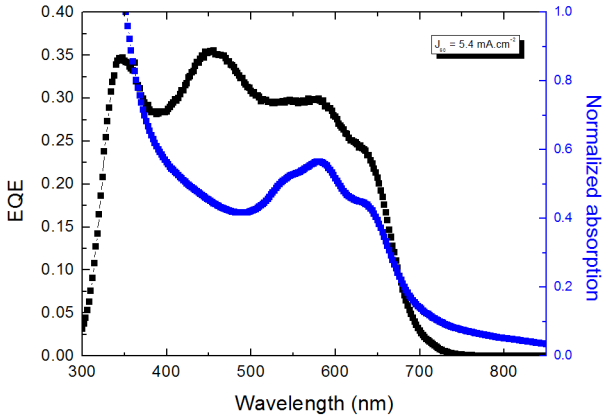

Figure 103: EQE of EBI-2T OSCs devices and UV-Visible absorption spectra of the corresponding films

4.2.4. EBI-BF-C_{16} in BHJ OSCs

Concerning EBI-BF derivatives, due to the low solubility and bad film formation of EBI-BF-C_{12}, only EBI-BF-C_{16} was tested in conventional BHJ OSCs. The thickness of the active layer was varied between 40 nm and 200 nm by varying ink concentration and speed deposition. Chloroform was used as the host solvent and the donor:acceptor ratio was fixed at 1:1. As shown in Figure 104, no clear trend stands out.

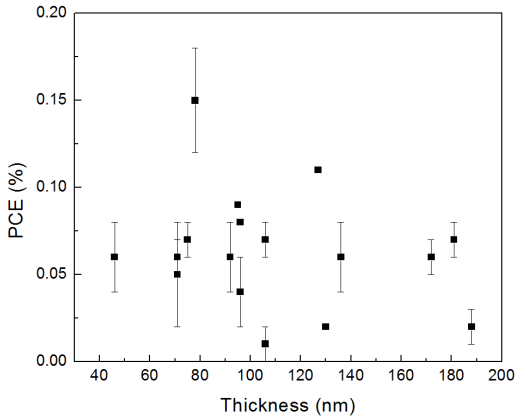

Figure 104: PCE of BHJ OSC based on EBI-BF-C_{16} versus active layer thickness

As EBI-BF-C_{16} did not have a eutectic feature, many donor/acceptor ratios were investigated: 1:3, 1:2, 1:1, 2:1, and 3:1. However no clear trend was observed due to poor OSC performances. The low PCE of BHJ OSCs based on EBI-BF-C_{16} must originate from an undesirable morphology limiting all steps of the photovoltaic process. To tackle this issue, various thermal annealing conditions and solvent additives were tested to improve the EBI-BF-C_{16}:$PC_{61}BM$ morphology but no significant improvement was obtained.

4.2.5. Discussion

EBI-2T exhibits the best PV performances in BHJ OSCs with a maximal PCE of 1.92%. In contrast, EBI-T and EBI-BF-C_{16} show very low PCE inferior to 0.5%. EBI-T is suspected to have a too low charge transport properties preventing charge to well separate in free charges or a bad morphology. For EBI-BF-C_{16}, we suspect an unfavorable morphology that limits the PV process.

4.3. Morphology study

In BHJ OSCs, the performance is highly dependent of the morphology of the active layer which should ideally be composed of three phases: an intermixed donor/acceptor phase, a pure crystalline donor phase and a pure crystalline acceptor phases. The intermixed network

promotes efficient and fast charge separation [31,32,34] whereas pure crystalline domains ensure charge transport to the electrodes [29]**.** Nevertheless, those crystalline domains should be in the range of exciton diffusion length, which is rarely beyond 10 nm for organic semiconductors [18,22]**.** To study the morphology of the different EBI/PCBM systems, AFM and XRD were performed on the active layer of the optimal devices of each material.

4.2.1. EBI-T morphology

AFM was carried out on EBI-T:$PC_{61}BM$ (2:3) blend film prepared similarly to the most efficient OSC based on EBI-T. Figure 105 exhibits the resulting height and phase images. The roughness was evaluated to be inferior to 4 nm which can facilitate a good interface with calcium. The phase images revealed relatively small domains of 50 -100 nm of both EBI-T and $PC_{61}BM$, offering desirable amount of donor/acceptor interfaces for good charge separation.

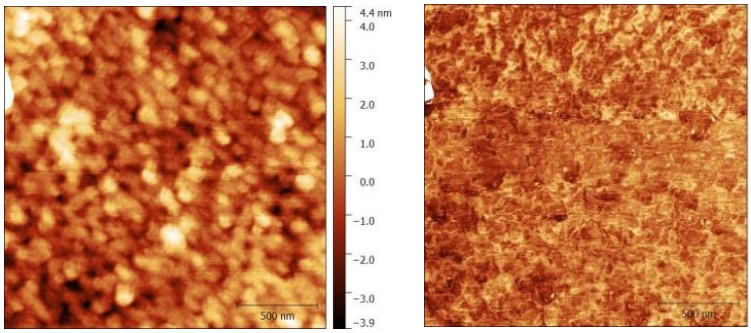

Figure 105: AFM images of EBI-T:$PC_{61}BM$ blend in a ratio 2:3: height (left) and phase (right)

As demonstrated in section 3.4, EBI-T is poorly crystalline suggesting that the pure domains of EBI-T are probably not crystalline. EBI-T : $PC_{61}BM$ system displays here a morphology composed of pure amorphous domains of EBI-T. This amorphous feature of EBI-T appeared to limit its charge carrier transport properties as seen with OTFT measurement. A low hole mobility can hamper an efficient dissociation of charge transfer exciton (CTE) which would rather recombine. The poor PV performances of EBI-T based BHJ OSCs can be ascribed to a too strong competition between CTE separation and CTE recombinations.

4.2.2. EBI-2T morphology

AFM was conducted on EBI-2T:$PC_{61}BM$ (2:3) blend film prepared similarly to the most efficient OSC based on EBI-2T. Figure 106 shows the resulting height and phase images. The film is also very smooth with a roughness inferior to 4 nm. The height images revealed small domains of 50-100 nm, promising for efficient charge separation. On phase images, a fine intermixed phase of both materials is visible along with some pure material domains. According

to the EBI-2T phase diagram, 2:3 EBI-2T:$PC_{61}BM$ ratio is in the hypoeutectic area meaning that the observed pure domains can be ascribed to primary crystals of $PC_{61}BM$. Hence, EBI-2T:$PC_{61}BM$ (2:3) blend film displays a morphology with finely intermixed structure between EBI-2T and $PC_{61}BM$ domains which provide enough donor/acceptor interfaces for good charge separation. Also, larger domains of $PC_{61}BM$ can ensure good electron transport.

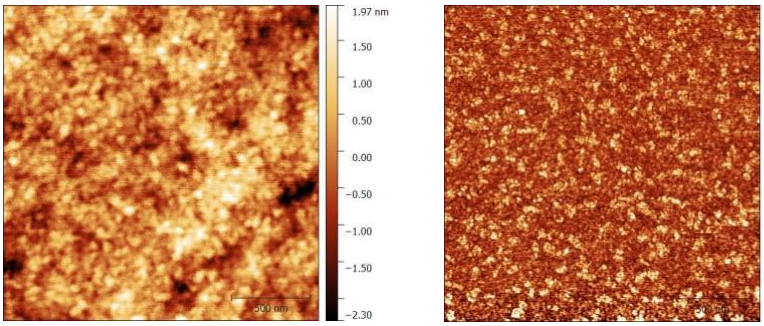

Figure 106: AFM images of EBI-2T:$PC_{61}BM$ blend in a ratio 2:3: height (left) and phase (right)

The morphology of EBI-2T:$PC_{61}BM$ (2:3) blend film was further investigated by XRD. Figure 107 compares the XRD spectra of EBI-2T:$PC_{61}BM$ (2:3) blend film with neat EBI-2T film. The same peak was observed with a d-spacing of 1.6 nm. The crystallite domain sizes of both films were calculated using Scherrer equation to be 39.4 nm for the neat film and 33.8 nm for the blend film. The presence of $PC_{61}BM$ induce a decreased in crystallite size by disturbing the crystallization of EBI-2T. This finding is in agreement with the observation that EBI-2T and $PC_{61}BM$ are miscible to form intermixed domains, but some pure EBI-2T crystalline domains exist.

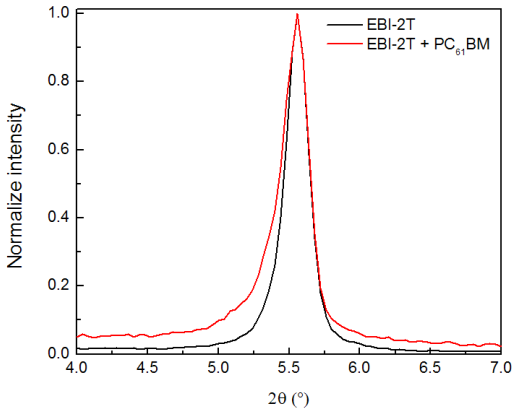

Figure 107: X-ray diffraction spectra of EBI-2T neat film and in blend

To summarize, EBI-2T:$PC_{61}BM$ (2:3) blend displays the three required domains: intermixed domains of EBI-2T:$PC_{61}BM$ and pure crystalline domains of both EBI-2T and $PC_{61}BM$. This optimal morphology justified the good performances of EBI-2T.

4.2.3. EBI-BF-C16 morphology

AFM was performed on EBI-BF-C_{16}: $PC_{61}BM$ (1:1) blend film. Figure 108 shows the resulting height and phase images. The film demonstrates a higher roughness than its predecessors with a roughness of 6.31 nm which is still smooth. In both height and phase images, large domains of 100-300 nm were observed which largely exceed the exciton diffusion length of 10 nm [22,141]. This morphology implies that most generated excitons recombine before reaching any donor/acceptors interfaces. According to phase images, only one material seems to be present on top of the morphology revealing also vertical phase segregation. In case of a $PC_{61}BM$ rich bottom and an EBI-BF-C_{16} rich top, the charge transport would not be efficient in conventional OSCs and would further explain the low PV performances of EBI-BF-C_{16} observed in conventional OSCs.

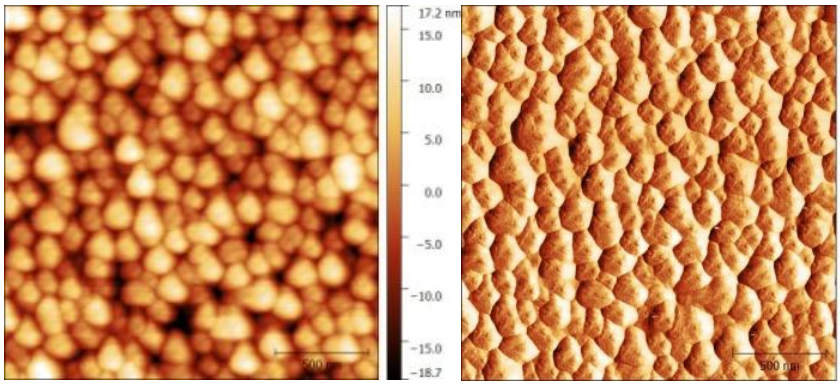

Figure 108: AFM images of blend film of EBI-BF-C_{16}:$PC_{61}BM$ in ratio 1:1: height (left) and phase (right)

The morphology of EBI-BF-C_{16}: $PC_{61}BM$ (1:1) blend was further investigated by XRD. Figure 109 superposes the XRD spectra of neat and blend film of EBI-BF-C_{16}. The blend film show a diffraction peak with a different *d*-spacing of 2 nm versus 2.3 nm in neat film. This change in *d*-spacing can be the result of a closer packing or a different orientation of the crystallite or even a new molecular ordering in presence of $PC_{61}BM$. The crystallite size in neat and blend film can't be compared as they may not correspond to the same packing.

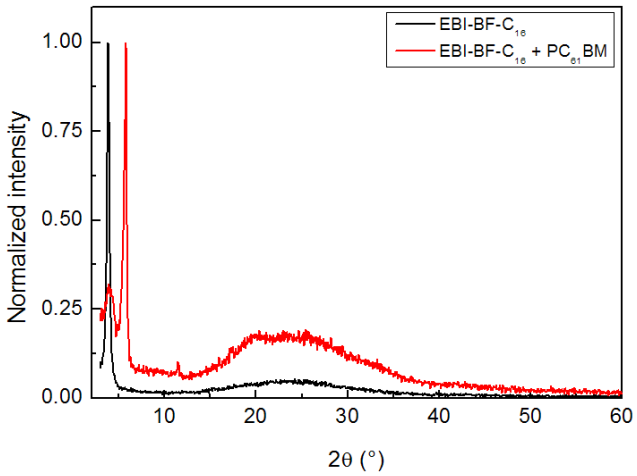

Figure 109: X-ray diffraction spectra of neat and blend film of EBI-BF-C_{16}

To conclude, the morphology of EBI-BF-C_{16}: $PC_{61}BM$ (1:1) blend presents morphology with large crystalline domains of EBI-BF-C_{16} and $PC_{61}BM$ along with a strong vertical segregation both harmful for exciton separation. If the vertical segregation is not in favor of conventional OSCs, the device suffers also from inefficient charge transport. The strong phase segregation is due to the non- miscibility of EBI-BF-C_{16} and $PC_{61}BM$ which crystallized separately without affecting each other crystallization.

4.2.4. Discussion

According to AFM and X-ray diffraction analysis, EBI-2T:$PC_{61}BM$ system displays the best morphology with intermixed donor/acceptor domains and pure crystalline domains of donor and acceptor, consistent with its good OSC performances. Concerning EBI-T:$PC_{61}BM$ system, an interesting phase segregation in small domains was also observed in AFM images however the poor crystallinity of EBI-T limited charge transports, explaining its low performances in OSC devices. According to this study, materials with a eutectic feature demonstrate adequate phase segregation. In contrast with EBI-T and EBI-2T blend, EBI-BF-C_{16}:$PC_{61}BM$ system exhibited large crystalline domains revealing a too strong phase segregation between donor and acceptor, limiting charge separation. This strong phase segregation is caused by the non-miscibility feature of EBI-BF-C_{16} and $PC_{61}BM$ as evidenced by their phase diagram. The planar conformation of EBI-BF-C_{16}, may induce intermolecular interactions that are stronger than that of EBI-BF-C16 with chloroform, therefore EBI-BF-C_{16} rather self-assemble preventing $PC_{61}BM$ to insert among them [148].

4.4. Conclusion

EBI-2T shows the highest PCE of 1.92 % due to good morphology and good light harvesting. This encouraging result validates the use of EBI building blocks to design efficient push-pull

semiconductors for OSCs applications. However, EBI-T and EBI-BF exhibit poor PV performances with a PCE below 0.25%. Even if EBI-T displays an adequate phase separation, the low mobility due to poor molecular packing is likely to give rise to strong bimolecular recombination. It is noteworthy that materials with eutectic feature seem to show good phase segregation for efficient charge separation. EBI-BF based OSCs suffers from unfavorable morphology with large domains of 100-200 nm and vertical phase segregation originating from the non-intermixing of EBI-BF-C_{16} and $PC_{61}BM$. This inappropriate morphology hampers a good exciton separation into free charge carriers.

5. CONCLUSION

In this report, a series of four EBI small molecules, employing the same D-A-D architecture but differing from their electron-rich units, were successfully synthesized and characterized. All EBI derivatives exhibit adequate energy levels to be introduced as donor semiconductors along with $PC_{61}BM$ for use in OSCs as shown in Figure 110. The gaps between their respective LUMO and the LUMO of $PC_{61}BM$ are superior to the theoretical value of 0.3 eV, necessary for efficient charge separation. Meanwhile their deep HOMO levels suggest a high V_{OC} superior to 1 V. As for light harvesting, EBI-2T displays the broadest absorption spectra up to 700 nm while EBI-T displays the narrowest.

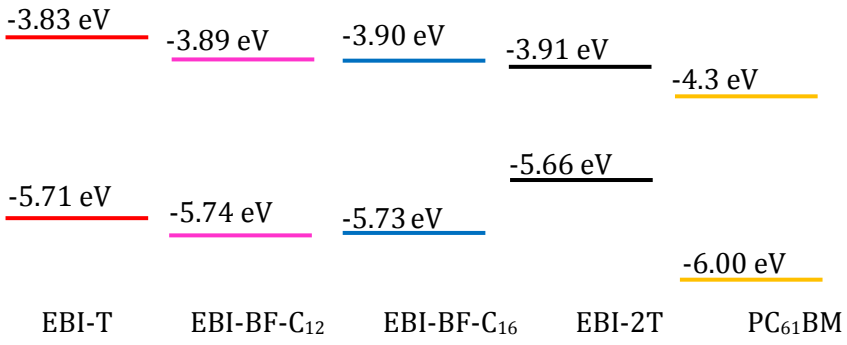

Figure 110: Energy levels scheme of all EBI derivatives along with $PC_{61}BM$

DFT calculations suggest that EBI-BF derivatives have coplanar conformations which are beneficial for high degree of crystallinity and subsequently for the charge transport properties. This is confirmed by the measurement in OTFTs: EBI-BF-C_{12} exhibits 4.35 x 10^{-3} $cm^2.V^{-1}.s^{-1}$ and EBI-BF-C_{16} exhibits 0.021 $cm^2.V^{-1}.s^{-1}$.Those mobilities are much higher than benzofuran-thienoisoindigo and isoindigo small molecules reported in the literature[173,195], confirming the beneficial effect of EBI planarity on charge transport. As EBI-2T also exhibits a hole mobility

around 10^{-3} $cm^2.V^{-1}.s^{-1}$, EBI-2T and EBI-BF materials should promote good FF. In opposition, EBI-T shows poor charge transport feature due to lack of crystallinity.

Among all the materials, EBI-2T demonstrates the highest PCE of 1.9 % when blended with $PC_{61}BM$ in BHJ OSCs. This high PCE is attributed to the broad absorption spectra and the appropriate morphology which is formed with $PC_{61}BM$. The low lying HOMO level of EBI-2T benefits a maximum V_{OC} of 0.9 V which is significantly higher than thienoisoindigo small molecules [53,172–175,196]. Due to its low charge transport properties, EBI-T display very low PV performances. However, like EBI-2T, the morphology of EBI-T is composed of domains of EBI-T and $PC_{61}BM$ in the range of the exciton diffusion length, this can be ascribed to their good miscibility as evidenced by their eutectic feature. Surprisingly, EBI-BF-C_{16} based OSCs yield PCE even lower than EBI-T. Through AFM images, we can identify the formation of large domains and vertical segregation, both limiting the number of donor:acceptor interfaces, which in turn causes the recombination of exciton instead of their separation. This investigation underlines the importance of the phase separation and its major contribution in the PV performance. This strong phase segregation originate from the non –miscibility of EBI-BF-C_{16} and $PC_{61}BM$ caused by the strong self-assemble capability of EBI-BF-C_{16} due to its planar conformation. It is interesting to point out that the molecular backbone has a relevant impact on the miscibility of EBI-BF-C_{16} and $PC_{61}BM$ and consequently the phase segregation.

To conclude, EBI is a promising building block to design novel organic semiconductors for OTFT and OSC applications. A planar conformation enhances the molecular packing and thus the charge transport properties. For OSCs, a material with a eutectic (when blended with PCBM) is preferable as it ensures a good phase segregation between the donor and the acceptor which is a crucial key for high PCE.

CHAPTER 5: CONCLUSION

The goal of this research was to design new solution-processable electron donating semiconductors for OSC applications. To this end, two series of donor semiconductors were engineered: one based on DPP oligomers and the second based on EBI small molecules. For each series, we aimed to establish some structure-properties relationships in order to correlate their PV performances with their structure.

5.1. DPP OLIGOMERS

A first series of three DPP based oligomers was synthesized. All have the specificity to contain three DPP cores to reduce the HOMO level. This series gives some insights into the potential of oligomers compared to small molecules and polymers. From a synthesis point of view, the purification of DPP oligomers was not straightforward as dimer by-products show similar polarity. Despite this challenge, it was still feasible to isolate the desired tri-DPP through hot column chromatography, significantly limiting the batch-to-batch variations usually observed with polymers. Moreover, Tri-DPP displays good film forming capability compared to general small molecules as evidenced by the reduced leakage currents. These observations are in agreement with oligomers acting as a compromise between small molecules and polymers.

For similar DPP oligomers, Nguyen *et al.* demonstrated that linear alkyl chains furnish better PV performances than branched alkyl chains due to better molecular packing [93]. Therefore, we designed and studied a coplanar DPP oligomer, called Tri-BTDPP, to elucidate if a further improvement of the molecular packing would further enhance the PV performances. As shown in chapter 3, Tri-BTDPP does display improved molecular packing. This results in a broader absorption spectrum up to the near infrared region, enhancing light harvesting, and a high hole mobility of 1×10^{-3} $cm^2.V^{-1}.s^{-1}$ for improved charge carrier transport. Despite those promising features, Tri-BTDPP displayed poor PV performances with a maximum PCE of 0.7% in inverted BHJ OSCs.

To understand the origins of the low performances, a careful study of the morphology was conducted which revealed a strong nanophase separation of donor and acceptor. Large domains of Tri-BTDPP were predominantly formed, limiting the amount of donor-acceptor interfaces, which are necessary for efficient charge separation. This result explains the low PV performances of Tri-BTDPP and highlights how an unfavorable morphology can be detrimental to the PV process. By analyzing the phase diagram of the Tri-BTDPP:$PC_{71}BM$ blend, we

demonstrated that the non-miscibility of both semiconductors is responsible for this harmful morphology as both compounds preferentially crystallize separately, rather than intermix.

Knowing the root cause of the inefficiency of Tri-BTDPP:$PC_{71}BM$ based OSCs gives some avenues for new molecular engineering. We suspected that the coplanar conformation of Tri-BTDPP would lead to high crystallinity and thus strong self-assembly which would, in tum, result in poor miscibility with $PC_{71}BM$. To identify if a more twisted conformation is susceptible to reduce the self-assembly tendency and thus improve the molecule's miscibility with $PC_{71}BM$, two other DPP oligomers were subsequently engineered: Tri-DPP-PT with phenyl end-capping and Tri-DPP-PT-C6 with phenyl end-capping and hexyl thiophene spacers. In the case of Tri-DPP-PT, its tendency towards lower degrees of self-assembly compared to Tri-BTDPP was validated by UV-Visible absorption and XRD measurements. This confirms that the curvature of the molecule controls the molecular packing and thus the self-assembly. However, the reduced crystallinity adversely affects the charge transport properties of Tri-DPP-PT compared to Tri-BTDPP, showing a reduced hole mobility of 4.52×10^{-5} $cm^2.V^{-1}.s^{-1}$. Conventional OSCs fabricated with Tri-DPP-PT and $PC_{71}BM$ display similar performances as Tri-BTDPP, except for the $V_{OC,}$ which rises to 0.7 V. Identical nanophase separations were also observed, indicating that Tri-DPP-PT does not have a better miscibility with $PC_{71}BM$. As for Tri-DPP-PT-C6, the introduction of hexyl chains on thiophene spacers induces a variation in crystal orientation confirming that side chains can tune the molecular packing as well. The PV performances were not sensitive to the change in crystal orientation and a similar morphology was observed, meaning that Tri-DPP-PT-C6 is not miscible with $PC_{71}BM$ either. These conclusions suggest that Tri-DPP-PT and Tri-DPP-PT-C6 still have a too planar conformation and consequently too strong tendency to self-assemble, however an even more twisted conformation may annihilate the charge transport properties.

5.2. EBI SMALL MOLECULES

A new class of small molecules with a simple D-A-D structure, based on an EBI electron deficient building block, were successfully synthesized and characterized. These materials demonstrate that EBI is a suitable building block to form semiconductors for application in OTFTs and BHJ OSCs. The planar geometry of EBI favors a desirable molecular packing and thus efficient charge transport, as illustrated with the EBI-2T and EBI-BF derivatives. The highest hole mobility of 0.021 $cm^2.V^{-1}.s^{-1}$ was achieved when EBI was combined with benzofuran end-capping as the whole molecular backbone has a coplanar conformation. These excellent charge transport properties surpass those of small molecules based on thienoisoindigo and isoindigo, emphasizing the potential of EBI derivatives in improving charge transport.

In conventional BHJ OSCs, the EBI-2T: $PC_{61}BM$ system showed the highest performances, with a maximum PCE of 1.92%, owing to the broad absorption spectrum of EBI-2T and the favorable morphology of the blend. The PCE values of EBI-2T-based devices are similar to those of isoindigo small molecules, validating the use of EBI as chromophore for OSC application. As for EBI-T and EBI-BF-C_{16}, their limited performances were caused by poor crystallinity preventing efficient charge transport, and unfavorable morphology limiting charge separation, respectively.

By scrutinizing the morphology and the phase diagram of each EBI:$PC_{61}BM$ blend, we establish that a donor-acceptor system with a eutectic phase diagram displays suitable nanophase separation for good charge separation. In stark contrast, donor-acceptor systems with poor depression of their melting point exhibit a non-miscibility of the donor and acceptor, which in turn result in excessive phase segregation.

5.3. GENERAL CONCLUSION

This thesis establishes some structure-properties relationships via the study of two series of donor materials. In both series, increasing the planar conformation grants better molecular packing and thus improves the charge transport properties of the molecule in OTFTs. Meanwhile, in OSCs, these planar molecules display limited miscibility with PCBM derivatives. This leads to morphologies with large domains of donor and acceptor materials which drastically reduces the PV performances of BHJ OSCs. In contrast, materials with dihedral angles of 20°-25° along their backbone appear to intermix favorably with PCBM and form morphologies with domains sizes in the range of the exciton diffusion length, ideal for efficient charge separation. These conclusions underline the importance of selecting the right donor-acceptor combination to tune not only the energy levels but also the molecular packing and the miscibility of the donor and acceptor materials.

5.4. PERSPECTIVES

This thesis identifies the key role played by the miscibility between donor and acceptor in morphology formation. Our research demonstrates that planar molecules do not show good miscibility with PCBM. The next step would be to identify how to control this miscibility. For instance, the use of solvent additives may change the intermolecular interactions and improve the miscibility. Furthermore, pursuing the testing of different donor spacers could help to determine the intermolecular interactions that prevent the miscibility of the molecules.

Concerning DPP oligomers, Chapter 1 introduces Tri-BTDPP, with its unique absorption spectra up to the near infra-red region. Figure 111-a compares the absorption spectra of P3HT and Tri-BTDPP neat films. The absorption spectra of both materials were found to be complementary and therefore a blend of both compounds results in a broad absorption spectrum from 400 nm to 1000 nm. We believe that ternary BHJ OSCs based on P3HT, Tri-BTDPP and PCBM could be a good avenue to reach a broad light harvesting and efficient PV performances. Furthermore, Figure 111-b illustrates the quenching study performed on P3HT with Tri-BTDPP and $PC_{61}BM$. Tri-BTDPP efficiently quenches P3HT, meaning that electron transfer is possible from P3HT to Tri-BTDPP. These observations suggest that Tri-BTDPP may also be tested as an electron acceptor for BHJ OSCs, along with P3HT. Moreover, regarding their optoelectronic properties, the three DPP oligomers could be embedded in photodetectors.

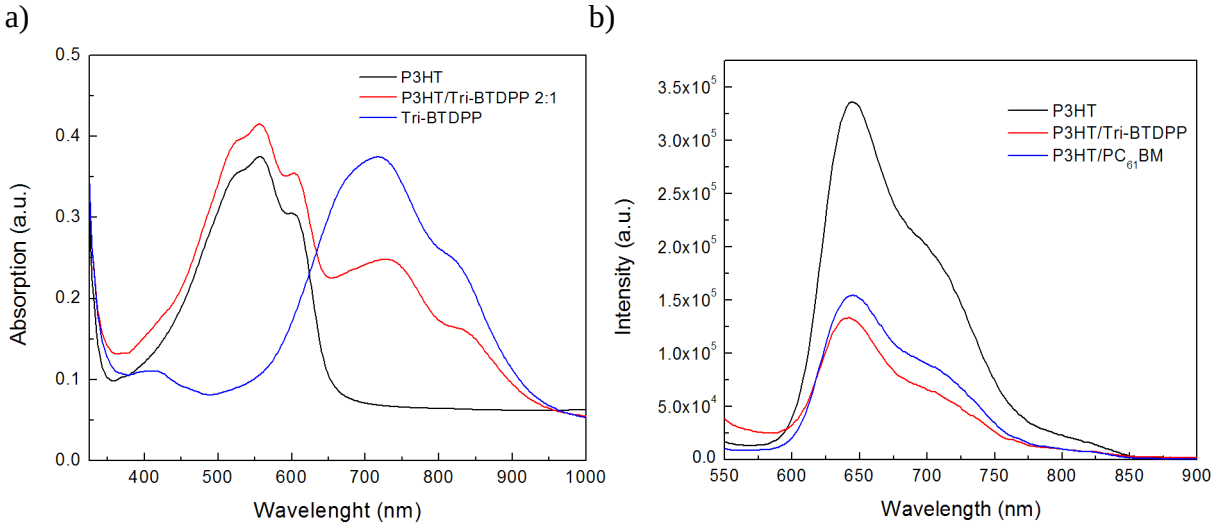

Figure 111: a) Absorption and b) photoluminescence spectra of a P3HT neat film, and a P3HT blend film with Tri-BTDPP and $PC_{61}BM$

Regarding EBI small molecules, EBI-2T exhibits an encouraging PCE of 2% in conventional BHJ OSCs without any special treatment. Compared to small molecule-based devices found in the literature, the J_{SC} and FF of EBI-2T-based OSCs are relatively low. With an optimized molecular design, both PV parameters can be enhanced. To raise the J_{SC}, EBI can, for instance, be combined with an extended π-conjugated electron-rich building block such as BDT and DTS to broaden the molecule's absorption spectrum and thus the light harvesting. Moreover, BDT and DTS are also known to provide efficient charge transport, which is good for a high FF.

APPENDICES

APPENDIX 1: LIST OF PUBLICATIONS USED FOR DPP REPORTS

- ✓ Ying Liua, Xiaoyan Du, Zuo Xiao, Jiamin Cao, Songting Tan, and Qiqun Zuo. Liming Ding, Solution processable low bandgap small molecule donors with naphthalene end-groups for organic solar cells. *Synthetic Metals,* **2012**, 162, 1665-1671
- ✓ Olivia P. Lee, Alan T. Yiu, Pierre M. Beaujuge, Claire H. Woo, Thomas W. Holcombe, Jill E. Millstone, Jessica D. Douglas, Mark S. Chen, and Jean M. J. Fréchet. Efficient small molecule bulk heterojunction solar cells with high fill factors via pyrene-directed molecular self-assembly. *Advanced materials*, **2011**, 23, 5359-5363
- ✓ Bright Walker, Arnold B. Tamayo, Xuan-Dung Dang, Peter Zalar, Jung Hwa Seo, Andres Garcia, Mananya Tantiwiwat, and Thuc-Quyen Nguyen. Nanoscale Phase Separation and High Photovoltaic Efficiency in Solution-Processed, Small-Molecule Bulk Heterojunction Solar Cells. *Advanced Functional Materials*, **2009**, 19, 3063-3069
- ✓ G. D. Sharma, M. Anil Reddy, K. Ganesh, Surya Prakash Singh, and M. Chandrasekharam. Indole and triisopropyl phenyl as capping units for a diketopyrrolopyrrole (DPP) acceptor central unit: an efficient D–A–D type small molecule for organic solar cells. *RSC Adv.,* **2014**, 4, 732-742
- ✓ Huitao Bai, Pei Cheng, Yifan Wang, Lanchao Ma, Yongfang Li, Daoben Zhu, and Xiaowei Zhan. A bipolar small molecule based on indacenodithiophene and diketopyrrolopyrrole for solution processed organic solar cells. *J. Mater. Chem. A*, **2014**, 2, 778-784
- ✓ Changyan Ji, Lunxiang Yin, Lihui Wang, Tao Jia, Shixiang Meng, Yingji Sun, and Yanqin Li. Linkage effects of linear D–π–A–π–D type diketopyrrolopyrrole-triphenylamine based solution-processable organic small molecule photovoltaic materials. *J. Mater. Chem. C*, **2014**, 2, 4019-4026
- ✓ Shifan Wang, Jie Yang, Zhiguo Zhang, Yuanyuan Hu, Xudong Cao, Hai Li, Youtian Tao, Yongfang Li, and Wei Huang. A new V-shaped triphenylamine/diketopyrrolopyrrole containing donor material for small molecule organic solar cells. *RSC Adv.,* **2015**, 5, 68192-68199
- ✓ Thomas Bura, Nicolas Leclerc, Rony Bechara, Patrick Lévêque, Thomas Heiser, and Raymond Ziessel. Triazatruxene-diketopyrrolopyrrole dumbbell-shaped molecules as photoactive electron donor for high-efficiency solution processed organic solar cells. *Advanced Energy Materials,* **2013**, 9, 1118-1124.
- ✓ C. H. Pavan Kumar, K. Ganesh, T. Suresh, Abhishek Sharma, K. Bhanuprakash, G. D. Sharma, and Malapaka Chandrasekharam. Influence of thermal and solvent annealing on the morphology and photovoltaic performance of solution processed, D–A–D type small molecule-based bulk heterojunction solar cells. *RSC Adv.,* **2015**, 5, 93579-93590

- ✓ K. Narayanaswamy, A. Venkateswararao, Vinay Gupta, Suresh Chand and Surya Prakash Singh. NIR absorbing D–π–A–π–D structured diketopyrrolopyrrole–dithiafulvalene based small molecule for solution processed organic solar cells. *Chem. Commun*., **2016**, 52, 210-213
- ✓ Chenmin Yu, Zitong Liu, Yang Yang, Jingjing Yao, Zhengxu Cai, Hewei Luo, Guanxin Zhang and Deqing Zhang. New dithienyl-diketopyrrolopyrrole-based conjugated molecules entailing electron withdrawing moieties for organic ambipolar semiconductors and photovoltaic materials. *J. Mater. Chem. C*, **2014**, 2, 10101-10109
- ✓ Ji-Hoon Kim, Jong Baek Park, Hoichang Yang, In Hwan Jung, Sung Cheol Yoon, Dongwook Kim, and Do-Hoon Hwang. Controlling the Morphology of BDTT-DPP-based Small Molecules via End-group Functionalization for Highly Efficient Single and Tandem Organic Photovoltaic Cells. *ACS Applied Materials & Interfaces,* **2015**, 7, 23866−23875
- ✓ Xiongwei Duan, Manjun Xiao, Jianhua Chen, Xiangdong Wang, Wenhong Peng, Linrui Duan, Hua Tan, Gangtie Lei, Renqiang Yang, and Weiguo Zhu. A*CS Appl. Mater. Interfaces*, **2015**, 7, 18292−18299
- ✓ Jae Woong Jung, Thomas P. Russell, and Won Ho Jo. A Small Molecule Composed of Dithienopyran and Diketo-pyrrolopyrrole as Versatile Electron Donor Compatible with Both Fullerene and Non-fullerene Electron Acceptors. *Chem. Mater.,* **2015**, 27, 4865−4870
- ✓ Nanjia Zhou, Sureshraju Vegiraju, Xinge Yu, Eric F. Manley, Melanie R. Butler, Matthew J. Leonardi, Peijun Guo, Wei Zhao, Yan Hu, Kumaresan Prabakaran, Robert P. H. Chang, Mark A. Ratner, Lin X. Chen, Antonio Facchetti, Ming-Chou Chen, and Tobin J. Marks. Diketopyrrolopyrrole (DPP) functionalized tetrathienothiophene (TTA) small molecules for organic thin film transistors and photovoltaic cells. *J. Mater. Chem. C*, **2015**, 3, 8932-8941
- ✓ Deping Qian, Bo Liu, Suhao Wang, Scott Himmelberger, Mathieu Linares, Mikhail Vagin, Christian Müller, Zaifei Ma, Simone Fabiano, Magnus Berggren, Alberto Salleo, Olle Inganäs, Yingping Zouf and Fengling Zhang. Modulating Molecular Aggregation by Facile Heteroatom Substitution of Diketopyrrolopyrrole based Small Molecules for Efficient Organic Solar Cells. *J. Mater. Chem. A*, **2015**, 3, 24349-24357
- ✓ Qing-Ru Yin, Jing-Sheng Miao, Zhuo Wu, Zheng-Feng Chang, Jin-Liang Wang, Hong-Bin Wu and Yong Cao. Rational design of diketopyrrolopyrrole-based oligomers for high performance small molecular photovoltaic materials via an extended framework and multiple fluorine substitution. *J. Mater. Chem. A*, **2015**, 3, 11575-11586
- ✓ Bing Chen, Yang Yang, Pei Cheng, Xingguo Chen, Xiaowei Zhan and Jingui Qina. Designing a thiophene-fused DPP unit to build an A–D–A molecule for solution-processed solar cells. *J. Mater. Chem. A* , **2015**, 3, 6894-6900
- ✓ Yoon Suk Choi, and Won Ho Jo. A strategy to enhance both VOC and JSC of A–D–A type small molecules based on diketopyrrolopyrrole for high efficient organic solar cells. *Organic Electronics,* **2013,** 14, 1621–1628
- ✓ Tobias Harschneck, Nanjia Zhou, Eric F. Manley, Sylvia J. Lou, Xinge Yu, Melanie R. Butler, Amod Timalsina, Riccardo Turrisi, Mark A. Ratner, Lin X. Chen, Robert P. H. Chang, Antonio Facchetti and Tobin J. Marks. Substantial photovoltaic response and morphology tuning in benzo[1,2-b:6,5-b']dithiophene (bBDT) molecular donors. *Chem. Commun.,* **2014**, 50, 4099-4101

- ✓ Yu-Ying Lai, Jyun-Ming Yeh, Che-En Tsai, and Yen-Ju Cheng. Synthesis, Molecular and Photovoltaic Properties of an Indolo[3,2- b]indole-Based Acceptor-Donor-Acceptor Small Molecule. *Eur. J. Org. Chem*., **2013**, 5076–5084
- ✓ Jong Won Lee , Yoon Suk Choi, Won Ho Jo. Diketopyrrolopyrrole-based small molecules with simple structure for high VOC organic photovoltaics. *Organic Electronics*, **2012,** 13, 3060–3066
- ✓ Xu Lin, Yuki Tani, Ryo Kanda, Ken-ichi Nakayama and Shiki Yagai. Indolocarbazoles end-capped with diketopyrrolopyrroles: impact of regioisomerism on the solid-state properties and the performance of solution-processed bulk heterojunction solar cells. J*. Mater. Chem. A*, **2013**, 1, 14686-14691
- ✓ Stephen Loser, Carson J. Bruns, Hiroyuki Miyauchi, Rocío Ponce Ortiz, Antonio Facchetti, Samuel I. Stupp, and Tobin J. Marks. A naphthodithiophene-diketopyrrolopyrrole donor molecule for efficient solution-processed solar cells. *J. Am. Chem. Soc.,* **2011**, 133, 8142–8145
- ✓ Bright Walker, Jianhua Liu,a Chunki Kim, Gregory C. Welch, Jin Keun Park, Jason Lin, Peter Zalar, ChristopherM. Proctor, Jung Hwa Seo, Guillermo C. Bazana and Thuc-Quyen Nguyen. Optimization of energy levels by molecular design: evaluation of bis-diketopyrrolopyrrole molecular donor materials for bulk heterojunction solar cells. *Energy Environ. Sci.,* **2013**, 6, 952-962
- ✓ Ling Zhang, Shaohang Zeng, Lunxiang Yin, Changyan Ji, Kechang Li, Yanqin Li, and Yue Wang. The synthesis and photovoltaic properties of A–D–A-type small molecules containing diketopyrrolopyrrole terminal units. *NewJ.Chem.,* **2013**, 37, 632-639
- ✓ Ailing Tang, Liangjie Li, Zhenhuan Lu, Jianhua Huang, Hui Jia, Chuanlang Zhan, Zhan'ao Tan, Yongfang Li and Jiannian Yao. Significant improvement of photovoltaic performance by embedding thiophene in solution-processed star-shaped TPA-DPP backbone. *J. Mater. Chem. A*, **2013**, 1, 5747-5757
- ✓ Qing-Cai Yu, Wei-Fei Fu, Jun-Hua Wan, Xiao-Feng Wu, Min-Min Shi, and Hong-Zheng Chen. Evaluation of heterocycle-modified pentathiophene-based molecular donor materials for solar cells. *ACS Appl. Mater. Interfaces*, **2014**, 6, 5798–5809
- ✓ Youming Zhang, Manjun Xiao, Ning Su, Juan Zhong, Hua Tan, Yafei Wang, Yu Liu, Yong Pei, Renqiang Yangb, and Weiguo Zhu. Efficient strategies to improve photovoltaic performance of linear-shape molecules by introducing large planar aryls in molecular center and terminals. *Organic Electronics,* **2015**, 17, 198–207
- ✓ Shi-Xin Sun, Yong Huo, Miao-Miao Li, Xiaowen Hu, Hai-Jun Zhang, You-Wen Zhang, You- Dan Zhang, Xiao-Long Chen, Zi-Fa Shi, Xiong Gong, Yongsheng Chen, and Hao-Li Zhang. Towards Understanding the Halogenation Effects in Diketopyrrolopyrrole-Based Small Molecule Photovoltaics. *ACS Applied Materials & Interfaces,* **2015**, 7, 19914-19922
- ✓ Tianxiang Liang, Liangang Xiao, Chang Liu, Ke Gao, Hongmei Qin, Yong Cao, and Xiaobin Peng. Porphyrin small molecules containing furan- and selenophene-substituted diketopyrrolopyrrole for bulk heterojunction organic solar cells. *Organic Electronics*, **2016**, 29, 127-134

- ✓ Hongmei Qin, Lisheng Li, Fangqing Guo, Shijian Su, Junbiao Peng, Yong Cao, and Xiaobin Peng. Solution-processed bulk heterojunction solar cells based on a porphyrin small molecule with 7% power conversion efficiency. *Energy Environ. Sci.,* **2014**, 7, 1397-1401
- ✓ Jianhua Liu , Yanming Sun , Preecha Moonsin , Martijn Kuik , Christopher M. Proctor , Jason Lin , Ben B. Hsu , Vinich Promarak , Alan J. Heeger , and Thuc-Quyen Nguyen. Tri - Diketopyrrolopyrrole Molecular Donor Materials for High-Performance Solution-Processed Bulk Heterojunction Solar Cells. *Adv. Mater.*, **2013**, 25, 5898–5903

APPENDIX 2: SYNTHESIS OF DPP DERIVATIVES

2,5-bis(2-ethylhexyl)-3,6-dithiophen-2-yl)pyrrolo[3,4-*c*]pyrrole-1,4-dione [197]**:**

In a 100 ml dry three-necked round bottom flask, 3,6-di(thiophen-2-yl)-2,5-dihydropyrrolo[3,4-c]pyrrole-1,4-dione (6 g, 0.02 mol, 1 eq) and potassium carbonate (9.12 g, 0.066 mol, 3.3 eq) were introduced. The system was purged under argon. 200 ml of DMF were added. The solution was heated at 120°C for 1 hour. 2-ethylhexyl bromide (11.59 g, 0.06 mol, 3 eq) was added. The mixture was heated at 140°C overnight. The solution was cooled down to room temperature. The solution was poured onto 500 ml of water. After stirring for 1 hour, the solid was filtrated and washed several times with methanol. The crude was further purified by silica gel chromatography (eluent: Hexane/DCM 20/80). The product was crystallized in isopropanol. A dark red solid was obtained (4 g, 38 %).

^{1}H NMR(300 MHz,$CDCl_3$) δ 8.89 (d, J= 3.3 Hz, 2H), 7.63 (d, J=3.6 Hz, 2H), 7.27 (d, J=3.6 Hz,2H), 4.03 (dd, J=7.3 Hz, 3.2 Hz, 4H), 1.86 (s,2H), 1.43-1.17 (m, 16H), 1.08-0.70 (m, 12H)

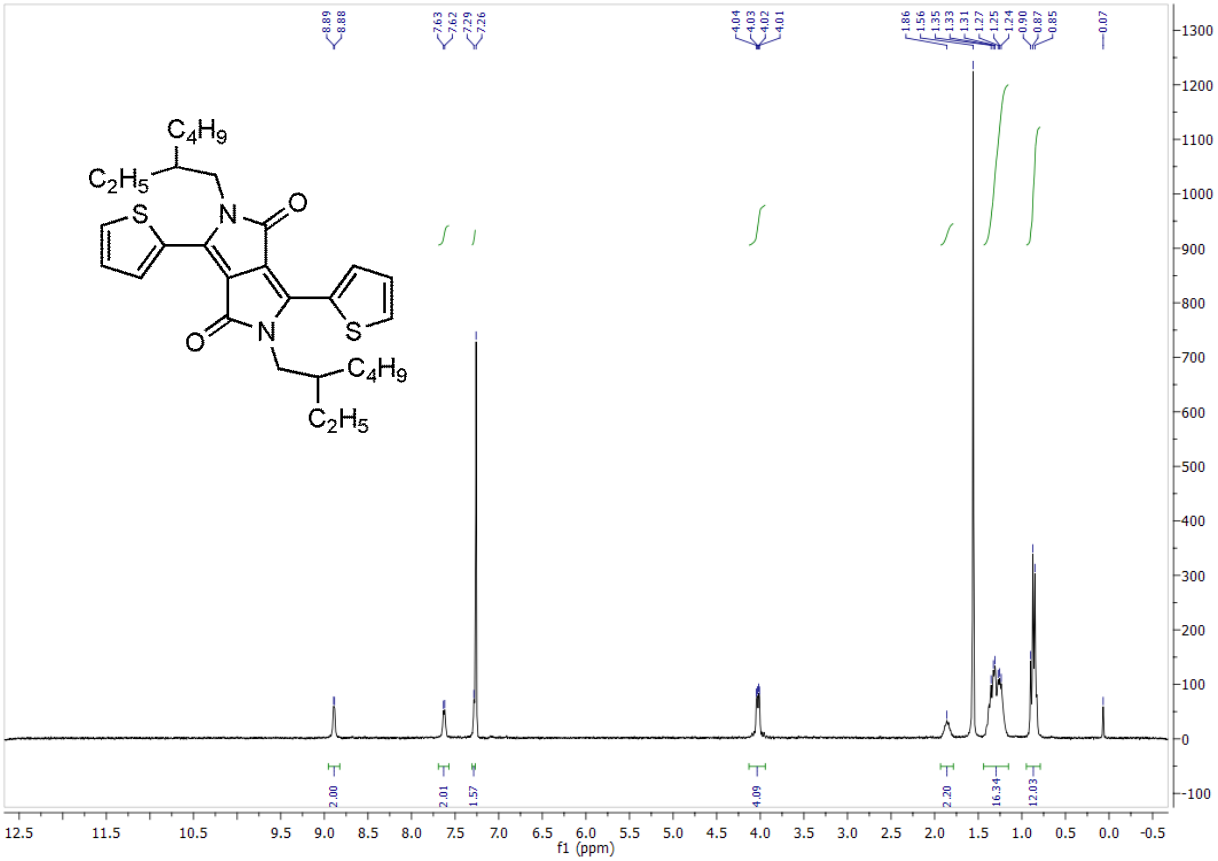

3-(5-bromothiophen-2-yl)-2,5-bis(2-ethylhexyl)-6-(thiophen-2-yl)pyrrolo[3,4-c]pyrrole-1,4(2H,5H)-dione (1) [197]**:**

At 5°C and under light exclusion, to a solution of 2,5-bis(2-ethylhexyl)-3,6-dithiophen-2-yl)pyrrolo[3,4-*c*]pyrrole-1,4-dione (2 g, 3.8 mmol, 1 eq) in 50 ml of chloroform, N-bromosuccinimide (0.68 g, 3.8 mmol, 1 eq) in few portions. The mixture was stirred at room temperature overnight. The product was extracted with chloroform and washed with brine three times. The organic phase was dried with sodium sulfate and the solvent was evaporated under vacuum. The crude was further purified by silica gel chromatography column (Hexane/AcOEt 96/4). 1.01 g of product were obtained (44 %).

^{1}H NMR(300 MHz,$CDCl_3$) δ 8.90 (d, J = 3.3 Hz, 1H), 8.63 (d, J=4.2 HZ, 1H), 7.64 (d, J=4.1 Hz, 1H), 7.28 (d, J=5.1 Hz, 1H), 7.22 (d, J= 4.2 Hz, 1H), 4.02 (dd, J=7.7 Hz, 3.8 Hz, 2H), 3.94 (dd, J= 7.8 Hz, 3.8 Hz, 2H), 1.84 (s, 2H), 1.47-1.14 (m, 17 H), 1.07-0.66 (m, 12H)

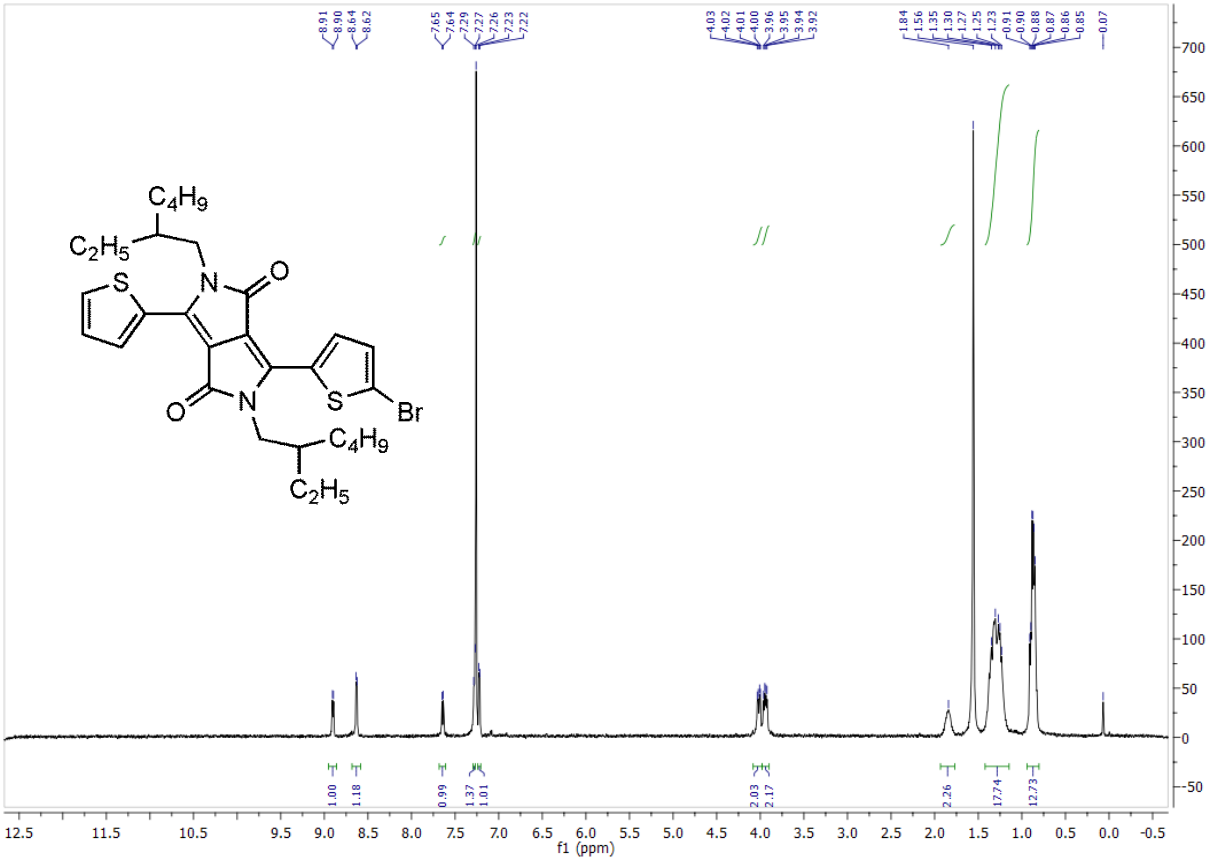

2,5-bis (2-octyldodecyl)-3,6-di(thiophene-2-yl)-2,5-dihydropyrrolo[3,4-c]pyrrole-1,4-dione:

In a 100 ml dry three-necked round bottom flask, 3,6-di(thiophen-2-yl)-2,5-dihydropyrrolo[3,4-c]pyrrole-1,4-dione (1.5 g, 0.005 mol, 1 eq) and potassium carbonate (2.1 g, 0.015 mol, 3 eq) were introduced. The system was purged under argon. 60 ml of DMF were added. The solution was heated at 120°C for 1 hour. 2-octyldodecyliodide (5.1 g, 0.013 mol, 2.5 eq) was added. The mixture was heated at 140°C overnight. The solution was cooled down to room temperature. The solution was poured onto 500 ml of water. After stirring for 1 hour, the solid was filtrated and washed several times with methanol. The crude was further purified by silica gel chromatography (eluent: Hexane/DCM 20/80). The product was crystallized in isopropanol. A dark red solid was obtained (1.53 g, 35.5 %).

^{1}H NMR(300 MHz,$CDCl_3$) δ 8.87 (d, J = 3.6 Hz, 2H), 7.62 (d, J = 3.6 Hz, 2H), 7.28 (m, 2H), 4.03-4.00 (m, 4H), 1.90 (m, 2H), 1.40-1.15 (m, 64H), 0.87-0.86 (m, 12H)

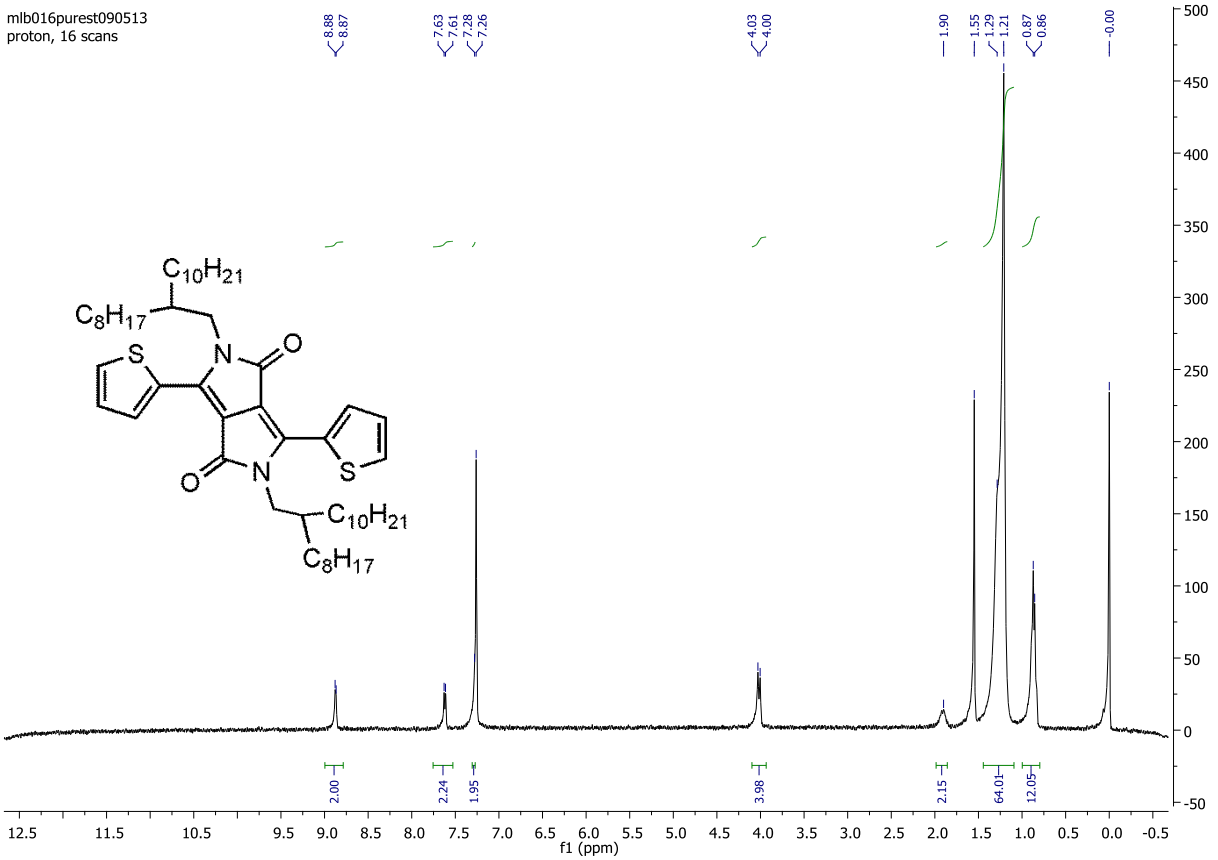

2,5-bis(2-octyldodecyl)-3,6-bis(5-(trimethylstannyl)thiophen-2-yl)-2,5-dihydropyrrolo[3,4-c]pyrrole-1,4-dione (2) [131]**:**

2,5-bis(2-octyldodecyl)-3,6-di(thiophene-2-yl)-2,5-dihydropyrrolo[3,4-c]pyrrole-1,4-dione (2 g, 0.023 mol, 1eq) was dissolved in 70 ml of anhydrous THF under argon protection. The solution was cooled down to -78°C and 1.8 of LDA solution (2M in hexane) was added dropwise. The mixture was stirred at this temperature for one hour and allowed to warm to -20°C- 0°C at which point was stirred an additional hour. The solution was cooled to -78°C and trimethyltin chloride (8 ml, 0.008 mol, 3.5 eq) was rapidly added. The mixture was allowed to warm to room temperature and was stirred overnight. 60 ml of cold water was added and the product was extracted with DCM. The organic phase was washed several times with water before being dried with sodium sulfate. The solvent was evaporated. The product was washed with methanol to obtain a sticky dark purple solid.

^{1}H NMR(300 MHz,$CDCl_3$) δ 8.98 (d, J = 2.4 Hz,2 H), 7.32 (d, J = 2.5 Hz, 2 H), 4.05-4.03 (d, J = 7.5 Hz, 4 H), 1.91 (s, 2 H), 1.45-1.20 (m, 64 H), 0.99 – 0.73 (m, 12 H), 0.56-0.24 (m, 18 H)

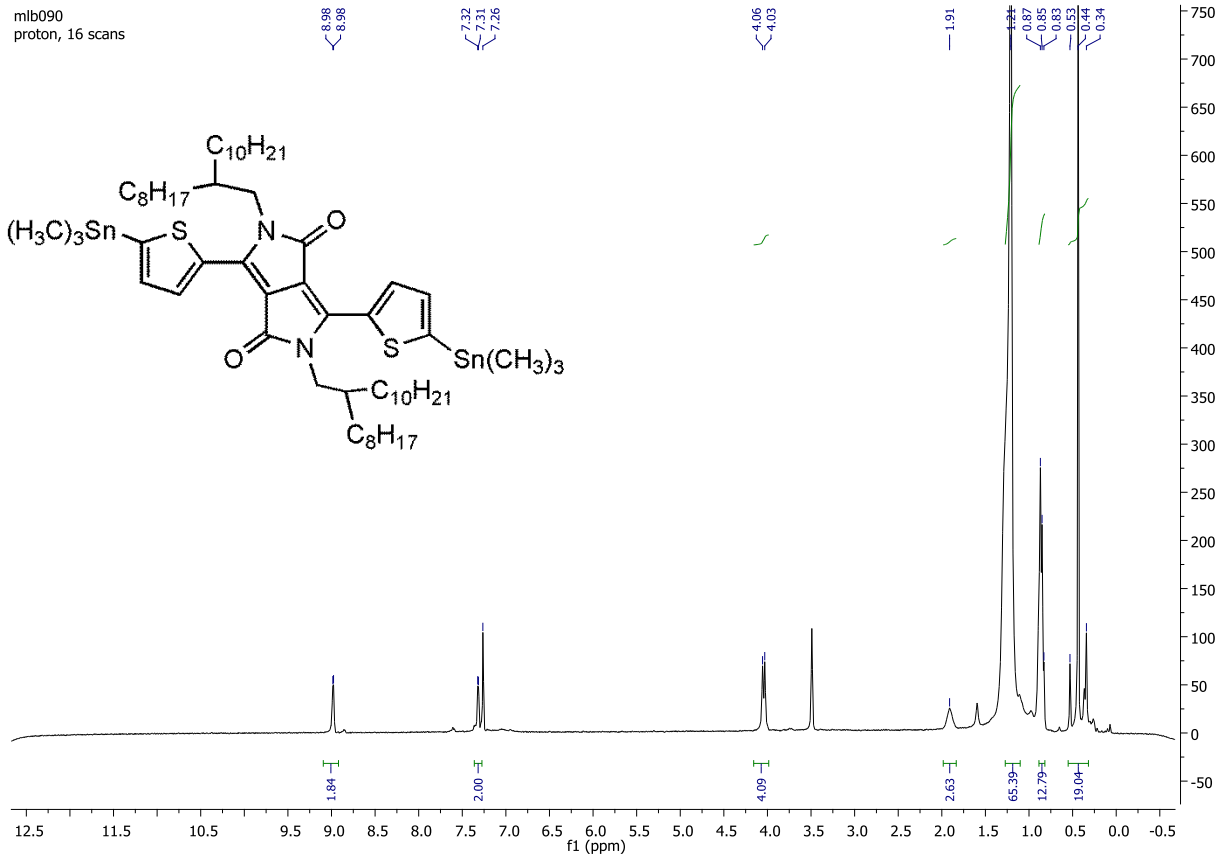

6,6'-((2,5-Bis(2-octyldodecyl)-3,6-dioxo-2,3,5,6-tetrahydropyrrolo[3,4-c]pyrrole-1,4-diyl)bis([2,2'-bisthiophene]-5',5-diyl))bis(2,5-bis(2-ethylhexyl)-3-(thiophen-2-yl)-2,5-dihydropyrrolo[3,4-c]pyrrole-1,4-dione) (Tri-BTDPP).

A 100 mL dry three-necked round bottom flask was charged with compound 1 (1.5 g, 0.0025 mol, 2.1 eq), compound 2 (1.40 g, 0.0012 mol, 1 eq), P(o-tolyl)$_3$ (28.7 mg, 0.09 mmol, 0.08 eq) and anhydrous toluene (49 mL) under argon. Then, $Pd_2(dba)_3$ (21.9 mg, 0.024 mmol, 0.02 eq) dissolved in anhydrous toluene (1 mL) was added into the flask through a syringe. The mixture was heated at 120 °C for 60 h during which the color of the solution turned from purple to blue. After cooling down to room temperature, the solution was poured into methanol (600 mL) and stirred for 30 min. The resulting precipitate was filtered and purified using column chromatography on silica gel with a mixture of dichloromethane (DCM) and hexane (with a volume ratio of 6:4) and then pure chloroform as eluent to afford 1.65 g (72%) of the crude product and 0.60 g (26%) of 6,6'-([2,2'-bithiophene]-5,5'-diyl)bis(2,5-bis(2-ethylhexyl)-3-(thiophen-2-yl)-2,5-dihydropyrrolo[3,4-c]pyrrole-1,4-dione) (**3**), a by-product formed by the mono-coupling of compound 1 and 2. The crude product obtained by the first column separation contains the target Tri-BTDPP and the by-product 3-(5'-(2,5-bis(2-ethylhexyl)-3,6-dioxo-4-(thiophen-2-yl)-2,3,5,6-tetrahydropyrrolo[3,4-c]pyrrol-1-yl)-[2,2'-bithiophen]-5-yl)-2,5-bis(2-octyldodecyl)-6-(thiophen-2-yl)-2,5-dihydropyrrolo[3,4-c]pyrrole-1,4-dione (**4**), formed by the homo-coupling of 1. 0.50 g of this crude product was further purified on silica gel column

chromatography at 50 °C using a mixture of chloroform/toluene (volume ratio: 1/1) as eluent to afford 0.39 g pure Tri-BTDPP as a dark blue solid and 0.11 g of the by-product 4. The total amounts of Tri-BTDPP and 4 in 1.65 g of the crude product are estimated to be 1.29 g (56%) and 0.36 g (16%), respectively.

Data for Tri-BTDPP:

^{1}δH NMR ($CDCl_3$, 400 MHz) 8.93 (2H, d, J = 4.2 Hz), 8.91 (2H, d, J = 4.2 Hz), 8.85 (2H, dd, J = 3.9, 1.1 Hz), 7.49 (2H, dd, J = 5.0, 1.0 Hz), 7.25 (4H, dd, J = 3.9, 3.5 Hz), 7.14 (2H, dd, J = 4.9, 4.0 Hz), 3.96 (12H, d, J=5.2 Hz), 2.00 - 1.71 (6H, m), 1.39 - 1.23 (35H, m), 1.22 - 1.05 (70H, m), 0.92 – 0.72 (41H, m)

^{13}C NMR ($CDCl_3$,400 MHz) δ 161.81, 161.69, 141.49, 141.19, 140.67, 139.33, 139.28, 137.43, 137.15, 135.95, 131.03, 130.14, 130.02, 129.95, 128.77, 126.12, 109.37, 109.08, 108.44, 77.56, 46.76, 46.30, 39.73, 39.46, 38.41, 32.26, 32.24, 31.60, 30.68, 30.56, 30.51, 30.45, 30.05, 29.99, 29.97, 29.92, 29.72, 29.70, 28.84, 28.69, 26.65, 24.02, 23.87, 23.47, 23.44, 23.03, 14.45, 14.38, 10.91, 10.83.

HR-MS (ESI): Found m/z $[M^+H]^+$ 1906.11094; calculated for $C_{114}H_{164}N_606S_6$ 1906.08759

Data for **3**:

^{1}H NMR ($CDCl_3$, 300 MHz) δ 9.05-8.84 (4H, m), 7.65 (2H, d, J=4.9 Hz), 7.43 (2H, d, J=4.2 Hz), 7.33 – 7.28 (1H, m), 7.23 – 7.18 (1H, m), 4.04 (8H, d, J= 7.1 Hz), 1.92 (4H,s), 1.44 – 1.07 (8H, m), 1.04-0.67 (26H, m).

^{13}C NMR ($CDCl_3$, 300 MHz) δ 161.62, 140.88, 140.55, 139.15, 136.68, 135.58, 130.80, 129.79, 128.50, 125.99, 108.85, 108.14, 46.30, 45.94, 39.31, 39.07, 37.97, 37.75, 31.91, 31.21, 30.05, 29.65, 29.36, 28.50, 28.34, 26.26, 23.63, 23.08, 22.68, 14.12, 10.56. HR-MS (ESI): Found m/z [M+H]+ 1383.87347; calculated for C84H127N404S4 1383.87110

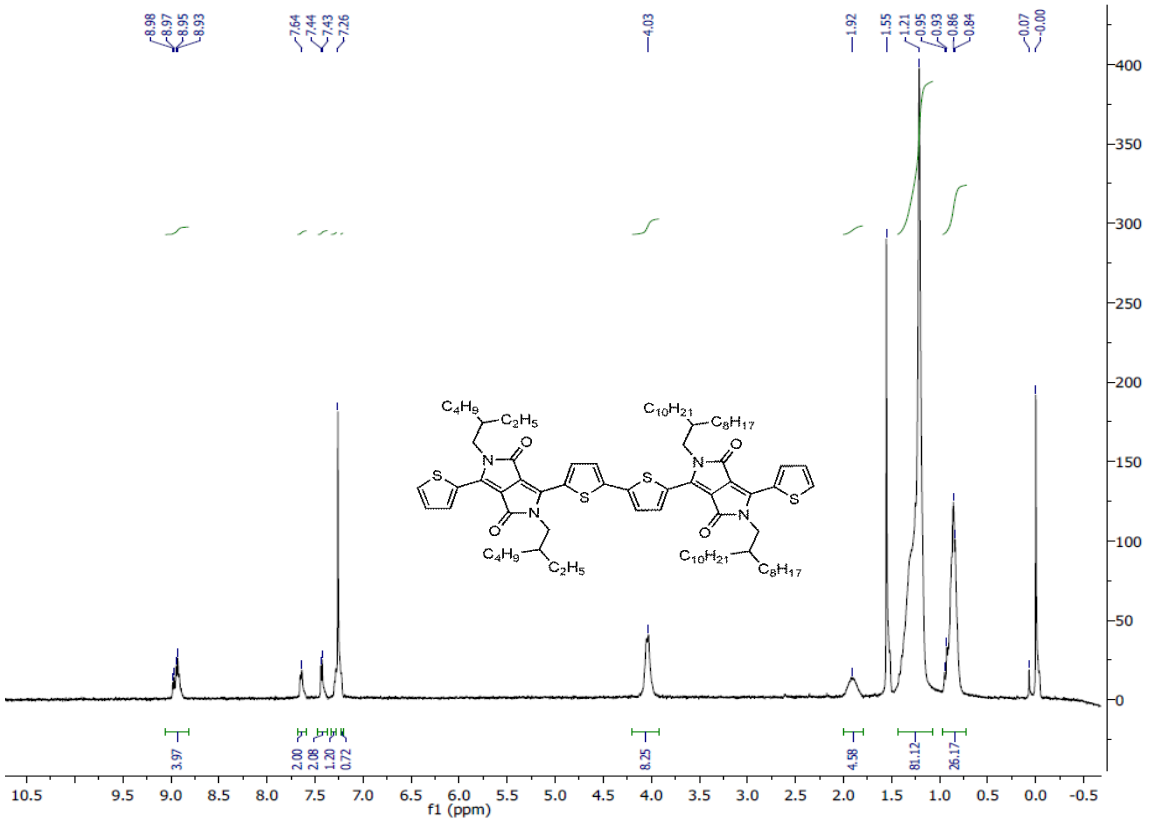
8.98
8.97
8.95
8.93
7.64
7.44
7.43
7.26
4.03
1.92
1.55
1.21
0.95
0.93
0.86
0.84
0.07
0.00
3.97
2.00
2.08
1.20
0.72
8.25
4.58
81.12
26.17
f1 (ppm)

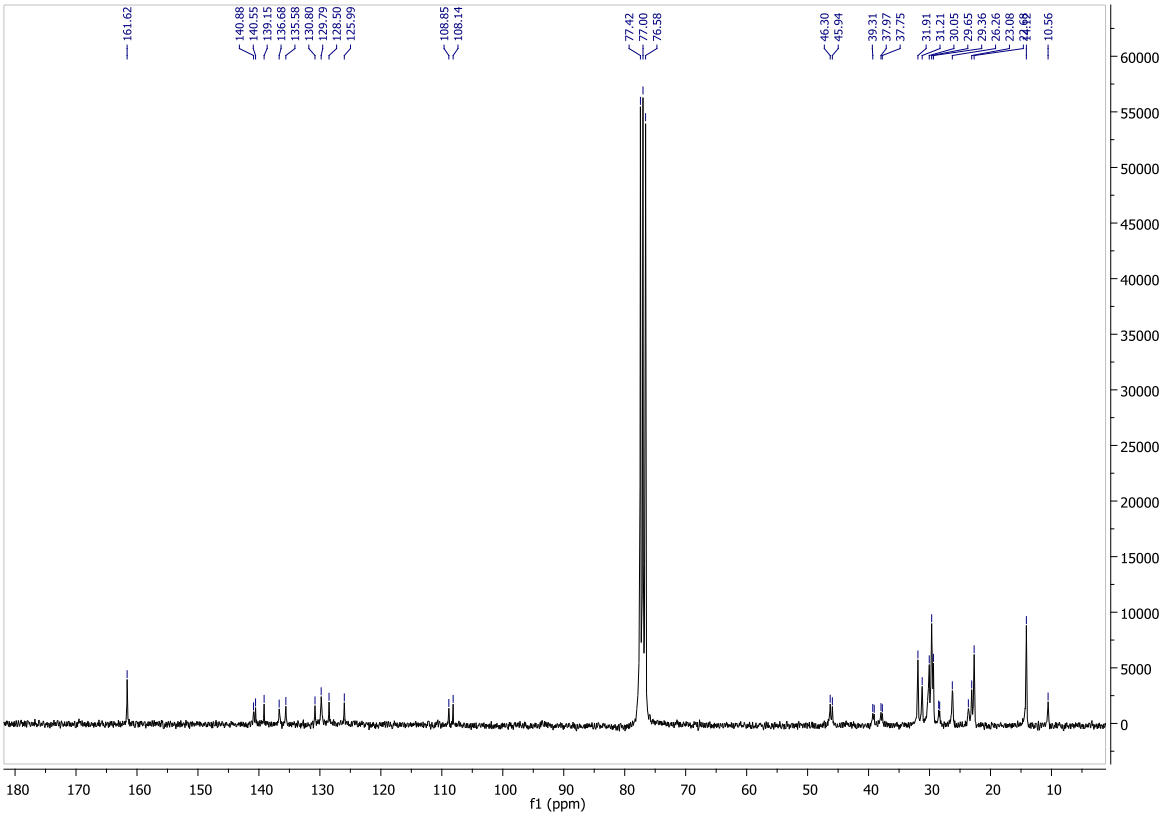
161.62
140.88
140.55
139.15
136.68
135.58
130.80
129.79
128.50
125.99
108.85
108.14
77.42
77.00
76.58
46.30
45.94
39.31
37.97
37.75
31.91
31.21
30.05
29.65
29.36
26.26
23.08
10.56
f1 (ppm)

Data for 4: MALDI-TOF: Found m/z $[M^+H]^+$ 1046.4; calculated for $C_{60}H_{79}N_4O_4S_4$ 1046. 7

3-phenyl-6-(thiophen-2-yl)-2,5-dihydropyrrolo[3,4-c]pyrrole-1,4-dione (11a) [134]**:**

Tert-amyl-alcohol was first dried and distilled. In a 100 ml dry three-necked round bottom flask, ethyl 5-oxo-2-phenyl-4,5-dihydro-1H-pyrrole-3-carboxylate (2.5 g, 0.0108 mol, 1 eq) and thiophene-2-carbonitrile (1.18 g, 0.0108 mol, 1 eq) were introduced. The system was purged under nitrogen atmosphere. 40 ml of tert-amyl-alcohol were added, followed by the solution in THF of sodium tert butoxide (2M) (9.18 ml, 0.0184 mol, 1.7 eq). The mixture was then heated at 90°C overnight. 40 ml of methanol were added. The solution was slowly neutralized with glacial acetic acid (1.1 ml) and refluxed for 15 min. After cooling down to room temperature, the product was filtrated and washed with water and methanol several times. 2.12 g of dark red solid were collected (67 %).

^{1}H NMR(300 MHz,DMSO) δ 11.25 (s,2H), 8.48-8.34 (m,2H), 8.27 (d, J = 3.7 Hz, 1H), 7.99 (d, J = 4.9 Hz, 1H), 7.62-7.48 (m, 3H), 7.35-7.27 (m,1H)

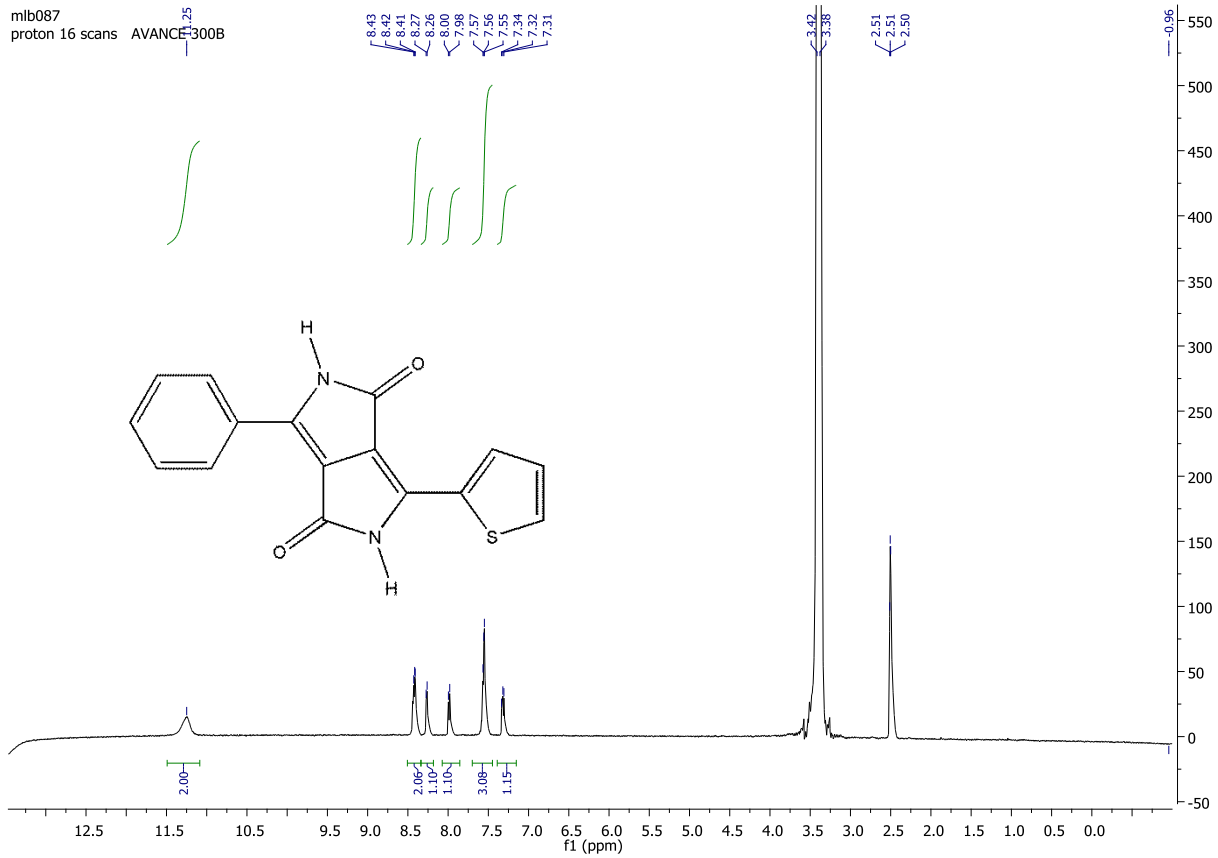

3-(4-hexylthiophen-2-yl)-6-phenyl-2,5-dihydropyrrolo[3,4-c]pyrrole-1,4-dione (11b):

Tert-amyl-alcohol was first dried and distilled. In a 100 ml dry three-necked round bottom flask, ethyl 5-oxo-2-phenyl-4,5-dihydro-1H-pyrrole-3-carboxylate (2.39 g, 0.01 mol, 1 eq) and 4-hexylthiophene-2-carbonitrile (2 g, 0.01 mol, 1 eq) were introduced. The system was purged under nitrogen atmosphere. 40 ml of tert-amyl-alcohol were added, followed by the solution in THF of sodium tert butoxide (2M) (8.5 ml, 0.017 mol, 1.7 eq). The mixture was then heated at 90°C overnight. 40 ml of methanol were added. The solution was slowly neutralized with glacial acetic acid (1 ml) and refluxed for 15 min. After cooling down to room temperature, the product was filtrated and washed with water and methanol several times. 2.56 g of dark red solid were collected (69 %).

^{1}H NMR(300 MHz,DMSO) δ 11.19 (s, 2H), 8.43-8.41 (m, 2H), 8.14 (s, 1H), 7.62 (s, 1H), 7.56-7.54 (m, 3H), 2.65-2.60 (t, 2H), 1.63-1.58 (m, 2H), 1.34-1.25 (m, 6H), 0.98-0.84 (m, 3H)

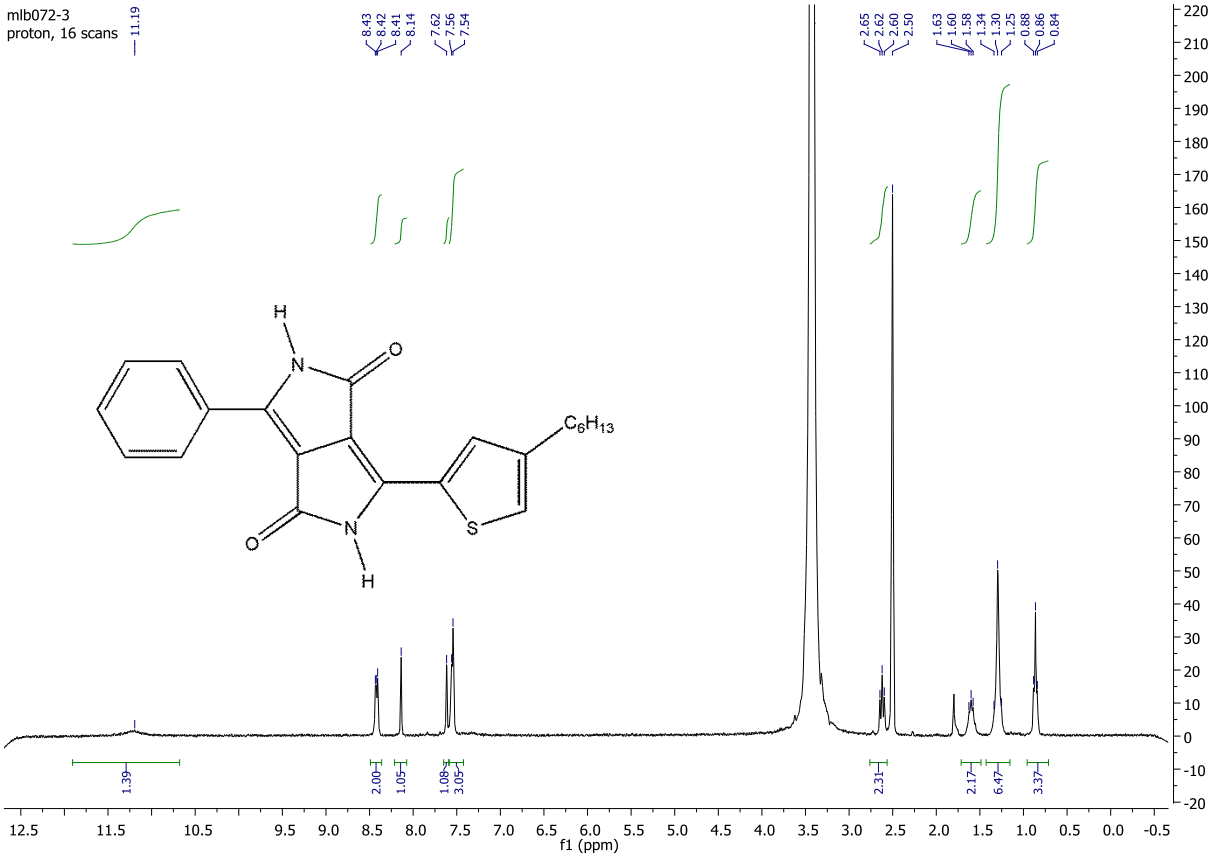

2,5-bis(2-ethylhexyl)-3-phenyl-6-thiophen-2-yl)-2,5-dihydropyrrolo[3,4-C]pyrrole-1,4-dione (12a):

In a 100 ml dry three-necked round bottom flask, 3-phenyl-6-(thiophen-2-yl)-2,5-dihydropyrrolo[3,4-c]pyrrole-1,4-dione (**10**) (1.25 g, 0.00425 mol, 1 eq) and potassium carbonate (2.35 g, 0.017 mol, 4 eq) were introduced. The system was purged under nitrogen. 50 ml of DMF were added. The solution was heated at 120°C for 30 minutes. 2-ethylhexylbromide (2.27 ml g, 0.0128 mol, 3 eq) was added. The mixture was heated at 120°C overnight. The solution was cooled down to room temperature. The solution was poured onto 70 ml of water. The product was extracted with chloroform (200 ml). The organic phase was dried with sodium sulfate. The solvent was evaporated under vacuum. The crude was further purified by silica gel chromatography (eluent: Hexane/EtAc 95/5). The product was crystallized in methanol. 0.62 g of dark red solid was obtained (28 %).

^{1}H NMR(300 MHz,$CDCl_3$) δ 8.92 (d, J = 3.8 Hz, 1H), 7.75 (dd, J_1 = 6.4 Hz, J_2 = 1.2 Hz, 2H), 7.65 (d, J = 5.1 Hz, 1H), 7.51 (m, 3H), 7.29 (d, J = 4.1 Hz, 1H), 3.95 (dd, J_1 = 7.8 Hz, J_2 = 1.5 Hz, 2H), 3.81 (dd, J_1 = 6.6 Hz, J_2 = 0.7 Hz, 2H), 1.83 (s, 1H), 1.51 (s, 1H), 1.37-1.00 (m, 16H), 0.86-0.67 (m, 6H), 0.75 (t, J = 6.5 Hz, 3H), 0.70 (t, J = 7.3 Hz, 3H)

^{13}C NMR(300 MHz,CHCl3) δ 162.29, 162.17, 146.92, 142.08, 135.57, 130.84, 130.64, 129.72, 128.76, 128.63, 168.40, 109.55, 107.90, 45.67, 45.05, 39.03, 38.54, 30.27, 28.38, 23.66, 23.01, 22.80, 13.97, 13.89, 10.47, 10.33

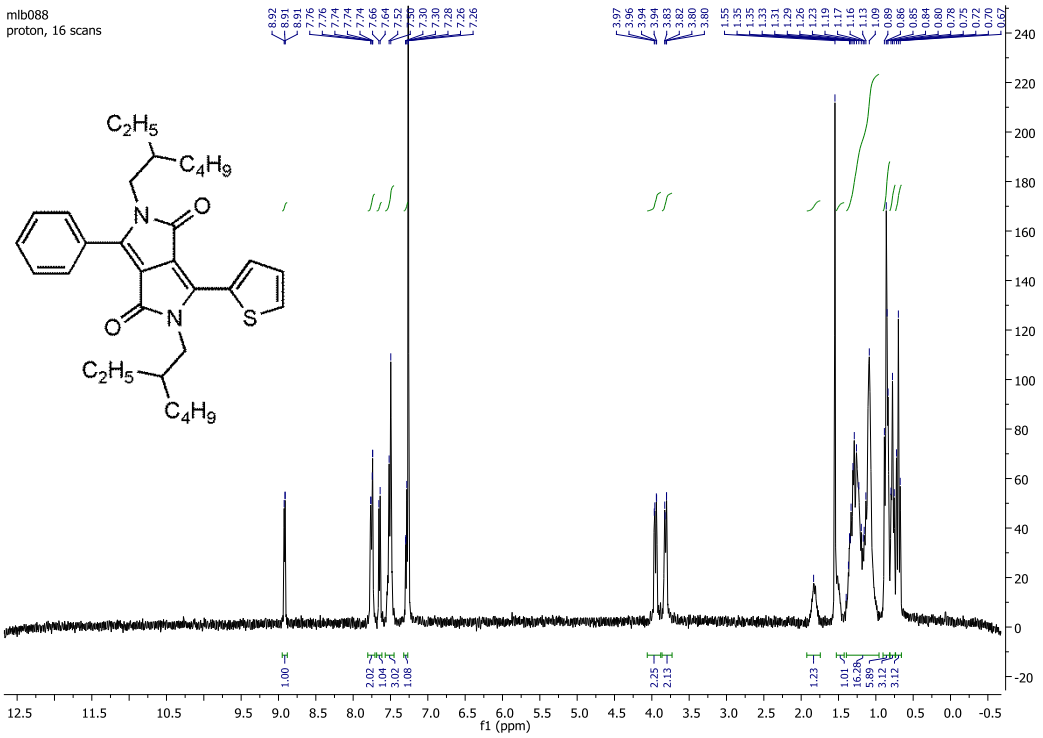

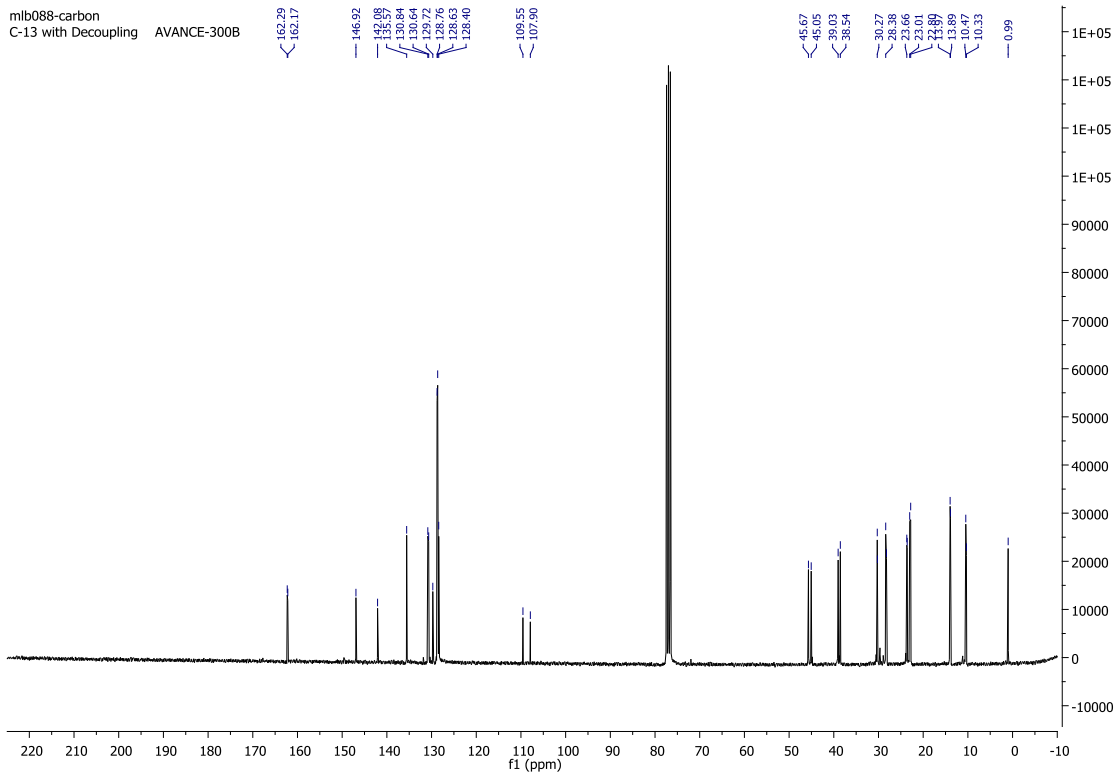

2,5-bis(2-ethylhexyl)-3-(4-hexylthiophen-2-yl)-6-phenyl-2,5-dihydropyrrolo[3,4-c]pyrrole-1,4-dione (12b):

In a 100 ml dry three-necked round bottom flask, 3-(4-hexylthiophen-2-yl)-6-phenyl-2,5-dihydropyrrolo[3,4-c]pyrrole-1,4-dione (2.3 g, 0.0061 mol, 1 eq) and potassium carbonate (3.31 g, 0.024 mol, 4 eq) were introduced. The system was purged under nitrogen. 70 ml of DMF were added. The solution was heated at 120°C for 40 minutes. 2-ethylhexylbromide (3.25 ml g, 0.0183 mol, 3 eq) was added. The mixture was heated at 120°C overnight. The solution was cooled down to room temperature. The solution was poured onto 100 ml of water. The product was extracted with chloroform (250 ml). The organic phase was dried with sodium sulfate. The solvent was evaporated under vacuum. The crude was further purified by silica gel chromatography (eluent: Hexane/EtAc 98/2). The product was crystallized in methanol. 1.9 g of dark red oil was obtained (52 %).

^{1}H NMR(300 MHz,TCE-d2) δ 8.58 (s, 1H), 7.68 (d, J = 4.3 Hz, 2H), 7.49 (d, J = 4.2 Hz, 3H), 7.27 (s, 1H), 3.79 (m, 4H), 2.66 (t, J = 7.6 Hz, 2H), 1.76 (s, 1H), 1.62 (m, 3H), 1.4-1.15 (m, 16H), 1.07 (m, 6H), 0.89-0.75 (m, 9H), 0.74-0.70 (m, 3H), 0.65-0.57 (m, 3H)

^{13}C NMR(300 MHz,CHCl3) δ 165.46, 165.08, 149.56, 147.92, 145.26, 139.40, 133.83, 132.37, 131.98, 131.74, 131.65, 129.78, 112.56, 110.64, 48.69, 47.98, 42.01, 41.47, 34.74, 33.49, 33.37, 33.24, 32.10, 31.52, 31.23, 26.69, 26.20, 25.94, 25.76, 17.33, 17.26, 17.15, 13.68, 13.57

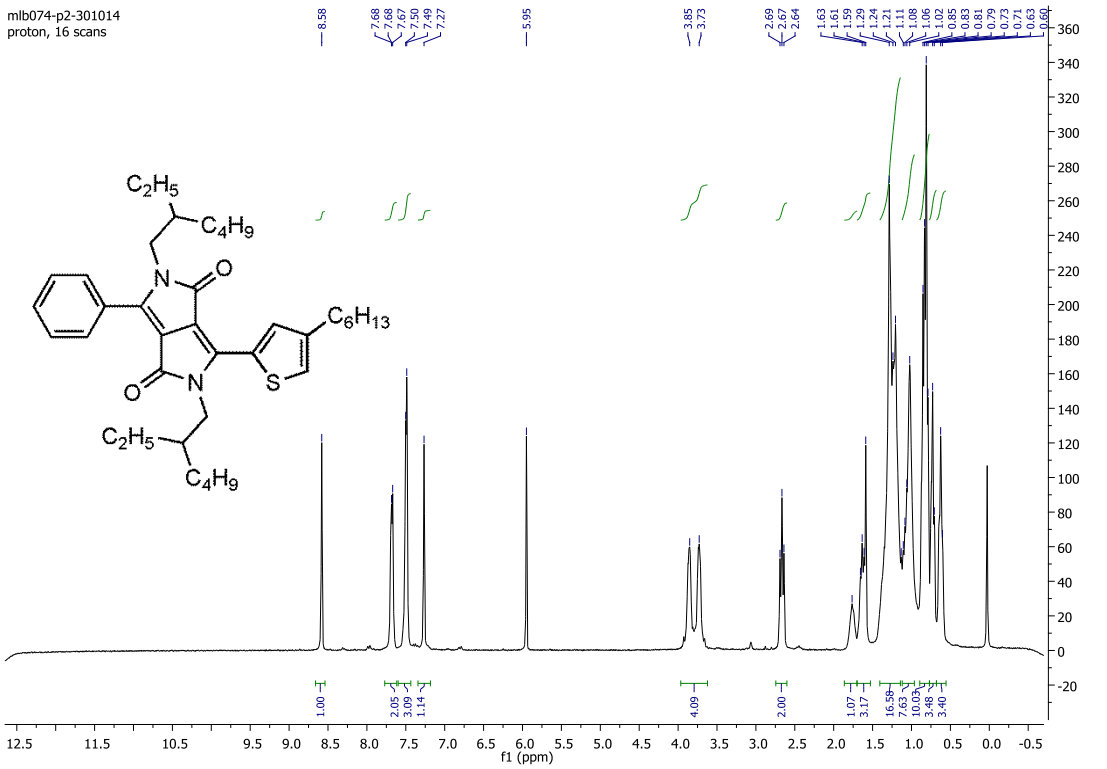
mlb074-p2-301014
proton, 16 scans
f1 (ppm)

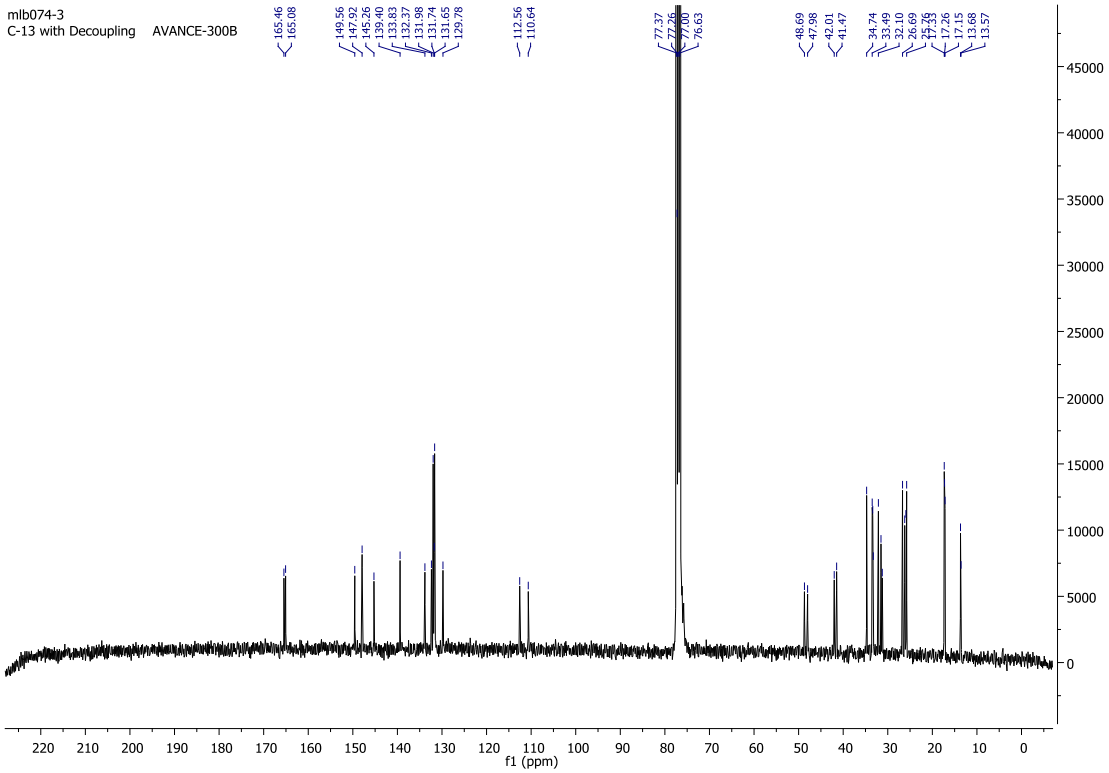
mlb074-3
C-13 with Decoupling AVANCE-300B
f1 (ppm)

3-(5-bromothiophen-2-yl)-2,5-bis(2-ethylhexyl)-6-phenyl-2,5-dihydropyrrolo[3,4-c]pyrrole-1,4-dione (13a):

At 5°C and under light exclusion, to a solution of 2,5-bis(2-ethylhexyl)-3-phenyl-6-thiophen-2-yl)-2,5-dihydropyrrolo[3,4-C]pyrrole-1,4-dione (1 g, 0.0019 mol, 1 eq) in 25 ml of chloroform, N-bromosuccinimide (0.34 g, 0.0019 mol, 1 eq) in few portions. The mixture was stirred at room temperature overnight. The product was extracted with chloroform and washed with brine three times. The organic phase was dried with sodium sulfate and the solvent was evaporated under vacuum. The crude was further purified by silica gel chromatography column (DCM/hexane 75/25). 0.65 g of product were obtained (57 %).

^{1}H NMR(300 MHz,$CDCl_3$) δ 8.58 (d, J = 3.7 Hz, 1H), 7.67(d, J = 4.2 Hz, 2H), 7.42 (m, 3H), 7.17 (d, J = 3.8 Hz, 1H), 3.97-3.60 (m, 4H), 1.74 (s, 1H), 1.42 (s, 1H), 1.32-0.89 (m, 16H), 0.89-0.53 (m, 12H)

^{13}C NMR(300 MHz,CHCl3) δ 162.04, 162.01, 147.42, 140.67, 135.47, 131.37, 131.10, 130.78, 128.79, 128.60, 128.49, 119.06, 109.41, 108.06, 45.73, 45.06, 39.04, 38.50, 30.23, 30.17, 28.33, 28.17, 23.62, 23.57, 23.00, 22.79, 13.99, 13.90, 10.45, 10.30

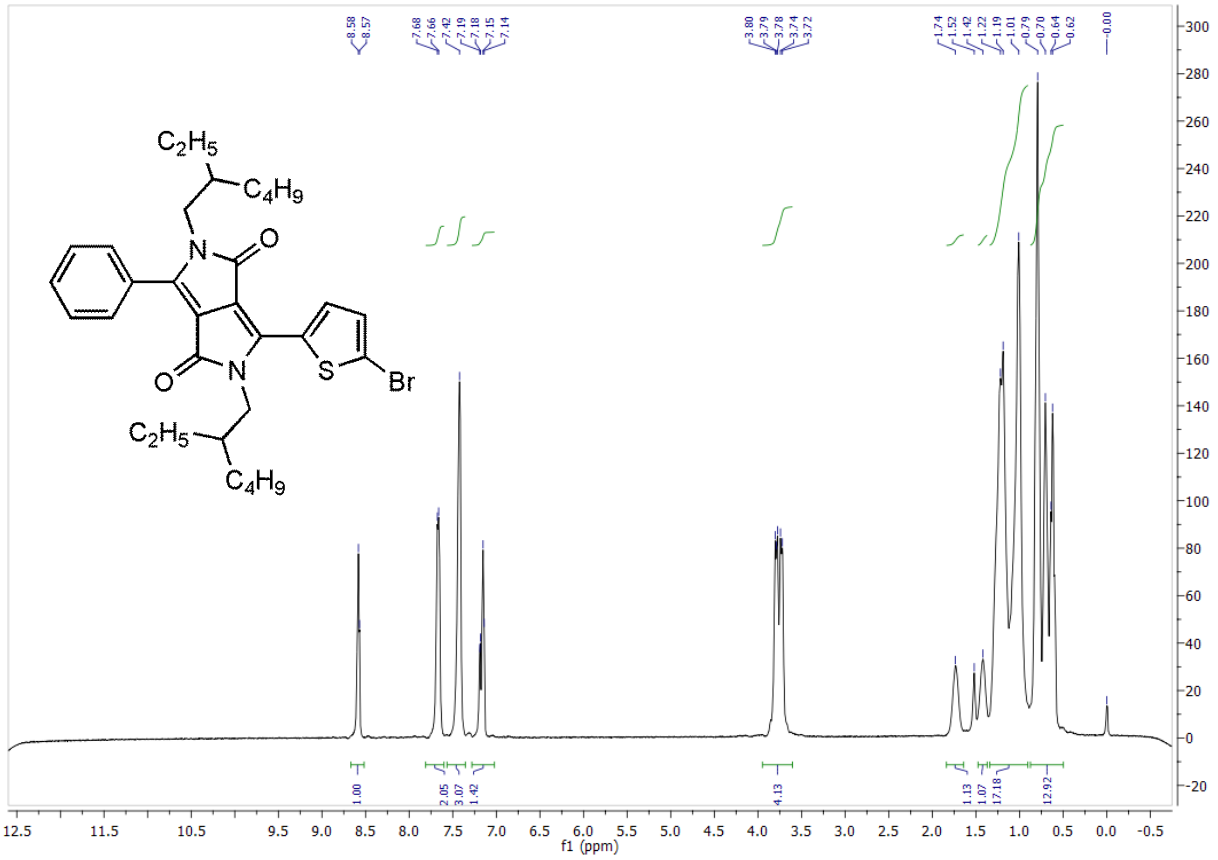

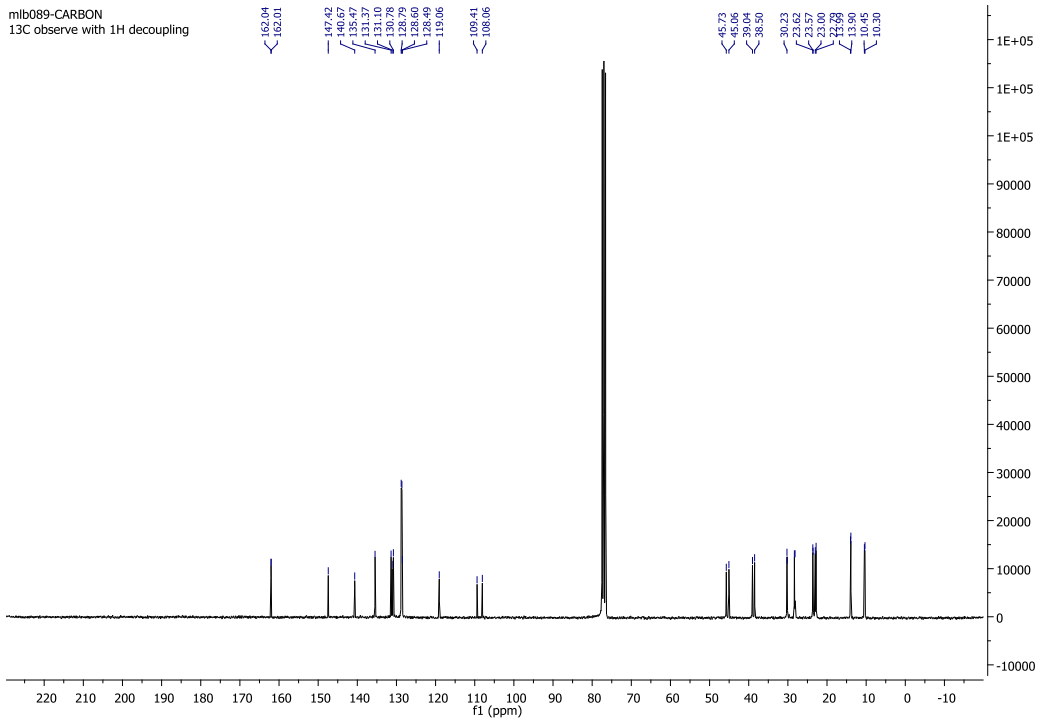

3-(5-bromo-4-hexylthiophen-2-yl)-2,5-bis(2-ethylhexyl)-6-phenyl-2,5-dihydropyrrolo[3,4-c]pyrrole-1,4-dione (13b):

At 5°C and under light exclusion, to a solution of 2,5-bis(2-ethylhexyl)-3-(4-hexylthiophen-2-yl)-6-phenyl-2,5-dihydropyrrolo[3,4-c]pyrrole-1,4-dione (1.8 g, 0.003 mol, 1 eq) in 40 ml of chloroform, N-bromosuccinimide (0.53 g, 0.003 mol, 1 eq) in few portions. The mixture was stirred at room temperature overnight. The product was extracted with chloroform and washed with brine three times. The organic phase was dried with sodium sulfate and the solvent was evaporated under vacuum. The crude was further purified by silica gel chromatography column (DCM/hexane 75/25). 1 g of dark red oil were obtained (50 %).

^{1}H NMR(300 MHz,TCE-d2) δ 8.37 (s, 1H), 7.67 (d, J = 4.9 Hz, 2H), 7.49 (m, 3H), 3.79-3.71 (m, 4H), 2.61 (t, J = 7.5 Hz, 2H) , 1.74 (s, 1H), 1.61 (s, 2H), 1.38-1.19 (m, 16H), 1.8-1.0 (m, 6H), 0.84-0.81 (m, 9H), 0.73 (m, 3H), 0.64 (m, 3H)

^{13}C NMR(300 MHz,CHCl3) δ 161.97, 161.86, 146.93, 143.80, 140.80, 135.73, 130.59, 129.11, 128.67, 128.55, 116.49, 109.37, 107.72, 45.62, 44.94, 39.03, 38.34, 31.53, 30.15, 29.58, 29.41, 28.91, 28.33, 28.10, 23.59, 23.00, 22.77, 22.59, 13.99, 13.89, 10.43, 10.33

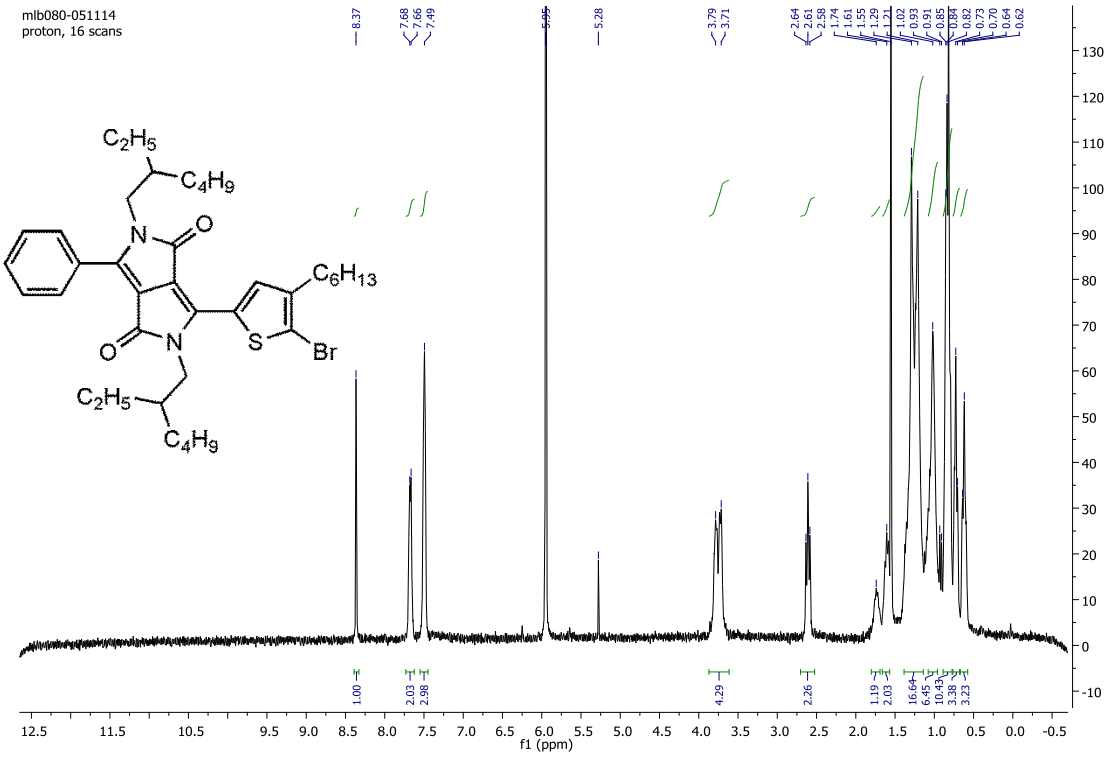
mlb080-051114
proton, 16 scans
f1 (ppm)

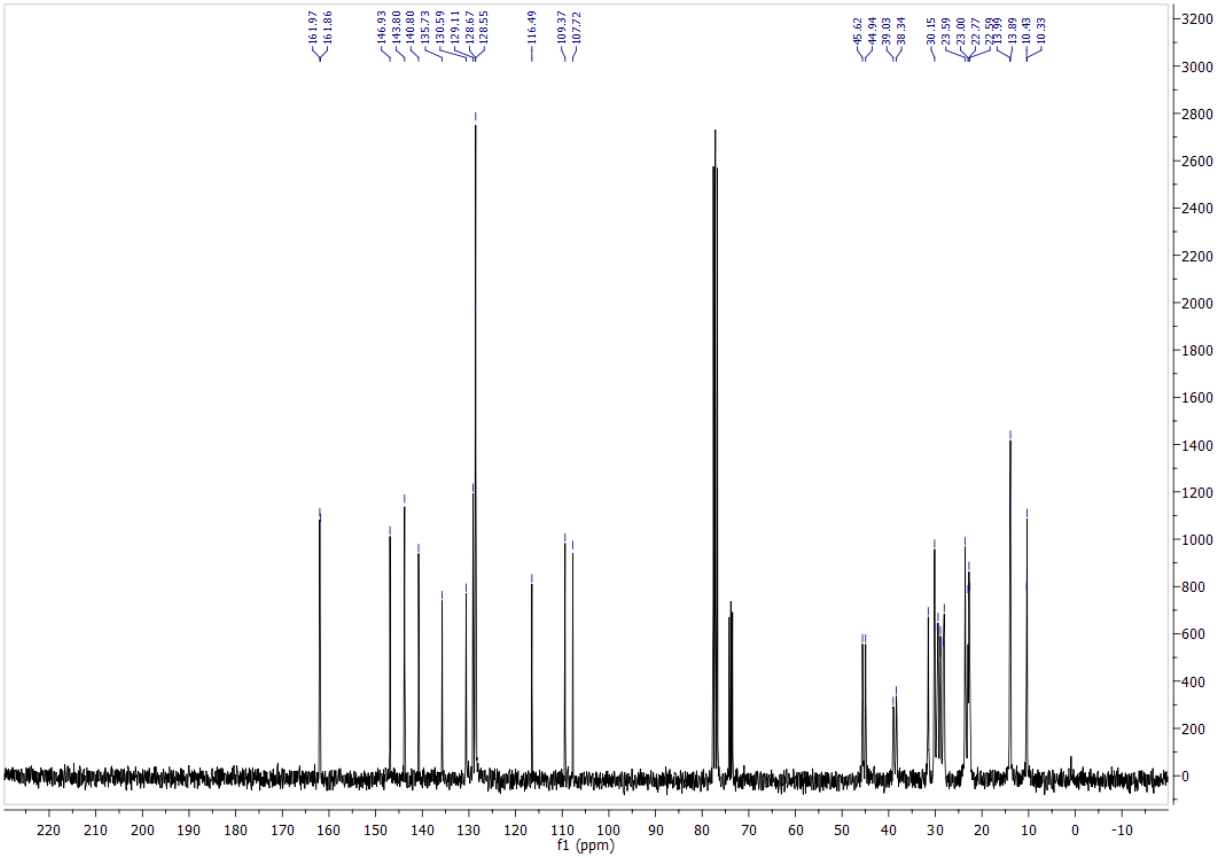
f1 (ppm)

6,6'-((2,5-bis(2-octyldodecyl)-3,6-dioxo-2,3,5,6-tetrahydropyrrolo[3,4-c]pyrrole-1,4-diyl)bis([2,2'-bithiophene]-5,5'-diyl))bis(2,5-bis(2-ethylhexyl)-3-phenyl-2,5-dihydropyrrolo[3,4-c]pyrrole-1,4-dione (Tri-DPP-PT):

A 50 ml dry three necked flask was charged with 3-(5-bromothiophen-2-yl)-2,5-bis(2-ethylhexyl)-6-phenyl-2,5-dihydropyrrolo[3,4-c]pyrrole-1,4-dione (0.600 g, 0.001, 2eq), 2,5-bis(2-octyldodecyl)-3,6-bis(5-(trimethylstannyl)thiophen-2-yl)-2,5-dihydropyrrolo[3,4-c]pyrrole-1,4-dione (0.596 g, 0.0005 mol, 1 eq) and trio(o-totyl)phosphine (12.1 mg, 0.00004, 0.08eq). The system was purged under argon. 20 ml of anhydrous toluene was added. Tris(dibenzylideneacetone)dipalladium(0) (9.1 mg, 0.00001, 0.02eq) was dissolved into 1 ml of anhydrous toluene and injected in the solution. The mixture was heated at 120°C for 60 H. After cooling down, the solution was poured on 400 ml of methanol. The precipitate was filtrated. The crude was further purified by silica gel chromatography column (toluene/chloroform 1/1). 400 mg of dark blue solid were obtained (42%).

^{1}H NMR(300 MHz,$CHCl_3$) δ 8.91 (d, J = 3.2 Hz, 4H), 7.74-7.73 (m, 4H), 7.47 (m, 6H), 7.41 (d, J = 2.9 Hz, 4H), 4.05 (d, J = 6.8 Hz, 4H), 3.97 (d, J = 7.7 Hz, 4H), 3.83 (d, J = 6.8 Hz, 4H), 1.95 (S, 2H), 1.86 (s, 2H), 1.49 (s, 2H), 1.34 (m, 22H), 1.21 (m, 62H), 1.09 (m, 12H), 0.87 (m, 24H), 0.78 (t, J = 6.7 Hz, 6H), 0.70 (t, J = 7.3 Hz, 6H)

^{13}C NMR(300 MHz,$CHCl_3$) δ 162.24, 162.07, 161.56, 147.43, 141.49, 141.37, 140.77, 139.30, 136.80, 129.94, 128.88, 128.84, 128.59, 126.25, 126.14, 109.69, 109.20, 108.89, 46.48, 45.83, 45.16, 39.31, 38.49, 38.04, 32.06, 31.43, 30.43, 30.23, 29.78, 29.52, 28.71, 28.37, 26.47, 23.90, 23.83, 23.25, 22.98, 22.85

6,6'-((2,5-bis(2-octyldodecyl)(3,6-dioxo-2,3,5,6-tetrahydropyrrolo[3,4-c]pyrrole-1,4-diyl)bis(3-hexyl-[2,2'-bithiophene]-5',5-diyl))bis(2,5-bis(2-ethylhexyl)-3-phenyl-2,5-dihydropyrrolo[3,4-c]pyrrole-1,4-dione) (Tri-DPP-PT-C6):

A 50 ml dry three necked flask was charged with 3-(5-bromo-4-hexylthiophen-2-yl)-2,5-bis(2-ethylhexyl)-6-phenyl-2,5-dihydropyrrolo[3,4-c]pyrrole-1,4-dione (0.500 g, 0.73 mmol, 2eq), 2,5-bis(2-octyldodecyl)-3,6-bis(5-(trimethylstannyl)thiophen-2-yl)-2,5-dihydropyrrolo[3,4-c]pyrrole-1,4-dione (0.435 g, 0.37 mmol, 1 eq) and trio(o-totyl)phosphine (8.9 mg, 0.0293 mmol, 0.08eq). The system was purged under argon. 15 ml of anhydrous toluene was added. Tris(dibenzylideneacetone)dipalladium(0) (6.7 mg, 0.0073, 0.02eq) was dissolved into 1 ml of anhydrous toluene and injected in the solution. The mixture was heated at 120°C for 60 H. After cooling down, the solution was poured on 270 ml of methanol. The precipitate was filtrated. The crude was further purified by silica gel chromatography column (chloroform/ hexan 70/30). 240 mg of dark blue solid were obtained (32%).

^{1}H NMR(300 MHz,$CHCl_3$) δ 9.07 (d, J = 4.02 Hz, 2H), 8.91 (s,2H), 7.80-7.74 (m, 4H), 7.56-7.48 (m, 6H), 7.42 (d, J = 4.02 Hz, 2H), 4.08 (d, J = 7.2Hz, 4H), 3.96 (d, J = 7.6 Hz, 4H), 3.85 (d, J= 7.1 Hz, 4H), 3.01-2.85 (m, 4H), 2.00 (s,2H), 1.90 (s, 2H), 1.87-1.70 (m, 4H), 1.57 (s,2H),

1.42-1.30 (m, 23 H), 1.27-1.17 (m, 62H), 1.16-1.05 (m, 12H), 0.98-0.74 (m, 37H), 0.7 (t, J = 7.3 HZ, 6H)

^{13}C NMR(300 MHz,$CHCl_3$) δ 162.26, 162.14, 161.63, 146.96, 142.34, 140.99, 140.44, 139.52, 139.26, 136.60, 135.91, 130.78, 130.23, 128.84, 128.66, 128.19, 127.68, 109.85, 108.93, 108.60, 46.57, 45.77, 45.17, 39.32, 38.49, 38.07, 31.93, 31.90, 31.72, 31.18, 30.30, 30.22, 30.13, 29.93, 29.66, 29.57, 29.44, 29.38, 29.35, 28.52, 26.25, 23.72, 23.64, 23.12, 22.86, 22.69

APPENDIX 3: SYNTHESIS OF EBI DERIVATIVES

(3Z)-6-bromo-3-((Z)-2-(6-bromo-2-oxoindolin-3-ylidene)ethylidene)indolin-2-one [180,181]**:**

A reaction of a mixture of 6-bromoindole-2,3-dione (15 g, 0.066 mol, 1 eq), propionic anhydride (50 ml) and pyridine (17 ml) was heated to reflux in a 100 ml three-necked round-bottom flask under argon for 30 min. After cooling, the dark red needles were separated, washed with acetone and ether several times and dried under vacuum at 100°C. After washing three times with chloroform, 4.6 g of (3*Z*)-6-bromo-3-((*Z*)-2-(6-bromo-2-oxo-1-propionylindolin-3-ylidene)ethylidene)-1-propionylindolin-2-one intermediate were obtained with a yield of 25%. Then, 4 g of the intermediate was further reacted with 0.8 g of KOH in 100 ml of ethanol under reflux for 20 minutes. The dark blue solid was separated, washed with acetone and ether. The potassium derivatives was neutralized with diluted HCl (0.20 M) in ethanol and then washed with water. 2.73 g of final product was obtained yielding 85%.

^{1}H NMR (DMSO, 300MHz): δ 10.81 (d, *J* = 21.7 Hz, 1H), 8.65 (d, *J* = 13.1 Hz, 1H), 8.07 (dd, *J* = 15.0, 10.8 Hz, 2H), 7.97 (d, *J* = 8.2 Hz, 1H), 7.18 (t, *J* = 7.6 Hz, 2H), 7.01 (d, *J* = 12.9 Hz, 2H).

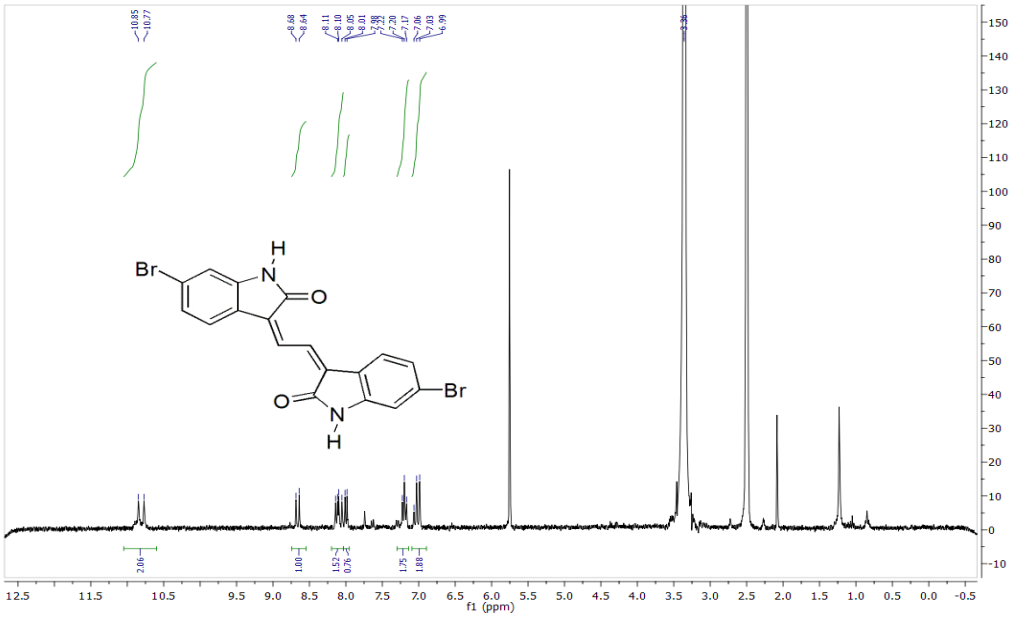

(3Z)-6-Bromo-3-((Z)-2-(6-bromo-1-(2-butyloctyl)-2-oxoindolin-3-ylidene)ethylidene)-1-(2-butyloctyl)indolin-2-one (2a):

In a two-necked round bottom flask, **1** (1.5 g, 3.4 mmol, 1 eq), potassium carbonate (1.81 g, 13.1 mmol, 3.9 eq) and 14 ml of DMF were introduced. 2-Butyloctyl bromide (2.5g, 10.0 mmol, 2.9 eq) was then added. The reaction was stirred at 70°C under argon for 20 h. 35 ml of deionized water were added and the product was extracted with dichloromethane (DCM). The organic phase was dried with sulphate sodium and DCM was evaporated under vacuum. The product was further purified on silica gel chromatography column using a mixture of Hexane and DCM (3:2) as eluent. The red solid was crystallized in isopropanol three times to get red needles. 612.8 mg of **2a** was obtained with a yield of 23%.

^{1}H NMR ($CDCl_3$, 300MHz): δ 8.94 (s, 2H), 7.47 (d, *J* = 8.2 Hz, 2H), 7.16 (d, *J* = 8.1 Hz, 2H), 6.91 (s, 2H), 3.58 (d, *J* = 7.2 Hz, 4H), 1.86 (s, 2H), 1.43 – 1.13 (m, 37H), 1.11 – 0.61 (m, 13H).

^{13}C NMR ($CDCl_3$, 300MHz) δ 167.18, 144.52, 130.28, 129.00, 124.98, 124.40, 122.36, 122.09, 112.06, 44.41, 36.25, 31.78, 31.58, 31.30, 29.62, 28.65, 26.40, 23.03, 22.62, 14.07, 14.03.

HR-MS (ESI): calculated for $C_{42}H_{58}O_2N_2Br_2$: 781.29514; found $(M+H)^+$: m/z 781.29378.

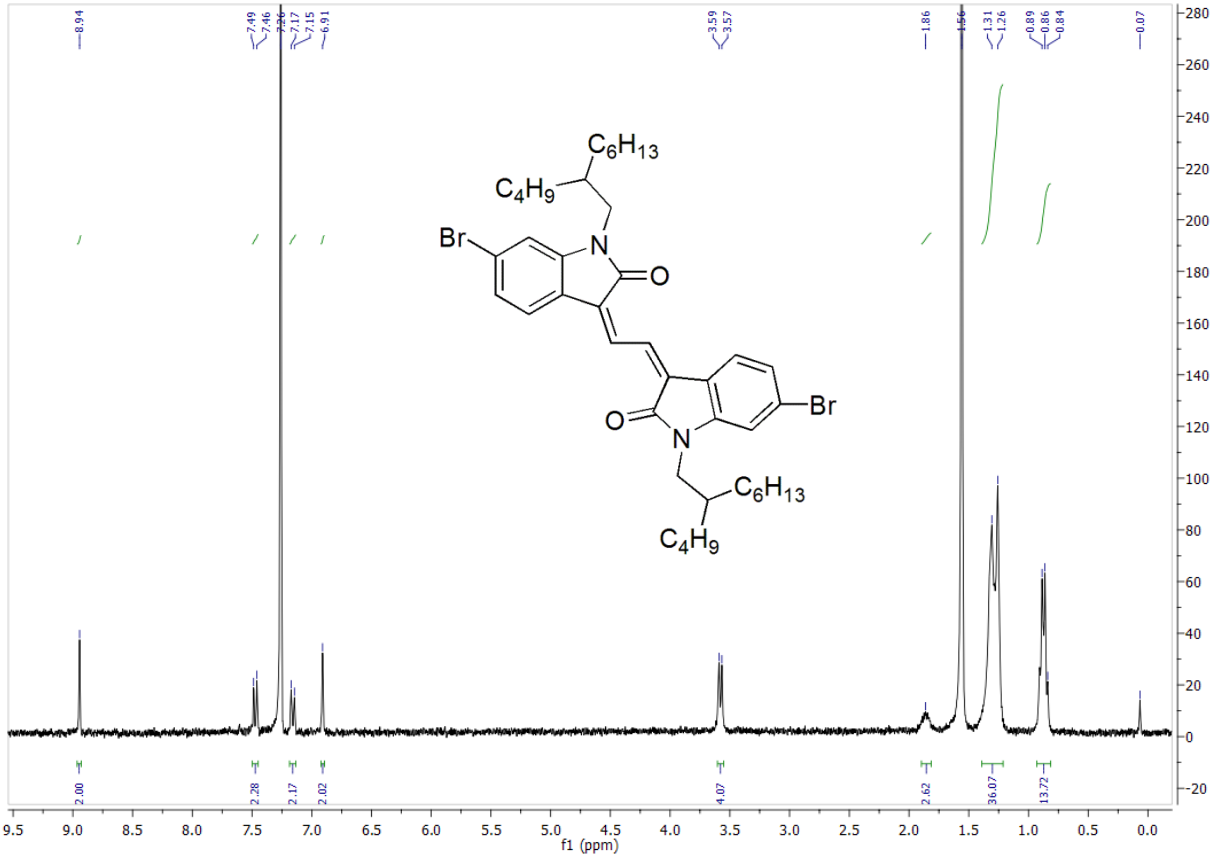
8.94
7.49
7.46
7.36
7.17
7.15
6.91
3.59
3.57
1.86
1.56
1.31
1.26
0.89
0.86
0.84
0.07
Br
N
O
C6H13
C4H9
O
N
Br
C6H13
C4H9
2.00
2.28
2.17
2.02
4.07
2.62
36.07
13.72
f1 (ppm)

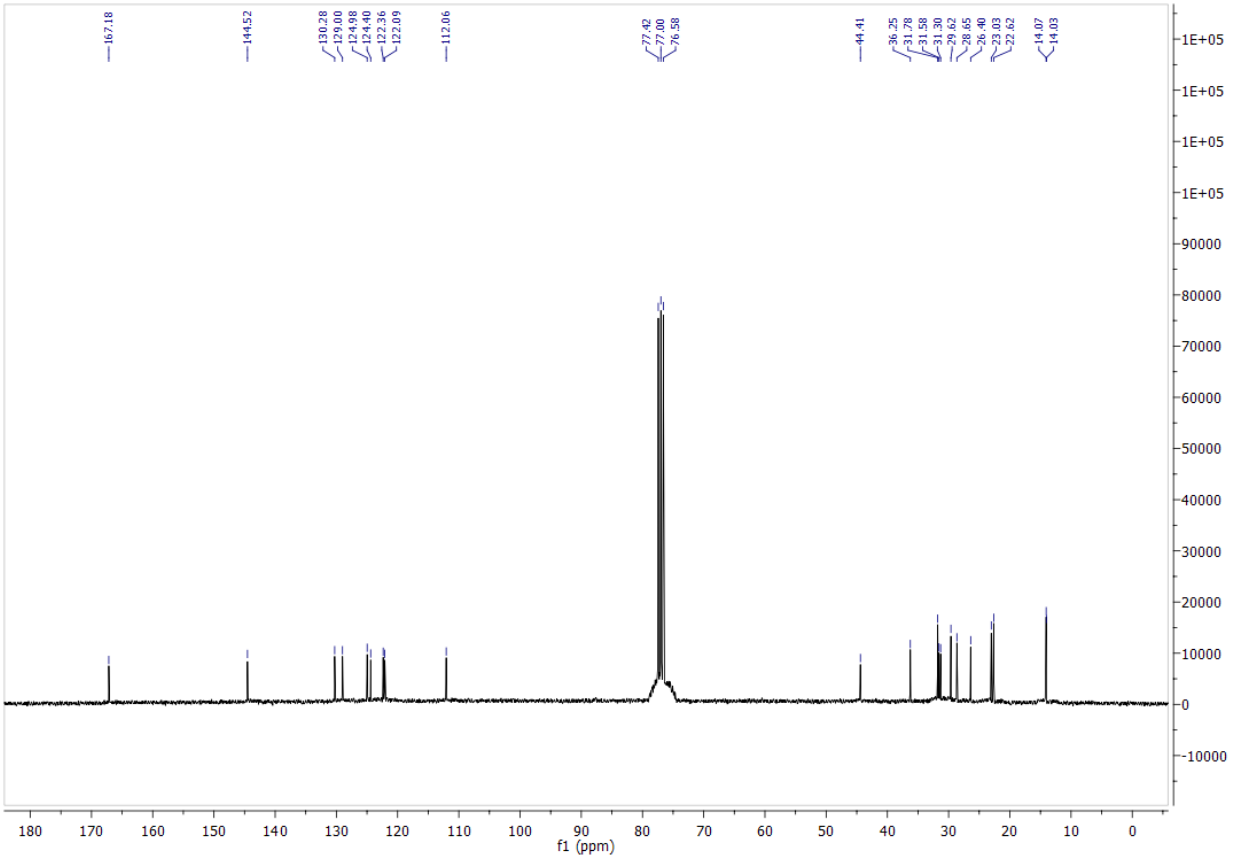

(3*Z*)-6-Bromo-3-((*Z*)-2-(6-bromo-1-(2-hexyldecyl)-2-oxoindolin-3-ylidene)ethylidene)-1-(2-hexyldecyl)indolin-2-one (2b):

In a two-necked round bottom flask, **1** (1.35 g, 0.003 mol, 1 eq), potassium carbonate (1.63 g, 0.0118 mol, 3.9 eq) and 13 ml of DMF were introduced. 2-hexyldecyl iodide (3.17 g, 0.009 mol, 3 eq) was then added. The reaction was stirred at 70°C under argon for 20 hours. 40 ml of deionized water were added and the product was extracted with DCM. The organic phase was dried with sulfate sodium and DCM was evaporated under vacuum. The product was further purified on silica gel chromatography column using a mixture of Hexane and DCM (65:35) as eluent. The red solid was crystallized in isopropanol three times to get red needles. 530 mg of **2b** was obtained giving a yield of 20%.

^{1}H NMR ($CDCl_3$, 300MHz) δ (ppm) 8.94 (S, 2H), 7.47 (d, J= 7.47 Hz, 2H), 7.16 (d, J=7.16 Hz, 2H), 6.91 (s, 2H), 3.57 (d, J=7.3 Hz, 4H), 1.86 (s, 2H), 1.47-1.11 (m, 49H), 0.95-0.78 (m, 12H)

^{13}C NMR ($CDCl_3$, 300MHz) δ (ppm) 167.19, 144.48, 130.27, 129.01, 124.98, 124.39, 122.35, 122.06, 112.07, 44.39, 36.20, 31.87, 31.78, 31.57, 31.55, 29.95, 29.63, 29.52, 29.28, 26.42, 26.39, 22.66, 22.63, 14.11, 14.09

HR-MS: calculated for $C_{50}H_{74}O_2N_2Br_2$: 893.41948; found $(M+H)^+$: m/z 893.41898

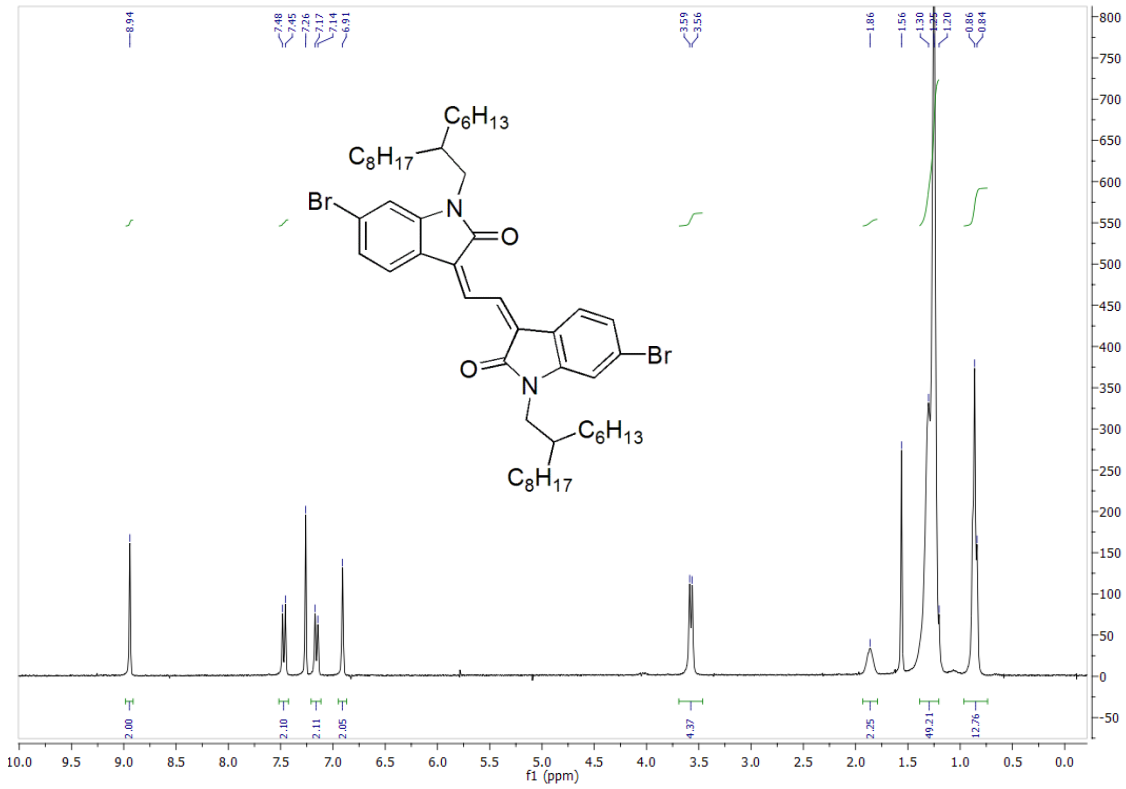

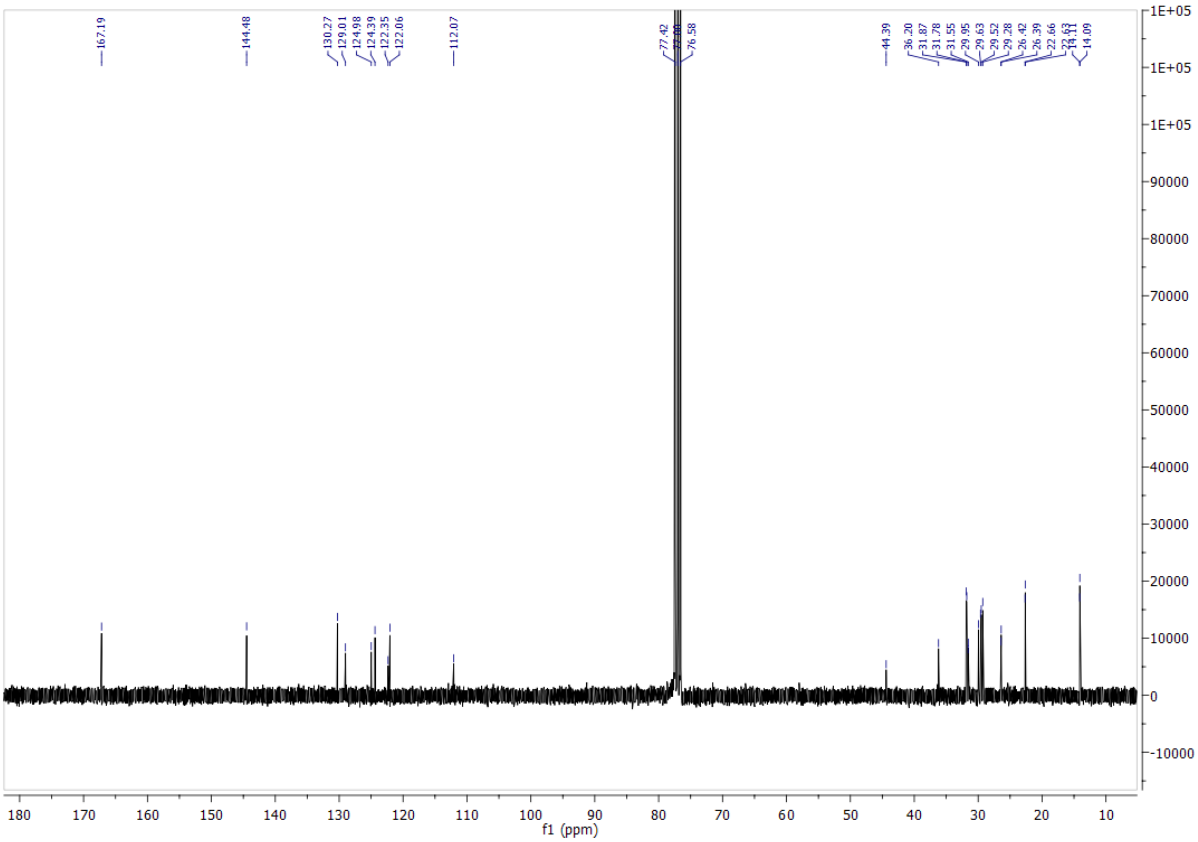

(3Z)-1-(2-butyloctyl)-3-((Z)-2-(1-(2-butyloctyl)-2-oxo-6-(thiophen-2-yl)indolin-3-ylidene)ethylidene)-6-(thiophen-2-yl)indolin-2-one (EBI-T):

2a (0.70 g, 0.9 mmol, 1 eq) and tributyl(thiophen-2-yl)stannane (0.57 ml, 1.8 mmol, 2 eq) were placed in a 50 ml dried flask and then, the flask was evacuated and back-filled with argon three times. Next, 30 ml of anhydrous toluene was poured into the flask. A mixture of $Pd_2(dba)_3$ (0.019 g, 0.018 mmol, 0.02 eq) and P(*o*-totyl)$_3$ (38.5 mg) which were separately introduced in 1 ml of anhydrous toluene were injected into the flask. The mixture was heated at 90°C under argon and stirred for 60 hours. Toluene was evaporated. The compound was purified on silica gel chromatography column with hexane and DCM (60:40) as eluent. The product was crystallized in isopropanol three times. 0.53 g of EBI-T was obtained giving a yield of 74.6%.

^{1}H NMR ($CDCl_3$, 300MHz) δ 8.96 (s,2H), 7.61 (d, J=7.9 Hz, 2H), 7.35 (dd, J1= 3.6 Hz, J2= 1.0 Hz, 2H), 7.32 (dd, J1= 5.1 Hz, J2= 1.0 Hz), 7.27 (dd, J1=7.9 Hz, J2= 1.5 Hz, 2H), 7.09 (dd, J1= 5.1 Hz, J2=3.6 Hz, 2H), 6.97 (d, J=1.1 Hz, 2H), 3.65 (d, J =7.4 Hz, 4H), 1.91 (s, 2H), 1.37-1.12 (m, 32H), 1.02-0.69 (m, 12H)

^{13}C NMR ($CDCl_3$, 300MHz) δ 167.66, 144.27, 143.98, 136.31, 130.27, 128.59, 128.21, 125.55, 123.69, 122.61, 121.70, 119.57, 105.80, 44.17, 36.42, 31.82, 31.76, 31.46, 29.65, 28.83, 26.60, 23.03, 22.63, 14.08

HR-MS (FD): calculated for C_{50} H_{64} O_2 N_2 S_2: 788.44092; found (M^+): m/z 788.44010

(3Z)-6-(benzofuran-2-yl)-3-((Z)-2-(6-(benzofuran-2-yl)-1-(2-butyloctyl)-2-oxoindolin-3-ylidene)ethylidene)-1-(2-butyloctyl)indolin-2-one (EBI-BF-C_{12}):

2a (0.41 g, 0.53 mmol, 1 eq) and trimethyl(benzofuran-2-yl)stannane (0.35 g, 1.26 mmol, 2.4 eq) were placed in a 50 ml dried flask and then, the flask was evacuated and back-filled with argon three times. Next, 15 ml of anhydrous toluene was poured into the flask. A mixture of $Pd_2(dba)_3$ (0.011 g, 0.011 mmol, 0.02 eq) and P(*o*-totyl)$_3$ (12.7 mg) which were separately introduced in 1 ml of anhydrous toluene were injected into the flask. The mixture was heated at 110°C under argon and stirred for 12 hours. Toluene was evaporated. The compound was purified on silica gel chromatography column with hexane and DCM (60:40) as eluent. The product was crystallized in isopropanol three times. 0.27 g of EBI-BF-C_{12} was obtained giving a yield of 55 %.

^{1}H NMR ($CDCl_3$, 300MHz) δ 8.98 (s, 2H), 7.68 (d, *J* = 7.9 Hz, 2H), 7.59 (d, *J* = 7.4 Hz, 2H), 7.52 (d, *J* = 7.6 Hz, 4H), 7.38 – 7.18 (m, 6H), 7.07 (s, 2H), 3.70 (d, *J* = 5.2 Hz, 4H), 1.97 (s, 2H), 1.46 – 1.17 (m, 32H), 1.01 – 0.74 (m, 12H).

^{13}C NMR ($CDCl_3$, 300MHz) δ 167.55, 155.50, 154.94, 143.91, 132.05, 130.32, 129.06, 128.86, 124.80, 123.52, 123.14, 121.56, 121.06, 118.71, 111.19, 104.61, 102.55, 44.22, 36.42, 31.87, 31.74, 31.44, 29.68, 28.82, 26.58, 23.06, 22.64, 14.15, 14.10

HR-MS (FD): calculated for C_{58} H_{68} O_4 N_2: 856.51857; found (M^+): m/z 856.51791

(3Z)-6-(benzofuran-2-yl)-3-((Z)-2-(6-(benzofuran-2-yl)-1-(2-hexyldecyl)-2-oxoindolin-3-ylidene)ethylidene)-1-(2-hexyldecyl)indolin-2-one (EBI-BF-C_{16}):

2b (0.55 g, 0.61 mmol, 1 eq), trimethyl(benzofuran-2-yl)stannane (0.41 g, 1.46 mmol, 2.4 eq) and P(o-totyl)$_3$ (14.8 mg, 0.05 mmol, 0.08 eq) were placed in a 50 ml dried flask and then, the flask was evacuated and back-filled with argon three times. Next, 17 ml of anhydrous toluene was poured into the flask. $Pd_2(dba)_3$ (0.013 g, 0.012 mmol, 0.02 eq) were separately introduced in 1 ml of anhydrous toluene and were injected into the flask. The mixture was heated at 110°C under argon and stirred for 24 hours. Toluene was evaporated. The compound was purified on silica gel chromatography column with hexane and DCM (50:50) as eluent. The product was crystallized in isopropanol three times. 0.44 g of EBI-BF-C_{16} was obtained giving a yield of 68.1 %.

^{1}H NMR (TCE-d2, 300MHz): δ 8.94 (s, 2H), 7.67 (d, *J* = 7.9 Hz, 2H), 7.57 (d, *J* = 7.5 Hz, 2H), 7.51 (d, *J* = 5.8 Hz, 4H), 7.36 – 7.18 (m, 6H), 7.08 (s, 2H), 3.65 (d, *J* = 7.3 Hz, 4H), 1.92 (s, 2H), 1.46 – 1.08 (m, 49H), 0.90 – 0.73 (m, 13H).

^{13}C NMR ($CDCl_3$, 300MHz) δ 167.51, 155.51, 154.93, 143.88, 132.02, 130.27, 129.06, 128.82, 124.78, 123.52, 123.13, 121.53, 121.04, 118.69, 111.19, 104.59, 102.52, 44.21, 36.41, 31.88, 31.75, 30.00, 29.68, 29.61, 29.32, 26.59, 22.65, 14.09

HR-MS (FD): calculated for C_{66} H_{84} O_4 N_2 : 968.64311; found (M^+): m/z 968.64439

(3Z)-1-(2-butyloctyl)-3_((Z)-2-(1-(2-butyloctyl)-2-oxo-6-(5-(thiophen-2-yl)thiophen-2-yl)indolin-3-ylidene)ethylidene)-6-(5-(thiophen-2-yl)thiophen-2-yl)indolin-2-one (EBI-2T):

To a three-necked round bottom flask were added **2a** (0.5 g, 0.64 mmol, 1 eq), 4,4,5,5-tetramethyl-2(5-(thiophen-2-yl)thiophen-2-yl)-1,3,2-dioxaborolane (0.41 g, 1.4 mmol, 2.2 eq), 10 ml of toluene and 10 ml of an aqueous solution of carbonate potassium (2M). The system was placed under argon. $Pd(PPh_3)_4$ (74 mg, 0.064 mmol, 0.1 eq) was added. The reaction was heated at 85°C for 24 hours. The product was extracted with DCM and washed with deionized water three times. The organic phase was dried with dehydrated sodium sulfate and DCM was removed under vacuum. The compound was further purified by silica gel chromatography column with chloroform/hexane (60:40) as eluent. 410 mg of EBI-2T were obtained giving a yield of 67 %.

^{13}C NMR ($CDCl_3$, 300MHz) δ 167.7, 144.03, 142.87, 137.55, 137.19, 135.94, 130.19, 128.60, 127.95, 124.73, 124.70, 124.42, 123.88, 122.75, 121.74, 119.19, 105.36, 44.22, 36.50, 31.88, 31.84, 31.54, 29.69, 28.90, 26.67, 23.07, 22.66, 14.13, 14.09

HR-MS (FD): calculated for C_{58} H_{68} O_2 N_2 S_4: 956.41636; found (M^+): m/z 952.41883

REFERENCES

[1] Becquerel E, Hebd CR. On electric effects under the influence of solar radiation. Seance AcadSci 1839:561.

[2] Fritts CE. New Form of Selenium Cell. Am J Sci 1883;26:465–72.

[3] Zhao J, Wang A, Green MA. High-efficiency PERL and PERT silicon solar cells on FZ and MCZ substrates. Sol Energy Mater Sol Cells 2001;65:429–35. doi:10.1016/S0927-0248(00)00123-9.

[4] Wu X. High-efficiency polycrystalline CdTe thin-film solar cells. Sol Energy 2004;77:803–14. doi:10.1016/j.solener.2004.06.006.

[5] Naghavi N, Spiering S, Powalla M, Cavana B, Lincot D. High-efficiency copper indium gallium diselenide (CIGS) solar cells with indium sulfide buffer layers deposited by atomic layer chemical vapor deposition (ALCVD). Prog Photovoltaics Res Appl 2003;11:437–43. doi:10.1002/pip.508.

[6] Clifford JN, Martínez-Ferrero E, Viterisi A, Palomares E. Sensitizer molecular structure-device efficiency relationship in dye sensitized solar cells. Chem Soc Rev 2011;40:1635–46. doi:10.1039/b920664g.

[7] Mishra A, Fischer MKR, Baüerle P. Metal-Free organic dyes for dye-Sensitized solar cells: From structure: Property relationships to design rules. Angew Chemie - Int Ed 2009;48:2474–99. doi:10.1002/anie.200804709.

[8] Snaith HJ. Perovskites : The Emergence of a New Era for Low-Cost , High-Efficiency Solar Cells. J Phys Chem Lett 2013;4:3623−3630. doi:10.1021/jz4020162.

[9] Green MA, Ho-Baillie A, Snaith HJ. The emergence of perovskite solar cells. Nat Phot 2014;8:506–14. doi:10.1038/nphoton.2014.134.

[10] Brabec CJ. Organic photovoltaics: technology and market. Sol Energy Mater Sol Cells 2004;83:273–92. doi:10.1016/j.solmat.2004.02.030.

[11] Hoppe H, Sariciftci NS. Organic solar cells: An overview. J Mater Res 2011;19:1924–45. doi:10.1557/JMR.2004.0252.

[12] Søndergaard RR, Hösel M, Krebs FC. Roll-to-Roll fabrication of large area functional organic materials. J Polym Sci Part B Polym Phys 2013;51:16–34. doi:10.1002/polb.23192.

[13] Singh M, Haverinen HM, Dhagat P, Jabbour GE. Inkjet printing-process and its applications. Adv Mater 2010;22:673–85. doi:10.1002/adma.200901141.

[14] Krebs FC, Jørgensen M, Norrman K, Hagemann O, Alstrup J, Nielsen TD, et al. A complete process for production of flexible large area polymer solar cells entirely using screen printing—First public demonstration. Sol Energy Mater Sol Cells 2009;93:422–41. doi:10.1016/j.solmat.2008.12.001.

[15] Kallmann H, Pope M. Photovoltaic Effect in Organic Crystals. J Chem Phys 1959;30:585–6.

[16] Tang CW. Two-layer organic photovoltaic cell. Appl Phys Lett 1986;48:183. doi:10.1063/1.96937.

[17] Kaur N, Singh M, Pathak D, Wagner T, Nunzi JM. Organic materials for photovoltaic applications: Review and mechanism. Synth Met 2014;190:20–6.

doi:10.1016/j.synthmet.2014.01.022.
[18] Heremans P, Cheyns D, Rand BP. Strategies for increasing the efficiency of heterojunction organic solar cells: material selection and device architecture. Acc Chem Res 2009;42:1740–7. doi:10.1021/ar9000923.
[19] Menke SM, Holmes RJ. Exciton diffusion in organic photovoltaic cells. Energy Environ Sci 2014;7. doi:10.1039/c3ee42444h.
[20] Riordan C, Hulstron R. What is an air mass 1.5 spectrum? [solar cell performance\ncalculations]. IEEE Conf Photovolt Spec 1990:1085–8. doi:10.1109/PVSC.1990.111784.
[21] Housecroft CE, Constable EC. The emergence of copper(<scp>i</scp>)-based dye sensitized solar cells. Chem Soc Rev 2015;44:8386–98. doi:10.1039/C5CS00215J.
[22] Peumans P, Yakimov A, Forrest SR. Small molecular weight organic thin-film photodetectors and solar cells. J Appl Phys 2003;93:3693. doi:10.1063/1.1534621.
[23] Scharber MC, Mühlbacher D, Koppe M, Denk P, Waldauf C, Heeger a. J, et al. Design Rules for Donors in Bulk-Heterojunction Solar Cells—Towards 10 % Energy-Conversion Efficiency. Adv Mater 2006;18:789–94. doi:10.1002/adma.200501717.
[24] Guo X, Zhou N, Lou SJ, Smith J, Tice DB, Hennek JW, et al. Polymer solar cells with enhanced fill factors. Nat Photonics 2013;7:825–33. doi:10.1038/nphoton.2013.207.
[25] Etxebarria I, Ajuria J, Pacios R. Solution-processable polymeric solar cells: A review on materials, strategies and cell architectures to overcome 10%. Org Electron 2015;19:34–60. doi:10.1016/j.orgel.2015.01.014.
[26] Cao W, Xue J. Recent progress in organic photovoltaics: device architecture and optical design. Energy Environ Sci 2014:2123–44. doi:10.1039/c4ee00260a.
[27] Yu G, Gao J, Hummelen JC, Wudl F, Heeger a. J. Polymer Photovoltaic Cells: Enhanced Efficiencies via a Network of Internal Donor-Acceptor Heterojunctions. Science (80-) 1995;270:1789–91. doi:10.1126/science.270.5243.1789.
[28] Ratcliff EL, Zacher B, Armstrong NR. Selective Interlayers and Contacts in Organic Photovoltaic Cells. J Phys Chem Lett 2011:1337–50. doi:10.1021/jz2002259.
[29] Ma W, Tumbleston JR, Wang M, Gann E, Huang F, Ade H. Domain Purity, Miscibility, and Molecular Orientation at Donor/Acceptor Interfaces in High Performance Organic Solar Cells: Paths to Further Improvement. Adv Energy Mater 2013;3:864–72. doi:10.1002/aenm.201200912.
[30] Collins B a., Tumbleston JR, Ade H. Miscibility, crystallinity, and phase development in P3HT/PCBM solar cells: Toward an enlightened understanding of device morphology and stability. J Phys Chem Lett 2011;2:3135–45. doi:10.1021/jz2014902.
[31] Li M, Liu J, Cao X, Zhou K, Zhao Q, Yu X, et al. Achieving balanced intermixed and pure crystalline phases in PDI-based non-fullerene organic solar cells via selective solvent additives. Phys Chem Chem Phys 2014;16:26917–28. doi:10.1039/C4CP04161E.
[32] Scarongella M, Paraecattil AA, Buchaca-Domingo E, Douglas JD, Beaupré S, McCarthy-Ward T, et al. The influence of microstructure on charge separation dynamics in organic bulk heterojunction materials for solar cell applications. J Mater Chem A 2014;2:6218–30. doi:10.1039/c3ta15112c.
[33] Yang X, Loos J. Toward high-performance polymer solar cells: The importance of morphology control. Macromolecules 2007;40:1353–62. doi:10.1021/ma0618732.
[34] Westacott P, Tumbleston JR, Shoaee S, Fearn S, Bannock JH, Gilchrist JB, et al. On the role of intermixed phases in organic photovoltaic blends. Energy Environ Sci

2013;6:2756–64. doi:10.1039/c3ee41821a.
[35] Dang MT, Hirsch L, Wantz G, Wuest JD. Controlling the morphology and performance of bulk heterojunctions in solar cells. Lessons learned from the benchmark poly(3-hexylthiophene):[6,6]-phenyl-C61-butyric acid methyl ester system. Chem Rev 2013;113:3734–65. doi:10.1021/cr300005u.
[36] Chang J-F, Sun B, Breiby DW, Nielsen MM, Sölling TI, Giles M, et al. Enhanced Mobility of Poly(3-hexylthiophene) Transistors by Spin-Coating from High-Boiling-Point Solvents. Chem Mater 2004;16:4772–6. doi:10.1021/cm049617w.
[37] Duong DT, Walker B, Lin J, Kim C, Love J, Purushothaman B, et al. Molecular solubility and hansen solubility parameters for the analysis of phase separation in bulk heterojunctions. J Polym Sci Part B Polym Phys 2012;50:1405–13. doi:10.1002/polb.23153.
[38] Dang MT, Wantz G, Bejbouji H, Urien M, Dautel OJ, Vignau L, et al. Polymeric solar cells based on P3HT:PCBM: Role of the casting solvent. Sol Energy Mater Sol Cells 2011;95:3408–18. doi:10.1016/j.solmat.2011.07.039.
[39] Kyaw AKK, Wang DH, Luo C, Cao Y, Nguyen TQ, Bazan GC, et al. Effects of solvent additives on morphology, charge generation, transport, and recombination in solution-processed small-molecule solar cells. Adv Energy Mater 2014;4:1–9. doi:10.1002/aenm.201301469.
[40] Vongsaysy U, Bassani DM, Servant L, Pavageau B, Wantz G, Aziz H. Formulation strategies for optimizing the morphology of polymeric bulk heterojunction organic solar cells: a brief review. J Photonics Energy 2014;4:040998. doi:10.1117/1.JPE.4.040998.
[41] Dang MT, Wuest JD. Using volatile additives to alter the morphology and performance of active layers in thin-film molecular photovoltaic devices incorporating bulk heterojunctions. Chem Soc Rev 2013;42:9105–26. doi:10.1039/c3cs35447d.
[42] Park JK, Kim C, Walker B, Nguyen T-Q, Seo JH. Morphology control of solution processable small molecule bulk heterojunction solar cells via solvent additives. RSC Adv 2012;2:2232. doi:10.1039/c2ra01182d.
[43] Hoven C V, Dang X-D, Coffin RC, Peet J, Nguyen T-Q, Bazan GC. Improved performance of polymer bulk heterojunction solar cells through the reduction of phase separation via solvent additives. Adv Mater 2010;22:E63–6. doi:10.1002/adma.200903677.
[44] Ma W, Yang C, Gong X, Lee K, Heeger AJ. Thermally Stable, Efficient Polymer Solar Cells with Nanoscale Control of the Interpenetrating Network Morphology. Adv Funct Mater 2005;15:1617–22. doi:10.1002/adfm.200500211.
[45] Ismail YAM, Soga T, Jimbo T. Investigation of Annealing and Blend Concentration Effects of Organic Solar Cells Composed of Small Organic Dye and Fullerene Derivative. Adv Optoelectron 2011;2011:1–10. doi:10.1155/2011/106276.
[46] Xue S, Yao L, Liu S, Gu C, Shen F, Li W, et al. Simultaneous enhancement of the carrier mobility and luminous efficiency through thermal annealing a molecular glass material and device. J Mater Chem 2012;22:21502. doi:10.1039/c2jm34663j.
[47] Jørgensen M, Norrman K, Krebs FC. Stability/degradation of polymer solar cells. Sol Energy Mater Sol Cells 2008;92:686–714. doi:10.1016/j.solmat.2008.01.005.
[48] Min J, Luponosov YN, Gerl A, Polinskaya MS, Peregudova SM, Dmitryakov P V., et al. Alkyl chain engineering of solution-processable star-shaped molecules for high-performance organic solar cells. Adv Energy Mater 2014;4:1–10.

doi:10.1002/aenm.201301234.
[49] Jung M, Yoon Y, Park JH, Cha W, Kim A, Kang J, et al. Nanoscopic management of molecular packing and orientation of small molecules by a combination of linear and branched alkyl side chains. ACS Nano 2014;8:5988–6003. doi:10.1021/nn501133y.
[50] Mei J, Bao Z. Side Chain Engineering in Solution-Processable Conjugated Polymers. Chem Mater 2014;26:604–15. doi:10.1021/cm4020805.
[51] Karsten BP, Janssen RAJ. Chain Length Dependence in Diketopyrrolopyrrole/Thiophene Oligomers. Macromol Chem Phys 2011;212:515–20. doi:10.1002/macp.201000695.
[52] Proctor CM, Love JA, Nguyen TQ. Mobility guidelines for high fill factor solution-processed small molecule solar cells. Adv Mater 2014:5957–61. doi:10.1002/adma.201401725.
[53] Odajima T, Ashizawa M, Konosu Y, Matsumoto H, Mori T. The impact of molecular planarity on electronic devices in thienoisoindigo-based organic semiconductors. J Mater Chem C 2014;2:10455–67. doi:10.1039/C4TC02170C.
[54] Do K, Kim C, Song K, Yun SJ, Lee JK, Ko J. Efficient planar organic semiconductors containing fused triphenylamine for solution processed small molecule organic solar cells. Sol Energy Mater Sol Cells 2013;115:52–7. doi:10.1016/j.solmat.2013.03.020.
[55] Lee OP, Yiu AT, Beaujuge PM, Woo CH, Holcombe TW, Millstone JE, et al. Efficient small molecule bulk heterojunction solar cells with high fill factors via pyrene-directed molecular self-assembly. Adv Mater 2011;23:5359–63. doi:10.1002/adma.201103177.
[56] Abdulrazzaq O a., Saini V, Bourdo S, Dervishi E, Biris AS. Organic Solar Cells: A Review of Materials, Limitations, and Possibilities for Improvement. Part Sci Technol 2013;31:427–42. doi:10.1080/02726351.2013.769470.
[57] Lin Y, Li Y, Zhan X. Small molecule semiconductors for high-efficiency organic photovoltaics. Chem Soc Rev 2012;41:4245–72. doi:10.1039/c2cs15313k.
[58] Liao S-H, Jhuo H-J, Yeh P-N, Cheng Y-S, Li Y-L, Lee Y-H, et al. Single junction inverted polymer solar cell reaching power conversion efficiency 10.31% by employing dual-doped zinc oxide nano-film as cathode interlayer. Sci Rep 2014;4:6813. doi:10.1038/srep06813.
[59] Kan B, Zhang Q, Li M, Wan X, Ni W, Long G, et al. Solution-processed organic solar cells based on dialkylthiol-substituted benzodithiophene unit with efficiency near 10%. J Am Chem Soc 2014;136:15529–32. doi:10.1021/ja509703k.
[60] Chen Y, Wan X, Long G. High performance photovoltaic applications using solution-processed small molecules. Acc Chem Res 2013;46:2645–55. doi:10.1021/ar400088c.
[61] Liu Y, Zhao J, Li Z, Mu C, Ma W, Hu H, et al. Aggregation and morphology control enables multiple cases of high-efficiency polymer solar cells. Nat Commun 2014;5:1–8. doi:10.1038/ncomms6293.
[62] Zhao J, Li Y, Yang G, Jiang K, Lin H, Ade H, et al. Efficient organic solar cells processed from hydrocarbon solvents. Nat Energy 2016. doi:10.1038/nenergy.2015.27.
[63] Kan B, Li M, Zhang Q, Liu F, Wan X, Wang Y, et al. A Series of Simple Oligomer-like Small Molecules Based on Oligothiophenes for Solution-Processed Solar Cells with High Efficiency. J Am Chem Soc 2015;11:3886–93. doi:10.1021/jacs.5b00305.
[64] Kim Y, Cook S, Tuladhar SM, Choulis SA, Nelson J, Durrant JR, et al. A strong regioregularity effect in self-organizing conjugated polymer films and high-efficiency polythiophene:fullerene solar cells. Nat Mater 2006;5:197–203. doi:10.1038/nmat1574.
[65] Neto B a. D, Lapis A a. M, da Silva Júnior EN, Dupont J. 2,1,3-Benzothiadiazole and

Derivatives: Synthesis, Properties, Reactions, and Applications in Light Technology of Small Molecules. European J Org Chem 2013;2013:228–55. doi:10.1002/ejoc.201201161.
[66] Chandran D, Lee K-S. Diketopyrrolopyrrole: A versatile building block for organic photovoltaic materials. Macromol Res 2013;21:272–83. doi:10.1007/s13233-013-1141-3.
[67] Sista P, Biewer MC, Stefan MC. Benzo[1,2-b:4,5-b']dithiophene building block for the synthesis of semiconducting polymers. Macromol Rapid Commun 2012;33:9–20. doi:10.1002/marc.201100671.
[68] He Z, Zhong C, Su S, Xu M, Wu H, Cao Y. Enhanced power-conversion efficiency in polymer solar cells using an inverted device structure. Nat Photonics 2012;6:593–7. doi:10.1038/nphoton.2012.190.
[69] Liao S-H, Jhuo H-J, Cheng Y-S, Chen S-A. Fullerene derivative-doped zinc oxide nanofilm as the cathode of inverted polymer solar cells with low-bandgap polymer (PTB7-Th) for high performance. Adv Mater 2013;25:4766–71. doi:10.1002/adma.201301476.
[70] Woo S, Hyun Kim W, Kim H, Yi Y, Lyu H-K, Kim Y. 8.9% Single-Stack Inverted Polymer Solar Cells with Electron-Rich Polymer Nanolayer-Modified Inorganic Electron-Collecting Buffer Layers. Adv Energy Mater 2014;4:1301692. doi:10.1002/aenm.201301692.
[71] Hoppe H, Sariciftci NS. Morphology of polymer/fullerene bulk heterojunction solar cells. J Mater Chem 2006;16:45. doi:10.1039/b510618b.
[72] Mishra A, Bäuerle P. Small molecule organic semiconductors on the move: promises for future solar energy technology. Angew Chem Int Ed Engl 2012;51:2020–67. doi:10.1002/anie.201102326.
[73] Lin Y, Li Y, Zhan X. Small molecule semiconductors for high-efficiency organic photovoltaics. Chem Soc Rev 2012;41:4245–72. doi:10.1039/c2cs15313k.
[74] Riede M, Mueller T, Tress W, Schueppel R, Leo K. Small-molecule solar cells-status and perspectives. Nanotechnology 2008;19:424001. doi:10.1088/0957-4484/19/42/424001.
[75] Sun Y, Welch GC, Leong WL, Takacs CJ, Bazan GC, Heeger AJ. Solution-processed small-molecule solar cells with 6.7% efficiency. Nat Mater 2012;11:44–8. doi:10.1038/nmat3160.
[76] Lin Y, Zhan X. Oligomer Molecules for Efficient Organic Photovoltaics. Acc Chem Res 2015. doi:10.1021/acs.accounts.5b00363.
[77] Zhou J, Zuo Y, Wan X, Long G, Zhang Q, Ni W, et al. Solution-processed and high-performance organic solar cells using small molecules with a benzodithiophene unit. J Am Chem Soc 2013;135:8484–7. doi:10.1021/ja403318y.
[78] Yang D, Yang Q, Yang L, Luo Q, Huang Y, Lu Z, et al. Novel high performance asymmetrical squaraines for small molecule organic solar cells with a high open circuit voltage of 1.12 V. Chem Commun (Camb) 2013;49:10465–7. doi:10.1039/c3cc46217j.
[79] Lee JW, Choi YS, Jo WH. Diketopyrrolopyrrole-based small molecules with simple structure for high VOC organic photovoltaics. Org Electron 2012;13:3060–6. doi:10.1016/j.orgel.2012.09.004.
[80] Liu J, Sun Y, Moonsin P, Kuik M, Proctor CM, Lin J, et al. Tri-diketopyrrolopyrrole molecular donor materials for high-performance solution-processed bulk heterojunction solar cells. Adv Mater 2013;25:5898–903. doi:10.1002/adma.201302007.
[81] He G, Li Z, Wan X, Zhou J, Long G, Zhang S, et al. Efficient small molecule bulk heterojunction solar cells with high fill factors via introduction of π-stacking moieties as end group. J Mater Chem A 2013;1:1801–9. doi:10.1039/C2TA00496H.

[82] Brocks G, Tol A. A theoretical study of polysquaraines. Synth Met 1996;76:213–6. doi:10.1016/0379-6779(95)03455-S.
[83] Kronenberg NM, Deppisch M, Würthner F, Lademann HW a, Deing K, Meerholz K. Bulk heterojunction organic solar cells based on merocyanine colorants. Chem Commun (Camb) 2008:6489–91. doi:10.1039/b813341g.
[84] Silvestri F, Irwin MD, Beverina L, Facchetti A, Pagani GA, Marks TJ, et al. Efficient Squaraine-Based Solution Processable Bulk-Heterojunction Solar Cells 2008:17640–1.
[85] Tamayo AB, Walker B, Nguyen T-Q. A Low Band Gap, Solution Processable Oligothiophene with a Diketopyrrolopyrrole Core for Use in Organic Solar Cells. J Phys Chem C 2008;112:11545–51. doi:10.1021/jp8031572.
[86] Li Y, Guo Q, Li Z, Pei J, Tian W. Solution processable D–A small molecules for bulk-heterojunction solar cells. Energy Environ Sci 2010;3:1427. doi:10.1039/c003946b.
[87] Ni W, Wan X, Li M, Wang Y, Chen Y. A–D–A small molecules for solution-processed organic photovoltaic cells. Chem Commun 2015;51:4936–50. doi:10.1039/C4CC09758K.
[88] Roncali J, Leriche P, Blanchard P. Molecular Materials for Organic Photovoltaics: Small is Beautiful. Adv Mater 2014;26:3821–38. doi:10.1002/adma.201305999.
[89] Qin H, Li L, Guo F, Su S, Peng J, Cao Y, et al. Solution-processed bulk heterojunction solar cells based on a porphyrin small molecule with 7% power conversion efficiency. Energy Environ Sci 2014;7:1397. doi:10.1039/c3ee43761b.
[90] Yang D, Yang L, Huang Y, Jiao Y, Igarashi T, Chen Y, et al. Asymmetrical Squaraines Bearing Fluorine-Substituted Indoline Moieties for High-Performance Solution-Processed Small-Molecule Organic Solar Cells. ACS Appl Mater Interfaces 2015;7:13675–84. doi:10.1021/acsami.5b03558.
[91] Tamayo AB, Dang X-D, Walker B, Seo J, Kent T, Nguyen T-Q. A low band gap, solution processable oligothiophene with a dialkylated diketopyrrolopyrrole chromophore for use in bulk heterojunction solar cells. Appl Phys Lett 2009;94:103301. doi:10.1063/1.3086897.
[92] Walker B, Tamayo AB, Dang X-D, Zalar P, Seo JH, Garcia A, et al. Nanoscale Phase Separation and High Photovoltaic Efficiency in Solution-Processed, Small-Molecule Bulk Heterojunction Solar Cells. Adv Funct Mater 2009;19:3063–9. doi:10.1002/adfm.200900832.
[93] Liu J, Sun Y, Moonsin P, Kuik M, Proctor CM, Lin J, et al. Tri-Diketopyrrolopyrrole Molecular Donor Materials for High-Performance Solution-Processed Bulk Heterojunction Solar Cells. Adv Mater 2013:1–6. doi:10.1002/adma.201302007.
[94] Huang J, Zhan C, Zhang X, Zhao Y, Lu Z, Jia H, et al. Solution-processed DPP-based small molecule that gives high photovoltaic efficiency with judicious device optimization. Appl Mater Interfaces 2013:2033–9. doi:10.1021/am302896u.
[95] Chen G, Sasabe H, Igarashi T, Hong Z, Kido J. Squaraine dyes for organic photovoltaic cells. J Mater Chem A 2015;3:14517–34. doi:10.1039/C5TA01879J.
[96] Wei G, Wang S, Sun K, Thompson ME, Forrest SR. Solvent-Annealed Crystalline Squaraine: PC70BM (1:6) Solar Cells. Adv Energy Mater 2011;1:184–7. doi:10.1002/aenm.201100045.
[97] Wei G, Wang S, Renshaw K, Thompson ME, Forrest SR. Solution-Processed Squaraine Bulk. ACS Nano 2010;4:1927–34.
[98] Chen G, Sasabe H, Sasaki Y, Katagiri H, Wang XF, Sano T, et al. A series of squaraine dyes: Effects of side chain and the number of hydroxyl groups on material properties and

photovoltaic performance. Chem Mater 2014;26:1356–64. doi:10.1021/cm4034929.
[99] Sasabe H, Igrashi T, Sasaki Y, Chen G, Hong Z, Kido J. Soluble squaraine derivatives for 4.9% efficient organic photovoltaic cells. RSC Adv 2014;4:42804–7. doi:10.1039/C4RA08171D.
[100] Chen Y, Zhu Y, Yang D, Luo Q, Yang L, Huang Y, et al. Asymmetrical squaraines for high-performance small-molecule organic solar cells with a short circuit current of over 12 mA cm $^{-2}$. Chem Commun 2015;51:6133–6. doi:10.1039/C5CC00704F.
[101] Paek S, Choi H, Jo H, Lee K, Song K, Siddiqui S a., et al. A new unsymmetrical near-IR small molecule with squaraine chromophore for solution processed bulk heterojunction solar cells. J Mater Chem C 2015;3:7029–37. doi:10.1039/C5TC00679A.
[102] Yang D, Yang Q, Yang L, Luo Q, Chen Y, Zhu Y, et al. A low bandgap asymmetrical squaraine for high-performance solution-processed small molecule organic solar cells. Chem Commun 2014;50:9346–8. doi:10.1039/C4CC03831B.
[103] Yang D, Jiao Y, Yang L, Chen Y, Mizoi S, Huang Y, et al. Cyano-substitution on the end-capping group: facile access toward asymmetrical squaraine showing strong dipole – dipole interactions as a high performance small molecular organic solar cells material. J Mater Chem A 2015;3:17704–12. doi:10.1039/C5TA03971A.
[104] Zeng S, Yin L, Ji C, Jiang X, Li K, Li Y, et al. D-π-A-π-D type benzothiadiazole-triphenylamine based small molecules containing cyano on the π-bridge for solution-processed organic solar cells with high open-circuit voltage. Chem Commun (Camb) 2012;48:10627–9. doi:10.1039/c2cc35754b.
[105] Guo S, Ning J, Körstgens V, Yao Y, Herzig EM, Roth S V, et al. The Effect of Fluorination in Manipulating the Nanomorphology in PTB7 : PC 71 BM Bulk Heterojunction Systems. Adv Energy Mater 2015:1401315. doi:10.1002/aenm.201401315.
[106] Cravino A, Roquet S, Leriche P, Alévêque O, Frère P, Roncali J. A star-shaped triphenylamine pi-conjugated system with internal charge-transfer as donor material for hetero-junction solar cells. Chem Commun (Camb) 2006:1416–8. doi:10.1039/b516781g.
[107] Ripaud E, Rousseau T, Leriche P, Roncali J. Unsymmetrical triphenylamine-oligothiophene hybrid conjugated systems as donor materials for high-voltage solution-processed organic solar cells. Adv Energy Mater 2011;1:540–5. doi:10.1002/aenm.201100065.
[108] Lin Y, Zhang Z-G, Bai H, Li Y, Zhan X. A star-shaped oligothiophene end-capped with alkyl cyanoacetate groups for solution-processed organic solar cells. Chem Commun 2012;48:9655–7. doi:10.1039/C2CC35333D.
[109] Shang H, Fan H, Liu Y, Hu W, Li Y, Zhan X. A solution-processable star-shaped molecule for high-performance organic solar cells. Adv Mater 2011;23:1554–7. doi:10.1002/adma.201004445.
[110] Paek S, Cho N, Song K, Jun M-J, Lee JK, Ko J. Efficient Organic Semiconductors Containing Fluorine-Substituted Benzothiadiazole for Solution-Processed Small Molecule Organic Solar Cells. J Phys Chem C 2012;116:121022051954006. doi:10.1021/jp305989g.
[111] Cho N, Paek S, Jeon J, Song K, Sharma GD, Ko J. Synthesis, optical and electrochemical properties of small molecules DMM-TPA[DTS(FBTTh3)3] and TPA[DTS(FBTTh3)3], and their application as donors for bulk heterojunction solar cells. J Mater Chem A 2014;2:12368. doi:10.1039/C4TA01768D.

[112] Kumar CV, Cabau L, Koukaras EN, Sharma GD, Palomares E. Efficient solution processed D1-A-D2-A-D1 small molecules bulk heterojunction solar cells based on alkoxy triphenylamine and benzo[1,2-b:4,5-b′]thiophene units. Org Electron 2015;26:36–47. doi:10.1016/j.orgel.2015.07.014.
[113] Huang J, Wang X, Zhang X, Niu Z, Lu Z, Jiang B, et al. Additive-Assisted Control over Phase-Separated Nanostructures by Manipulating Alkylthienyl Position at Donor Backbone for Solution-Processed, Non-Fullerene, All-Small-Molecule Solar Cells. Appl Mater Interfaces 2014;6:3853–62. doi:10.1021/am406050j.
[114] Gupta V, Kyaw AKK, Wang DH, Chand S, Bazan GC, Heeger AJ. Barium: an efficient cathode layer for bulk-heterojunction solar cells. Sci Rep 2013;3:1965. doi:10.1038/srep01965.
[115] Zhou J, Wan X, Liu Y, Zuo Y, Li Z, He G, et al. Small Molecules Based on Benzo[1,2-b:4,5-b']dithiophene Unit for High-Performance Solution-Processed Organic Solar Cells. J Am Chem Soc 2012;134:16345–51. doi:10.1021/ja306865z.
[116] Ni W, Li M, Wan X, Feng H, Kan B, Zuo Y, et al. A high-performance photovoltaic small molecule developed by modifying the chemical structure and optimizing the morphology of the active layer. RSC Adv 2014;4:31977. doi:10.1039/C4RA04862H.
[117] Cardona CM, Li W, Kaifer AE, Stockdale D, Bazan GC. Electrochemical considerations for determining absolute frontier orbital energy levels of conjugated polymers for solar cell applications. Adv Mater 2011;23:2367–71. doi:10.1002/adma.201004554.
[118] Pommerehne J, Vestweber H, Guss W, Mahrt RF, Bässler H, Porsch M, et al. Efficient two layer leds on a polymer blend basis. Adv Mater 1995;7:551–4. doi:10.1002/adma.19950070608.
[119] Horowitz G. Organic field-effect transistors. Adv Mater 1998;10:365–77. doi:1.
[120] Bura T, Leclerc N, Bechara R, Lévêque P, Heiser T, Ziessel R. Triazatruxene-diketopyrrolopyrrole dumbbell-shaped molecules as photoactive electron donor for high-efficiency solution processed organic solar cells. Adv Energy Mater 2013;3:1118–24. doi:10.1002/aenm.201300240.
[121] Jung JW, Russell TP, Jo WH. A Small Molecule Composed of Dithienopyran and Diketo-pyrrolopyrrole as Versatile Electron Donor Compatible with Both Fullerene and Non-fullerene Electron Acceptors for High Performance Organic Solar Cells. Chem Mater 2015:150619095214008. doi:10.1021/acs.chemmater.5b01799.
[122] Kim J-H, Park JB, Yang H, Jung IH, Yoon SC, Kim D, et al. Controlling the Morphology of BDTT-DPP-based Small Molecules via End-group Functionalization for Highly Efficient Single and Tandem Organic Photovoltaic Cells. ACS Appl Mater Interfaces 2015:151012141738002. doi:10.1021/acsami.5b05248.
[123] Harschneck T, Zhou N, Manley EF, Lou SJ, Yu X, Butler MR, et al. Substantial photovoltaic response and morphology tuning in benzo[1,2-b:6,5-b']dithiophene (bBDT) molecular donors. Chem Commun (Camb) 2014;50:4099–101. doi:10.1039/c3cc49620a.
[124] Qian D, bo liu, Wang S, Himmelberger S, Linares M, Vagin M, et al. Modulating Molecular Aggregation by Facile Heteroatom Substitution of Diketopyrrolopyrrole based Small Molecules for Efficient Organic Solar Cells. J Mater Chem A 2015:24349–57. doi:10.1039/C5TA06501A.
[125] Duan X, Xiao M, Chen J, Wang X, Peng W, Duan L, et al. Improving Photovoltaic Performance of the Linear A-Ar-A-type Small Molecules with Diketopyrropyrrole Arms by Tuning the Linkage Position of the Anthracene Core. ACS Appl Mater Interfaces

2015;7:18292–9. doi:10.1021/acsami.5b03338.
[126] Liang T, Xiao L, Liu C, Gao K, Qin H, Cao Y, et al. Porphyrin small molecules containing furan- and selenophene-substituted diketopyrrolopyrrole for bulk heterojunction organic solar cells. Org Electron 2016;29:127–34. doi:10.1016/j.orgel.2015.11.035.
[127] Kumar CHP, Ganesh K, Suresh T, Sharma A, Bhanuprakash K, Sharma GD, et al. Influence of thermal and solvent annealing on the morphology and photovoltaic performance of solution processed, D–A–D type small molecule-based bulk heterojunction solar cells. RSC Adv 2015;5:93579–90. doi:10.1039/C5RA16812K.
[128] Yu C, Liu Z, Yang Y, Yao J, Cai Z, Luo H, et al. New dithienyl-diketopyrrolopyrrole-based conjugated molecules entailing electron withdrawing moieties for organic ambipolar semiconductors and photovoltaic materials. J Mater Chem C 2014;2:10101–9. doi:10.1039/C4TC01872A.
[129] Liu J, Sun Y, Moonsin P, Kuik M, Proctor CM, Lin J, et al. Tri-diketopyrrolopyrrole molecular donor materials for high-performance solution-processed bulk heterojunction solar cells. Adv Mater 2013;25:5898–903. doi:10.1002/adma.201302007.
[130] Sun B, Hong W, Yan Z, Aziz H, Li Y. Record high electron mobility of 6.3 $cm^2 V^{-1} s^{-1}$ achieved for polymer semiconductors using a new building block. Adv Mater 2014;26:2636–42, 2613. doi:10.1002/adma.201305981.
[131] Lee J, Jang M, Lee SM, Yoo D, Shin TJ, Oh JH, et al. Fluorinated benzothiadiazole (BT) groups as a powerful unit for high-performance electron-transporting polymers. Appl Mater Interfaces 2014:20390–9. doi:10.1021/am505925w.
[132] Sahu D, Tsai C-H, Wei H-Y, Ho K-C, Chang F-C, Chu C-W. Synthesis and applications of novel low bandgap star-burst molecules containing a triphenylamine core and dialkylated diketopyrrolopyrrole arms for organic photovoltaics. J Mater Chem 2012;22:7945. doi:10.1039/c2jm16760c.
[133] Hong W, Chen S, Sun B, Arnould M a., Meng Y, Li Y. Is a polymer semiconductor having a “perfect” regular structure desirable for organic thin film transistors? Chem Sci 2015;6:3225–35. doi:10.1039/C5SC00843C.
[134] Stas S, Balandier J-Y, Lemaur V, Fenwick O, Tregnago G, Quist F, et al. Straightforward access to diketopyrrolopyrrole (DPP) dimers. Dye Pigment 2013;97:198–208. doi:10.1016/j.dyepig.2012.12.005.
[135] Song S, Jin Y, Park SH, Cho S, Kim I, Lee K, et al. A low-bandgap alternating copolymer containing the dimethylbenzimidazole moiety. J Mater Chem 2010;20:6517–23. doi:10.1039/c0jm00772b.
[136] Perez LA, Chou KW, Love JA, Van Der Poll TS, Smilgies DM, Nguyen TQ, et al. Solvent additive effects on small molecule crystallization in bulk heterojunction solar cells probed during spin casting. Adv Mater 2013;25:6380–4. doi:10.1002/adma.201302389.
[137] Leong WL, Welch GC, Kaake LG, Takacs CJ, Sun Y, Bazan GC, et al. Role of trace impurities in the photovoltaic performance of solution processed small-molecule bulk heterojunction solar cells. Chem Sci 2012;3:2103. doi:10.1039/c2sc20157g.
[138] He Y, Zhao G, Peng B, Li Y. High-yield synthesis and electrochemical and photovoltaic properties of indene-C70 bisadduct. Adv Funct Mater 2010;20:3383–9. doi:10.1002/adfm.201001122.
[139] Huang Q, Li H. Recent progress of bulk heterojunction solar cells based on small-molecular donors. Chinese Sci Bull 2013;58:2677–85. doi:10.1007/s11434-013-5930-z.

[140] Destouesse E, Chambon S, Courtel S, Hirsch L, Wantz G. Solution-Processed Small-Molecule Bulk Heterojunctions: Leakage Currents and the Dewetting Issue for Inverted Solar Cells. ACS Appl Mater Interfaces 2015;7:24663–9. doi:10.1021/acsami.5b06964.
[141] Luhman WA, Holmes RJ. Enhanced exciton diffusion in an organic photovoltaic cell by energy transfer using a phosphorescent sensitizer. Appl Phys Lett 2009;94:153304. doi:10.1063/1.3120566.
[142] Ruderer MA, Guo S, Meier R, Chiang HY, Körstgens V, Wiedersich J, et al. Solvent-induced morphology in polymer-based systems for organic photovoltaics. Adv Funct Mater 2011;21:3382–91. doi:10.1002/adfm.201100945.
[143] Karagiannidis PG, Georgiou D, Pitsalidis C, Laskarakis A, Logothetidis S. Evolution of vertical phase separation in P3HT:PCBM thin films induced by thermal annealing. Mater Chem Phys 2011;129:1207–13. doi:10.1016/j.matchemphys.2011.06.007.
[144] Jo J, Na S-I, Kim S-S, Lee T-W, Chung Y, Kang S-J, et al. Three-Dimensional Bulk Heterojunction Morphology for Achieving High Internal Quantum Efficiency in Polymer Solar Cells. Adv Funct Mater 2009;19:2398–406. doi:10.1002/adfm.200900183.
[145] Sirringhaus H, Brown PJ, Friend RH, Nielsen MM, Bechgaard K, Langeveld-Voss BMW, et al. Two-dimensional charge transport in self-organized, high-mobility conjugated polymers. Nature 1999;401:685–8. doi:10.1038/44359.
[146] Lindqvist C, Bergqvist J, Feng C, Gustafsson S, Bäcke O, Treat ND, et al. Fullerene Nucleating Agents: A Route Towards Thermally Stable Photovoltaic Blends. Adv Energy Mater 2014;4:1301437. doi:10.1002/aenm.201301437.
[147] Sharenko A, Treat ND, Love JA, Toney MF, Stingelin N, Nguyen T. Use of a commercially available nucleating agent to control the morphological development of solution-processed small molecule bulk heterojunction organic solar cells. J Mater Chem A 2014;2:15717–21. doi:10.1039/C4TA03469D.
[148] Jackson NE, Kohlstedt KL, Savoie BM, Olvera De La Cruz M, Schatz GC, Chen LX, et al. Conformational order in aggregates of conjugated polymers. J Am Chem Soc 2015;137:6254–62. doi:10.1021/jacs.5b00493.
[149] Choi M-H, Ko EJ, Han YW, Lee EJ, Moon DK. Control of polymer-packing orientation in thin films through chemical structure of D-A type polymers and its application in efficient photovoltaic devices. Polymer (Guildf) 2015;74:205–15. doi:10.1016/j.polymer.2015.08.003.
[150] Song KW, Choi MH, Han MH, Moon DK. Open circuit voltage increase by substituted spacer and thieno[3,4-c]pyrrole-4,6-dione for polymer solar cells. J Ind Eng Chem 2014;20:426–34. doi:10.1016/j.jiec.2013.04.037.
[151] Song KW, Song HJ, Lee TH, Heo SW, Moon DK. An effect on the side chain position of D-pi-A-type conjugated polymers with sp(2)-hybridized orbitals for organic photovoltaics. Polym Chem 2013;4:3225–35. doi:10.1039/c3py00195d.
[152] Akkuratov A V., Susarova DK, Moskvin YL, Anokhin D V., Chernyak A V., Prudnov FA, et al. A strong influence of the positions of solubilizing alkyl side chains on optoelectronic and photovoltaic properties of TTBTBTT-based conjugated polymers. J Mater Chem C 2015;3:1497–506. doi:10.1039/C4TC02432J.
[153] Livi F, Zawacka NK, Angmo D, Jørgensen M, Krebs FC, Bundgaard E. Influence of Side Chain Position on the Electrical Properties of Organic Solar Cells Based on Dithienylbenzothiadiazole- alt -phenylene Conjugated Polymers. Macromolecules 2015;48:3481–92. doi:10.1021/acs.macromol.5b00589.

[154] Metten B, Kostermans M, Van Baelen G, Smet M, Dehaen W. Synthesis of 5-aryl-2-oxopyrrole derivatives as synthons for highly substituted pyrroles. Tetrahedron 2006;62:6018–28. doi:10.1016/j.tet.2006.04.005.
[155] Takagi J, Sato K, Hartwig JF, Ishiyama T, Miyaura N. Iridium-catalyzed C–H coupling reaction of heteroaromatic compounds with bis(pinacolato)diboron: regioselective synthesis of heteroarylboronates. Tetrahedron Lett 2002;43:5649–51. doi:10.1016/S0040-4039(02)01135-8.
[156] Stalder R, Mei J, Reynolds JR. Isoindigo-based donor-acceptor conjugated polymers. Macromolecules 2010;43:8348–52. doi:10.1021/ma1018445.
[157] Jung EH, Jo WH. π-Extended low bandgap polymer based on isoindigo and thienylvinylene for high performance polymer solar cells. Energy Environ Sci 2014;7:650. doi:10.1039/c3ee42297f.
[158] Ho C-C, Chen C-A, Chang C-Y, Darling SB, Su W-F. Isoindigo-based copolymers for polymer solar cells with efficiency over 7%. J Mater Chem A 2014;2:8026. doi:10.1039/c4ta01083c.
[159] Dong X, Deng Y, Tian H, Xie Z, Geng Y, Wang F. Isoindigo-based low bandgap conjugated polymer for o-xylene processed efficient polymer solar cells with thick active layers. J Mater Chem A 2015;3:19928–35. doi:10.1039/C5TA05352H.
[160] Tao Q, Xia Y, Xu X, Hedström S, Bäcke O, James DI, et al. D–A 1 –D–A 2 Copolymers with Extended Donor Segments for Efficient Polymer Solar Cells. Macromolecules 2015;48:1009–16. doi:10.1021/ma502186g.
[161] Deng Y, Liu J, Wang J, Liu L, Li W, Tian H, et al. Dithienocarbazole and isoindigo based amorphous low bandgap conjugated polymers for efficient polymer solar cells. Adv Mater 2014;26:471–6. doi:10.1002/adma.201303586.
[162] Yue W, Ashraf RS, Nielsen CB, Collado-Fregoso E, Niazi MR, Yousaf SA, et al. A Thieno[3,2-b][1]benzothiophene Isoindigo Building Block for Additive- and Annealing-Free High-Performance Polymer Solar Cells. Adv Mater 2015:4702–7. doi:10.1002/adma.201501841.
[163] Elsawy W, Lee C-L, Cho S, Oh S-H, Moon S-H, Elbarbary A, et al. Isoindigo-based small molecules for high-performance solution-processed organic photovoltaic devices: the electron donating effect of the donor group on photo-physical properties and device performance. Phys Chem Chem Phys 2013;15:15193–203. doi:10.1039/c3cp52151f.
[164] Areephong J, San Juan RR, Payne A-J, Welch GC. A narrow band gap isoindigo based molecular donor for solution processed organic solar cells. New J Chem 2015;39:5075–9. doi:10.1039/C5NJ00436E.
[165] Ren Y, Hailey AK, Hiszpanski AM, Loo Y. Isoindigo-Containing Molecular Semiconductors : E ff ect of Backbone Extension on Molecular Organization and Organic Solar Cell Performance. Chem Mater 2014:6570–7. doi:10.1021/cm503312c.
[166] Graham KR, Wieruszewski PM, Stalder R, Hartel MJ, Mei J, So F, et al. Improved Performance of Molecular Bulk-Heterojunction Photovoltaic Cells through Predictable Selection of Solvent Additives. Adv Funct Mater 2012;22:4801–13. doi:10.1002/adfm.201102456.
[167] Zhang Y, Xiao M, Su N, Zhong J, Tan H, Wang Y, et al. Efficient strategies to improve photovoltaic performance of linear-shape molecules by introducing large planar aryls in molecular center and terminals. Org Electron 2015;17:198–207. doi:10.1016/j.orgel.2014.12.004.

[168] Kim G, Kang SJ, Dutta GK, Han YK, Shin TJ, Noh YY, et al. A thienoisoindigo-naphthalene polymer with ultrahigh mobility of 14.4 cm2/V·s that substantially exceeds benchmark values for amorphous silicon semiconductors. J Am Chem Soc 2014;136:9477–83. doi:10.1021/ja504537v.
[169] Dutta GK, Han A-R, Lee J, Kim Y, Oh JH, Yang C. Visible-Near Infrared Absorbing Polymers Containing Thienoisoindigo and Electron-Rich Units for Organic Transistors with Tunable Polarity. Adv Funct Mater 2013;23:5317–25. doi:10.1002/adfm.201300536.
[170] Chen C-M, Sharma S, Li Y-L, Lee J-J, Chen S-A. Thienoisoindigo-based copolymer with fused thieno[3,2-b]thiophene as a donor in thin film transistor applications with high performance. J Mater Chem C 2014;3:33–6. doi:10.1039/C4TC02355B.
[171] Hasegawa T, Ashizawa M, Matsumoto H. Design and structure–property relationship of benzothienoisoindigo in organic field effect transistors. RSC Adv 2015;5:61035–43. doi:10.1039/C5RA07660A.
[172] Nketia-Yawson B, Kang H, Shin E-Y, Xu Y, Yang C, Noh Y-Y. Effect of electron-donating unit on crystallinity and charge transport in organic field-effect transistors with thienoisoindigo-based small molecules. Org Electron 2015;26:151–7. doi:10.1016/j.orgel.2015.07.038.
[173] Han P, Gong X, Lin B, Jia Z, Ye S, Sun Y, et al. Solution processable low bandgap thienoisoindigo-based small molecules for organic electronic devices. RSC Adv 2015;5:50098–104. doi:10.1039/C5RA07889J.
[174] Kang H, An S, Walker B, Song S, Kim T, Kim JY, et al. Thienoisoindigo (TIIG)-Based Small Molecules for Understanding of StructureProperty-Device-Performance Correlations. J Mater Chem A 2015;3:9899. doi:10.1039/C5TA00016E.
[175] Chen Y, Du Z, Chen W, Han L, Liu Q, Sun M, et al. Near-infrared response thienoisoindigo-based small molecule for solution-processed bulk-heterojunction solar cells. Synth Met 2014;187:24–9. doi:10.1016/j.synthmet.2013.10.017.
[176] Lei T, Wang JY, Pei J. Design, synthesis, and structure-property relationships of isoindigo-based conjugated polymers. Acc Chem Res 2014;47:1117–26. doi:10.1021/ar400254j.
[177] Lei T, Dou J, Cao X, Wang J, Pei J. Electron-Deficient Poly(p□phenylene vinylene) Provides Electron Mobility over 1 cm 2 V −1 s −1 under Ambient Conditions. J Am Chem Soc 2013:12168–71. doi:10.1021/ja403624a.
[178] Lei T, Dou J-H, Cao X-Y, Wang J-Y, Pei J. A BDOPV-Based Donor-Acceptor Polymer for High-Performance n-Type and Oxygen-Doped Ambipolar Field-Effect Transistors. Adv Mater 2013;25:6589–93. doi:10.1002/adma.201302278.
[179] Li S, Yuan Z, Yuan J, Deng P, Zhang Q, Sun B. An expanded isoindigo unit as a new building block for a conjugated polymer leading to high- performance solar cells. J Mater Chem A 2014:5427–33. doi:10.1039/c3ta15291j.
[180] Katner AS, W JA. The Condensation of Isatin with Propionic Anhydride. J Chem Soc 1965;2:1455–60. doi:10.1039/JR9650001455.
[181] Chen S, Sun B, Guo C, Hong W, Meng Y, Li Y. 3,3'-(Ethane-1,2-diylidene)bis(indolin-2-one) based conjugated polymers for organic thin film transistors. Chem Commun (Camb) 2014;50:6509–12. doi:10.1039/c4cc02840f.
[182] Zhang L, Colella NS, Cherniawski BP, Mannsfeld SCB, Briseno AL. Oligothiophene semiconductors: Synthesis, characterization, and applications for organic devices. ACS Appl Mater Interfaces 2014;6:5327–43. doi:10.1021/am4060468.

[183] Mehmood U, Al-Ahmed A, Hussein IA. Review on recent advances in polythiophene based photovoltaic devices. Renew Sustain Energy Rev 2016;57:550–61. doi:10.1016/j.rser.2015.12.177.
[184] Marrocchi A, Lanari D, Facchetti A, Vaccaro L. Poly(3-hexylthiophene): synthetic methodologies and properties in bulk heterojunction solar cells. Energy Environ Sci 2012;5:8457. doi:10.1039/c2ee22129b.
[185] Graham KR, Mei J, Stalder R, Shim JW, Cheun H, Steffy F, et al. Polydimethylsiloxane as a Macromolecular Additive for Enhanced Performance of Molecular Bulk Heterojunction Organic Solar Cells. ACS Appl Mater Interfaces 2011:1210–5. doi:10.1021/am2000328.
[186] Ripaud E, Demeter D, Rousseau T, Boucard-Cétol E, Allain M, Po R, et al. Structure–properties relationships in conjugated molecules based on diketopyrrolopyrrole for organic photovoltaics. Dye Pigment 2012;95:126–33. doi:10.1016/j.dyepig.2012.03.021.
[187] Liu J, Walker B, Tamayo A, Zhang Y, Nguyen T-Q. Effects of Heteroatom Substitutions on the Crystal Structure, Film Formation, and Optoelectronic Properties of Diketopyrrolopyrrole-Based Materials. Adv Funct Mater 2013;23:47–56. doi:10.1002/adfm.201201599.
[188] Viterisi A, Gispert-Guirado F, Ryan JW, Palomares E. Formation of highly crystalline and texturized donor domains in DPP(TBFu)2:PC71BM SM-BHJ devices via solvent vapour annealing: implications for device function. J Mater Chem 2012;22:15175. doi:10.1039/c2jm31235b.
[189] Hu H, He J, Zhuang H, Shi E, Li H, Li N, et al. Triggering DRAM/SRAM memory behaviors by single atom substitution to alter the molecular planarity. J Mater Chem C 2015;3:8605–11. doi:10.1039/C5TC02014J.
[190] Yassin A, Leriche P, Allain M, Roncali J. Donor–acceptor–donor (D–A–D) molecules based on isoindigo as active material for organic solar cells. New J Chem 2013;37:502. doi:10.1039/c2nj40879a.
[191] Zhao J, Swinnen A, Assche G Van, Manca J, Vanderzande D, Mele B Van. Phase Diagram of P3HT / PCBM Blends and Its Implication for the Stability of Morphology Phase Diagram of P3HT / PCBM Blends and Its Implication for the Stability of Morphology 2009:1587–91. doi:10.1021/jp804151a.
[192] Wolfer P, Schwenn PE, Pandey AK, Fang Y, Stingelin N, Burn PL, et al. Identifying the optimum composition in organic solar cells comprising non-fullerene electron acceptors. J Mater Chem A 2013;1:5989–95. doi:10.1039/c3ta10554g.
[193] Deribew D, Renaud C, Fleury G, Brochon C, Cloutet E, Vignau L, et al. Optimization of the Bulk Heterojunction Composition for Enhanced Photovoltaic Properties : Correlation between the Molecular Weight of the Semiconducting Polymer and Device Performance. J Phys Chem B 2011:12717–27. doi:10.1021/jp207669j.
[194] Müller C, Ferenczi T a. M, Campoy-Quiles M, Frost JM, Bradley DDC, Smith P, et al. Binary Organic Photovoltaic Blends: A Simple Rationale for Optimum Compositions. Adv Mater 2008;20:3510–5. doi:10.1002/adma.200800963.
[195] Park YJ, Seo JH, Elsawy W, Walker B, Cho S, Lee J-S. Enhanced performance in isoindigo based organic small molecule field-effect transistors through solvent additives. J Mater Chem C 2015;3:5951–7. doi:10.1039/C5TC00605H.
[196] Karakawa M, Aso Y. Narrow-optical-gap π-conjugated small molecules based on terminal isoindigo and thienoisoindigo acceptor units for photovoltaic application. RSC Adv

2013;3:16259. doi:10.1039/c3ra42444h.
[197] Sahu D, Tsai C-H, Wei H-Y, Ho K-C, Chang F-C, Chu C-W. Synthesis and applications of novel low bandgap star-burst molecules containing a triphenylamine core and dialkylated diketopyrrolopyrrole arms for organic photovoltaics. J Mater Chem 2012;22:7945. doi:10.1039/c2jm16760c.